https://doi.org/10.35662/unine-thesis-2814

University of Neuchâtel, Switzerland

Faculty of Sciences

Center for Hydrogeology and Geothermics
(CHYN)

Mechanics of fault reactivation and its application to stress measurements

A Thesis Presented for the Degree of

Doctor of Sciences

by

Maria KAKURINA

Accepted on the recommendation of the examiners:

Prof. Benoît Valley, University of Neuchatel

Dr. Yves Guglielmi, Lawrence Berkeley National Laboratory

Dr. Christophe Nussbaum, Swisstopo

Prof. Stephen A. Miller, Université de Neuchâtel

Prof. Arno Zang, University of Potsdam

Defended on December 19, 2019

UNIVERSITÉ DE NEUCHÂTEL

Faculté des Sciences
Secrétariat-décanat de Faculté
Rue Emile-Argand 11
2000 Neuchâtel – Suisse
Tél : + 41 (0)32 718 21 00
E-mail : secretariat.sciences@unine.ch

IMPRIMATUR POUR THESE DE DOCTORAT

La Faculté des sciences de l'Université de Neuchâtel autorise l'impression de la présente thèse soutenue par

Madame Maria KAKURINA

Titre:

"Mechanics of fault reactivation and its application to stress measurements"

sur le rapport des membres du jury composé comme suit:

- Prof. ass. Benoît Valley, co-directeur de thèse, Université de Neuchâtel, Suisse
- Dr Yves Guglielmi, co-directeur de thèse, Lawrence Berkeley National Laboratory , Berkeley, USA
- Prof. Arno Zang, Université de Potsdam, Allemagne
- Dr Christophe Nussbaum, Swisstopo, Saint-Ursanne, Suisse
- Prof. Stephen A. Miller, Université de Neuchâtel, Suisse

Neuchâtel, le 19 décembre 2019

Le Doyen, Prof. P. Felber

P. Fel

Wingardium Leviosa!

Acknowledgements

First and foremost, I would like to express my sincerest gratitude to my supervisor Prof. Benoît Valley for his guidance, support, and scientific input throughout the years of my PhD. I was extremely lucky to have a supervisor who cared so much about my work, helped in clarification of any question and supported me in any situation. I also wish to express my deepest gratitude to Prof. Yves Guglielmi for his constant assistance, insightful suggestions, guidance and help throughout the project when I was in Neuchâtel and when I visited Lawrence Berkeley National Laboratory. My sincere thanks also goes to Dr. Christophe Nussbaum for his assistance and constructive comments on the project, especially on geological questions, and his help in providing the funding that allowed me to go to Berkeley and contribute to my research. I could not have imagined having better mentors for my PhD study. Without their assistance and precious support it would not be possible to conduct this research.

I also thank the Mont Terri Lab team for being so kind and helpful during my lab visits and to the Berkeley Lab team for hosting me during my short visits in their lab and helping me with everything I needed. I thank Dr. Branko Damjanac and the Itasca team for proving me with the 3DEC license throughout my PhD. Thanks to Prof. Steve Miller and Prof. Arno Zang for examining my project and giving constructive comments.

My sincere thanks also goes to Dr. Julien Straubhaar and Przemyslaw Juda for their help on mathematical and programming aspects of the thesis. I also thank my colleagues and friends from the University for stimulation discussions and all the fun we had in the last four years. I am also very thankful to my family that was supporting me every day during my stay away from home. And of course, my friends outside of the University who have been generous with their support and inspire me to pursue my ambitions.

M. K.

Summary

In this research project, we studied the mechanics of fault reactivation due to fluid injection and estimated in-situ stress from flow rate, pressure and the dislocation record collected during fault reactivation tests. In-situ stress estimation is an essential part of any underground project. This is particularly true for challenging projects as deep geothermal energy exploitation, nuclear waste disposal and CO_2 capture and storage. These projects have the potential to reactivate faults through stress perturbations induced by fluid injection or underground excavation. The correct estimation of the in-situ stresses and fault mechanics activation due to stress perturbation is important to provide safe and stable design of these projects.

In this work, we developed a protocol to estimate the in-situ stress by using the data of three dimensional (3D) displacement induced by fluid injection. The displacement data is obtained using the Step-Rate Injection method for Fracture in-Situ properties (SIMFIP), which allows coupled flowrate-pressure-three dimensional displacement monitoring during the fluid injection. The protocol was applied to two fault activation experiments conducted in two different types of rocks – shales at the Mont Terri rock laboratory, Switzerland, and carbonates at the Rustrel Low Noise Underground Laboratory (LSBB). Both experiments show complex coupled flowrate-pressure-3D displacement response during the injection.

Our stress inversion protocol relies on the combination of fracture slip orientation data and pressure and flow rate analyses. A fundamental step in our work was to verify the validity of the Wallace-Bott hypothesis under inhomogeneous pressure field. This allows us to use the slip orientation as a robust indicator of the resolved shear stress direction on the tested fracture plane and thus to use stress inversion techniques to deduce far-field stresses. A second important step was to develop a rational to identify fracture slip orientation within the complex displacement signal recorded during a test. This complex signal results from the superposition of multiple hydromechanical coupled processes. We based our approach on the analyses of displacement rate during constant pressure injection steps. Finally, we develop a methodology to systematically integrate our data and estimate the far field stress. Our method allows to estimate the complete stress tensor from a single injection test opening future opportunities for acquiring profiles of full stress tensor along

exploration boreholes. At the two sites where we applied our methodology, the Mont Terri and LSBB, our derived stress estimates are in good agreement with independent stress characterization of the sites. We propose to further develop the methodology in the future by improving the injection protocol and by testing it in other locations and geological environments.

Keywords: geomechanics, fault reactivation, fluid injection, SIMFIP probe, 3-dimentional in-situ displacement, induced slip, stress state, stress inversion

Résumé

DANS ce projet de recherche, nous avons étudié la mécanique de la réactivation des failles due à l'injection de fluide et les contraintes in situ estimées à partir du débit, de la pression et du record de dislocation collecté lors des tests de réactivation des failles. L'estimation des contraintes in situ est un élément essentiel de tout projet souterrain. Cela est particulièrement vrai pour les projets difficiles comme l'exploitation de la géothermie profonde, l'élimination des déchets nucléaires et la capture et le stockage du CO_2. Ces projets ont le potentiel de réactiver des failles par des perturbations de contraintes induites par l'injection de fluide ou l'excavation souterraine. L'estimation correcte des contraintes in situ et de l'activation de la mécanique des défauts due à la perturbation des contraintes est importante pour fournir une conception sûre et stable de ces projets. Dans ce travail, nous avons développé un protocole pour estimer la contrainte in situ en utilisant les données du déplacement tridimensionnel (3D) induit par l'injection de fluide. Les données de déplacement sont obtenues à l'aide de la méthode d'injection à débit progressif pour les propriétés de fracture in situ (SIMFIP), qui permet une surveillance couplée débit-pression-déplacement tridimensionnel pendant l'injection de fluide. Le protocole a été appliqué à deux expériences d'activation de failles menées dans deux types différents de roches: des schistes au laboratoire de roches du Mont Terri, en Suisse, et des carbonates au laboratoire souterrain à faible bruit de Rustrel (LSBB). Les deux expériences montrent une réponse complexe couplée débit-pression-déplacement 3D pendant l'injection. Notre protocole d'inversion de contrainte repose sur la combinaison de données d'orientation de glissement de rupture et d'analyses de pression et de débit. Une étape fondamentale de notre travail a été de vérifier la validité de l'hypothèse de Wallace-Bott sous champ de pression inhomogène. Cela nous permet d'utiliser l'orientation de glissement comme un indicateur robuste de la direction de la contrainte de cisaillement résolue sur le plan de fracture testé et ainsi d'utiliser des techniques d'inversion de contrainte pour déduire les contraintes de champ lointain. Une deuxième étape importante a été de développer un repere pour identifier l'orientation du glissement de fracture dans le signal de déplacement complexe enregistré pendant un essai. Ce signal complexe résulte de la superposition de multiples processus couplés hydromécaniques. Nous

avons basé notre approche sur les analyses du taux de déplacement lors des étapes d'injection à pression constante. Enfin, nous développons une méthodologie pour intégrer systématiquement nos données et estimer la contrainte en champ lointain. Notre méthode permet d'estimer le tenseur de contrainte complet à partir d'un test d'injection unique ouvrant de nouvelles opportunités pour acquérir des profils de tenseur de contrainte complet le long de forages d'exploration. Aux deux sites où nous avons appliqué notre méthodologie, le Mont Terri et LSBB, nos estimations de stress dérivées sont en bon accord avec la caractérisation indépendante du stress des sites. Nous proposons de développer davantage la méthodologie à l'avenir en améliorant le protocole d'injection et en le testant dans d'autres emplacements et environnements géologiques.

Mots-clés: géomécanique, réactivation des failles, injection de fluide, sonde SIMFIP, déplacement in situ tridimensionnel, glissement induit, état de contrainte, inversion de contrainte

Contents

Summary **9**

Résumé **11**

1 Introduction **17**
1.1 Motivations . . . 17
1.2 Context of the thesis . . . 22
1.3 Objectives . . . 23
1.4 Structure of the thesis . . . 24

2 Geological context of the Mont Terri lab and FS experiment **25**
2.1 Mont Terri laboratory and FS experiment . . . 25
2.2 Geological setting . . . 26
2.3 Data and methodology . . . 27
2.4 Structural elements observed in the boreholes . . . 28
2.4.1 Bedding fractures . . . 28
2.4.2 Calcite veins . . . 29
2.4.3 Scaly clays . . . 29
2.4.4 Fault gouge . . . 29
2.4.5 Fault planes . . . 30
2.5 Rock types of the Main Fault . . . 33
2.6 Detailed structural analyses of tested intervals . . . 40
2.6.1 Borehole BFS1 – Test 37.65 – Monitoring interval . . . 40
2.6.2 Borehole BFS1 – Test 47.2 . . . 40
2.6.3 Borehole BFS2 – Test 37.2 . . . 43
2.6.4 Borehole BFS2 – Test 40.6 . . . 44
2.6.5 Borehole BFS2 – Test 44.65 . . . 46
2.7 Conclusions . . . 49

3 Injection protocol and initial data evaluation **51**
3.1 Test 37.2 . . . 52
3.1.1 Step-by-step pressure increase injection using manual pump . 53

3.1.2 Pulse tests using the engine pump . . . 55
3.1.3 Pressure step-up injection using engine pump. . . . 57
3.2 Test 40.6 m . . . 59
3.2.1 Step-by-step pressure increase injection using manual pump . 59
3.2.2 Pulse tests using the engine pump . . . 60
3.2.3 Step-rate injection using the engine pump . . . 61
3.3 Test 47.2 m . . . 62
3.3.1 Step-by-step pressure increase injection using manual pump . 63
3.3.2 Constant flowrate injection using manual pump . . . 64
3.3.3 Step-rate injection . . . 64
3.4 Test 44.65 m . . . 65
3.5 Numerical investigation of displacements in elastic rock mass . . . 65
3.5.1 Methodology and parameters of the numerical model . . . 66
3.5.2 Results of the numerical investigation . . . 67
3.6 Conclusions . . . 68

4 Slip perturbation during fault reactivation by a fluid injection 71
4.1 Abstract . . . 71
4.2 Introduction . . . 72
4.3 Theoretical background . . . 76
4.3.1 Orientation of the resolved shear stress (Wallace-Bott hypothesis) . . . 76
4.3.2 Problem statement and conceptual model . . . 78
4.4 Methodology . . . 80
4.4.1 Background and assumptions of numerical approach . . . 80
4.4.2 Parameters of the numerical model . . . 82
4.4.3 Eshelby analytical solution . . . 84
4.5 Results . . . 85
4.5.1 Misfit angle numerical and analytical . . . 85
4.5.2 Sensitivity analysis . . . 89
4.6 Discussion . . . 91
4.7 Conclusions . . . 94
4.8 Acknowledgements . . . 95

5 In-situ direct displacement information on fault reactivation during fluid injection 97
5.1 Abstract . . . 97
5.2 Introduction . . . 98
5.3 SIMFIP probe . . . 100
5.4 Geological and experimental settings . . . 101

5.5 Injection protocols of the conducted tests and its first interpretation . 104
5.5.1 Injection protocol for shales and carbonates 105
5.5.2 General analysis of the coupled pressure-flowrate-displacement data 108
5.6 Protocol for pre-processing the displacement data to identify slip vectors 110
5.6.1 Isolating time windows when the injection pressure in the chamber is constant 110
5.6.2 Identification of a pseudo-linear displacement-vs-pressure response 111
5.6.3 Identification of the highest displacement rate 112
5.7 Analysis of the slip vectors orientation 113
5.7.1 Shales 113
5.7.2 Carbonates 117
5.8 Discussion 122
5.8.1 Borehole near field response to a fluid 122
5.8.2 Isolating displacement events on natural reactivated fractures 123
5.8.3 Estimation of fracture normal stress 125
5.8.4 The Comparison between shales and carbonates behavior . . . 126
5.9 Conclusions 128
5.10 Acknowledgements 128

6 Estimation of the full stress tensor from fluid injection induced fault dislocation data 129
6.1 Abstract 129
6.2 Introduction 129
6.3 Stress state at study sites 133
6.4 Displacement and Pressure datasets 133
6.5 Methodology for stress tensor estimation 136
6.5.1 Reduced stress tensor 137
6.5.2 Stress magnitudes and reduction of the possible stress solutions 139
6.5.3 Constructing confidence intervals for a mean of in-situ stresses 141
6.6 Results 142
6.6.1 Mont Terri test site 142
6.7 Application to stress measurements in carbonates at the LSBB test site 144
6.8 Discussion 147
6.8.1 LSBB test site 149
6.9 Conclusions 150
6.10 Acknowledgements 151

7 Synthesis, Conclusions, Outlook **153**

7.1 Synthesis 153

7.2 Conclusions 156

7.3 Outlook 156

Appendices **159**

Chapter 1

Introduction

1.1 Motivations

COUPLED hydromechanical processes are important for the development of deep engineering projects, particularly for shaping the future energy portfolio to reduce unwanted effects of climate change. This concerns mitigation techniques like CO_2 storage, developing alternative energy production (e.g., geothermal) and finding safe subsurface waste storage options (e.g., radioactive or produced water). In all these applications, subsurface pressure changes associated with each technology can have undesirable consequences like fault reactivation and associated microseismicity, which will affect confinement safety (radioactive waste), cap rock integrity (CO_2), or lead to abandonment of geothermal projects. Thus, a better understanding of fault mechanics under increased pressure conditions is required for safe applications of these technologies. In turn, this requires a better understanding of the in-situ stress state because it has a primary effect on fault mechanics.

In-situ stress orientations and magnitudes have a first order effect on the stability of underground constructions, such as tunnels, mines, boreholes, nuclear waste and CO_2 storage. Magnitudes and orientations of stresses are used to establish safe design and excavation of the underground openings, and define the most favorable drilling parameters for borehole stability. Errors in in-situ stress estimation lead to rock failure, collapses and bursting, which not only result in economic losses, but can also have unwelcomed societal and environmental consequences (e.g., leakage, contamination, seismicity etc.).

The challenges associated with stress estimation promoted the development of variety measurement techniques. The techniques are based on hydraulic injections, strain measurements, orientation of breakouts (i.e., stress induced wellbore failure), and focal mechanisms from earthquakes. For obtaining robust estimates, the techniques are typically combined due to individual advantages and limitations in each

method. For example, hydraulic fracturing gives an estimation only of minimum principal stresses magnitude, while focal mechanisms only estimate stress orientations and ratio. The combinations of methods make the stress measurements time consuming and economically unfavorable and requires the combination of a broad field of expertise.

It has always been a challenge to estimate the in-situ stress state due to the rock heterogeneity, which controls rock strength, and the existence of fault zones, which can lead to stress rotations. Each stress measurement techniques provide stress estimate at different scale (e.g. cm-scale for overcoring techniques, m-scale for hydraulic fracturing) and it is unclear what is the relevant stress estimation scale. Generally, the deeper the application, the more difficult it is to estimate the in-situ stress [Zang and Stephansson, 2009]. In addition, each engineering application causes stress perturbations because of the activity itself. Underground openings cause stress concentration, which can lead to deformation and failure on the walls (e.g., spallings, collapses, fracturing, and creep). Fluid injections during oil and gas or CO_2 storage operations and geothermal energy production, cause stress magnitude and orientation changes and can induce seismicity. Therefore, the stress state estimation should include the knowledge of both: the regional stress state and possible stress perturbations.

As highlighted in many studies, discontinuities (e.g. faults and joints) and rock heterogeneity have a dominant effect on stress perturbations. Such perturbation occurs at all scale as can be shown by the study of stress orientation variations using borehole failure observation, as for example along 5 km deep geothermal boreholes in Soultz-sous-Forêts in France [Valley and Evans, 2007, Valley, 2007, Moein et al., 2019]. The most significant and largest scale variations of maximum horizontal stress coincided with the most significant fracture zones intersected by the investigated wells. Shamir and Zoback [1992] also observed the stress variations associated with active faults in the Cajon Pass well, located 4.2 km from the San Andreas fault in Southern California. Sahara et al. [2014] inferred that the deviation in breakouts orientations occur in the vicinity of fault cores. They suggested that the breakouts orientations are strongly influenced by the fracture orientation. The heterogeneity in breakout orientations increases with multiple fracture families and fracture density. Shamir and Zoback [1992] also interpreted that the borehole breakouts heterogeneities formed as a result of rock mechanical properties, such as weak zones with different elastic moduli, rock strength and fracture patterns. Rajabi et al. [2017] observed the rotations of breakouts by 90° near fractures in relatively homogeneous rock mass and stable tectonic settings. Such strong local variation calls for caution when interpreting stress measurement estimate resulting from few point measurements. When occurring continuously along a well, borehole breakouts

are the best indicators to characterize stress orientation and its heterogeneities, but it does not provide robust stress magnitude estimates.

Chang and Jo [2015] suggested that the stress magnitudes variations are controlled by the frictional property of natural discontinuities. The local stress perturbations are guided by heterogeneous distribution of natural discontinuities having various frictional properties. The movements of pre-existing faults are also considered to be the reason of stress perturbations by Barton and Zoback [1994]. They confirmed that the stress drops along the activated faults are sufficient to perturb the local stress. Valley et al. [2014] explained the heterogeneity of local stress field by stress release on natural fractures. Yale [2003] found that influence of the fault zone on stress perturbation is dependent on the difference between the magnitudes of the maximum and minimum horizontal stress: the smaller is the difference, the larger the influence of the fault's zone. The assumption of stress perturbation occurrence between the horizontal stress components was also used by Schoenball and Davatzes [2017]. Recently, Lei and Gao [2019] showed that large stress perturbations can be induced by the increase of the rock heterogeneity and far-field stress ratio. If the rock is highly heterogeneous and the stress ratio is low, then the stress perturbations are controlled by the matrix. If the stress ratio increases, the stress distribution becomes more affected by fractures. In the homogeneous rock matrix the stress is affected by fractures even under low stress ratio.

One of the method to estimate the complete stress tensor in a fractured media is a Hydraulic Tests on Pre-existing Fractures (HTPF), proposed by Cornet and Valette [1984]. The test is executed in a sealed section of the borehole isolated by a straddle packer. The test consists of the re-opening of pre-existing fractures by injected a fluid using step-up pressure cycles in the sealed section. Various approaches are used to analyses the pressure and flow rate data in order to obtain an estimation of the fractures normal stress. At least 6 measurements of differently oriented fractures is required to estimate the complete stress tensor, which requires the assumption that the stress state is homogeneous. In view of the literature survey presented above, this assumption is not likely to be valid in many subsurface systems. Since the orientations of the fractures play an important role in stress estimation, therefore, borehole imaging techniques or core logging are required prior the test.

Assumptions about stress homogeneity, necessity of single differently orientated fractures in the tested interval, and large number of tests arise limitations to the HTPF method. Moreover, the HTPF test focusses only on fracture opening, ignoring fracture dislocation and associated dilatation, which likely occurs prior to fracture opening. The interpretation of HTPF data are based on simplistic assumption of fracture reactivation, largely because the available data, only pressure and flow rate, do not allow understanding of the details of the reactivation mechanics. However,

fracture slip can be used for stress computation. This is a common technique in paleo stress inversion from fault/striae datasets [Angelier, 1990, Carey, 1974] and in situ stress inversion from focal mechanisms of earthquakes [Michael, 1987, Gephart and Forsyth, 1984, Angelier, 2002].

The slip orientation is the key parameter for the stress inversion. Since the beginning of the last decade, the orientation of the in situ slip is possible to measure using the step-rate injection method for fracture in situ properties - SIMFIP [Guglielmi et al., 2013]. The SIMFIP probe allows coupled monitoring of pressure, flowrate and 3-dimensional displacement during fault reactivation experiment.

Fault reactivation experiments using the SIMFIP probe have already been executed and analyzed in several underground laboratories and different rock types – shales at Mont Terri in Switzerland [Guglielmi et al., 2017, Jeanne et al., 2017, 2018b, Guglielmi, 2016, Guglielmi et al., 2019] and at Tournemire in France [De Barros et al., 2016, Guglielmi et al., 2015b, Rivet et al., 2016], and carbonates at Low Noise Underground laboratory LSBB [Derode et al., 2015, Guglielmi et al., 2015a, Duboeuf et al., 2017, Duboeuf, 2018, Cappa et al., 2018, 2019]. These experiments were mainly focused on estimating fault hydromechanical properties at the decameter scale, couplings between fault slip, fluid pressure and induced seismicity, and understanding in situ fault permeability variations. An increase of permeability during fluid injection can be beneficial in providing pathways for Enhanced Geothermal systems (EGS) in hot dry rocks [Jeanne et al., 2014] or problematic, e.g. fault leakage at nuclear waste storage site [Guglielmi et al., 2017], CO_2 sequestration sites [Zoback and Gorelick, 2012] or micro-seismicity associated to EGS, which can lead to suspension of geothermal developing projects [Häring et al., 2008, Edwards et al., 2015].

In both, shales and carbonates, the results showed that the fault permeability increases during the fluid injection. In shales, Guglielmi et al. [2015c] and Guglielmi et al. [2015b] showed that little stress changes (e.g., underground excavations) as well as micromillimiter displacement can induce a high leakage potential without generating any noticeable seismicity or being aseismic. In carbonates, an increase of permeability was also observed under a slow and dilatant aseismic slip, which was followed by the slip rate increase, reduced dilatancy and micro-seismic events [Guglielmi et al., 2015a].

In Mont Terri shales, the relations between slip, changes in permeability and mechanisms leading to seismicity were studied by Jeanne et al. [2018b]. They found that the hydromechanical behavior during fluid diffusion is very complex. Ruptures induced by same injection protocols can either create or destroy the fluid diffusion pathways, which makes the permeability quite heterogeneous. Similar pressure increase conditions also induce different slip behavior along the reactivated fault.

Depending of fluid diffusivity, the rupture either favors or impedes secondary ruptures. In addition, rupture area is larger than the pressurized area. Jeanne et al. [2018b] discussed that due to this difference in dimension, it is not straightforward to relate seismic events to change in fault permeability. In Tournemire shales, De Barros et al. [2016] observed that the seismic events also occurred far from the injection points and strongly sensitive to the structural heterogeneity and permeability. They showed that the presence of fluid does not favor seismicity near the injection areas. This result is consistent with observations from the experiment in carbonates in LSBB, where the 96 % of the slip in pressurized zone is slow and aseismic [Duboeuf et al., 2017, Duboeuf, 2018]. Also in carbonates, Cappa et al. [2018] analyzed the interaction between fault permeability increase, induced stress perturbation and the growth of aseismic slip using hydromechanical modelling. The authors shows that the permeability increases and stress perturbation and friction weakening behavior affect the pressure diffusion and slip growth. The authors showed that the permeability increases induces the growths of the aseismic slip zones.

Based on the results of these reactivation experiments, it was proposed that the aseismic deformation and related stress perturbation transferred thought aseismic failure can trigger seismic events [Guglielmi et al., 2015a, Duboeuf et al., 2017, Duboeuf, 2018, De Barros et al., 2018, 2019, Cappa et al., 2019]. The aseismic motion can be an additional mechanics of seismic events occurrence together with well-known fluid pressure diffusion, coulomb stress transfer and poro-elastic effects [Coulomb, 1773, Hubbert and Rubey, 1959, Ellsworth, 2013].

These results were confirmed by the recent founding from De Barros et al. [2019] and Moein et al. [2019]. Analyzing data from the experiments in both shales and carbonates, De Barros et al. [2019] estimated the magnitudes of earthquakes by evaluating seismic energy released during fluid injection using the data from ten injection experiments performed in shales and carbonates. They explained that the variability of number and magnitudes of the seismic events between tests by the presence of aseismic motion. In addition, De Barros et al. [2019] demonstrated that the released energy correlates with the injected volume and associated aseismic deformation. Moein et al. [2019] also showed that the magnitude of seismic events can be predicted as a function of the injection volume and associated rupture size distribution.

By combining the injection protocol from the HTPF method to capture critical stress magnitudes with the measurement of fracture dislocation to capture critical orientations during fluid injection, one can analyze the stress perturbations associated with the fluid injection induced aseismic and seismic motion to estimate the full stress tensor. In addition to the estimation the stress perturbation and in situ stresses, such a method could mitigate stress estimation uncertainty and improve

economic favorability of such tests. This method also quantifies the orientation and magnitudes of the stress state using a tensorial approach, which considers the inherent relations between the orientations and the magnitudes.

To test the validity of this measurement technique, this thesis focuses on an injection test that was part of the Fault Slip (FS) experiment, which was executed in unweathered and unaltered fault zone in Opalinus Clays at the Mont Terri rock laboratory. The technique is also applied to carbonates in the Low-Noise Underground Laboratory (LSBB) in France. The main motivation of this study is to understand what the additional information about the deformation brings in terms of the estimation of the in-situ stress state. This motivation also leads to understanding the mechanics of fault reactivation. The mechanics of fault reactivation reflect the evolution of the coupling between fault slip, pore pressure and fluid migrations.

1.2 Context of the thesis

Clay rich formations are considered to be a natural barrier for a radionuclide and fluid (water, hydrocarbons, CO_2) migration and are selected for radioactive waste disposable operations. Faults crossing these formations could jeopardize their barrier role. Such faults are difficult to study on surface exposure because of its quick alteration at the Earth's surface. The Mont Terri rock laboratory provides exceptional conditions to investigate the unweathered, perfectly exposed scaly fault zone architecture through clay-rich formation.

Prior study performed at the Mont-Terri laboratory on a large fault crossing the laboratory (called the Main Fault) demonstrated that the permeability of the fault and associated fault rocks is similar to the surrounding clay shale and thus do not present a preferential flow path way. However, the waste disposal operations will generate pore pressure increase (e.g., due to thermal effects or CO_2 generation related to steal canister oxidation). Such pressure increase has the potential to reactivate faults and thus it is unclear how the permeability of the fault may evolve with time when reactivated. Thus, the main objective of the FS experiment at the Mont-Terri lab is assessing fault stability and permeability evolution in the case of pore pressure increase.

In order to study fault reactivation, it is required to capture displacements at the injection point, as it is not possible to rely on microseismic data only because it is expected that a large part of the reactivation is occurring in an aseismic manner. The SIMFIP probe developed by Guglielmi et al. [2013] is an ideal tool for such application. In addition to deformation, the SIMFIP probe monitors flowrate and pressure occurring during the fluid injection. The protocol applied in Mont-Terri was designed to capture fault activation and register flow characteristics changes

associated with fault activation. Similar data are available from another fault reactivation experiment conducted in limestones in the LSBB. These data will be used to compare the coupled hydromechanical response obtained from different rock types.

Many aspects are involved in such an experiment with complex hydromechanical coupling. The in-situ stress has a primarily control on the rock mass response to injection. Even if this was not the primary goal of the FS experiment, this led to the idea that the injection / displacement data from the FS experiment could also be used as a way to estimate in-situ stresses. This idea is at the root of this research work and drives the objectives described below.

1.3 Objectives

The main objectives of this PhD thesis are the following:

1. Building a highly-detailed structural model of the fault zone in the vicinity of the injection zone at Mont Terri, with particular emphasis on the orientation of the fractures and faults.

2. Interpreting the overall flowrate-displacement-pressure records during the injection tests at Mont Terri.

3. Understanding the reliability for stress inversion of the slip orientation measured during the fluid injection in terms of validity of the Wallace-Bott hypothesis.

4. Understanding the primary activated effects during injection experiments, and their effect on the measured displacement. Based on this understanding, develop a protocol for displacement data processing to simplify the complex response of the displacement data and extract the relevant slip orientation during the injection that can be used for stress inversion.

5. Developing a protocol for using the processed displacement data in stress inversion and understanding if the displacement information can be a basic tool to develop new techniques to measure stress in deep boreholes.

This thesis is mainly focused on the pressure-flowrate-displacement response during fault reaction experiments in the Opalinus Clays at Mont Terri Rock Laboratory. For comparison and to further validate the proposed approaches, we applied it also to a fault reactivation data set in carbonates acquired at the LSBB.

1.4 Structure of the thesis

The thesis is built around the five objectives listed above and consequently consists of five main chapters. Chapter 2 covers the geology of the experimental site in Mont Terri and gives a structural description of the injection intervals. Chapter 3 gives an overview of the flowrate-pressure-displacement response during the fluid injection. In addition, we numerically simulate a reversible rock mass response to fluid injection to understand how it affects the anchors measurements. Chapter 4 investigates if the measured slip during the fluid injection can be used for stress inversion based on the Wallace-Bott hypothesis. This chapter was published as: *Kakurina, M., Guglielmi, Y., Nussbaum, C. and Valley, B., 2019. Slip perturbation during fault reactivation by a fluid injection. Tectonophysics, 757, pp.140-152.* Chapters 5 and 6 cover main objectives related to processing of the data in order to identify slip vectors, and its application to the stress inversion. Chapters 5 and 6 also consider another case study in carbonates in LSBB. This case study was chosen to compare the flowrate-pressure-displacement response between shales and carbonates. We plan to submit Chapters 5 and 6 for journal publications and thus these chapters are written as stand-alone manuscripts. The final section of the thesis (Chapter 7) summarizes the main outcome of the research work and propose directions for future studies.

Chapter 2

Geological context of the Mont Terri lab and FS experiment

2.1 Mont Terri laboratory and FS experiment

The Opalinus Clay formation is considered to be a potential caprock for future nuclear waste disposal in Switzerland. The Mont Terri Rock Laboratory provides exceptional conditions to investigate its hydrogeological, geochemical and mechanical properties of the Opalinus Clay in-situ. The Mont Terri rock laboratory is located in the canton of Jura, near St. Ursanne, Switzerland. The laboratory can be accessed via the safety gallery of the Mont Terri motorway tunnel and consists of 3 main galleries – Gallery 98, Gallery 08 and Gallery 18 and many experimental niches. Over 150 experiments have already been performed in the URL [Bossart et al., 2018, 2017, Bossart, 2007]. One of them is a Fault Slip (FS) experiment that was executed in Mont Terri in 2015 [Guglielmi, 2016, Guglielmi et al., 2017].

The FS experiment is located at the south end of Mont Terri URL Gallery 08 (Figure 2.1). It is conducted in-situ in un-weathered Opalinus clay fault zone penetrated by boreholes and aims at exploring its stability. The FS experiment consists of injecting fluids in the upper, middle and lower parts of the main tectonic structure within the Opalinus Clay, so-called the Main Fault, using the SIMFIP probe [Guglielmi et al., 2013].

The FS experiment was conducted in two phases [Guglielmi, 2016]. Phase 1 was conducted in June 1-12, 2015 in the borehole BFS1, which was drilled 3 weeks before the beginning of the phase. Phase 1 included an installation of the seismic monitoring system in borehole BFS3 and conducting the test at 47.2 m below the gallery floor in BFS1 using one SIMFIP probe (S1). Phase 2 was conducted between October 14 and November 19, 2015. The phase 2 included the installation of the second SIMFIP probe (S2) in borehole BFS1 at 37.65 m below the gallery floor and

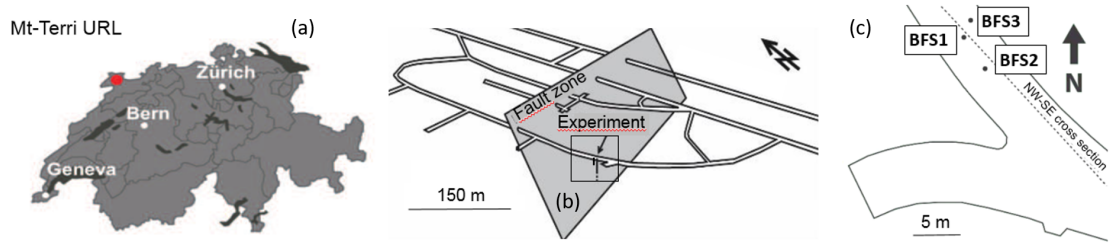

Figure 2.1: The location of FS experiment: (a) location of the Mont Terri URL, (b) Experiment location in Mont Terri URL; (c) Map of the boreholes geometry in the FS experiment zone [Guglielmi, 2016]

conducting three injection tests at 37.2 m, 40.6 m and 44.65 m below the gallery floor in BFS2 using the SIMFIP probe (S1). The probe S2 in BFS1 was mostly used for monitoring of injections conducted in BFS2. The borehole BFS2 was drilled 2 weeks before the beginning of phase 2.

The boreholes BFS1, BFS2 and BFS3 intersect the entire Main Faults zone that gives an opportunity to investigate its architecture by analyzing available core and borehole optical televiewer data.

This section describes a detailed structural mapping of the Main Fault from boreholes data for the FS-experiment in Mont-Terri Rock laboratory. The main objectives of this section are:

1. Document detailed structural analyses of three FS boreholes, that are fully cored, logged and spaced 1.7 to 4.3 m apart;
2. Characterize the statistical distributions of fracture spacing populations associated with the Main Fault;
3. Develop a fault rock type approach relevant for the Mont-Terri main fault setting;
4. Provide a detailed optical televiewer image of the structures within each injection interval;
5. Develop a 2D model for the Main Fault zone in the experiment vicinity;
6. Analyze the fault kinematic indicators and evaluate the paleostresses which could be potentially responsible for fault slip during the geological history of the Main Fault.

2.2 Geological setting

The Mont Terri laboratory is entirely located in the Opalinus Clay in the southern limb of the Mont Terri anticline about 300 m below the surface. Opalinus Clay are

Torcian-Aalenian marine sediment up to 160 m thick that consist of argillaceous clay shale rock. Clay minerals compose 40-80% of the Opalinus clay shales [Bossart, 2011].

There are different facies of Opalinus clays that can be distinguished: shaly in the lower part of the formation, sandy facies in the middle and upper part of the formation, and carbonate-rich, sandy in the middle part of the formation [Blaesi et al., 1991, Schaeren and Norbert, 1989, Thury and Bossart, 1999]. The various facies are explained by different sedimentary environment during the time of deposition.

The investigated area is in the shaly facies of the Opalinus Clay and belongs to the southern limb of the Mont Terri Anticline. Bedding dips SSE between 50° in the southern part to 30° in the northern part of the laboratory. The anticline was formed in the late Miocene and Pliocene and lead to a complex pattern of thrusted faults, extensional faults and strike slip faults [Nussbaum et al., 2011, Jaeggi et al., 2017]. The fold axis is almost perpendicular to the SSE-NNW tectonic stress direction during the Middle Miocene Jura thrusting phase.

The Main Fault is a large tectonic fault zone in the center of the Opalinus formation and can be traced on all Mont Terri tunnel intersections. Three boreholes (BFS1, BFS2 and BFS3) cross the Main Fault, which also outcrops along the tunnel walls ∼20 m up dip from the boreholes. Generally, the Main Fault is a shear zone with NW trusting. The thickness of the fault zone varies laterally from 1 m in the outcrops and up to 6.5 m in the boreholes. The Main Fault has three main fracture systems, that were also observed in the Mont Teri Rock laboratory outcrops [Nussbaum et al., 2011, Jaeggi et al., 2017]: (1) moderately SSE-dipping reverse faults, (2) low angle SW-dipping fault planes and flat-lying (sub-horizontal) faults and (3) moderately to steeply inclined N to NNE-striking sinistral strike-slip faults. More detailed geological setting is described by Nussbaum et al. [2011], Jaeggi et al. [2017], Bossart et al. [2017, 2018], Hostettler et al. [2018].

2.3 Data and methodology

The initial data provided for the present work are (1) the data obtained by an optical televiewer (OPTV) and (2) cores.

Optical televiewer logging yields an image of the inside of a borehole using visible light optics. It provides a continuous, detailed and oriented 360° true color image with possibility to obtain a complete feature analysis that includes dip, strike, frequency and fracture aperture. A total of 150 m of the boreholes have been logged in three FS boreholes. However, in this work only data relevant for the FS experiment and from the same interval with core sampling were investigated, that is 43 m (see Table 2.1).

Table 2.1: The depths of detailed mapping of FS boreholes and injection intervals

Borehole	Depth of detailed mapping	Injection (i)/monitoring(m) interval, m	Center of the displacement cage, m	Relation to a Main Fault
BFS1	35.0-49.0	36.31-38.79 (m)	37.65	within
		45.84-48.32 (i)	47.2	beneath
BFS2	35.0-50.0	35.85-38.33 (i)	37.2	above
		39.25-41.73 (i)	40.6	above
		43.30-45.78 (i)	44.65	within
BFS3	35.0-49.0	-	-	-

There are different types of discontinuities observed in the core and by optical televiewer including bedding planes fractures, faults planes, scaly clays, veins, broken zones and artificial drilling discontinuities. Every discontinuity has been correlated between the core and the optical borehole image. Dip direction and azimuth have been measured for each fracture. In addition, the slickenside analyses of the fault planes reveal the slip direction, surface polishing and roughness. The slip direction, its sense and fracture orientations in the injected intervals were used to estimate a paleo stress orientations using an inversion method by Angelier [1990]. Since the tectonic history of the Main Fault and the Mont Terri anticline is very complex [Nussbaum et al., 2011, Jaeggi et al., 2018, Hostettler et al., 2018], the paleostress estimation in this work is simplistic and include the result of multiple tectonic events.

The statistical distribution of fracture spacing population was taken as the basis for rock type classification. We used the classification to correlate the types between the boreholes and build a 2D model (vertical section perpendicular to fault strike) of the FS experiment.

2.4 Structural elements observed in the boreholes

There are several structural elements observed during the core mapping: bedding and fault plane fractures, veins, scaly clays, including shear zones, microlithons, S-C bands and microfolds. Artificial discontinuous and broken or absent zones are noted in the borehole description, but not analyzed in this work.

2.4.1 Bedding fractures

Bedding fractures are essentially parallel to the bedding planes of Opalinus Clay formation. Generally they are orientated N30°-N60° dipping 30°-50°SE. Bedding fractures are distinguished from the fault planes by absence of slickensides on it. These fractures are observed in all investigated boreholes with higher concentration outside the fault boundaries. These fractures have likely a cohesive component but

it is assumed that they lose it due to tensional stresses that may occur during core transportation and drying while exposed to ambient air humidity conditions.

2.4.2 Calcite veins

Calcite veins are open tensile fractures filled with calcite. Calcite vein are often associated with slickensides. There are some healed thick veins observed in BFS1 and BFS2. The calcite veins occur either continuously (Figure 2.2a) or discontinuously (Figure 2.2b). The width of calcite veins varies from several millimeters to centimeters. Generally, veins have SW-dipping direction, but there are some dipping to SSE.

Calcite veins usually occur near the fractured zone or scaly clay layers, even being intersected by another fault plane. That suggests early to syntectonic calcite precipitation. Calcite veins show decreased in porosity and assumed to act as local seals during fault zone development [Laurich et al., 2014, Laurich, 2015].

2.4.3 Scaly clays

Scaly clay is a highly strained fabric that mainly occurs in larger zones at the bottom of the Main Fault boundary (up to 2 m), and also in smaller zones or as isolated lenses ranging from 1 to 20 cm in the top or in the middle of the Main Fault. There are two facies of scaly clays observed in investigated boreholes. The scaly clay facies 1 comprises a scaly fabric that has a relative low "tensile strength" since it can be usually broken by hands into smaller fish-like flakes, bounded by shiny polished skilensides surfaces. This facies is mostly observed in the lower part of the Main Fault or in small lenses up to several centimeters width. The scaly clay facies 2 consists of larger microlithons, that are intersected by thin shear zones, and cannot be easily disintegrated and often associated with very fractured rock mass. The facies 1 and 2 often occur together.

The scaly clay developed by progressive increase of the density of thin shear zones [Laurich et al., 2014]. With such increasing spacial frequency of slickensides, the scaly clay aggregates may form microfolds (Figure 2.2c), S-C shear bands and crenulation cleavage.

2.4.4 Fault gouge

Fault gouge has been observed in the BFS2 and in the outcrops. It occurs along the upper boundary of the Main Fault as up to 2 cm thick continuous band or in other part of the Main Fault as discontinuous bands and lenses always related to the scaly clay [Jaeggi et al., 2017]. It has darker color compared to the host rock

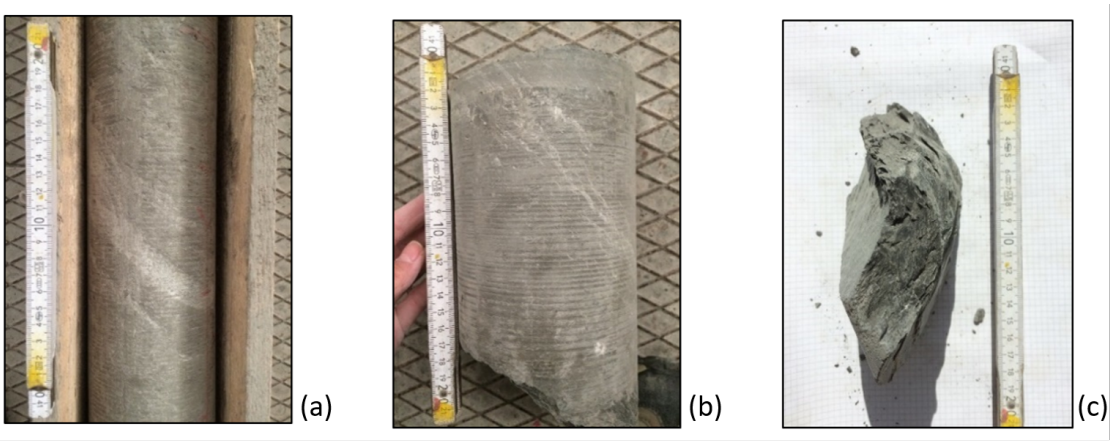

Figure 2.2: (a) Continuous and (b) discontinuous calcite veins; (c) Microfold in BFS3

because of decreasing calcite content, finer particle and reduced porosity. The gouge microstructures indicate a cataclastic evolution accompanied by calcite pressure solution, strong particle reorientation and formation of internal thin shear zones at later stages of gouge formation [Laurich et al., 2014].

2.4.5 Fault planes

Most of the fault planes observed in the boreholes are smooth, planar and have shiny, striated slickenside surfaces. However, some of them are polished, dark or have ragged, matt parts. According to Laurich [2015] and Laurich et al. [2014], this variation is caused by different calcite content that is low in restraining and high in releasing parts of the slickenside surfaces. The orientation of different kinds of grooves, steps and striae is mainly consistent with a reverse kinematics of the Main Fault indicative of a thrust paleostress regime, however the tectonic history of the Main Fault is known to be complex [Nussbaum et al., 2011, Jaeggi et al., 2018, Hostettler et al., 2018]. The fault planes observed in the boreholes can be compiled into three fault systems: (i) moderately SSE-dipping reverse faults, (ii) low angle SW-dipping fault planes and (iii) moderately to steeply inclined N to NNE-striking faults.

2.4.5.1 SSE-dipping fault system

These fault planes are generally subparallel to the bedding planes; however, the dip can vary from 30° to 70°. The SSE-dipping fractures are the most frequently observed fault set in the boreholes. They are present in both internal and external zones of the Main Fault. Fault surfaces are either polished or striated (Figure 2.3a,b). Polished surfaces do not give a clear information about the shear direction, while the striated surfaces indicate the thrusting faulting with a slip direction towards to

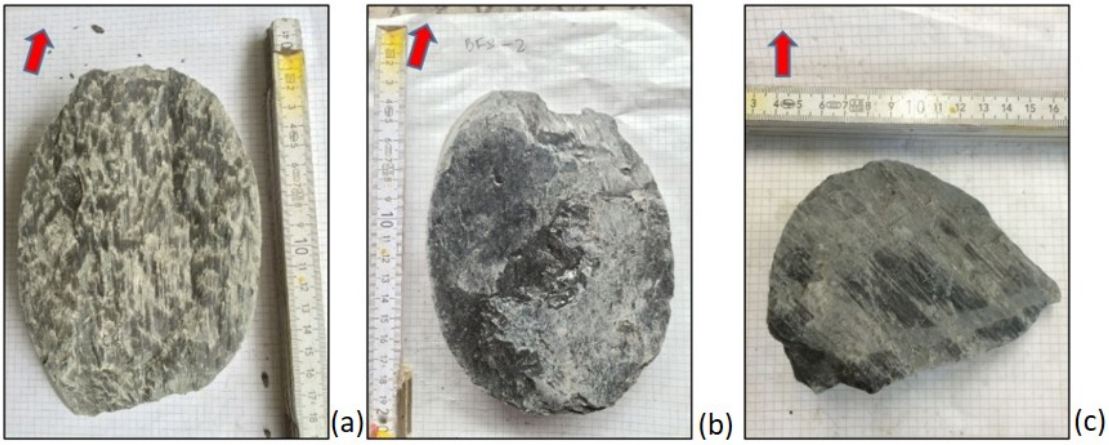

Figure 2.3: (a) Striated and (b) polished SSE-dipping fault plane, (c) – SE70° dipping fault plane with very long striae

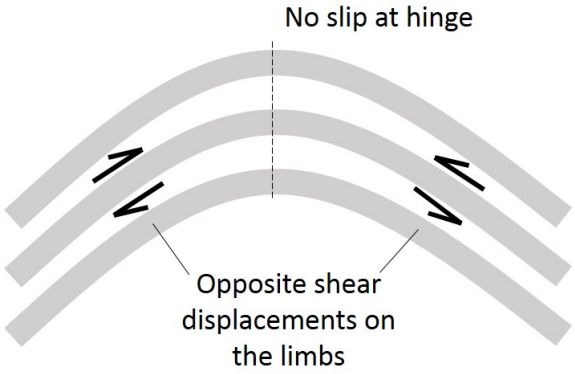

Figure 2.4: Schematic representation of flexural slip folding and the direction of slip on the bedding planes.

N-NNW. This shear sense of movement is consistent with the expected slip direction for flexural slip taking place during the anticline folding (Figure 2.4) but could be also related to thrusting regime. In very highly-deformed zones the slickensides are very shiny. Some striations of the faults in these highly-deformed zones were rotated from NW to N.

The length of striae varies from several millimeters to a few centimeters. Generally, it was observed that the steeper fracture planes (dip up to 70°) have longer striae, up to several centimeters (Figure 2.3c), compared to the low and moderate dip planes (up to 50°) whose striae do not exceed a few centimeters. This could be an indication of larger amount of slip on the steepest plane. Especially it was observed in highly deformed (very fractured) zones.

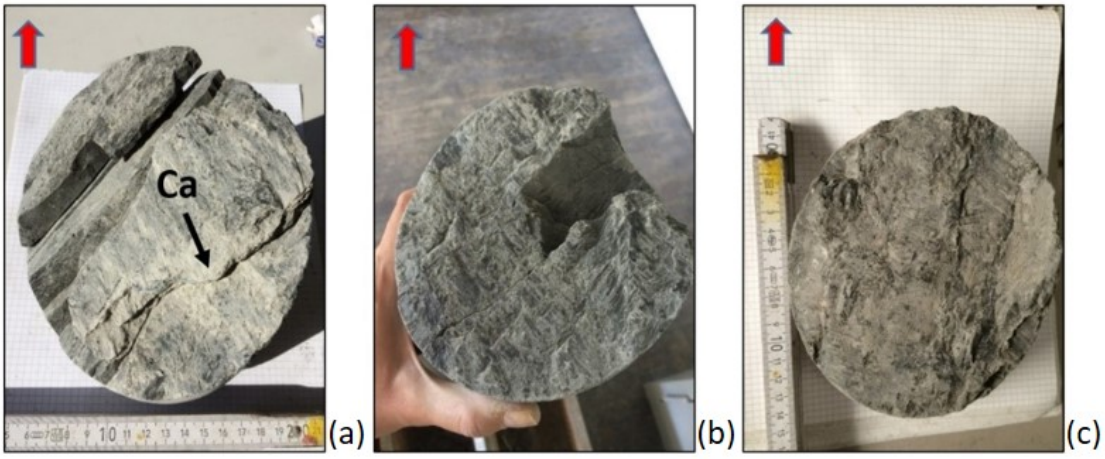

Figure 2.5: SW-dipping faults with (a) SE-dipping fault with normal stepped striation of the and with 1 cm thick calcite mineralization (BFS3, 37.0 m), (b) NW-dipping thrust striation (BFS2, 49.0 m), (c) unclear/overprinted striation (BFS2, 41.66 m)

2.4.5.2 SW dipping fault system

The SW-dipping fracture planes have average dip angles around 20°, however, there are some fracture planes dipping up to 40°. These fractures might have developed during SW-NE lateral extension as a response to the NNW displacement of the bedding planes during Mont Terri anticline formation [Nussbaum et al., 2011]. The striations of the fault usually associated with calcite mineralization and sometimes stepped (Figure 2.5a). Mainly there are three types of striations observed: SE-dipping striation that indicates normal faulting (Figure 2.5a), and NW- and SE-dipping striation indicating thrust movement (Figure 2.5b). In some cases, the SE-dipping striation is overprinted by NW-thrust striation (Figure 2.5c). According to Nussbaum et al. [2011], these SW-dipping planes were reactivated by thrusting movement. The occurrence of thrusted SE-dipping striation is not clear. It can be noticed, that both SE-dipping striations (normal and thrust) can be interpreted as (sinistral and dextral) lateral faults. In some intervals (BFS3 36.5, 37.0 m and BFS1, 37.5 m), SW-dipping fractures are intersected by the SSE-dipping fault planes.

During the structural investigations, there were some low angle SEE-dipping faults observed, that according to Nussbaum et al. [2011], are branches from moderate SEE-dipping faults. These planes have NNW-trending striation that indicates their thrust nature.

2.4.5.3 N-to NNE-striking fault system

This fault system is rarely observed in the boreholes. These fault planes have 20° to 40° dip towards the east (Figure 2.6). The striation observed on these planes is parallel to the striation observed on the SE-dipping fault plan and indicated

Figure 2.6: NNE-striking fault plane

thrust towards NNW. This fault system is assumed to appear at the same time as SSE-dipping system because of the same direction of striation and no evidence of overlapping.

2.5 Rock types of the Main Fault

The architecture of the Main Fault is very complex. It comprises complex multiple fault core and associated damage zones and zones of intact rock. To develop an accurate model of the Main Fault zone, fault rock types were defined and identified in each borehole and used for potential cross borehole correlation. The cross correlation is an attempt to represent the structures beyond the borehole walls, although it is clear that there could be fractures that are not cut by any of the borehole and, therefore cannot be considered.

The investigated rock mass within the borehole was classified into 4 rock types. Initially the classification has been made based on visual observations (Table 2.2, Appendix A.1). Later the rock types have been calibrated by statistically estimated spatial fracture distributions in boreholes (Figure 2.7, 2.8, 2.9). The distributions were calculated excluding the bedding fracture planes. In highly fractured parts of the boreholes, the number of fractures was underestimated due to the difficulty in identifying each fracture.

The core of the fault is defined as "the structural, lithological and morphological portion of the fault where the majority of slip is accommodated" [Caine et al., 1996]. The core is comprised of high strain material [Mitchell and Faulkner, 2009] and generally includes clay rich gouge, altered breccias and cataclasites [Caine et al., 1996]. The core zone usually shows a reduction in permeability and porosity that surrounding intact rock [Caine et al., 1996], as it accommodates the majority of

Table 2.2: Fault rock types of the Main Fault

Rock type	Rock type I	Rock type II	Rock type III	Rock type VI
Structural elements	Scaly clay and gouge	SE-dipping fault system with centimeter layers of scaly clay	SE, SW-dipping and N- to NNE-striking fault 4system	Intact rock
Fracture intensity	-	>20/m	10-20/m	<10/m
Core example (50 cm length)				

displacement [Sibson, 1977]. Therefore, the fault core can be demarcated from the surrounding damage zone by (i) lower permeability, (ii) lower fracture intensity.

In the Main Fault, the "fault core" that is a zone with maximum displacement will be considered to comprise the scaly clay and gouge facies. Scaly clays, including shear zones, microlithons, S-C bands and microfolds, occur in isolated, sharply bounded thin lenses (see BFS1 and BFS2), and at the bottom and the top of the Main Fault in larger scale (BFS3). Due to its low permeability [Marschall et al., 2004] and very deformed texture, the scaly clays facies together with gouge will be considered as a rock type I.

In contrast, the surrounding damage zone often has greater permeability than the intact rock [Caine et al., 1996]. According to Mitchell and Faulkner [2009], the intensity of fractures in the damage zone reaches 100/m before cataclasis converts the rock to fault core material. In the Main Fault, the damage zone that will contribute the "rock type II" has fracture intensity more than ∼20/m and is usually associated with scaly clay facies. This rock type is characterized by the very densified SSE-dipping fractures with a very shiny and well-striated surface with NNW-slip direction.

The rock type III also corresponds to the "damage zone". It is characterized by rhombohedral non-deformed blocks intersected by set of SSE-dipping fault planes, SW-low-dipping fault planes usually associated with calcite mineralization and N to NNE-striking faults. Slickenside analysis of SSE-dipping faults with well-striated surfaces indicates that the slip direction has a top to NNW shear sense, while SW-

Table 2.3: Boundaries of the Main Fault.

Borehole	Upper boundary		Lower boundary		Thickness [m]
	Depth [m]	Dip dir [°]/Dip Angle [°]	Depth [m]	Dip dir [°]/Dip Angle [°]	
BFS1	37.5	135.5°/57.2°	44.93	155.6°/42.2°	7.31
BFS2	44.00	128.2°/62.5°	48.39	155.3°/48.2°	4.39
BFS3	37.61	135.9°/45.0°	42.19	146.3°/64.0°	4.58

low-dipping fault planes have various different shear sense. Between the Main Fault boundaries (highly deformed mass of rock types I and II), rock type III comprises healed and open calcite veins. Rock type IV comprises not-tectonically deformed intact rock that displays some fracturing due to initial loading. The fracture intensity around 5/m.

The schematic cross-correlation of the rock types is presented in Figure 2.10. Boundaries of the Main Fault are associated with Rock type I and Rock type II. In the outcropping gallery 2008-fault zones, the upper fault boundary plane is oriented N066° and dipping 45°SE and the lower boundary plane is oriented N075° and dipping 40°SE [Guglielmi, 2016]. The Main Fault boundaries are shown in Table 2.3.

The assignment of the rock types to the outcropping Main Fault zone, described by Nussbaum et al. [2011] and Jaeggi et al. [2017] , is shown in Appendix A.2.

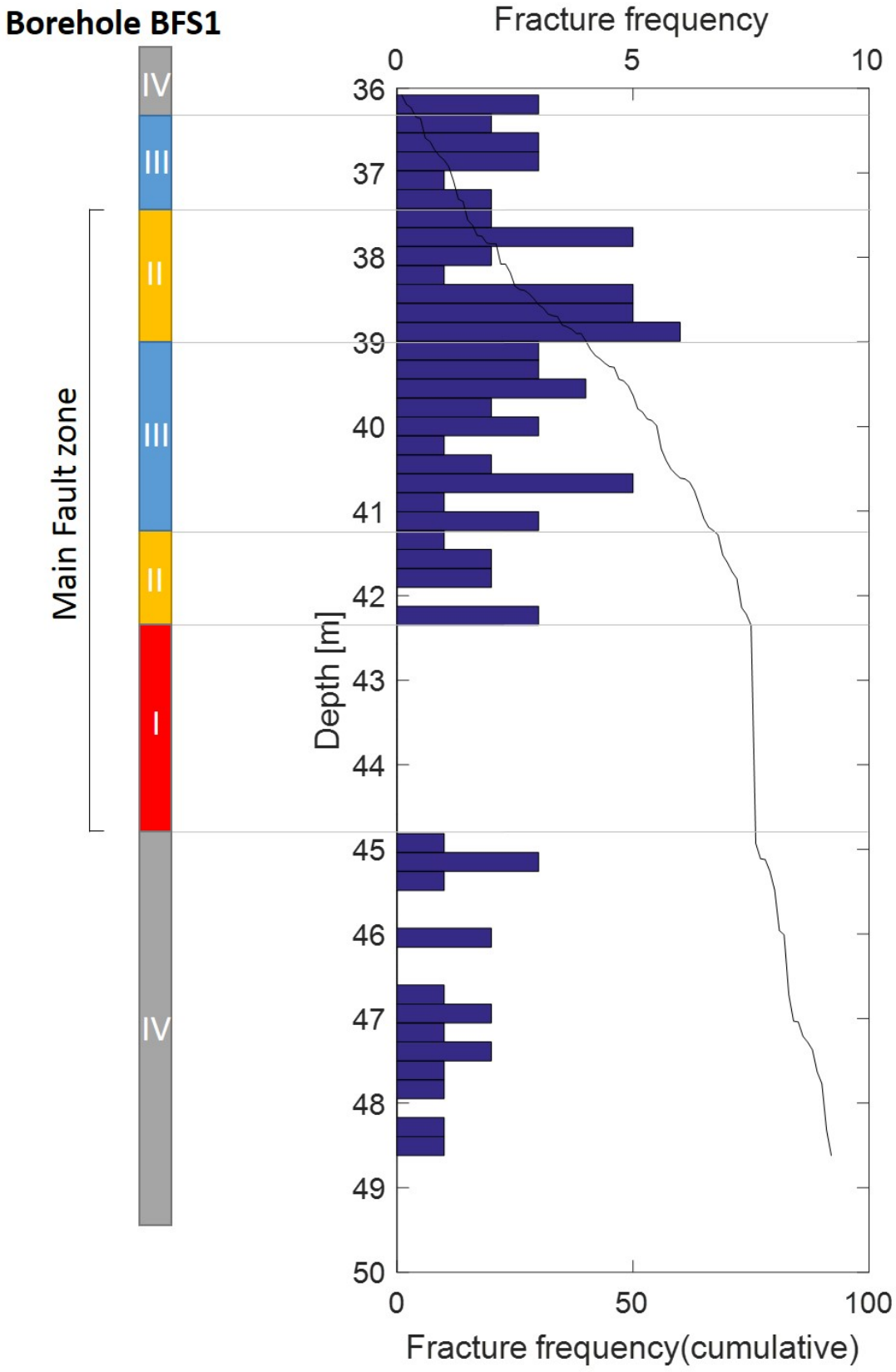

Figure 2.7: Rock types (left) and histogram of spacial fracture distribution and its cumulative distribution excluding bedding planes (right) in BFS1

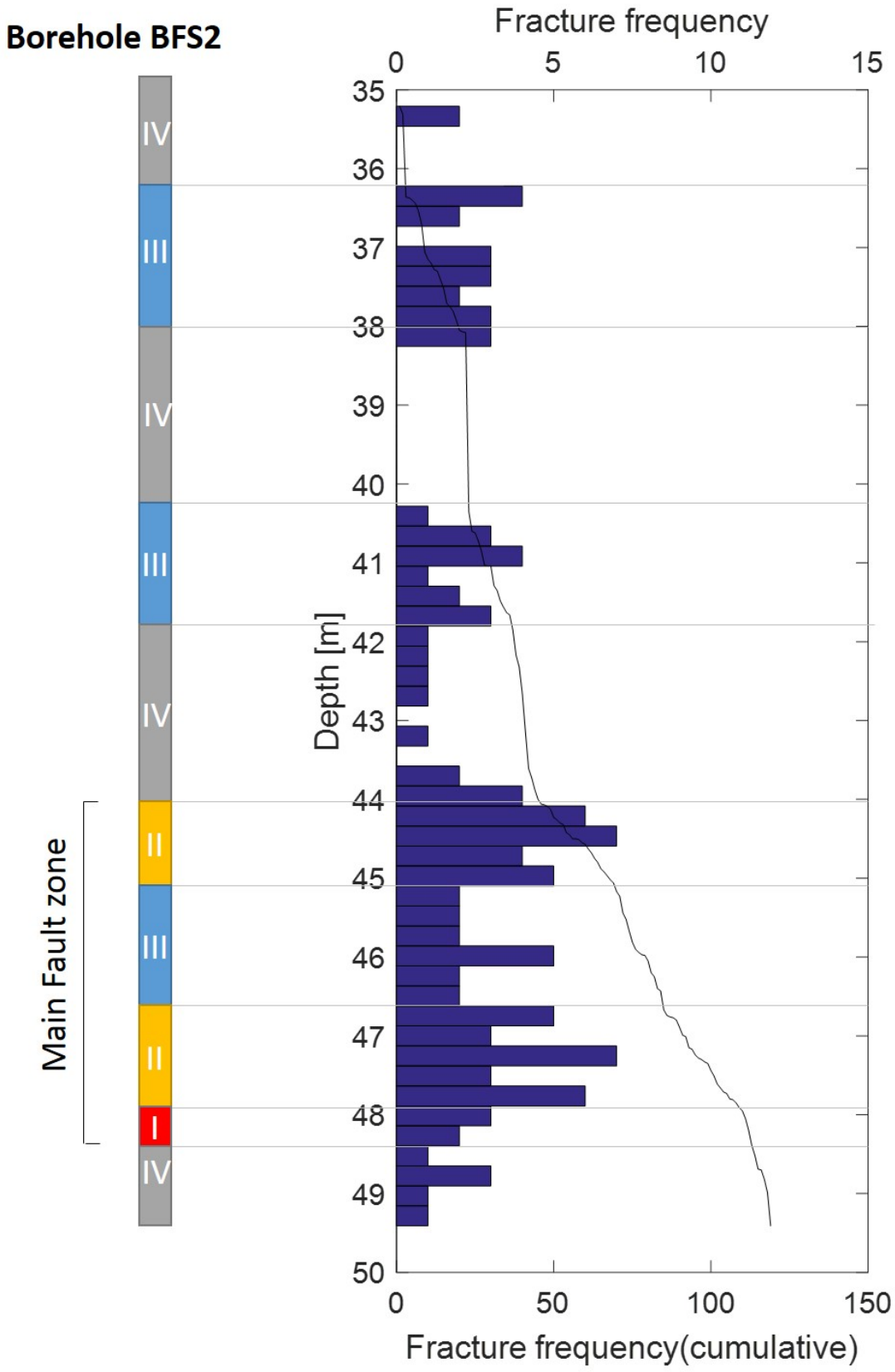

Figure 2.8: Rock types (left) and histogram of spacial fracture distribution and its cumulative distribution excluding bedding planes (right) in BFS2

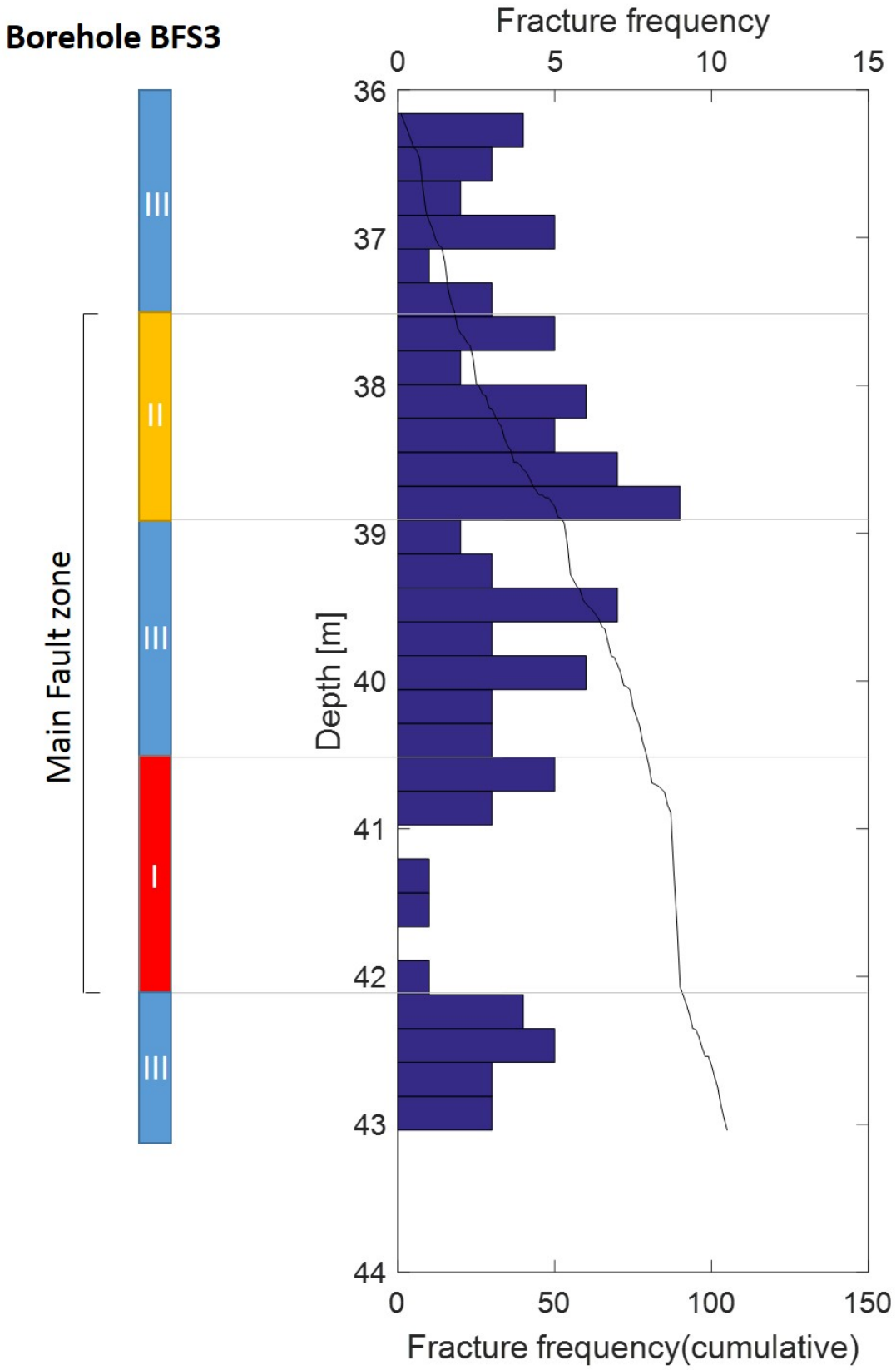

Figure 2.9: Rock types (left) and histogram of spacial fracture distribution and its cumulative distribution excluding bedding planes (right) in BFS3

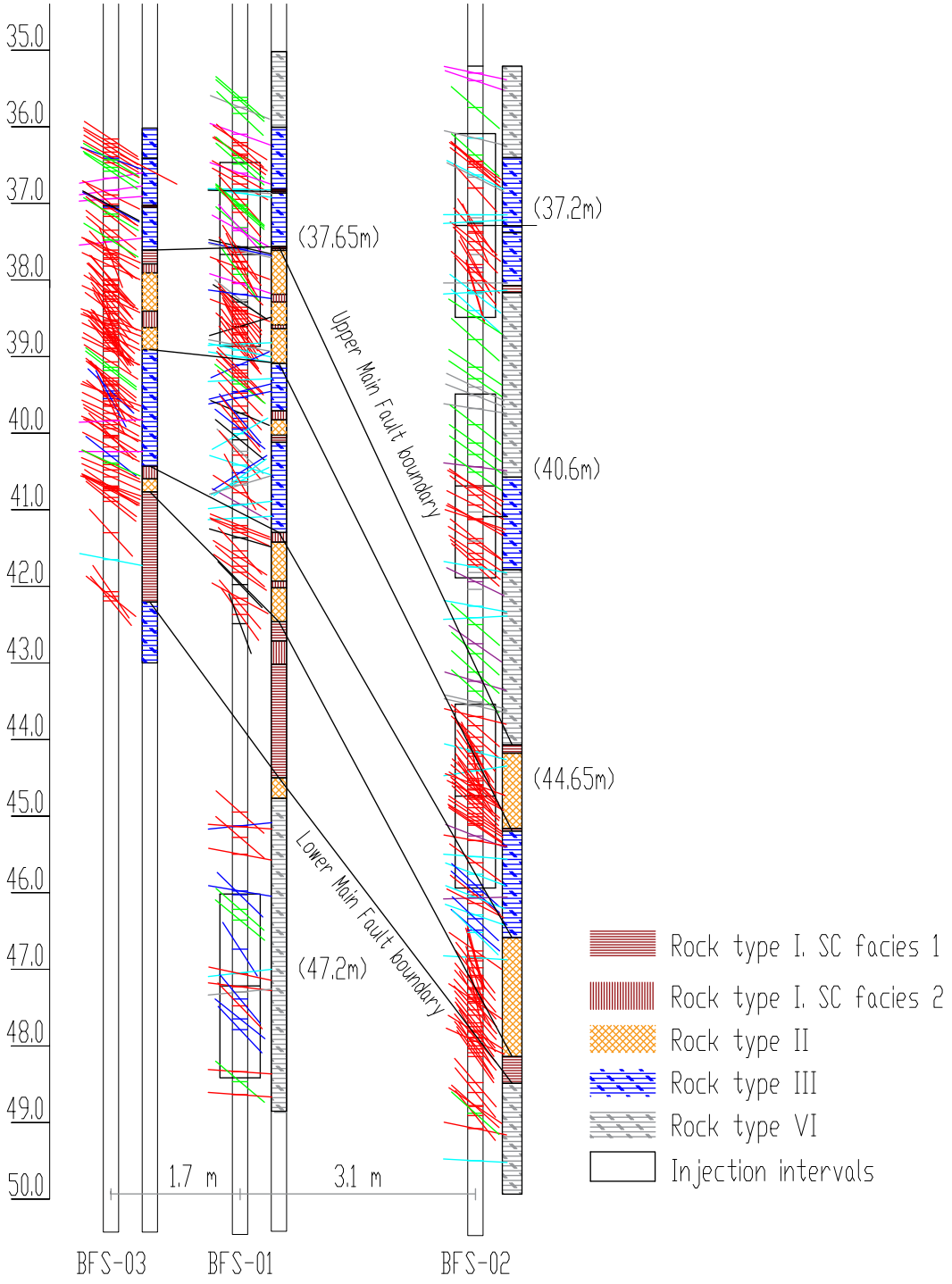

Figure 2.10: 2D model of the investigated area

2.6 Detailed structural analyses of tested intervals

2.6.1 Borehole BFS1 – Test 37.65 – Monitoring interval

This interval was mostly used to monitored injections, conducted at 37.2, 40.6 and 44.65 m below the gallery floor in BFS2. There were additional injections at low pressure performed in this test interval at the end of the experiment period, however, they will not be analyzed in this work. The displacement sensor in this interval is centered at 37.65 m depth in borehole BFS1 within the Main fault zone upper boundary which is located at 37.5 m depth.

The structural analyses of the interval is shown in Figure 2.11. The interval contains 38 fractures including 7 bedding plane fractures, 4 N-striking fractures (NN), 22 SE-dipping fractures with 4 of them containing calcite (SE), 5 SW-dipping fractures with 2 of them containing calcite (SW). The dominant SE-dipping discontinuity family is N10 to N80 dipping 21to-63°SE sub-parallel to the bedding planes. The SW-dipping fault system is E110 to E140 dipping 13 to 27°SE. Both SE- and SW-dipping fault systems have fault planes containing calcite. The calcite veins that are mentioned in the OPTV image were observed only in the WellCAD software. The NS-striking family is averagely N15 to N30 dipping 20to-50°SE.

The interval contains two rock types: Rock type II and Rock type III. The Rock type II in the lower part contains very fractured zone with 2 decimeter width layers of scaly clays facies 1 and 2, respectively. The upper part of the investigated interval corresponds to the Rock type III and contains two a centimeter-thick scaly clay (facies 1) layers. The border between Rock type II and Rock type III is defined by E110°-20°SW at 37.5 m fault plane that contain a centimeter scaly clay layer.

The lineations on the fault planes mainly indicates NW thrust movements (Figure 2.11c). One of the observed SW-dipping fault indicates normal faulting to the SE. The inverted stress sate shows that the maximum principal stress is subhorizontal and trends towards NW, when the minimum principal stress is subvertical.

2.6.2 Borehole BFS1 – Test 47.2

In this interval, the test using one SIMFIP probe was performed. During this phase, there was no second SIMFIP probe set in monitoring mode. The displacement center is centered at 47.2 m depth below the Main fault lower boundary. This interval is the deepest of all the tests, and its location was chosen to estimate the stress state in intact rock, that is close, but outside to the fault boundaries.

The structural analyses of the interval is shown in Figure 2.12. The interval comprises 13 structural elements, where there are 3 bedding plane fractures, 6 SSE-

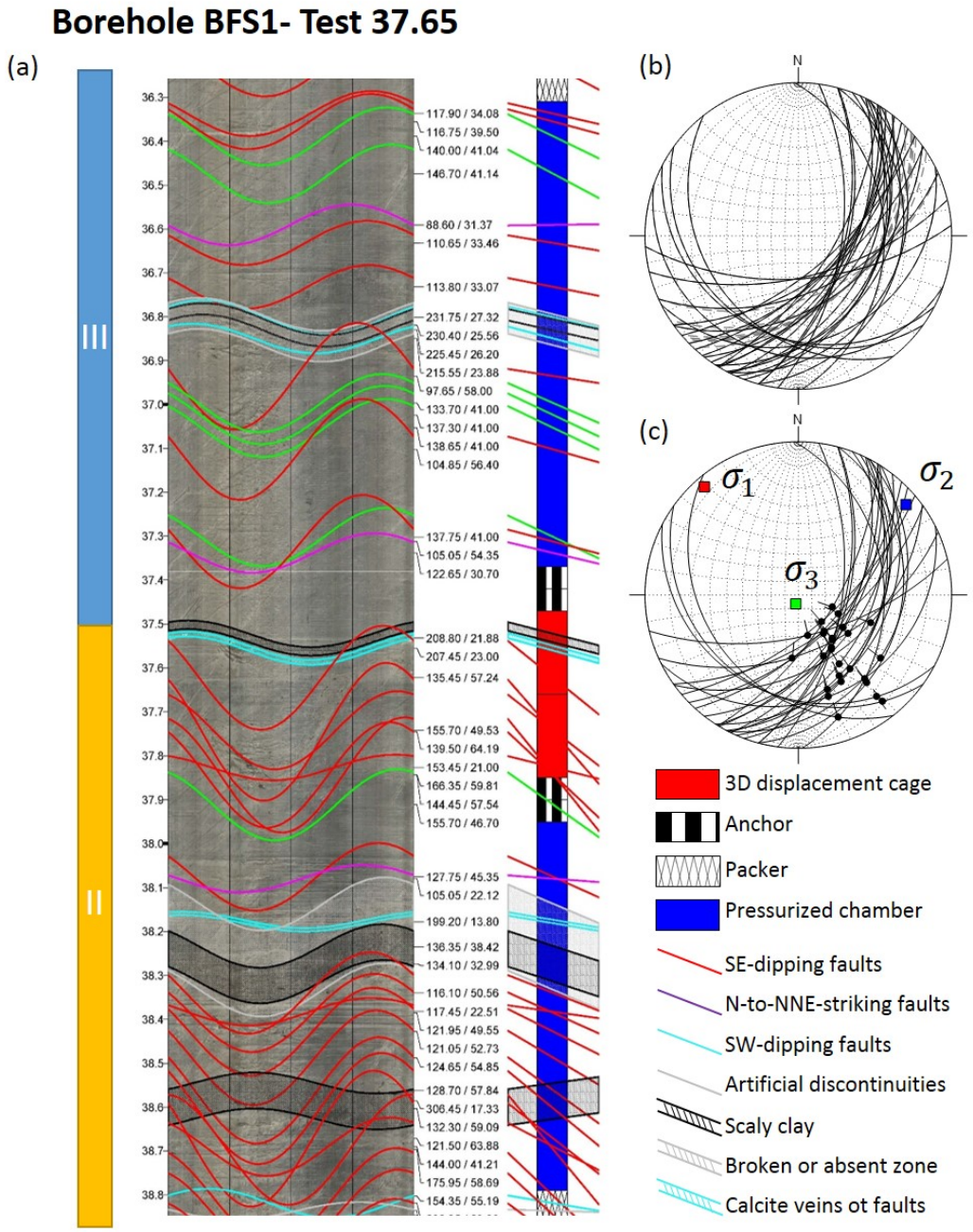

Figure 2.11: (a) Fault rock types and OPTV log view of the tested interval BFS1-37.65m with sinusoids of interpreted fracture traces; (b) Stereographic projection of the fractures main structures (lower hemisphere) ; (c) Stereographic projection of the fractures with slip direction

dipping faults (fault SE), where two of them contain calcite slickensides, 1 SW-dipping fault (fault SW) and 3 calcite veins. The bedding fractures are parallel to the bedding planes and oriented N57° to N68° dipping 39° to 46°SE. The SSE-dipping faults oriented N53° to N79°. There are several sub-horizontal SSE-dipping faults with dip range 4°-12°SE, that are located between the upper and lower anchors of the displacement sensor and in the lower part of investigated interval. The two other SSE-dipping faults have a dip 45°SE and 58°SE, respectively. Two calcite

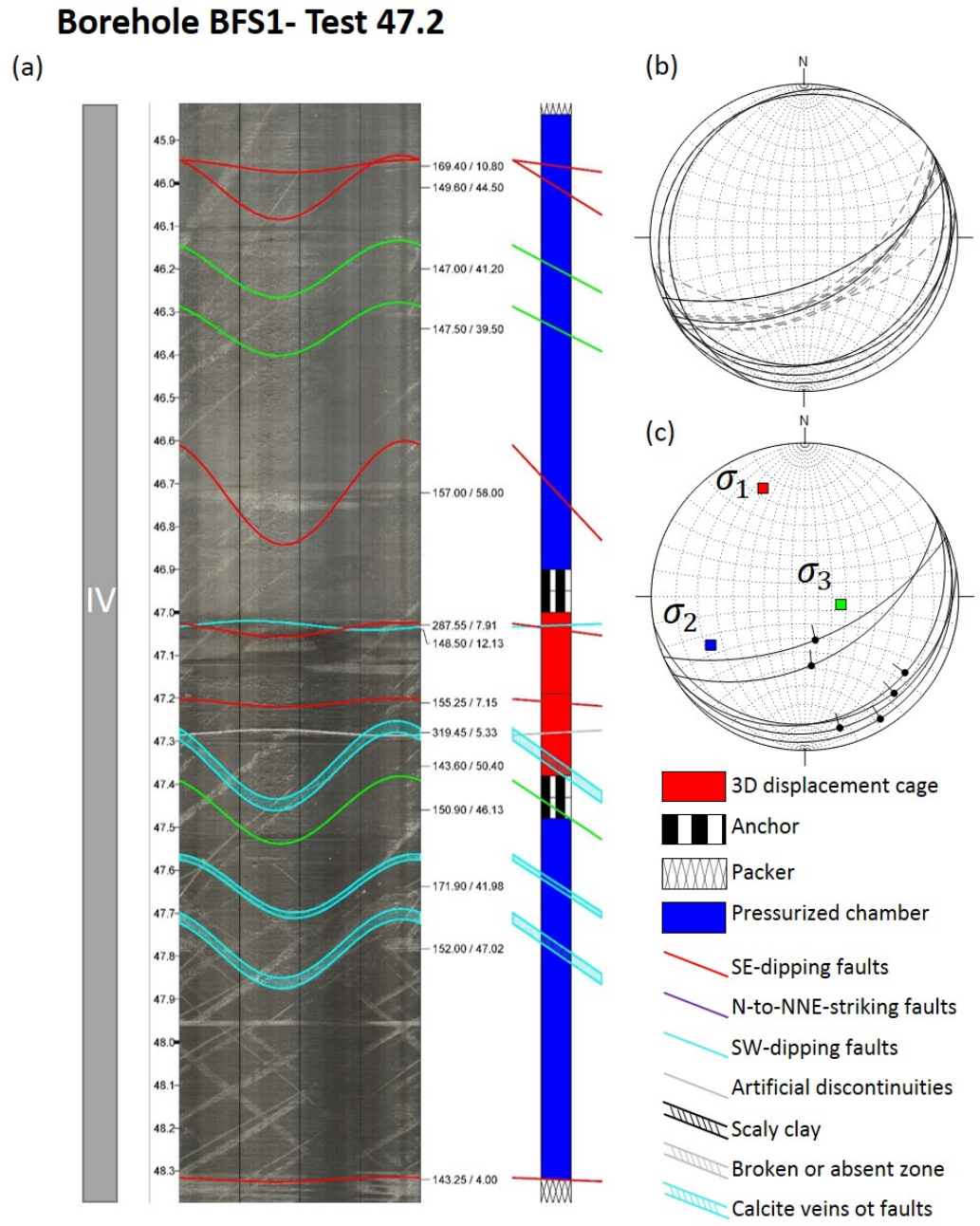

Figure 2.12: (a) Fault rock types and OPTV log view of the tested interval BFS1-47.2m with sinusoids of interpreted fracture traces; (b) Stereographic projection of the fractures main structures (lower hemisphere) ; (c) Stereographic projection of the fractures with slip direction

veins are characterized by discontinues healing, when the third one has a continuous calcite filling up to 2 cm.

All observed striations of SSE-dipping faults indicate thrusting movement to NNE (Figure 2.12c). As for the interval at 37.65 m below the gallery floor, the maximum principal stress is sub-horizontal and trends towards NNW, the principal minimum stress is sub-vertical. The interval belongs to the Rock Type IV, which comprises intact rock. The bedding in the interval is clearly observed.

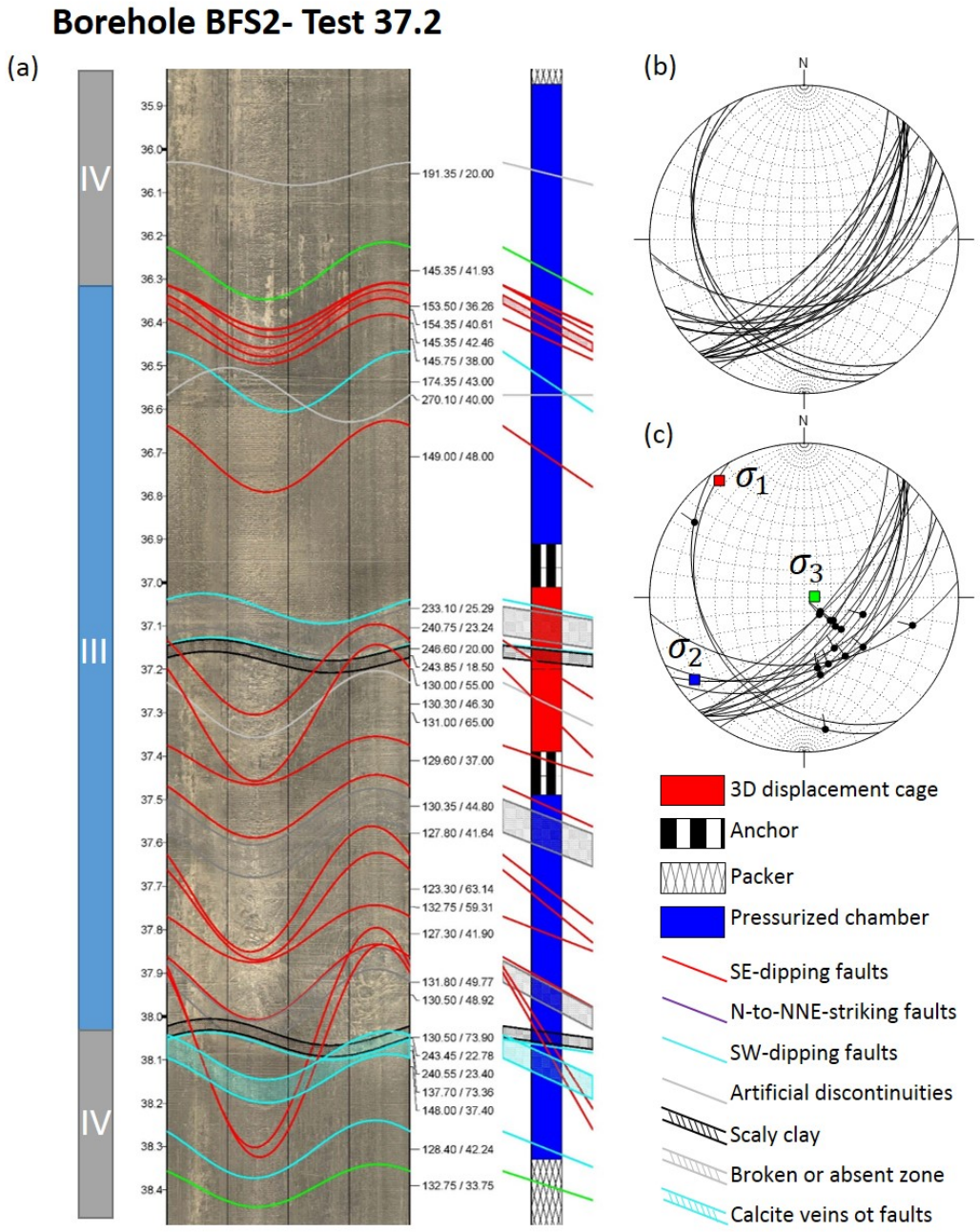

Figure 2.13: (a) Fault rock types and OPTV log view of the tested interval BFS2-37.2m with sinusoids of interpreted fracture traces; (b) Stereographic projection of the fractures main structures (lower hemisphere) ; (c) Stereographic projection of the fractures with slip direction

2.6.3 Borehole BFS2 – Test 37.2

The test at depth 37.2m below the gallery08 floor has been conducted during the FS phase 2 [Guglielmi, 2016]. This is the shallowest investigated interval. During all the experiments of the FS phase 2, the monitoring has been done by second SIMFIP probe that was set at 37.65 m depth in borehole BFS1. The displacement sensor is centered above the Main fault boundary.

The structural analyses of the interval is shown in Figure 2.13. There were 23 structural discontinuities identified within the interval. The main (16 fractures) discontinuity family is SSE-dipping fault system that has orientation N33° to N64° and dips in range 36° to 74°SE. The plane surfaces dipping more than 65°SE have shiny but dredging slickensides. The rest slickensides surfaces are generally sharp, dull, sometimes stepped or slightly curved. Two SW-dipping fault planes at 37.17 and 38.05 m depth contain a centimeter-thick scaly clay layer. Within the interval, there were two rock types identified: Rock type III in the middle (36.3-38.0 m) and Rock type IV in the upper and lower part of the investigated interval. However, the OPTV image shows, that the structure of the rock mass between these two clay layers is different: the rock mass seems more deformed and perturbed, though in cores it is intact and intersected by slickensides that may reduce the size of the zone with Rock type III. Nevertheless, this zone of Rock type III that is above the Main Fault zone may be considered as a secondary fault zone [Guglielmi, 2016].

Other structural elements defined are 1 bedding plane, 4 SW-dipping fault, in which one of them with calcite slickenside (fault SW with Ca), and 2 calcite veins (Ca vein). A calcite vein at 38.10 m depth is 5 cm with discontinues calcite streaks. A calcite vein at 38.3 m has 0.5 cm thickness.

The slip direction for all fault planes tends to NW (Figure 2.13, c). The orientations of the principal stresses are consistent with the ones, defined in the intervals of the BFS1.

2.6.4 Borehole BFS2 – Test 40.6

The test at depth 40.6m below the gallery08 floor also has been conducted during the FS phase 2. As it was mentioned before, the second SIMFIP probe was set in monitoring mode at 37.65 m depth in borehole BFS1. The displacement sensor is centered above the Main Fault upper boundary.

The structural analyses of the interval is presented in Figure 2.14. There are 18 structural discontinuities identified in the interval. The dominant fault family corresponds SE-dipping fault system with orientations N20° to N78° and dips in range 20° to 40°SE. The slickensides are becoming more planar and shiny closer to the lower part of the interval, when in the middle part, the fault surfaces occurred to be slightly curved, sharped. In the lower part of the interval a SE-dipping fault planes intersects SW-dipping fault plane with calcite slickenside. These fractures comprise the Rock type III, which starts below the fault plane 130°/36° at 40.6 m depth. Above this fault plane, the clay in intact and comprise the Rock type IV. It contains 4 bedding fractures that most probably occur due to core transportation, and 1 NNE-striking fault in the lower part of the intact zone.

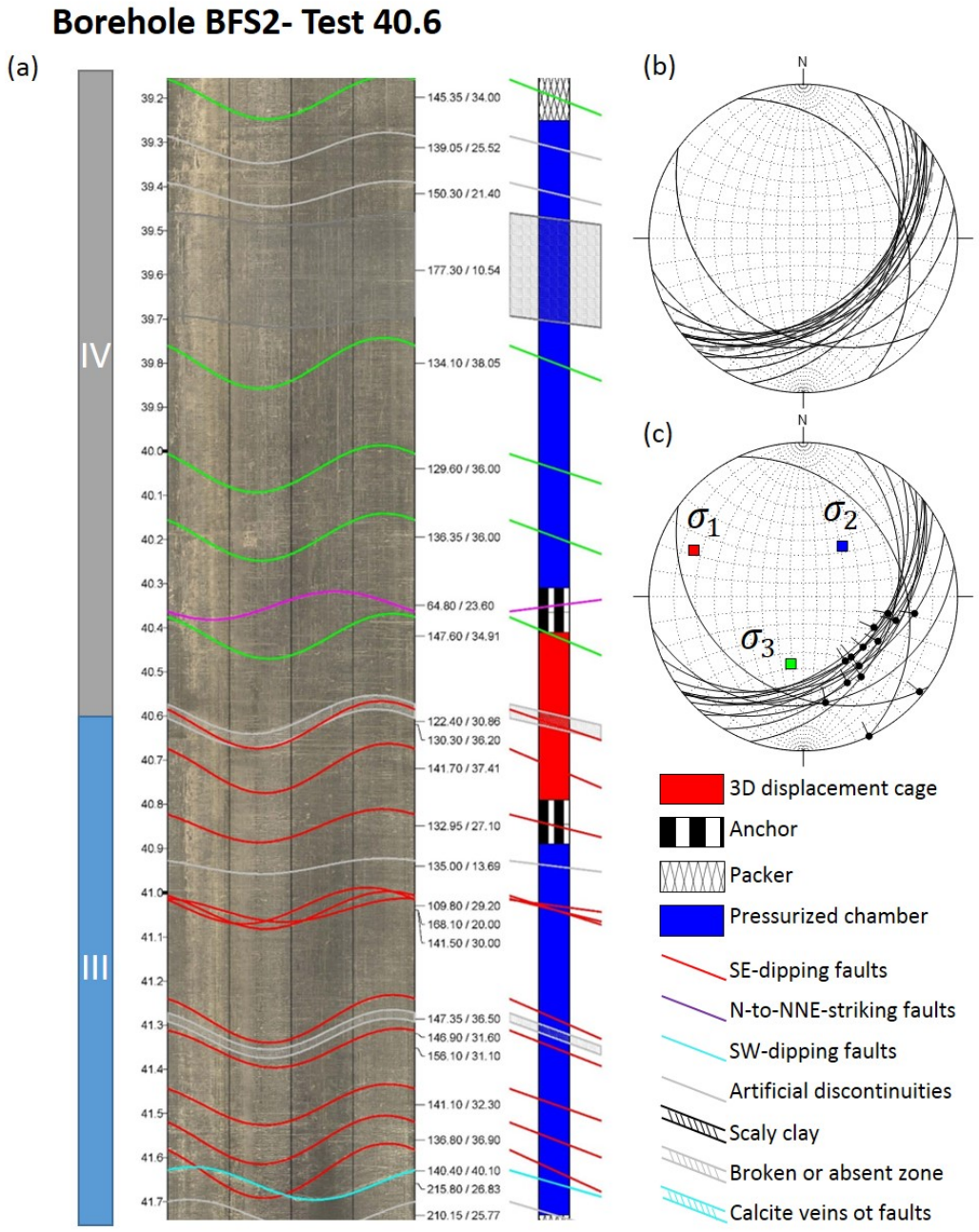

Figure 2.14: (a) Rock-types and OPTV log view of the tested interval BFS2-40.6m with sinusoids of interpreted fracture traces; (b) Stereographic projection of the fractures main structures (lower hemisphere) ; (c) Stereographic projection of the fractures with slip direction

The slip direction of SE-dipping fault mainly indicates NW-thrusting movement (Figure 2.14c). The estimated paleo stresses are consistent with the previously estimated stress orientations, however, the minimum principal stress is rotated 40° towards SSW.

2.6.5 Borehole BFS2 – Test 44.65

The test at depth 44.65 m below the gallery08 floor has been conducted during the FS phase 2. The second monitoring SIMFIP probe was set at 37.65 m depth in the borehole BFS1. The displacement center is set at 44.65 m depth that is 0.65 m below the Main fault zone, therefore this is the only interval that can estimate the fault reactivation conditions and hydromechanical coupled response within the Main Fault itself.

The interval contains three rock types (Figure 2.15). The Rock Type IV is in the upper part of the interval and includes 1 bedding and three SE-dipping fault planes, where one of them contains calcite. The upper boundary of the Main Fault starts at 44.0 m and characterized by a 5 cm thick layer of scaly clays (facies 1). The interval is highly fractured mostly by SE-dipping faults with directions vary from N030° to N090°, dipping 35° to >75°SE. Fracturation is intense to about one meter below the upper boundary and finishes with a cm-thick layer of the scaly clay (facies 1) at depth 45.1 m. These fractures might be Riedel structures and/or bedding reactivation surfaces associated to the Main Fault development. The fault surfaces above 44.60 m are planar, very well-striated, and sometimes curvilinearly-striated (Figure 2.16a) or intersected by other faults surfaces (Figure 2.16b). Below 44.6 m there are two types of surfaces occur: one is planar, with long striae (up to several cm) or almost polished (Figure 2.16c), others are non-planer, sometimes curves or stepped (Figure 2.16d). Below 45.1 m the interval is less fractures and comprises Rock type III.

The striation indicates NW-thrusting movement (Figure 2.15c). The orientations of the principal stresses are consistent with the orientation of the paleostresses defined before in all injection intervals.

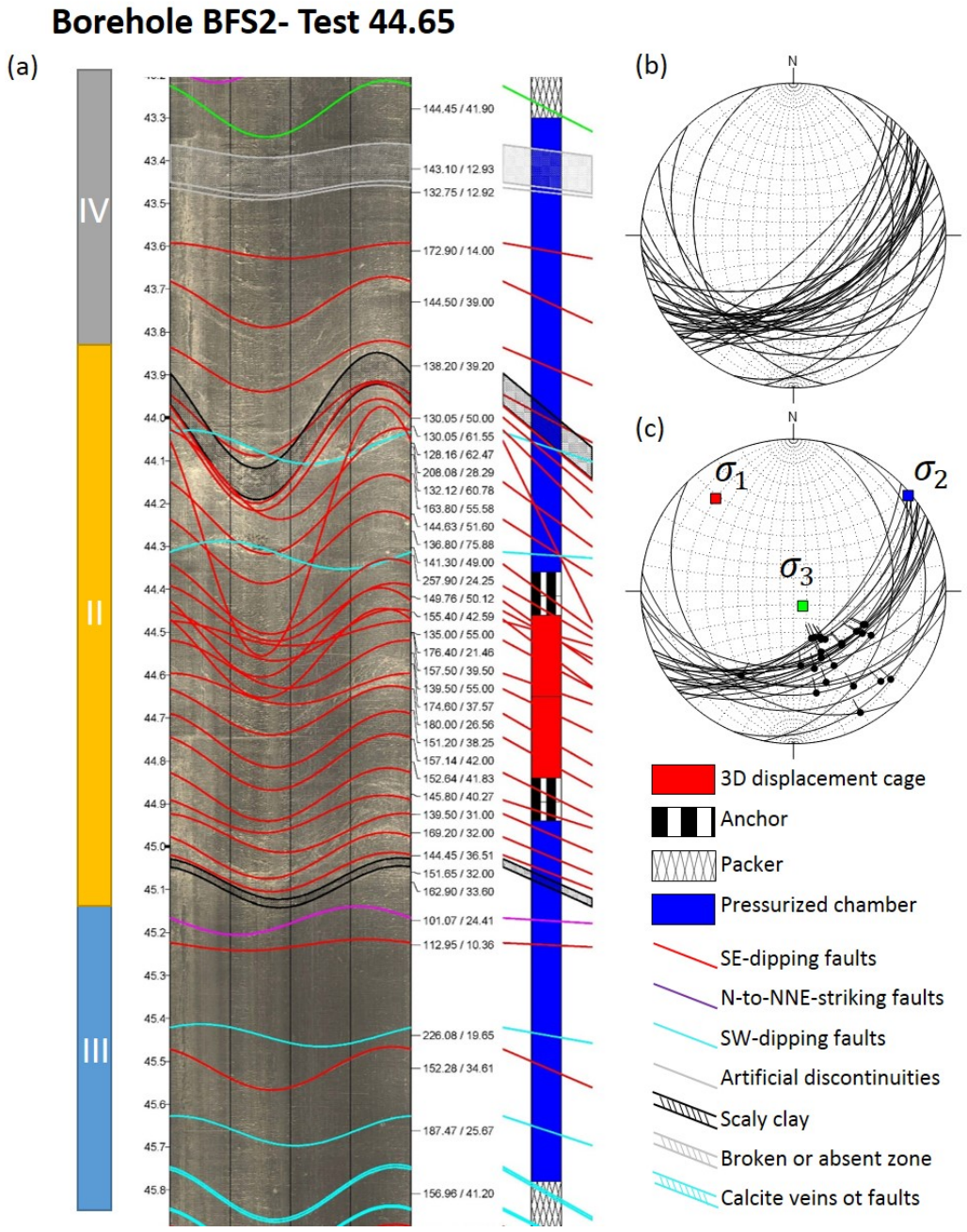

Figure 2.15: (a) Fault rock types and OPTV log view of the tested interval BFS2-44.65m with sinusoids of interpreted fracture traces; (b) Stereographic projection of the fractures main structures (lower hemisphere) ; (c) Stereographic projection of the fractures with slip direction

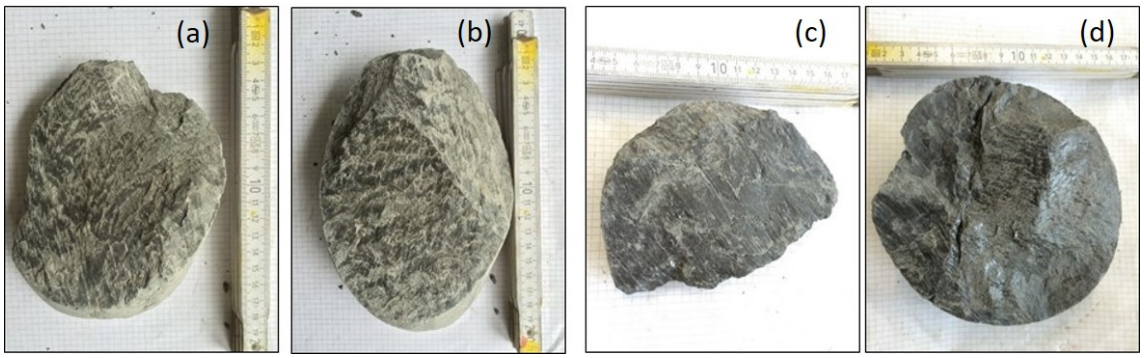

Figure 2.16: Different striation of Rock type IV. (a) Well-striated fault surface; (b) Well-striated intersected fault planes; (c) Long-striated "polished" fault surface ; (d) Non-planar striated fault surface

2.7 Conclusions

Based on our results, we defined the following outcomes:

1. The Main fault zone consists of a thrust zone that includes scaly clay and non-scaly fabrics intersected by various density of secondary fault planes.

2. There are several structural elements defined during borehole investigation: SSE-dipping reverse faults, (2) SW-dipping fault planes and (3) N to NNE-striking fault, which are consistent with the fault systems observed in the Mont Terri rock laboratory [Nussbaum et al., 2011]

3. Four rock types are implemented to simulate fracture location between the boreholes for hydromechanical coupling simulation.

4. A 2D model of the Main Fault zone in the experiment vicinity is developed.

5. Detailed structural analyses of each injection interval is provided.

6. Kinematic analyses of slip directions in all tested intervals indicate the same tectonic regime, where the maximum principal stress is sub-horizontal and trends SE-NW, resulting in NNW trusting striations. This tectonic regime is consistent with the Mont Terri anticline folding [Nussbaum et al., 2011].

7. Complexity of the Main fault architecture and its high heterogeneity is likely to impact the fault rock response to fluid injection and its reactivation.

Chapter 3

Injection protocol and initial data evaluation

In this chapter, we present an overview of the flowrate-pressure-displacement response of each test. We look at the overall response of each test to get a global idea of the rock mass response to injection. The main goal of this chapter is to understand which test can provide the more reliable data for the stress inversion. For example, the measurement of shut-in pressure gives an estimation of the normal stress on a fracture [Haimson and Cornet, 2003]. Pulse tests help in understanding the limits of reversible response of the rock mass [Cappa et al., 2006]. Moreover, to compare the results of the stress estimation with the regional stress state, the chosen injected intervals should be located far from the fault zone, in rock volumes where the stresses are not perturbed by faulting. Chapter 2 showed that the interval at 44.65 below the gallery floor is located within the Main Fault zone core. We assume that the response from this highly fractured injection interval is complex, and therefore this test will not be analyzed here. For each test the experimental protocol follows the same preparation steps for the injections:

- Installation of the probe at the designated borehole depth.
- Inflation of packers between 0.6 to 1 MPa to seal the interval and anchor the displacement sensor to the borehole wall.
- Packer pressure increase to the operating pressure of 3.5 MPa. During the injection, the packer pressure is adjusted so that its pressure is 0.2 MPa above the chamber pressure.
- Saturation of the chamber with water and equilibrating the pressure in the chamber with the formation pressure.

At this stage the chamber is prepared for the injection test. The detailed description of the SIMFIP probe operations is given by Guglielmi [2016], Guglielmi et al.

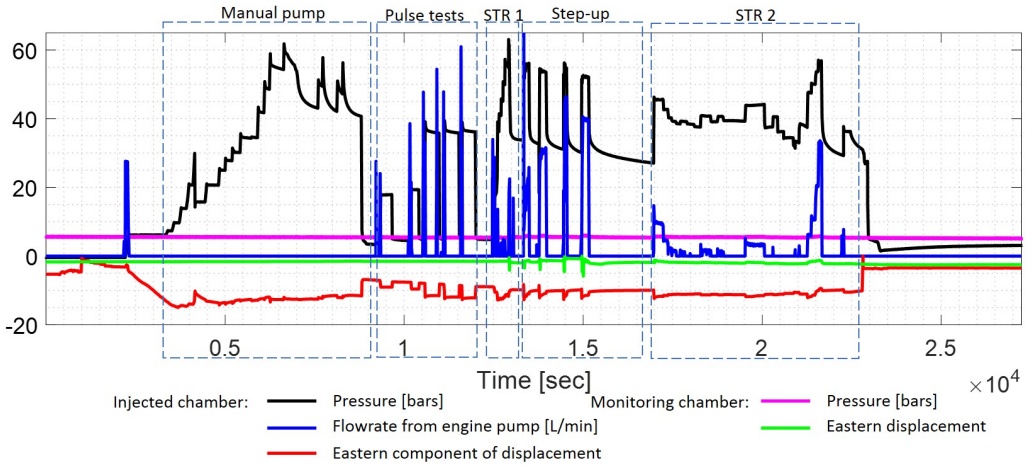

Figure 3.1: Pressure, flowrate and a western displacement component records during the injection in the injected interval at 37.2 and monitored intervals at 37.65. The eastern displacement was chosen randomly to represent one of three displacement components measured during the injection. The magnitudes of the displacement component is relative.

[2013] and in Chapter 5. Generally, the injection protocol consists of repeated high-pressure step-rate injections to activate fractures in the interval and low-pressure pulse tests to characterize the activated fractures, using manual or engine pumps. The maximum injected volume with the manual pump during a step-rate injection does not exceed 10 L, while the engine pump injected volume may reach 150 L. The injection with the manual pump is used to analyze the response of the rock mass near the borehole. The injection with the engine pump allows investigating larger areas of the fault zone. In some tests, manual and engine pump injections end with a shut-in period. The flowrate-pressure-displacements sampling rate is 10 Hz. At the end of the test, the injection chamber is left until equilibrium with the initial formation pressure. The anchors of the displacement cage are retracted, and the packers are deflated. In details each test displays a slightly different series of injections cycles as explained in the following sections.

3.1 Test 37.2

The injection test at 37.2 m in shales occurred over ∼5.5 hours and included one injection with increasing pressure steps conducted with a manual pump, low-pressure pulse tests, and two injections with increasing pressure steps conducted with an engine pump (labeled as STR1 and STR2 in Figure 3.1; Guglielmi [2016]).

Figure 3.1 shows the flowrate-pressure-displacement response of the rock mass to the fluid injection in the injection interval at 37.2 m below the gallery in the borehole BFS2 and monitoring interval at 37.65 m below the gallery floor in the

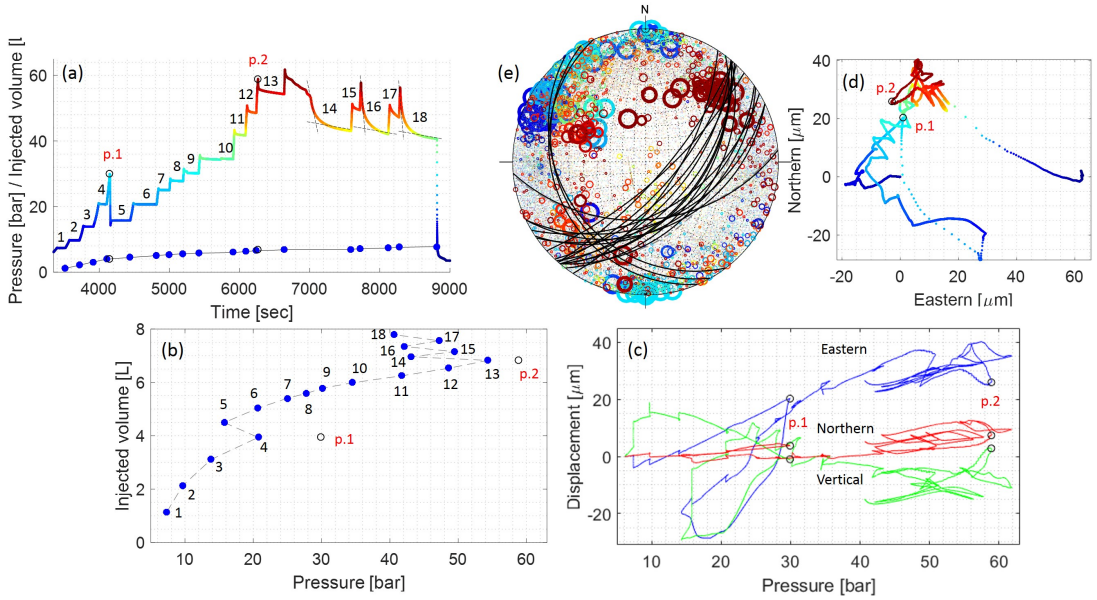

Figure 3.2: (a) Pressure and flowrate vs time during injection with the manual pump. The blue markers at flowrate record correspond to the weighted injected volume in the end of a pressure step. Colors on the pressure records correspond to the values of pressure (b) Pressure-vs-injected flowrate, (c) Eastern, Northern and Vertical displacement components vs injected pressure. (d) 2D view of Eastern vs Northern displacement. The colors correspond to the pressure magnitude from (a) (e) Stereoprojection of displacement orientation measured every 10Hz. The size of the markers correspond to the displacement magnitude measured every 10Hz. The colors correspond to the pressure magnitude from (a)

borehore BFS1. To analyze the response, the data was subdivided into the different injection phases (manual pump, STR1, STR2, etc).

3.1.1 Step-by-step pressure increase injection using manual pump

The injection using the manual pump took about 2 hours. The analysis of the injection with the manual pump is given in Figure 3.2. The pressure and cumulative injected volume vs time are given in Figure 3.2a. The volume injected is calculated by summing the total fluid injected at the end of each pressure step. Figure 3.2a shows that the pressure injection consists of 18 pressure steps. There were 6 pressure drops during the injection, which correspond to the steps 5, 9 13, 14, 16, and 18, respectively. Figure 3.2b shows that all the pressure drops except the pressure drop at the step 9 are associated with significant injected volume variations.

The first pressure drop of 1.6 MPa at the pressure step 5 occurs when the injected pressure reaches 3 MPa (point 1, Figure 3.2a). Figures 3.2c shows that before the first pressure drop the signal tends to be linear. The pressure drop at 3 MPa is accompanied by a 72 μm displacement which is oriented towards South and then rotates towards SE (upwards) (Figure 3.2d). After this pressure drop the displace-

ment rotates towards NW until 5.9 MPa, followed by the pressure drop of 0.3 MPa, which corresponds to the pressure step 13 (point 2, Figure 3.2d). The associated displacements of 18 μm rotates towards NE and is parallel to the strike of the SE-dipping fractures and normal to the SW-dipping fractures. Overall, the response is very complex which might be associated with the existence of 2 fracture families in the interval – SW- and SE-dipping fractures (Figure 3.2e). The low volume of injected fluid does not allow activating a large patch of the fracture. Therefore, the response most likely is affected by activation of both fracture families in the interval.

The pressure steps 14, 16 and 18 were meant to estimate the instantaneous shut-in pressure (Figure 3.3). The instantaneous shut-in pressures are estimated by intersecting the tangent lines of the instantaneous pressure decline with the "stabilized" pressure and vary between 4.3 and 4.5 MPa. First pressure shut-in decline (pressure step 14) demonstrates a sharp pressure change at 5.4 MPa. Figure 3.3b also shows that the displacements become linear only below 4.7 MPa and are oriented towards NW-SE. The displacements above 4.7 MPa display a complex response due to the activation of several fractures at a high injection pressure (Figure 3.3c). The second pressure shut-in (pressure step 16, Figure 3.3d) shows a more clear displacement response. Figure 3.3e demonstrates that there is a kink in displacements around 5.4 MPa. At this pressure, the displacements rotate from SSW to SE (Figure 3.3f). Third pressure shut-in (pressure step 18, Figure 3.3g) shows 2 displacement kinks at 4.2 and 5.3 MPa (Figure 3.3h). Figure 3.3i shows rotation from NNW from SE. It is clear due to the analysis of the three shut-in pressure declines, that there is a closure of more than one fracture. Considering the existence of two fracture families in the interval, we assume that the first closure at 5.3-5.4 MPa corresponds to the activation of SW-dipping fractures, and the closure at 4.3-4.5 MPa to the activation of the SE-dipping fractures.

Figure 3.1 shows that the pressure and the displacement in the monitoring interval are constant, which shows no connection between the injected and monitored intervals during the injection with the manual pump.

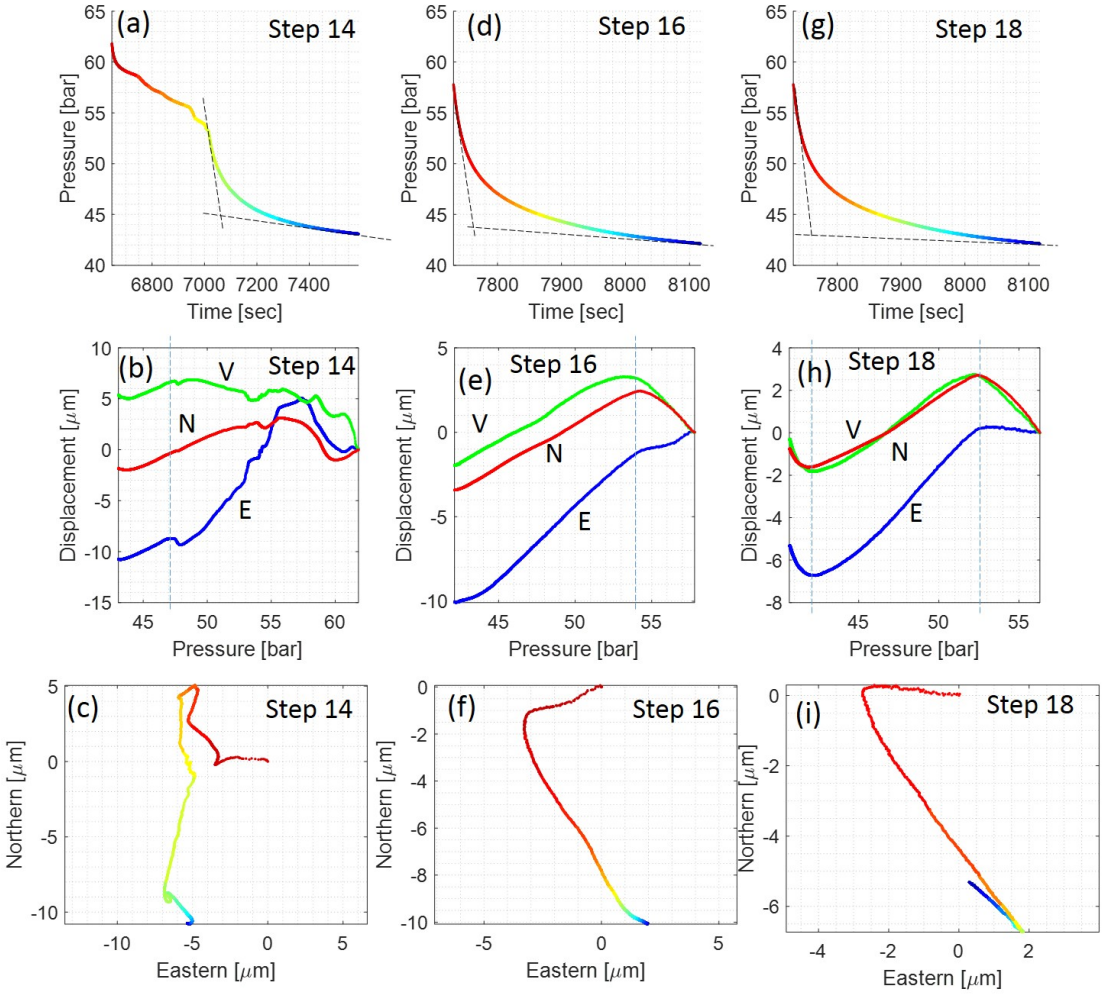

Figure 3.3: (a), (d) and (g) the zoom in on pressure vs time records during the pressure steps 14, 16 and 18 from Figure 3.2a, respectively. The colors correspond to the pressure magnitude from Figure 3.2a; (b), (e) and (h) Eastern (E), Northern (N) and Vertical (V) displacement components vs injected pressure, (c), (f) and (i) – 2 D view on Northern vs Eastern Displacements for pressure steps 14, 16 and 18 from Figure 3.2a, respectively. The colors correspond to the pressure magnitude from Figure 3.2a

3.1.2 Pulse tests using the engine pump

The injection with the manual pump is followed by 2 low-pressure and 3 higher-pressure pulse tests (Figure 3.4) using the engine pump. The low-pressure and higher-pressure tests reached a maximum of 1.9 and 3.9 MPa (Figure 3.4a). Figure 3.4 shows that the steady state flowrate in the end of each pressure step is close to 0 L/min, indicating that there is no flow into fractures below 3.9 MPa. The linear relationship of the displacement with the pressure during the pulse tests informs that the displacement below 3.9 MPa represents the reversible response of the rock mass (Figure 3.4b). The most dominant orientation of the displacements during the pulse tests is normal to the SE-dipping fractures (Figure 3.4c,d). Jeanne et al. [2017] showed that this direction resulted in the transverse isotropic elastic deformation of

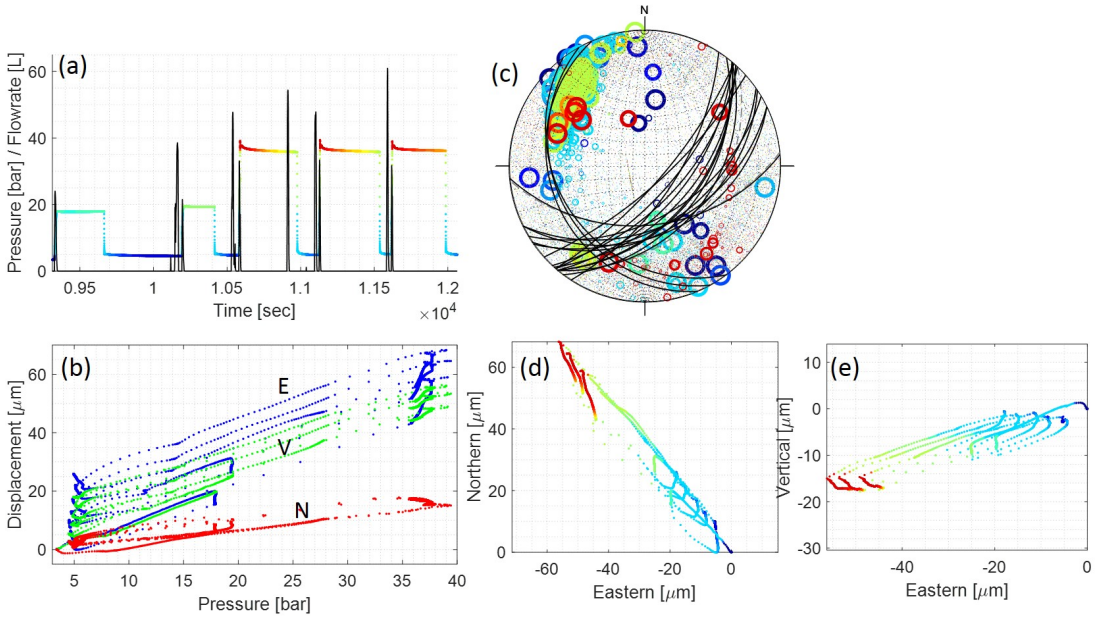

Figure 3.4: (a) Pressure and flowrate vs time during pulse tests. Colors on the pressure records correspond to the values of pressure (b) Eastern (E), Northern (N) and Vertical (V) displacement components vs injected pressure. (c) Stereoprojection of displacement orientation measured every 10Hz. The size of the markers correspond to the displacement magnitude measured every 10Hz. The colors correspond to the pressure magnitude from (a); (d) and (e) 2D view of Eastern vs Northern and Eastern vs Vertical displacements, respectively. The colors correspond to the pressure magnitude from (a).

the rock mass around the chamber. At the maximum pressure of the higher-pressure pulse we observe small pressure drops. The trend of the orientations during these pressure drops is parallel to the SE-dipping fractures. These pressure drops may indicate that the pressure of 3.9 MPa is a start of fracture activation and these results in small permanent displacements at the end of the pressure decrease (Figure 3.4d,e).

Up to 3.9 MPa, the displacement-vs-pressure behavior during the pressure increase in the higher-pressure pulse tests is linear. The repeatability of the linear behaviour during the higher-pressure pulse cycles demonstrate the reversible rock mass response. It may also indicate that the pressure drop at 3 MPa during the manual pump injection, which is below 3.9 MPa, most likely does not reflect the behavior of fractures in the interval. The displacement record during the manual pump test is complex and we cannot explain all the observed displacement. The manual pump test is the first ever pressure increase in this test interval and we suspect that initial adjustment of the anchor and displacement measuring system can be responsible for the observed complex signal.

3.1.3 Pressure step-up injection using engine pump.

The description of the first pressure step-up injection with the engine pump (STR1) is given in Chapter 5. Here, we focus on the pressure step-up cycles at the end of the STR1, which were performed to better estimate the shut-in pressure (Figure 3.1, Step up cycles). There is a clear displacement signal in the monitoring interval, which is located 3.5 m apart. The detailed analysis of the displacements and pressures in the monitoring chamber is beyond the scope of this PhD thesis.

The analysis of the displacements during the step-up cycles is given in Figure 3.5. The pressure shut-in decline demonstrates a kink in the pressure before the stabilization of the pressure and flowrate versus time. The kink occurs at 4.6-4.7 MPa. It can be observed that the displacements above the kink at 4.6-4.7 MPa are mostly E-W trending, when below – NW-SE trending. Comparing to the results of the displacements during from the shut-in pressure with the manual pump, we can assume that the kinks observed there at higher pressures might be correlated with the kinks observed during the engine pump. As it was shown for the manual pump, we can assume that displacements above the kink are related to the closure of the SW-dipping fractures, followed by the closure of the SE-dipping fractures below the kink. These results are also consistent with the regional stress in Mont Terri estimated by Martin and Lanyon [2003], postulating that the maximum principal stress is sub-vertical. Considering this orientation, we assume that the SE-dipping fractures with steeper dipping angles area activated at lower pressure than the SW-dipping fractures with lower dipping angles. We assume, that the decrease of kinks of pressure from 5.3-5.4 MPa to 4.6-4.7 MPa and from 4.3-4.5 MPa to 2.7-3.4 MPa is related to significantly larger area of the activated fracture patch due to the increase of flowrate. Figure 3.5 shows that the shut-in pressure decreases with every step-up cycle, which is also accompanied by the flowrate increase. This confirms that the transition between the manual and engine pump associated with the flowrate increase can significantly decrease the shut-in pressure on reactivated fractures.

The second pressure step-up injection with the engine pump (STR2) was conducted to estimate hydraulic permeability of the reactivated faults. In comparison to the STR1 the pressure steps were applied in a different way (Figure 3.6a). The displacements show a complex response; however, it is possible to observe that the displacements at >4 MPa are normal to the SE-dipping fractures (Figure 3.6b). The permeability estimated by Henry et al. [2018] by applying a Dupuit-Thiem formula [Doe and Remer, 1981, Quinn et al., 2011], which gives a fault zone permeability between 10^{-14} – 10^{-13} m^2.

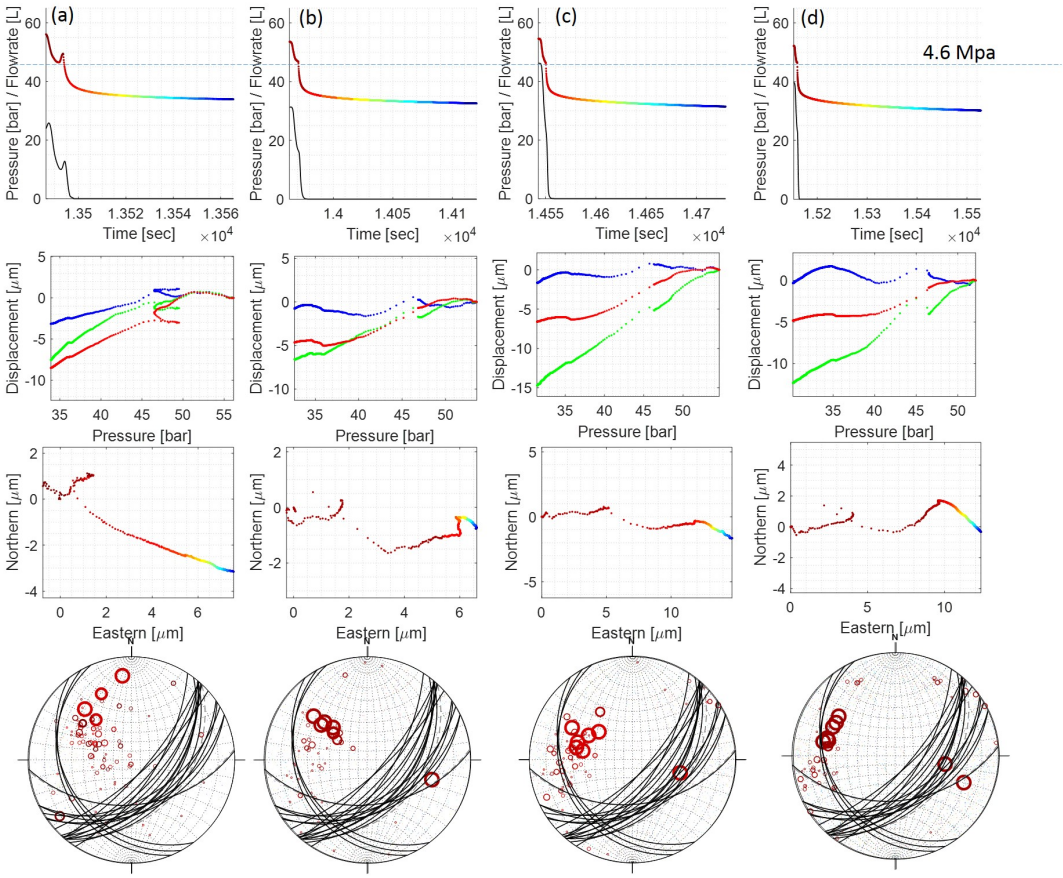

Figure 3.5: Columns (a), (b), (c) and (d) are pressure-flowrate-displacement data analyses for the step ups given in Figure 3.1

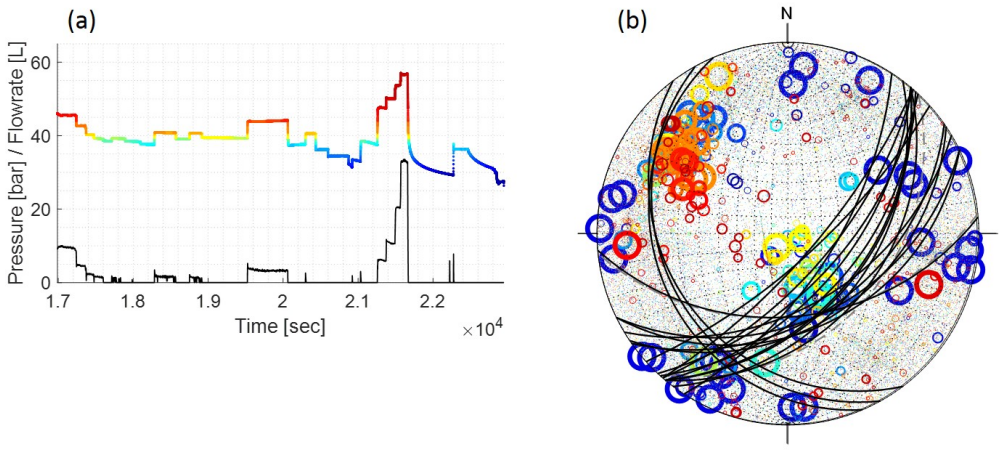

Figure 3.6: (a) Pressure and flowrate vs time during STR 2. Colors on the pressure records correspond to the values of pressure; (b) Stereoprojection of displacement orientation measured every 10Hz. The size of the markers correspond to the displacement magnitude measured every 10Hz. The colors correspond to the pressure magnitude from (a);

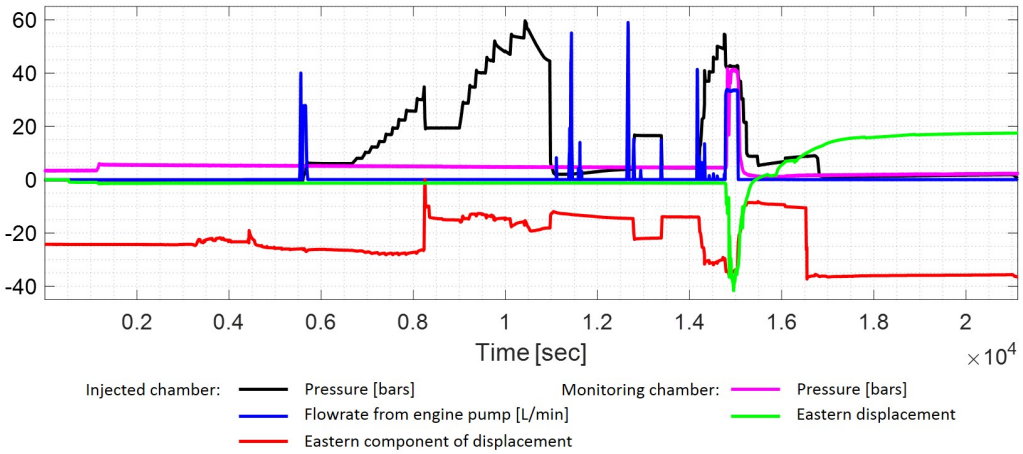

Figure 3.7: Pressure, flowrate and a displacement component records during the injection in the injected interval at 40.6 (BFS2) and monitoring chamber at 37.65 (BFS1). The displacement component is in relative magnitudes

3.2 Test 40.6 m

3.2.1 Step-by-step pressure increase injection using manual pump

The injection test at 40.6 m in shales lasted ∼3 hours and included one injection with increasing pressure steps conducted with a manual pump, one low-pressure pulse test, and one injection with increasing pressure steps conducted with an engine pump STR1 [Guglielmi, 2016, Figure 3.7]. The flowrate-displacement-pressure response during this injection test was studied in detail by Guglielmi et al. 2019. Here we give a brief summary of the results.

The injection using the manual pump took over 1.5 hours. The analysis of the injection with the manual pump is given in Figure 3.8. The test consists of 17 pressure steps (Figure 3.8a). The injection includes 2 pressure drops, which occurred at step 10 and 17. Both pressure drops are accompanied with a significant decrease of flowrate (Figure 3.8b). First pressure drop of 1.6 MPa occurs at 3.4 MPa (Point 1, Figure 3.8a). An abrupt displacement of 54 μm occurs in the beginning of the pressure drop, which is oriented towards ESE (100°/26°). Guglielmi et al. 2019 shows that this displacement vector matches with slip vectors calculated on the different SE-dipping faults intersecting the interval under the regional stress state, calculated by Martin and Lanyon [2003]. Below 1.7 MPa the vectors show linear response of the displacement and pressure Guglielmi et al. [2019]. These vectors are oriented normal to the SE-dipping fault system (Figure 3.8c). As we mentioned above, this orientation matches the orientation of the transverse isotropic elastic deformation of shales Jeanne et al. [2017]. The displacements between this elastic

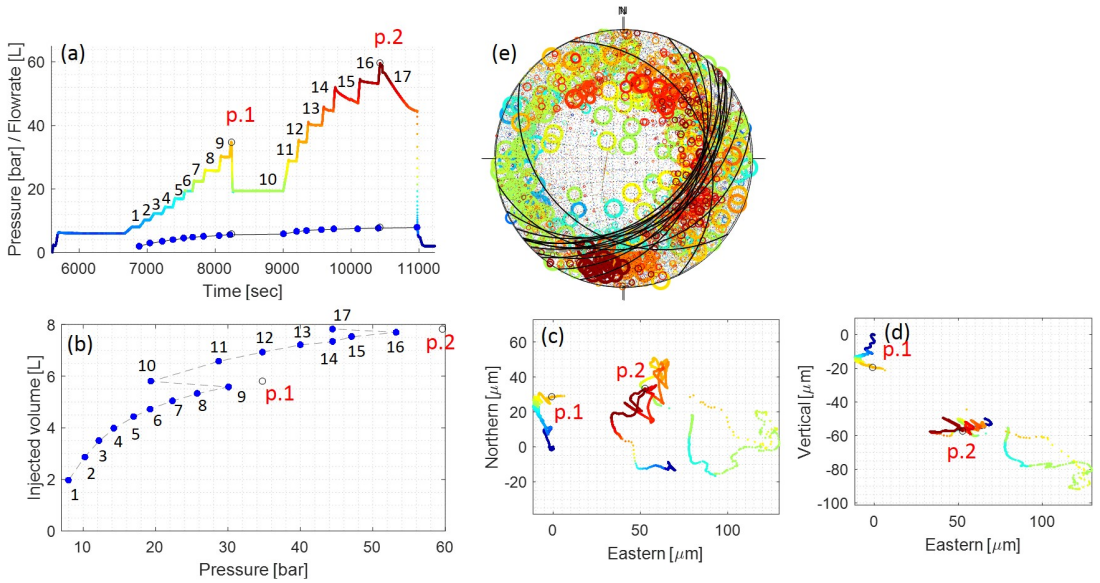

Figure 3.8: (a) Pressure and flowrate vs time during pulse tests. Colors on the pressure records correspond to the values of pressure (b) Eastern (E), Northern (N) and Vertical (V) displacement components vs injected pressure. (c) Stereoprojection of displacement orientation measured every 10Hz. The size of the markers correspond to the displacement magnitude measured every 10Hz. The colors correspond to the pressure magnitude from (a); (d) and (e) 2D view of Eastern vs Northern and Eastern vs Vertical displacements, respectively. The colors correspond to the pressure magnitude from (a).

response below 1.7 MPa and pressure drop at 3.4 MPa show small fracture opening with a slight shear component Guglielmi et al. [2019]. The second pressure drop of 0.2 MPa occurs at 5.9 MPa (Point 2, Figure 3.8a) and is associated to displacements oriented towards SSW (Figure 3.8e). The response in between two pressure drops is complex. The injection using the manual pumps ends on the injection chamber opening until the pressure equilibrates to the formation pressure of 0.6 MPa. The displacement and pressure records in the monitoring chamber indicate that there is no connection between the injection and the monitoring chamber.

3.2.2 Pulse tests using the engine pump

The pulse test followed by the injection with the manual pump reached a maximum pressure of 1.7 MPa (Figure 3.9a). The linear response between the pressure and displacement has a small offset during the pressure decrease (Figure 3.9b). The orientation of the displacements during the pulse test is consistent with the orientation of the abrupt displacement occurred during the manual injection at the first pressure drop at 3.4 MPa (Figure 3.9c,d). Such a consistency in orientation and in the offset may mean that the pulse test either represents the response of the reactivated fracture patch or can be interpreted as a response to the pore pressure

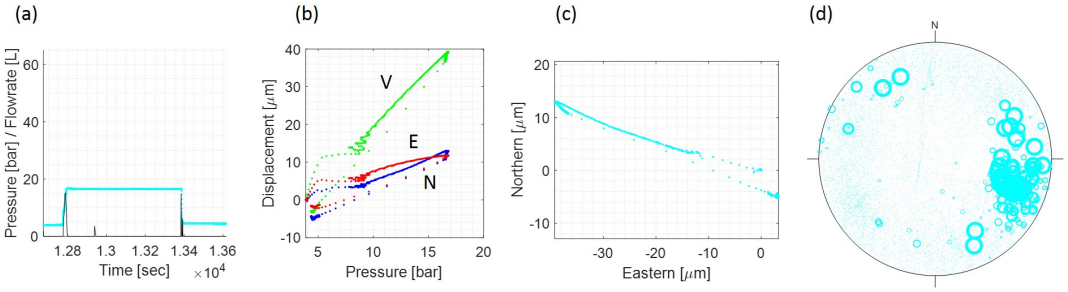

Figure 3.9: (a) Pressure and flowrate vs time during pulse tests. Colors on the pressure records correspond to the values of pressure, (b) Eastern (E), Northern (N) and Vertical (V) displacement components vs injected pressure, (c) 2D on Eastern vs Northern components displacements, (d) Stereoprojection of displacement orientation measured every 10Hz. The size of the markers correspond to the displacement magnitude measured every 10Hz.

readjustment during the backflow into the chamber similarly to what observed by [Guglielmi et al., 2019].

3.2.3 Step-rate injection using the engine pump

The pressure step-up injection using the engine pump consists of 8 pressure steps up and 4 pressure steps down (Figure 3.10a). Figures 3.10a and b show that there is a significant flowrate increase up to 33 L/min, associated with a pressure drop of 1.2 MPa occurred after the injection of the maximum pressure of 5.4 MPa (Figure 3.10b). The displacements during the pressure drop are oriented towards SW-NE (Figure 3.10d, e). The pressure drop is followed by a strong pressure and displacement signal in the monitoring interval. The linearity in the displacement response is observed below 3.5 MPa during the pressure increase (Figure 3.10c). The displacements trend NW-SE, which is consistent with the elastic response of the chamber. The displacements between 3.5 and 5.4 represent a complex response which mostly trends NW-SE, when at high pressures it rotates towards SW upwards (Figure 3.10e). After the pressure drop, the displacements rotate back to the NW-SE trend. The total injected volume during the injection with the engine pump is 143.1 L.

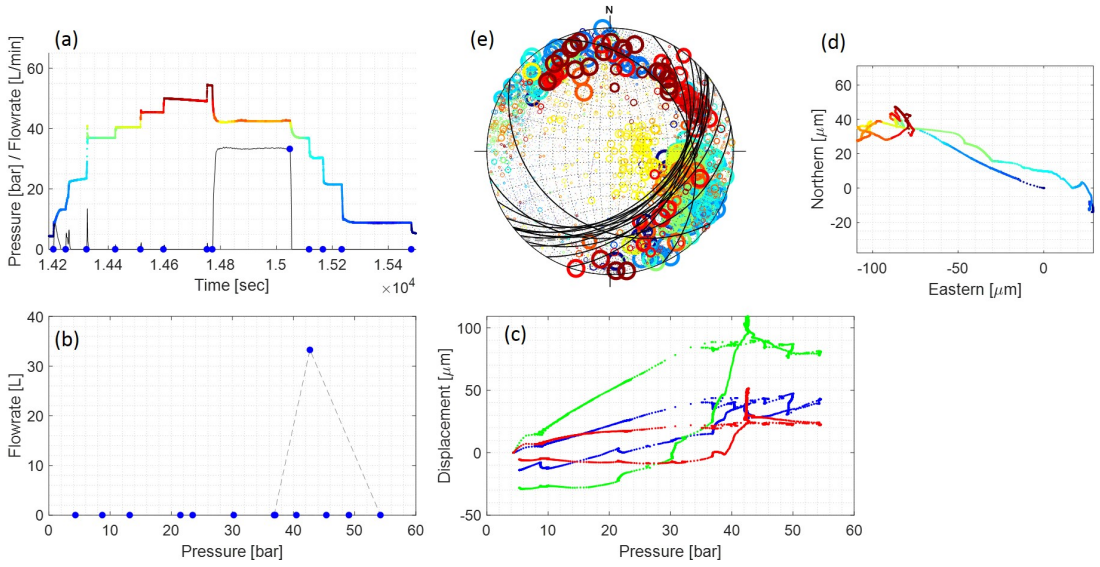

Figure 3.10: (a) Pressure and flowrate vs time during the step-rate injection using the engine pump. Colors on the pressure records correspond to the values of pressure (b) Pressure-vs-injected flowrate, (c) Eastern (E), Northern (N) and Vertical (V) displacement components vs injected pressure, (d) 2D view of Eastern vs Northern displacement. The colors correspond to the pressure magnitude from (a), (e) Stereoprojection of displacement orientation measured every 10Hz. The size of the markers correspond to the displacement magnitude measured every 10Hz. The colors correspond to the pressure magnitude from (a)

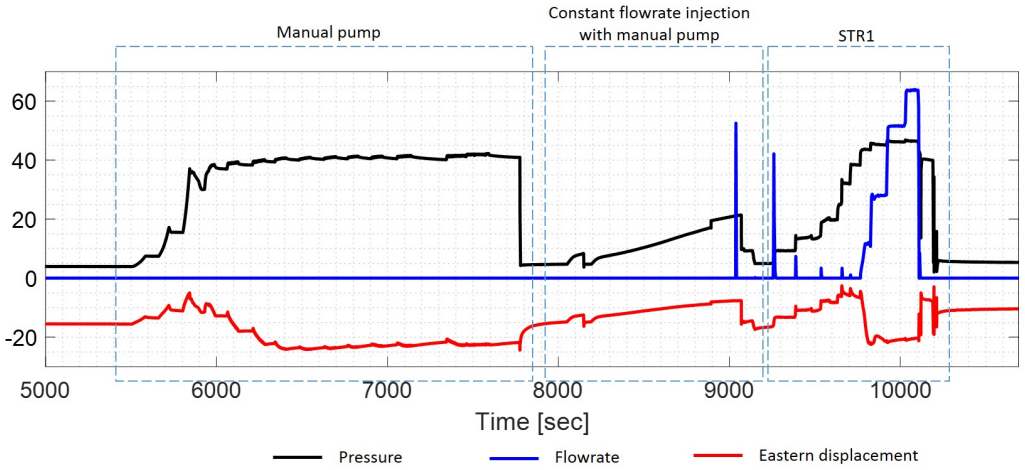

Figure 3.11: Pressure, flowrate (from engine pump) and eastern component of the displacement records vs time

3.3 Test 47.2 m

The injection test 47.2 m took over 1 hour 45 minutes. The test consists of step up injections using manual pump, constant flowrate injection using manual pump and pressure step-up injection using engine pump (Figure 3.11).

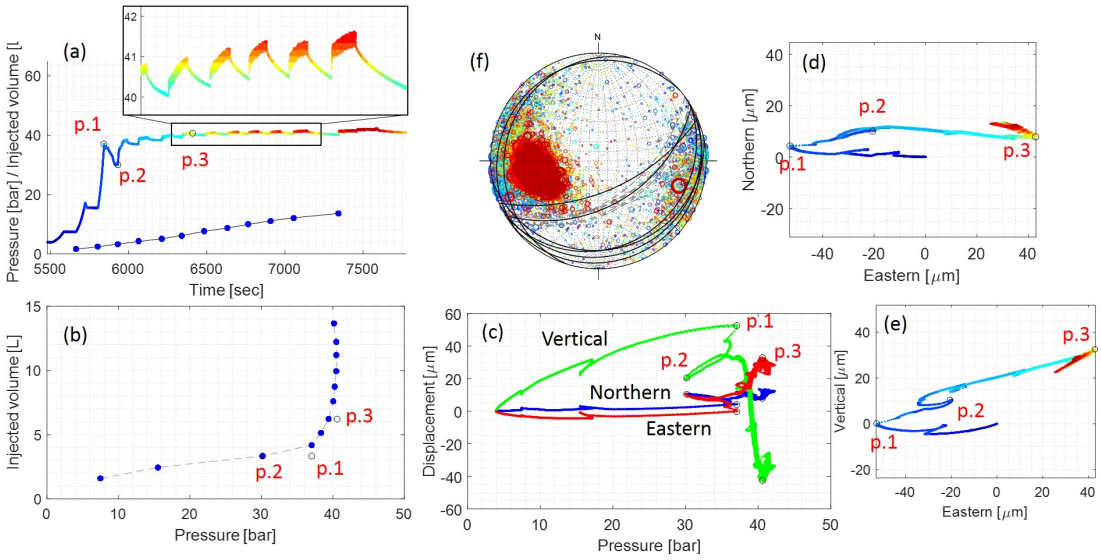

Figure 3.12: (a) Pressure and flowrate vs time during the injection with the manual pump. The blue markers at flowrate record correspond to the weighted injected volume in the end of a pressure step. Colors on the pressure records correspond to the values of pressure (b) Injected volume in the end of the pressure step vs imposed pressure, (c) Displacement components vs Pressure, (d) Northern vs Eastern displacement components, (e) Vertical vs Eastern displacement components, (f) Projection of the displacement orientation captured every 10Hz

3.3.1 Step-by-step pressure increase injection using manual pump

The injection test with the manual pump consists of 14 steps (Figure 3.12a). First three pressure increase steps reached 3.7 MPa (Point 1 in Figure 3.12), which is followed by a pressure drop of 0.2 MPa and a pressure decay (shut-in) in the chamber until 3 MPa (Point 2 in Figure 3.12), when the fluid is pumped in again. The pressure decay is accompanied by an exponential flowrate increase (Figure 3.12b) and the beginning of non-linear behavior between pressure and displacement components (Figure 3.12c). The shut-in pressures estimated during manual injection are around 4.1 MPa and given in Figure 3.12a. Figures 3.12d and 3.12e show that below 3.7 MPa the displacements are oriented towards W. During the pressure decay the displacements rotate towards EEN (upwards) until the next pressure step increase. At the next pressure step the displacement rotates towards EES (upwards) until the pressure of 4.1 MPa (Point 3 in Figure 3.12). The maximum pressure reached during the injection with the manual pump is 4.2 MPa. Figure 3.12f shows that overall displacement during injection varying in East-West direction.

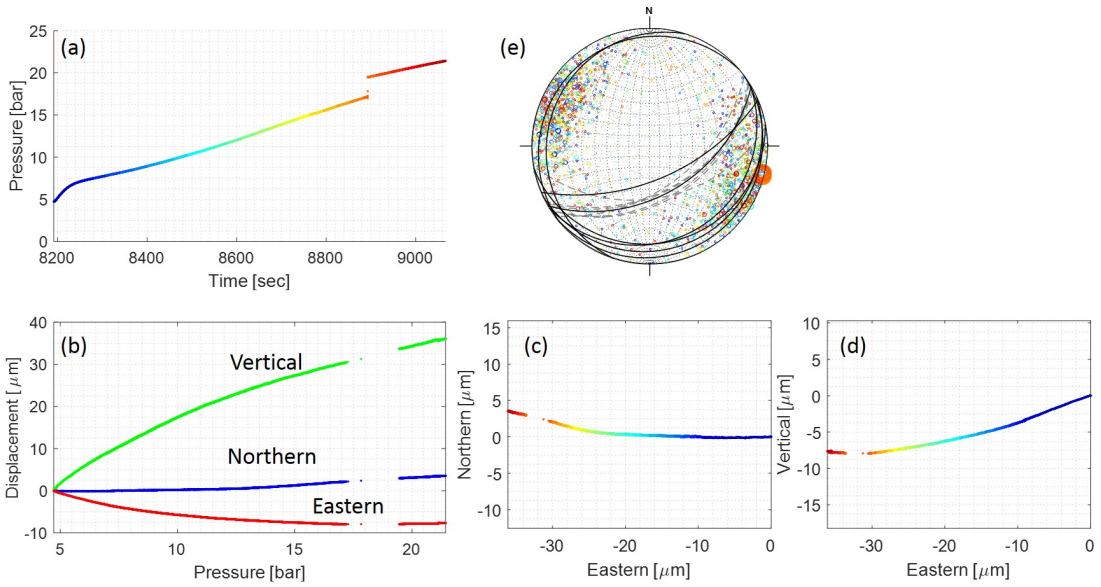

Figure 3.13: (a) Pressure and flowrate vs time during the injection with the manual pump; (b) Displacement components vs Pressure; (c) Northern vs Eastern displacement components, (d) Vertical vs Eastern displacement components; (e) Projection of the displacement orientation captured every 10Hz

3.3.2 Constant flowrate injection using manual pump

The results of the constant flowrate injection using the manual pump is given in Figure 3.13. The pumped volume during this injection is 4.1 L. Pressure vs. displacement component is linear (Figure 3.13b), however, it is observed that an abrupt displacement at 3.1 MPa and oriented towards WWN (upwards, Figure 3.13c,d). Figure 3.13e shows that overall displacement is oriented WWN-EES, which is consistent with an orientation of the elastic response of the rock mass.

3.3.3 Step-rate injection

The injection using the engine pump consists of 11 pressure steps (Figure 3.14a). The linear pressure-displacement behavior ends at 3.3 MPa (point 1 in Figure 3.14c) and oriented towards W (downwards, Figure 3.14 d,e). At 3.3 MPa the displacement rotate towards E (upwards, Figure 3.14 d,e). The next sharp displacement occurs at 4.3 MPa and is associated to a significant flowrate increase (point 2 to point 3 in Figure 3.14a and b). During the pressure step of 4.3 MPa from point 2 to point 3 there is a displacement of 102 μmm, which is oriented towards E (upwards). The consistency between the orientation of the displacement at the pressure drop at 3.3 MPa (point 1 at Figure 3.14a) and the orientation of the displacement at the pressure step of 4.3 MPa (from point 2 to point 3 at Figure 3.14a) indicate that a

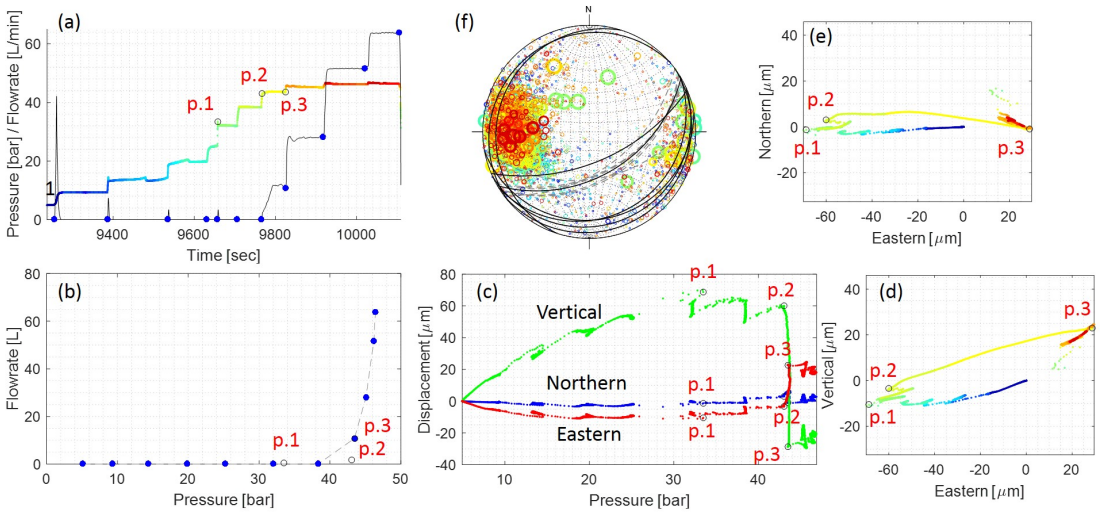

Figure 3.14: (a) Pressure and flowrate vs time during the injection with the manual pump. The blue markers at flowrate record correspond to the weighted injected volume in the end of a pressure step. Colors on the pressure records correspond to the values of pressure (b) Injected volume in the end of the pressure step vs imposed pressure, (c) Displacement components vs Pressure, (d) Northern vs Eastern displacement components, (e) Vertical vs Eastern displacement components, (f) Projection of the displacement orientation captured every 10Hz

fault was reactivated at 3.3 MPa and then opened after adding 1 MPa to the system. The pressure steps after 4.3 MPa are consistent with the steps of injected flowrate.

3.4 Test 44.65 m

The injection at the depth of 44.65 m takes over 3.5 hours. The test consists of step-up injection using manual pump, a pulse test, STR1 and STR 2 using engine pump. The injection interval is located within the Main Fault core and highly fractured, therefore, the response obtained during the injection is very complex. The maximum imposed pressure reached 5 MPa, however, no significant leakage into the formation is observed.

3.5 Numerical investigation of displacements in elastic rock mass

Sections 3.1-3.4 illustrated the complex chamber response during the fluid injection in the investigated tests. It was shown that at low injected pressure the SIMFIP probe captured displacements, which often follow a linear pressure-displacement relationship. In this section we want to test what would be the elastic contribution to

Table 3.1: Tested models

Intact Rock	**Fault between the anchors**	**Fault 0.25 m above the anchors**	**Fault 0.25 below the anchors**
Isotropic (Model 1)	Isotropic with a low stiffness fault (Model 3)	Isotropic with a low stiffness fault (Model 7)	Isotropic with a low stiffness fault (Model 9)
	Isotropic with a high stiffness fault (Model 5)		
Transverse Isotropic (Model 2)	Trans.Isotrop. with a low stiffness fault (Model 4)	Trans.Isotrop. with a low stiffness fault (Model 8)	Trans.Isotrop. with a low stiffness fault (Model 10)
	Trans.Isotrop. with a high stiffness fault (Model 6)		

the deformation measured by the anchor in various elastic situations. We performed three-dimensional discrete-element-method numerical models of low pressure pressurization of a borehole that penetrates (i) an isotropic intact rock, (ii) a transverse isotropic intact rock and (iii) an intact rock with a single elastic fracture. The main objective of this study is to understand the influence different rock mass properties and stiffness of fractures on anchor displacement during the elastic response. We compare the response of anchors that measure the deformation applied to isotropic and transverse isotropic rocks, as well as low and high stiffness fractures. In addition, we compared the response of the anchors when the fracture is located between, above or below anchors. We didn't run a systematic sensitivity study on all parameters (e.g. fault orientation, stress orientation, stress ratio,...) but analyses a series of combination that are inspired and relevant for condition encountered in our Mont-Terri test and thus can be used to help us interpreting our Mont-Terri data. Table 3.1 summarizes all 10 models, tested in this numerical study.

3.5.1 Methodology and parameters of the numerical model

To build the numerical model, we used the distinct element code 3DEC (Cundall, 1988; Hart et al., 1988). The model geometry is given in Figure 3.15. A block model of $2.8 \times 2.8 \times 2.4$ m^3 is crossed by a borehole with a diameter 0.14 m (Figure 3.15a). Both a fault crossing the borehole and a plane of isotropy are orientated 130°/55°. The model is discretized into deformable tetrahedral zones. The size of the zones gradually increases from 0.016 m in the vicinity of the borehole to 0.1 m close to the borders of the model. To represent the anchors we select specific node on a tetrahedral zone as "anchor points" and monitor their movement on the borehole wall (Figure 3.15b). We then compute for each anchor a center point by considering the center of a circumscribed circle to the tree anchor location. Finally the displacement is estimated by comparing the change of position of these two

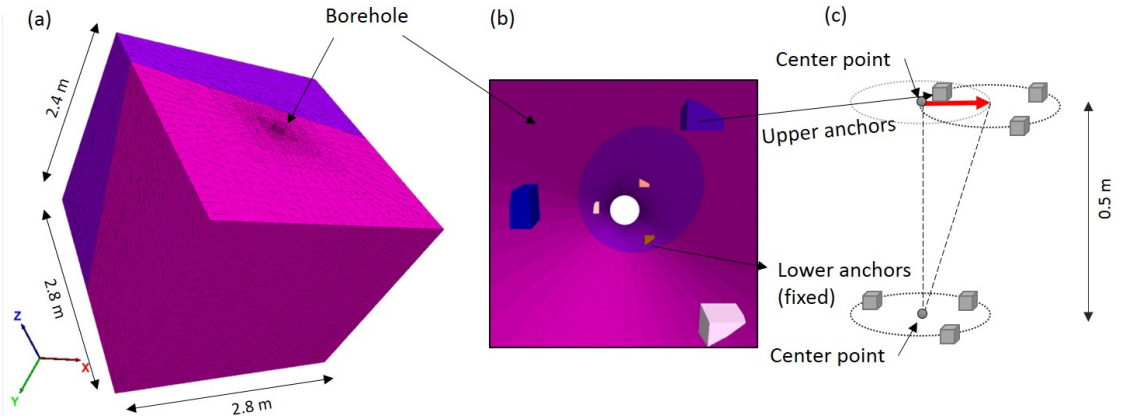

Figure 3.15: (a) Tested block model (b) Borehole with lower and upper anchors intersected by the fault, (c) Displacement vector on upper anchors, considering the lower one is fixed.

center points and computing its norm, considering the lower one as fixed (Figure 3.15c).

Roller and pressure boundary conditions were applied to external vertical and horizontal model faces, respectively. Equivalent stress of σ_{xx} = 3.0 MPa, σ_{yy} = 5.0 MPa, σ_{zz} = 6.0 MPa was applied to all the model nodes. The magnitudes of the stresses are inspired from Martin and Lanyon [2003]. The orientations of the stresses are parallel to the axis of the model. The elastic properties for the intact rock and fractures are inspired from the Mont Terri case and are given in Table 3.2 [Bossart, 2011]. For the model matrix with used either isotropic material behavior or transverse isotropic material behavior with the parameters given in Table 3.2. The behavior of elastic fracture is controlled by its normal and shear stiffness (Table 3.2). We test two models of stiffness of the fracture: high (K_n =500 GPa/m, K_s =250 GPa/m) and low (K_n=20 GPa/m, K_s=2 GPa/m).

Pressure increase within the borehole is modelled by applying a stress boundary condition, no pressure diffusion in the rock or the fracture is considered. We applied a pressure of 2 MPa to the borehole walls to induce elastic deformation. Computation is run until the unbalanced force gets below a standard threshold of 10^{-5}.

3.5.2 Results of the numerical investigation

The results of the numerical modeling are shown in Table 3.3 and Appendix B.1.

Table 3.3 shows that the difference between isotropic and transverse isotropic rock mass is small. We assume that such a small difference can result from a slight offset between specified anchor locations within the nodes of tetrahedral mesh. Consequently, there is no difference in the deformation of the borehole between isotropic and transverse isotropic rock. The main difference between the results of the models is due to the presence of the fracture and differences in its stiffness and location.

Table 3.2: Properties of the numerical models.

Isotropic rock material model	
Bulk modulus [GPa]	5.9
Shear modulus [GPa]	2.3
Transverse isotropic rock material model	
Young's Modulus normal to bedding [GPa]	2.8
Young's Modulus parallel to bedding [GPa]	7.2
Poisson ratio 12	0.24
Poisson ratio 13	0.33
Shear Modulus [GPa]	1.2
Fault elastic model	
Normal stiffness K_n [GPa/m]	500 (or 20)
Shear stiffness K_s [GPa/m]	250 (or 2)

Table 3.3: Results of the numerical models

Model	Isotropic models	Displacement [μm]	Model	Transverse isotropic models	Displacement [μm]
1	No fracture	0.5	2	No fracture	0.84
Fault between anchors					
3	Low stiffness fault	36.33	4	Low stiffness fault	32.9
5	High stiffness fault	1.76	6	High stiffness fault	1.17
Fault 0.25 m above the anchors					
7	Low stiffness fault	22.61	8	Low stiffness fault	20.60
Fault 0.25 m below the anchors					
9	Low stiffness fault	9.26	10	Low stiffness fault	8.78

Thus, the largest deformation is observed between the anchors on the borehole, which is intersected by a lower stiffness fault. The smallest deformation belongs to the models with a high stiffness fault. The models, where the fault intersects the borehole above or below the anchors show less deformation in comparison to the models, where the fault intersected the borehole between the anchors.

3.6 Conclusions

The results of the preliminary interpretation of the flowrate-pressure-displacement response are given in Table 3.4. We observe that the significant values of pressure between the tests are not consistent between each other. It may be related to different structures intersecting intervals. Moreover, the tests 37.2 and 40.6 are located above the Main Fault zone, and test 47.2 below. In Chapters 5 and 6 we will focus on the flowrate-pressure-displacement response during the injection

Table 3.4: Summary of the results

Test	Pump	End of linear displacement vs pressure response [MPa]	Significant change in displacement orientation [MPa]	Shut-In Pressure [MPa]
37.2	Manual	3	5.9	4.3-4.5 5.3-5.4
	Pulse	3.9	-	-
	STR 1 (end)	-	-	4.6-4.7 2.7-3.4
40.6	Manual	1.7	3.4 5.9	-
	STR	3.5	5.4	
47.2	Manual	3.7	4.1	4.1
	SRT	3.3	4.3	-

at 37.2 m below the gallery floor. This test was chosen because i) it is located more far away from the fault zone that other tests, ii) it includes the estimation of the shut-in pressure, which can help in estimation of the in-situ stress.

For the numerical modelling conclusion are the following:

1. Without the influence of a fracture, the displacement captured by the anchor is very low. This is expected because only radial displacement occurs which cannot be captured by the anchors. In addition the displacement field around both the anchor is identical, resulting in a null relative displacement.

2. The presence of a fracture has induced heterogeneous displacement field around the borehole which results in relative displacement of the anchor. The softer the fracture the larger is this effect. With our parameters, the relative displacement norm reach some tens of microns. However, our models neglect the balancing effects that could arise on a fracture due to pressure diffusion.

3. The displacement with a fracture between the anchors is higher than the displacement with a fracture above or below the anchors.

Chapter 4

Slip perturbation during fault reactivation by a fluid injection

Maria Kakurina[1], **Yves Guglielmi**[2], **Christophe Nussbaum**[3], **and Benoît Valley**[1]

[1]University of Neuchâtel, CHYN, Neuchâtel, Switzerland, [2]Lawrence Berkeley National Laboratory, Berkeley, CA, United States [3]Swisstopo, Wabern, Switzerland

This chapter was published as: Kakurina, M., Guglielmi, Y., Nussbaum, C. and Valley, B., 2019. Slip perturbation during fault reactivation by a fluid injection. Tectonophysics, 757, pp.140-152. Maria Kakurina performed the analysis and did the modeling, as well as provided the structure of the main text. Yves Guglielmi, Christophe Nussbaum and Benoît Valley provided insights on field studies and the experimental set up. All the authors contributed to the writing and discussion of the results of the manuscript.

4.1 Abstract

Slip orientation inferred from fault striae or focal mechanism datasets is commonly used in stress inversion methods based on the Wallace-Bott hypothesis. The hypothesis postulates that slip on a fault plane is collinear with the orientation of the resolved shear stress. It is valid for a single planar fault subjected to a homogeneous far-field stress. However, the experimental displacement data from an induced fault reactivation experiment, conducted in the Mont Terri rock laboratory, Switzerland, indicated multiple triggered slip orientations, thus disallowed solutions of the inversion problem. We present numerical and analytical results of slip on a reactivated fracture containing non-uniform fluid pressure distributions. Using these models, we evaluate the reasons for the inconsistency of our observations and the

traditional Wallace-Bott hypothesis and test the physical effects of various parameters on fault slip. In the fully coupled hydromechanical numerical model (three-dimensional distinct element method), fluid pressure is increased stepwise from a point within the fault (assumed planar and singular) until shear reactivation of the fault is induced. We studied two different models with high and low fault plane stiffness to represent hard and soft rock masses, respectively. The model shows that high fault stiffness preserves the planar fault plane, while low fault stiffness permits dilation and morphology changes of the fracture related to fluid pressure diffusion. The highest slip perturbation was observed in the low stiffness model due to the change of the fracture shape, controlled by the non-uniform pressure distribution. The Eshelby analytical solution confirmed that the more the fracture is dilated, the more the corresponding resolved shear stress is perturbed. Additionally, when compared to dilation and fault aperture, the friction angle has the most influence on the angular difference between geomechanical slip vectors and resolved shear stress.

4.2 Introduction

Stress inversion methods have been developed since the middle of the last century in order to estimate the in-situ stress state using focal mechanisms from earthquakes or fault slip deduced from slickenside measurements on fault planes. Generally, these inversion methods are based on the Wallace [1951] and Bott [1959] hypotheses (referred later as WB hypothesis), stating that the slip on the fault plane occurs in the direction of the maximum resolved shear traction. In 1959, Bott demonstrated that the slip direction on reactivated plane depends on the principal stress orientation, the stress ratio and the orientation of the fault plane. In addition, the WB hypothesis is based on a number of assumptions: (i) faults are planar, (ii) intact rock blocks are unbreakable, (iii) stress state is uniform, (iv) all movements are caused by the same stress tensor, (v) neither block rotation nor stress perturbation occur along the faults, and (vi) movements on each fault are independent from each other.

The WB hypothesis is used to predict the kinematics of newly formed faults [Anderson, 1951, Wallace, 1951] and to estimate the potential for reactivation of natural preexisting faults planes under given regional stress states Bott [1959]. Different methods and algorithms to reconstruct the paleostress states using the WB hypothesis were developed by many authors [Angelier, 1990, 1979, 1975, Arthaud, 1969, Blenkinsop et al., 2006, Carey, 1976, Carey and Brunier, 1974, Célérier et al., 2012, Delvaux and Sperner, 2003, Etchecopar et al., 1981, Gephart and Forsyth, 1984, Hansen, 2013, Lisle, 1998, 1992, Reches, 1987, Yamaji, 2000]. These methods were used in numerous regional studies [Angelier et al., 1985, Barrier and Angelier, 1986, Bergerat, 1987, Lacombe et al., 1990, Le Pichon et al., 1988, Letouzey, 1986,

Liesa and Simón, 2009, Mattauer and Mercier, 1980, Mercier et al., 1989, Vandycke et al., 1991, Zoback et al., 1981].

However, it is legitimate to question the validity and expect limitations of the WB hypothesis for the stress estimation methods since many of the underlying assumptions are not respected in field cases. Field observations of geometrical complexity of fault surfaces and fault networks [Jaeggi et al., 2017, Nussbaum et al., 2011, Wallace and Morris, 1986, Wibberley and Shipton, 2010], evidences of local stress perturbations from observed microstructures [Hancock, 1985, Laurich et al., 2014, Petit, 1987, Soliva et al., 2010], curved lineations on the local shear planes [Twiss and Gefell, 1990] imply that the mechanical problems of stress inversions are overly simplified and seem to disagree with the Wallace-Bott (WB) assumptions.

Numerical investigations of the WB assumptions, examined by Dupin et al. [1993], Kaven et al. [2011], Maerten [2000], Nieto-Samaniego and Alaniz-Alvarez [1997], Pascal [2002], Pollard et al. [1993] demonstrated that the slip direction can be strongly influenced by the mechanical interactions between closely spaced faults within the same tectonic stress regime. The mechanical interactions are partly attributed to elastic deformations that cause local stress perturbations acting on one fault plane as induced by slip on another fault plane. Indeed, in the vicinity of fault intersections, the slip direction can deviate up to 50° from the direction of resolved shear stress [Maerten, 2000]. The mechanical interactions are accompanied with strain hardening behavior characterized by an increase in the fault surface roughness and by changes in deformation mode from a simple frictional sliding to a combination of sliding, dilation and formation of new fractures.Nieto-Samaniego and Alaniz-Alvarez [1997] demonstrated that those interactions affect the slip direction and, therefore, may invalidate the WB hypothesis. If fault spacing is large enough to prevent these mechanical interactions, the slip tends to follow the theoretical WB predictions.

According to the WB hypothesis, for non-planar faults, such as highly curved faults, corrugated faults, lineated portions of stylolitic surfaces, and flexural slip folds, the directions of resolved shear stress in general give a set of slip directions of rigid fault blocks, which is generally kinematically questionable [Lisle, 2013]. For example, Lisle [2013] demonstrated that the anisotropy of the shear strength arising from simple fault plane topography can lead to significant angular differences between the directions of resolved maximum stress and the slip direction. Potential slip for a corrugated fault plane is oblique to the maximum resolved shear stress direction. The author also showed that the magnitudes of the high resolved shear stress (90% of the maximum values) are defined within tolerance of $\pm$ 26° of the slip direction implying that in practice a high variability around the theoretical maximum shear stress direction is expected.

More recently, Lejri et al. [2015] examined the effect of all possible Andersonian stress regimes, half space effect, fault fluid pressure, sliding friction, Poisson's ratio and various idealized fault geometries in relation to the validity of the WB assumptions. They confirmed that high angular differences (later referred as misfit angle) exist between geomechanical slip vectors and resolved shear stress under specific fault configurations such as intersecting faults or highly corrugated fault surfaces, invalidating the WB assumptions. These effects are slightly reduced when faults touch the traction free surface of the Earth where no confinement is applied. The propensity for a fault to slip at the surface is increased and slip gradients are greater than on an isolated fault at depth. According to Lejri et al. [2015], the increase of the fault friction globally lowers slip magnitude, hence mechanical interaction, and reduces the misfit angle between the slip direction and resolved shear stress. The friction effects were also investigated by Pascal [2002], who concluded that the sliding friction reduces slip perturbation and validates the WB assumptions. The Poisson's ratio has a very small effect on the misfit angles [Lejri et al., 2015].

Uniform fluid pressure inside the intersecting fault planes affects the resulting slip orientations [Lejri et al., 2015, Maerten et al., 2018]. Greater fluid pressure leads to higher misfit angles [Lejri et al., 2015]. This is related to the fact, that fluid pressure reduces the effective normal stress on a fault plane and thus may affect both the slip magnitude and slip vector orientation, violating the WB hypothesis. In addition, uniform fluid pressure increase in an intersecting fault situation will generate stress perturbations due to the resulting elastic deformation of the surrounding rock mass that can also explain deviation from the WB hypothesis.

Pore pressure increased by fluid injection in the vicinity of the injection borehole propagates and decays in the amplitude away from the borehole, governed by hydraulic diffusion [Shapiro et al., 2003]. This is another important effect to consider when injecting in a fracture or fault is that pressure diffusion is progressive leading to a non-homogenous pressure field. Such pressure diffusion effects are known to eventually induce seismicity (i.e. fracture slips) in the surrounding rock mass [Ellsworth, 2013, Evans et al., 2012, Guglielmi et al., 2008, McGarr, 2014, Shapiro et al., 1999, Shapiro and Dinske, 2009, Zoback and Harjes, 1997]. The question is whether slip under a non-uniform pressure field obeys or disobeys the WB hypothesis? An example from the Geysers geothermal field, Martínez-Garzón et al. [2016] observed that slip deviation occurs on faults during periods of high injection rates close to the injection wells. In the Basel Fluid-Injection Experiment the misfit between expected slip vectors and slip vectors deduced from the focal mechanisms was less than 15 degrees and more than 80 % of the slip vectors were consistent with those expected under the estimated uniform stress pattern [Terakawa et al., 2012].

The consequences of a non-uniform pressure field is a non-uniform fracture open-

ing and shear. During fluid injection, a fracture opens progressively from the borehole to the fracture tip. Stress transfers are associated with these non-uniform deformation fields leading to stress perturbations that could explain violation of the WB hypothesis [Cornet and Julien, 1989, Roche et al., 2018]. With time pressure diffusion tends to equilibrate the pressure distribution leading to a more uniform fracture shape and thus at such stage it is expected that the WB hypothesis is valid again.

In this paper, we focus on the evaluation of the theoretical bases related to the WB hypothesis in the context of stress inversion of the slip data obtained during fault reactivation by a fluid injection. The slip data is measured using the SIMFIP probe developed by Guglielmi et al. [2013]. Compared to a standard double packer system, in addition to flowrate and pressure monitoring the SIMFIP probe measures the three-dimensional (3D) displacement in the injection chamber. The direct in-situ measurement of the 3D displacement corresponding to slip on reactivated faults allows estimation of the principal stress orientations and relative magnitudes by solving the inverse stress problem.

The SIMFIP probe was used to conduct the Fault Slip (FS) experiment of fault reactivation in shale rocks at the Mont Terri rock laboratory [Guglielmi, 2016, Guglielmi et al., 2017]. The experiment focusses on understanding the conditions of fault stability and activation, as well as on evolution of the coupling between fault slip, pore pressure and fluid migration in shales. One of the main goals of the FS experiment is to develop a protocol for estimating the in-situ stress using the additional displacement data information. The FS experiment consists of a sequence of pressure-controlled fluid injections into 2.4 m long intervals within the main tectonic zone of the Mont Terri rock laboratory, called the Main Fault, to reactivate the fault planes and to induce fault slip, which can be used to solve the stress inversion problem (Figure 4.1a). The orientations (dip direction / dip angle convention is used in this chapter) of the two boundary planes of the Main Fault vary with dip direction ranging from 140° to 165° and the dip angle – from 40° to 65° [Guglielmi et al., 2017]. In total, there were five injection tests performed. Here, we investigate the results of the test conducted above the Main Fault at the depth of 40.6 m below the laboratory floor (300 m.a.s.l.). The pressure and flowrate time variations conducted at the test are shown in Figure 4.1b. The initial pressure steps are achieved by small volume injections (insignificant flowrate). When the pressure reaches 5.3 $\pm$ 0.1 MPa a significant flow rate is required to maintain the pressure which indicates fault opening. Deformation is measured during this pressure/flow history. Deformation occurs even during constant pressure in the injection chamber even with insignificant flowrate prior to fault opening pressure and we interpret this as an indication of fault rupture – fault slip (Note: the slip vector analyzed in this

chapter is taken in a different way than Chapters 5 and 6). The orientations of the slip vectors are shown in Figure 4.1c. It is demonstrated that slip orientation rotates in a counterclockwise direction from 029°/20° at the injection 1 to the direction of 345°/16° at the injection 2, then to the direction of 313°/17° at the injection 3. After the slip vector rotates slightly clockwise to the direction of 330°/0° at the injection 4 and then in a counterclockwise direction again at the injection 4b and 5, having the directions of 325°/17° and 320°/40°, respectively. The vector at the injection 6 has an orientation of 050°/60°, which does not follow the rotation tendency discussed above, however, this vector was measured after the fault opening, and therefore additional processes can influence its orientation. The difference in slip orientation at each pressure step does not make the stress inversion possible because the WB assumption of the stress homogeneity is not satisfied. We expect that the cause of slip deviation is in the non-uniform pressure distribution and altered fracture aperture. To investigate these complex interactions between pore pressure distribution inside the fracture and slip orientation, we built a numerical model that includes pressure diffusion and fluid flow along the fracture coupled with fracture deformation, using the three-dimensional distinct element code 3DEC [Itasca Consulting Group, 2007]. We estimate the role of changes in fracture shape during fluid injection on stress perturbations using the analytical solution of stress perturbation around an ellipsoidal fracture provided by Eshelby [1957]. This analytical solution helps in understanding the impact of the shape of the pressure activated patch on the orientations of the slip vectors. For both numerical and analytical methods, two particular models are presented here, with a high and a low fracture stiffness to emulate a fault within more competent (carbonates) and less competent (shales) rocks. The stiffness will determine the opening of the fracture affecting its shape and is thus expected to be a controlling parameter on slip direction perturbations.

In addition to the fracture stiffness coefficients, a multi-parametric study including (i) friction angles, (ii) dilation angles, and (iii) aperture was performed to understand the effect of each parameter on the misfit angle between the simulated slip vectors affected by the pressure non-uniform distribution and the resolved shear stress direction relevant in the WB hypothesis.

4.3 Theoretical background

4.3.1 Orientation of the resolved shear stress (Wallace-Bott hypothesis)

The rake of the displacement that is consistent with the resolved shear stress according to the Wallace-Bott hypothesis can be computed by methods proposed

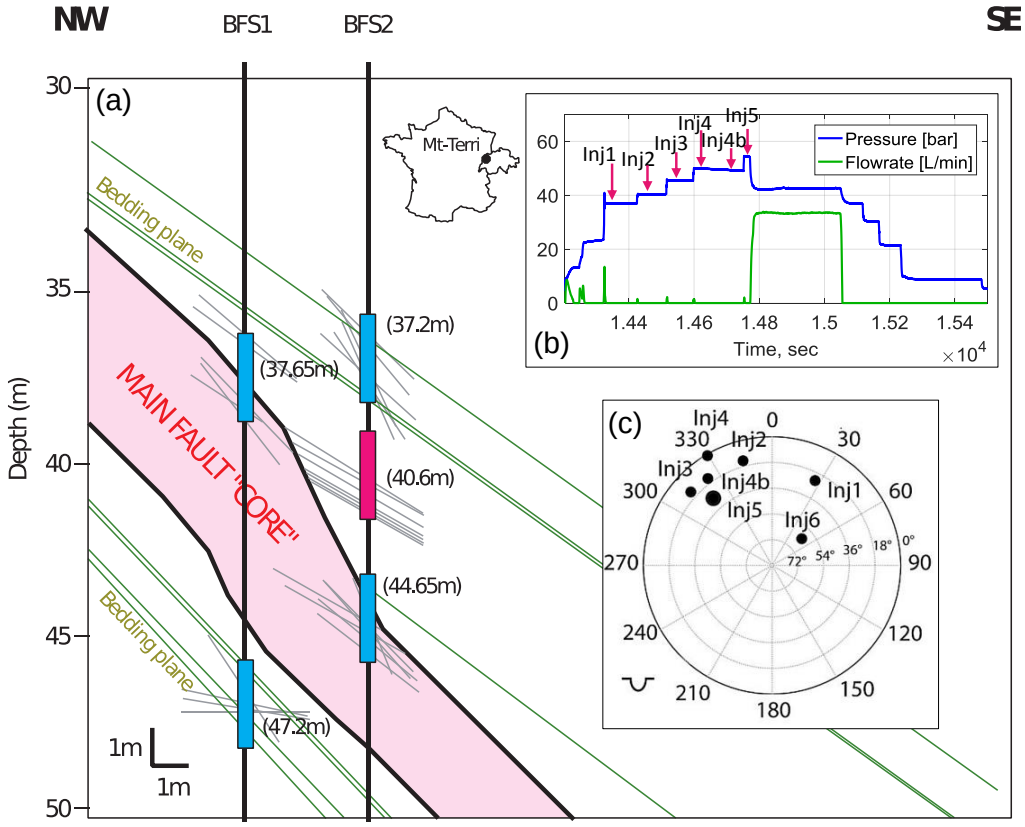

Figure 4.1: (a) Simplified cross-section of the structural setting of the FS experiment (modified from Guglielmi [2016]). The locations of the test intervals are figured by the blue and pink (investigated) rectangles. (b) Pressure and injected flowrate variations monitored at the injected interval of 40.6 m depth. (c) Stereographic projection of the plastic displacement vectors picked at constant pressure, shown by pink arrows on (b).

by Bott [1959] and Jaeger et al. [2009]. The normal and shear traction components on the plane P with a dip angle θ and a dip direction of λ can be expressed in a local Cartesian coordinate system (x',y',z') with x' down dip, y' horizontal and z' normal to P (Figure 4.2). The dip angle and dip direction are defined relatively to the far field principal stress coordinate system x -axis (σ_1), y-axis (σ_2) and z -axis (σ_3). The normal and shear components on the plane P are given by:

$$\sigma = (\sigma_1 \cos^2 \lambda + \sigma_2 \sin^2 \lambda) \sin^2 \theta + \sigma_3 \cos^2 \theta \tag{4.1}$$

$$\tau_{z'y'} = -\frac{1}{2}(\sigma_1 - \sigma_2) \sin \theta \sin 2\lambda \tag{4.2}$$

$$\tau_{z'x'} = \frac{1}{2}(\sigma_1 \cos^2 \lambda + \sigma_2 \sin^2 \lambda - \sigma_3) \sin 2\theta \tag{4.3}$$

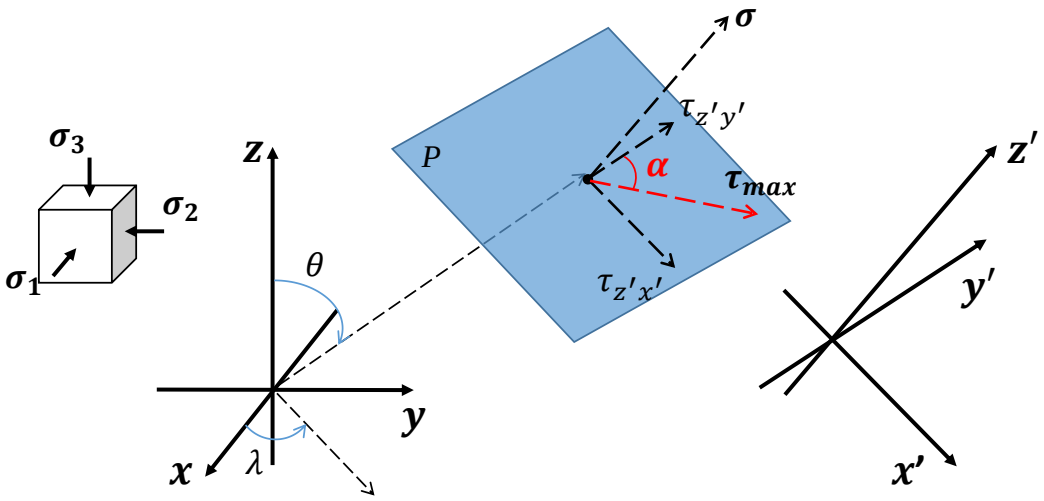

Figure 4.2: Principal stress coordinate system (x,y,z) and local Cartesian coordinate system (x′,y′,z′) with the slip vector α of the maximum resolved shear stress. The plane P (blue rectangle) is expressed in a local coordinate system with dip angle θ and dip direction λ relatively to the principal stress coordinate system.

The rake α of the maximum shear traction on the plane is obtained combining Eqs. (4.2) and (4.3) and is given by:

$$\alpha = \arctan \frac{\tau_{x'z'}}{\tau_{y'z'}} = \arctan \frac{2(\cos^2 \lambda + R \sin^2 \lambda) \cos \theta}{(1 - R) \sin 2\lambda} \tag{4.4}$$

where $R = (\sigma_2 - \sigma_3)/(\sigma_1 - \sigma_3)$ is refered as the stress ratio. In Eq. (4.4), the direction of the maximum resolved shear stress (τ_{max}) on a plane depends only on the plane orientation with respect to the principal stress orientations and their magnitude ratio R. In our study, we used the implementation of these equations in Faultkin software [Allmendinger et al., 2011, Marrett and Allmendinger, 1990] to compute the rake of the maximum resolved shear traction.

4.3.2 Problem statement and conceptual model

When fluid is injected in a fault zone (we will initially make the simplification that the fault is represented as a single planar fracture), it activates a series of thermo-hydromechanical processes that will affect the rock mass condition and the fracture shape (Figure 4.3).

We assume isothermal fluid injection and, thus, focus only on the following hydromechanical processes. When fluid is injected in the fault, the fluid will diffuse preferentially in the fault itself and the diffusion will be controlled by the hydraulic aperture of the fault. This will first induce an elastic response of the fracture and

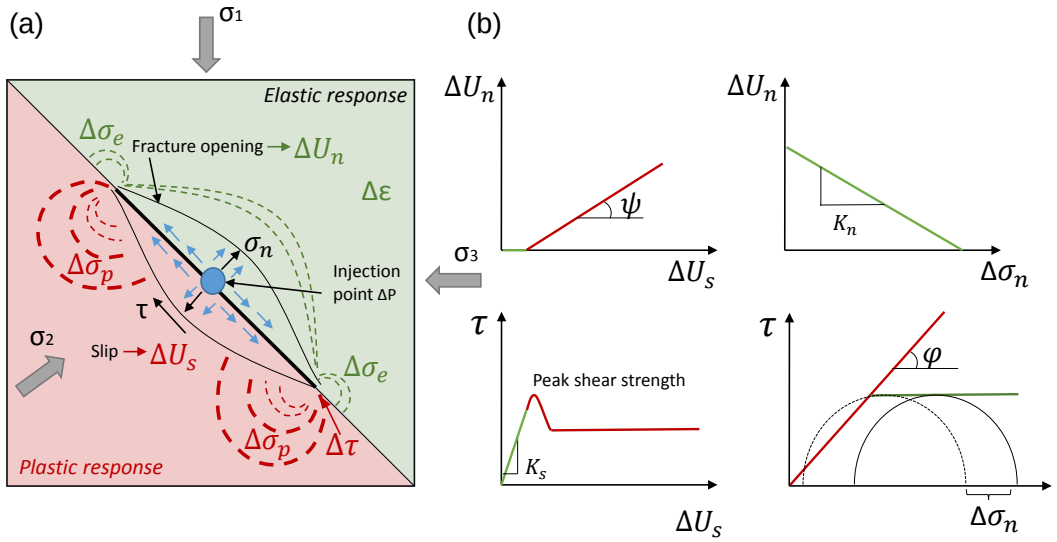

Figure 4.3: (a) Stress redistributions around a fracture during elastic and plastic responses (modified from Pollard [1987]). (b) Main stress-displacement relations, containing fault response to injection, where τ- shear stress, σ- normal stress, ΔUs- shear displacement, ΔUn – normal displacement, ϕ – friction angle, ψ – dilation angle, $\Delta\varepsilon$ – rock deformation.

the rock mass surrounding it. The pressure increase in the fault plane will generate an elastic opening of the plane with a normal displacement component (ΔUn) that in turn will modify the hydraulic aperture and involve a non-linear diffusion process. The opening of the fault plane will be accommodated by the deformation of the surrounding rock inducing elastic stress changes e around the injection point. The deformation and the stress changes will be controlled by the stiffness properties of the fault plane and of the surrounding rock as well as by the non-homogeneous pressure distribution around the injection location. Such a complex fully coupled hydromechanical process is likely to induce some local rotation of the principal stresses, resulting eventually in the "violation" of the WB hypothesis.

In addition, the pressure increase in the fault plane will reduce the effective normal stress eventually driving the plane to shear failure associated with slip. In contrast to the elastic response described above, the slip associated to shear failure is typically not reversible and we will refer to it as plastic deformation. The initiation of slip is controlled by on one hand the frictional properties of the plane (no cohesion is assumed) and on the other hand the shear traction τ acting on the plane that depends on the local stress state (Mohr-Coulomb criterion). The frictional properties are assumed to be invariant, although modification of the frictional properties due to wetting and/or lubrication or other rock/fluid interactions are possible. Associated with fault slip, stress will be redistributed with a relaxation of the shear stress on the fault plane and a concentration of stresses near the fault tip ($\Delta\sigma_p$). Mechanical

dilation of the fault plane can be associated with fault slip in order to accommodate asperities present on the plane. This will again be accommodated by the surrounding rock mass inducing stress changes and it will modify the hydraulic aperture of the plane which will affect the pressure distribution in the fault plane. Some of the fluid pressure may also leak in the rock matrix implying a poroelastic response of the rock including both deformation and stress changes. However, in our simulation with 3DEC, we will neglect flow and pressure changes within the rock blocks.

It is obvious from the conceptual model described above that fluid injection in fault planes initiate a series of interdependent hydromechanical processes (referred as hydromechanical coupling). These processes that are schematically represented in Figure 4.3 will locally affect the stress state and the fracture shape, and thus may change the direction of the local shear traction causing variations of the slip vector orientation. Since stress inversion techniques consist in interpreting this slip vector direction for constraining the in-situ stress state, it is legitimate to ask ourselves about the impact of these processes on in-situ stress estimation from the interpretation of fluid injection data.

4.4 Methodology

4.4.1 Background and assumptions of numerical approach

We use the distinct element code 3DEC [Cundall, 1988, Hart et al., 1988] to simulate the fracture as a discontinuity separating two compartments represented as two blocks that are free to move, rotate and separate relative to one another. Here we work with fully coupled hydromechanical simulations, that means that solid deformations influence the fluid pressures and the fluid pressure affect the mechanical stresses and strains. Thus, most of the processes described in our conceptual model above are included in our simulations. The mechanical model in 3DEC is assumed to be quasi-static, meaning that the inertial forces are neglected, and the model stays at a state of force equilibrium, or a state of steady flow of material if the model fails.

We assume that the rock blocks are linearly elastic, homogeneous and isotropic. Since we only consider short duration injections in a medium with a strong permeability contrast between the high permeable fracture and the low permeable surrounding rock mass, we consider zero porosity rock blocks such that no fluid diffuses and no poroelastic effects are taking place in the rock blocks.

Contacts exist between the two deformable blocks at each node of the fracture. The behavior of the fracture is represented by an area contact Coulomb slip model. The code uses an explicit algorithm so that information propagates through the model dynamically (time-domain dynamic algorithm). At each time step, the laws

of motion and constitutive equations are jointly applied to calculate normal and shear forces at each contact, which then are used in the calculation of the block motion. In the elastic range, the fracture behavior is governed by the fracture normal and shear stiffnesses (units are Pa.m−1), K_n and K_s as described by Eqs. (4.5) and (4.6):

$$\Delta F_n = -K_n \Delta U_n A_c \tag{4.5}$$

$$\Delta F_s = -K_s \Delta U_s A_c \tag{4.6}$$

where A_c is the contact area, ΔU^n and ΔU^s are the normal and shear displacements increments, ΔF^n and ΔF^s are the normal and shear force increments.

Slip occurs when the force conditions on the plane reach the Mohr-Coulomb criteria:

$$F_{s\,max} = cA_c + F_n \tan\phi \tag{4.7}$$

where c and ϕ are the fracture cohesion and friction angle, respectively. Fracture asperities overriding is captured through a dilation model that is activated when the joint is at slip. The normal displacement ΔU_n leads to a dilation of

$$\Delta U_n(dil) = \Delta U_s \tan\psi \tag{4.8}$$

where ψ is the dilation angle.

In the model, fluid flow is simulated within the fracture, and not in the surrounding porous medium. The fracture is represented by parallel walls with an equivalent hydraulic aperture u_h. Fluid flowrate per unit width of the idealized fracture follows the cubic law [Witherspoon et al., 1980].

$$q = -\frac{u_h^3 \rho g}{12\mu} \nabla_h = -k_H \nabla_h \tag{4.9}$$

where k_H is the hydraulic conductivity of the fracture (m/s); ∇_h is the gradient in hydraulic head, ρ is the fluid density (kg/m^3), g is the acceleration due to gravity (m/s^2) and μ is the fluid viscosity (Pa. s).

Coupling equation (4.8) and (4.9) implies that in the elastic range, the hydraulic conductivity varies as a function of the effective stress as [Detournay, 1980]:

$$k_H = \frac{\rho g}{12\mu}(u_{h0} + \Delta U_n)^3 = \frac{\rho g}{12\mu}\Big(u_{h0} + \frac{\Delta F_n}{A_c K_n}\Big)^3 = \frac{\rho g}{12\mu}\Big(u_{h0} + \frac{\Delta \sigma_n^{'}}{K_n}\Big)^3 \tag{4.10}$$

where u_{h0} is the fracture aperture at zero normal stress and $\Delta\sigma_n^{'}$ is the increment

in the Terzaghi effective normal stress which is written in simplified form as [Walsh, 1981]:

$$\Delta\sigma_n^{'} = \Delta\sigma_n - \alpha\Delta P_p \tag{4.11}$$

where ΔP_p is the increment in the pore pressure and the effective stress coefficient $\alpha \sim 1$.

In the plastic range, the cubic law is adapted with the hydraulic conductivity of the fracture varying (1) as a function of the effective stress ('elastic' equivalent hydraulic aperture u_{he}) and (2) as a function of dilation induced by fracture slip ('slip' equivalent hydraulic aperture u_{hs}), as

$$k_H = \frac{\rho g}{12\mu}(u_{he} + u_{hs})^3 = \left(u_{h0} + \frac{\Delta\sigma_n^{'}}{K_n} + u_{hs}\right)^3 \tag{4.12}$$

u_{hs} is simply taken equal to the dilation induced at fracture slip $\Delta U_n(dil)$.

4.4.2 Parameters of the numerical model

The model geometry and conditions are inspired from the conditions at the Mont Terri experiment site. The geometry of the 3DEC model is shown in Figure 4.4a. The model outer boundaries form a cube with a 20 m long edge. The model is split in two blocks by a planar joint oriented 140°/60°. There are active and inactive areas of the joint in the model. Active joint area simulates the fracture behavior and is referred as fracture. The radius of the fracture is 5 m. Inactive joint area represents the intact rock and isolates the active fracture area from the model boundaries. Inactive joint areas are prevented from slipping by setting the cohesion and friction values to a high level and elastic parameters are chosen to be compatible with rock mass deformation.

The model is discretized into deformable tetrahedral zones (in total 186703 zones). The size of the tetrahedral zones in the central part of the block containing the fracture are twice as small as in the region farther from the fracture (0.4 and 0.8 m, respectively). The joint is surrounded by a continuous elastic material.

Equivalent stress and pressure initial and boundary conditions are applied to all model nodes and external model faces, respectively. Principal stress magnitudes were inspired from the Mont Terri estimated in-situ stress state respectively of Martin and Lanyon [2003]: $\sigma_{xx} = 3.0$ MPa, $\sigma_{yy} = 5.0$ MPa, $\sigma_{zz} = 6.0$ MPa, and in-situ pore pressure: $Pp = 0.5$ MPa. The stresses are aligned with the orientation of the model coordinate axes.

The material properties of the reference model are listed in Table 4.1. We use two reference models with high and low fracture stiffness values. The high stiffness

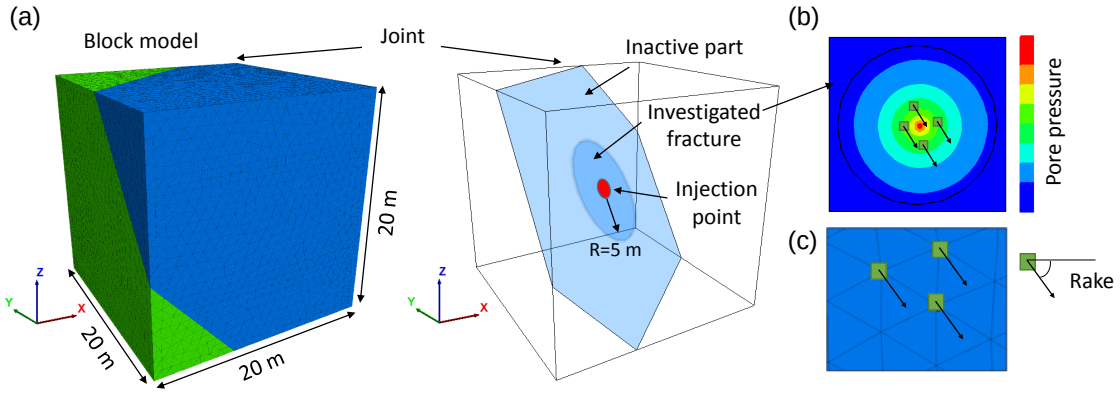

Figure 4.4: (a) Three-dimensional model with planar joint, (b) pore pressure distribution and deformation is modelled and tracked for further analyses, (c) sub-contacts (section of the joint) in conditions exceeding the failure conditions (slip) are tracked. The slip direction of the sub-contacts is recorded and its rake direction is computed.

Table 4.1: Properties of the numerical model.

Block		**Joint**	***Active part***	***Inactive part***
Mass density [kg/m3]	2450	Normal stiffness [GPa/m]	500 (or 20)	500 (or 20)
Bulk modulus [GPa]	5.9	Shear stiffness [GPa/m]	250 (or 2)	250 (or 2)
Shear modulus [GPa]	2.3	Friction angle [°]	22	40
		Cohesion [MPa]	0	11024
Fluid		Aperture, [m]	110-6	
Fluid density [kg/m3]	1000			
Bulk modulus [GPa]	2			
Viscosity [Pa.s]	0.01			

model contains normal and shear fracture stiffnesses of 500 and 250 GPa/m, when the low stiffness model – 20 and 2 GPa/m, respectively.

Cycles of fluid pressure are applied to a specific flow-knot, located in the middle of the fracture to simulate the injection. Although a fluid pressure of 1.8 MPa would be enough to induce slip on the fracture for the present stress state and plane orientation, we used the initial pressure of 2.0 MPa to increase the velocity of the fluid penetration and facilitate the visualization of the slip results. The following pressure steps were applied with an increment of 0.5 MPa. In total, we applied 6 injection steps. There is no gravity in the model, therefore the pressure is diffusing radially away from the injection point (Figure 4.4b). Initially the fracture is deforming elastically and controlled by the shear and normal stiffness. Eventually, sub-contacts within the joint reach slip conditions (failure). The orientation of the slip vectors of each slipping sub-contact is computed at each time step (Figure 4.4c). Time duration of a pressure step is fixed long enough to reach a homogeneous pressure inside the activated fracture patch where all the sub-contacts reach slip conditions.

4.4.3 Eshelby analytical solution

Because of the fluid pressure gradient imposed by the radial fluid diffusion, we assume that the fracture normal deformation will implicitly lead to an oblate spheroid fracture shape. To estimate the stress perturbation around the spheroidal fracture filled with water we used the analytical solution proposed by Eshelby [1957] for ellipsoidal inclusions. Eshelby's solution is formulated for an infinite, isotropic and linear elastic matrix with an embedded ellipsoidal inhomogeneity referred as the inclusion Eshelby [1957, 1961, 1959]. The analytical solution provides us with the stresses and strain around an ellipsoidal inclusion. The analytical solution does not capture: (i) transient stress changes associated with fracture tip propagation, (ii) heterogeneous stress distribution inside the inclusion due to the fluid injection. However, it is possible to estimate the direction of the traction force close to the interface between the inclusion and the matrix, which is considered bonded. Here we follow the analytical method proposed by Healy [2009] for a spheroidal inhomogeneity, where the semi axes are $a_1 = a_2 \neq a_3$.

Eshelby derived that the elastic stress inside the inclusion is homogeneous, meaning that it does not depend on the position inside the inclusion. The elastic field inside the inclusion is calculated using the fourth-rank Eshelby tensor that depends on the ellipsoid dimensions and the Poisson's ratio of the matrix [Eshelby, 1957, Mura, 1982] The strain (ε) and stress (σ) are given as following:

$$\varepsilon = \varepsilon^{\mathbf{0}} + \mathbf{S} \colon \varepsilon^{**} \tag{4.13}$$

$$\sigma = \sigma^{\mathbf{0}} + \mathbf{C^0}[\mathbf{S} - \mathbf{I}] \colon \varepsilon^{**} \tag{4.14}$$

where $\varepsilon^{\mathbf{0}}$ and $\sigma^{\mathbf{0}}$ are the remote homogeneous stress strain and stresses, $\mathbf{S}$ is the Eshelby tensor and $\mathbf{I}$ – the identity matrix. The remote strain is related to the remote stress though the Hooke's Law. The eigen strain ε^{**} is the strain that the inclusion would experience if all the matrix constrains are removed [Mura, 1982]. The eigen strain is given by:

$$\varepsilon^{**} = (\mathbf{S} + \mathbf{A})^{-1} \colon (\mathbf{B} \colon \varepsilon^{t} - \varepsilon^{0}) \tag{4.15}$$

where ε^t is the prescribed eigenvalues, $\mathbf{A} = [\mathbf{C^1} - \mathbf{C^0}]^{-1} \cdot \mathbf{C^0}$, $\mathbf{B} = [\mathbf{C^1} - \mathbf{C^0}]^{-1} \cdot \mathbf{C^1}$, where $\mathbf{C^0}$ and $\mathbf{C^1}$ is a stiffness of the inclusion and matrix, respectively.

$$\varepsilon(x) = \varepsilon^{\mathbf{0}} + \mathbf{G}(\mathbf{x}) \colon \varepsilon^{**} \tag{4.16}$$

$$\sigma(x) = \sigma^{\mathbf{0}} + \mathbf{C^0} \cdot \mathbf{G}(\mathbf{x}) \colon \varepsilon^{**} \tag{4.17}$$

where $\mathbf{G}(\mathbf{x})$ is an another fourth-rank tensor being a function of ellipsoid geometry, Poisson's ratio of the matrix and the coordinate position. To simplify, the Eshelby tensor $\mathbf{S}$ is the interior-point Eshelby's tensor, and $\mathbf{G}(\mathbf{x})$ is the exterior-point Eshelby's tensor (see Eshelby [1957], Healy [2009], Ju and Sun [2001, 1999], Meng et al. [2012], Mura [1982] for details).

Therefore, Eshelby's solution enables fracture to be filled with a material having properties equivalent to water with an elastic modulus of 2.0 GPa, and Poisson's coefficient of 0.49. A spherical oblate ellipsoidal inclusion, representing the fracture opening during the fluid injection, is defined by the ratio of its vertical semi-axis to the horizontal semi-axis. The vertical axis is given by the normal displacement of the fracture, and the horizontal – by its radius.

4.5 Results

4.5.1 Misfit angle numerical and analytical

For the stress state and geometry of the reference case presented above, the orientation of the resolved shear stress predicted by the Wallace-Bott hypothesis has a rake angle of 43°. The misfit angle of slipping sub-contacts between the predicted WB orientation and the numerical 3DEC orientation for the first pressure step of 2 MPa is shown in Figure 4.5. In the beginning of the pressurizing (Figure 4.5 A), slipping sub-contacts are only observed very close to the injection point. The closer the sub-contact is located to the injection point, the less misfit angle is observed. The sub-contacts of the low stiffness model show the misfit up to 15°, while the misfit angles of the high stiffness model are below 5°. With fluid diffusion into the fracture, the slipping area grows (Figure 4.5 B). For both models the slip direction deviation from the WB hypothesis is primarily occurring close to the activated fracture patch tip (Figure 4.5 B), where the strain gradient (or the aperture gradient) is higher and, thus, the stress perturbation is the most severe. However, in comparison to the high stiffness model, the low stiffness model shows the gradual increase of the deviation from the injection point to the fracture tips. This observation occurs due to the higher deformability of the low stiffness fracture that induces larger intact rock deformation. At the end of the pressure step all sub-contacts for both models achieve slipping conditions. A deviation less than 5° is still observed on the tips of the low stiffness fracture, while all the slip vectors of the high stiffness fracture are consistent with the predicted value by the Wallace-Bott hypothesis.

To avoid the boundary effects and investigate only the effect of the fluid pressure on the slip deviation, in the following section we analyzed the orientation of the slip vectors for both vectors with a 3 m activated patch radius. The summery of the misfit

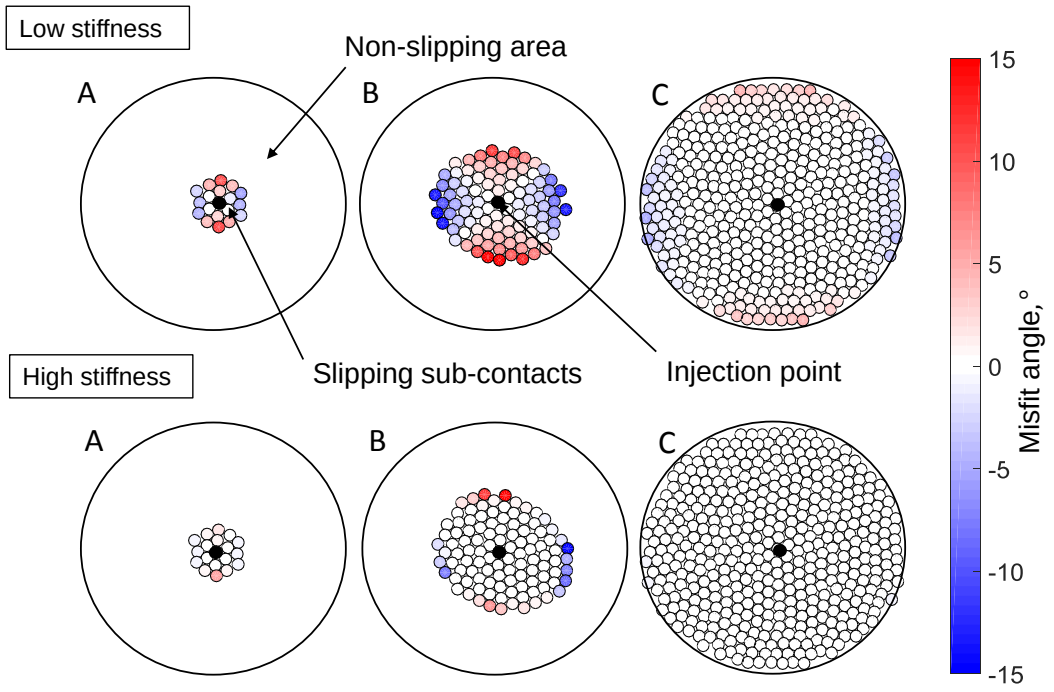

Figure 4.5: Misfit angle of the fractures with low and high stiffnesses at different time of the activated patch growth: A –In the beginning of the pressurizing, B – in the middle and C – in the end of pressurizing. For the exact time of A, B, C refer to the Figure 4.6. Fracture radius – 5 m.

angles measured away from the fracture boundaries at every time step is shown in Figure 4.6. Firstly, it is demonstrated that the first activated sub-contact located at the injection point is consistent with the WB hypothesis for the high stiffness model and is deviated for the low stiffness model. In the low stiffness case, as the fluid diffuses into the fracture the misfit angle trends towards zero (i.e., towards the WB predicted vector), while the slip vector of the high stiffness fracture stays consistent with the WB predicted vector. The same tendency observed later for activated sub-contacts for both models: with time, the deviated vectors become consistent with the WB predicted vectors. For the visualization of the misfit angles we used the range of $\pm 30°$, because the principal misfit angles are in this range. However, we observed an individual sub-contact starting deviation at -90° in the beginning of the pressurizing for the low stiffness fracture, meaning that the deviation is observed at the very beginning of the pressurizing at the location of the injection for the low stiffness fracture. The high stiffness fracture does not show the deviation at the beginning of the pressurizing. At the same time the magnitude of the slipping vectors increases with fluid diffusion. Figure 4.6 shows that the vector deviation decreases with the increasing magnitude. Moreover, all vectors consistent with the WB hypothesis have a slip magnitude of more than 1 μm. The deviated vectors

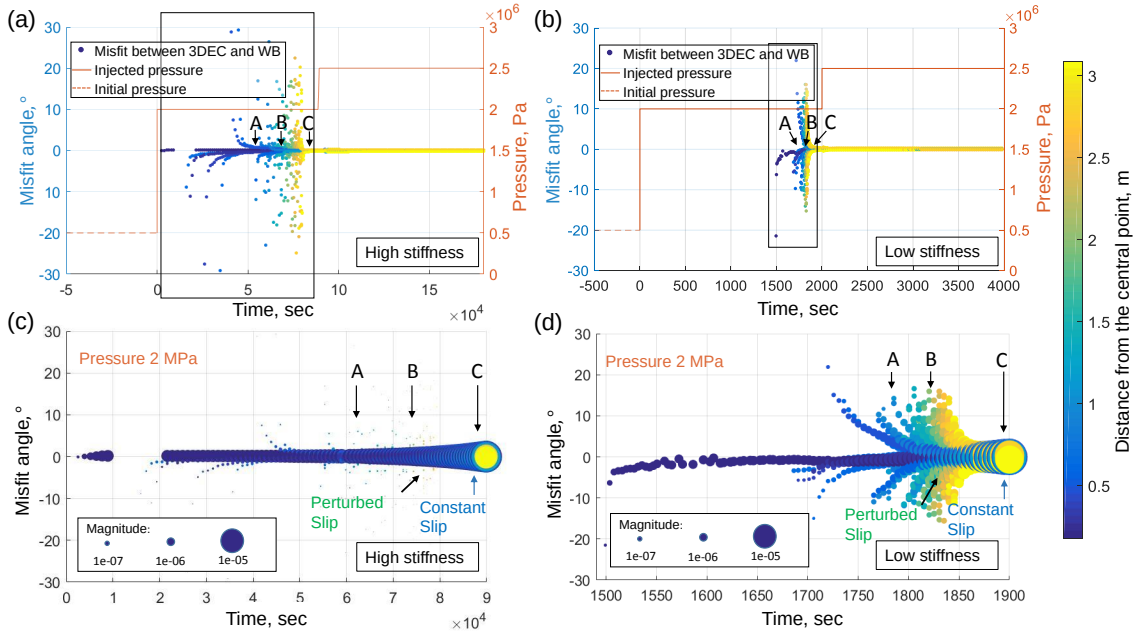

Figure 4.6: Misfit angle for the high (a,c) and low (b,d) stiffness model with increasing injection pressure. Figures (c) and (d) is a zoomed in part with slipping vectors magnitudes corresponding to rectangles in (a) and (b). The amount of the points corresponds to the amount of the slipping sub-contacts within the fracture, and the color indicates the distance of these sub-contacts from the injection point. A, B, C – time of investigated activated patch in Figure 4.5.

in the low stiffness model have larger slip magnitudes (typically > 1 μm) than the deviated vectors in the high stiffness model (typically < 0.1 μm).

Secondly, the stiffness difference results in the speed difference of the rupture propagation along the fracture plane: propagation is quicker for the low stiffness model. This is observed because here the 3DEC simulation is pressure controlled, meaning that for the same pressure step, a larger fluid volume is required to maintain the pressure step in the low stiffness model compared to the high stiffness one (This volume depends on the fracture aperture and on the rock mass properties). Consequently, high stiffness model takes more time to fulfill the fracture.

Thirdly, Figure 4.6 shows that that once the fracture is fulfilled with the fluid (at the first pressure step of 2 MPa), the slip deviation does not increase for the higher-pressure injections. Slip direction becomes constant and consistent with the WB hypothesis.

The shape of the activated fracture patch of 3 m, which is related to the distribution of the fracture aperture under the pressure diffusion of 2 MPa is illustrated in Figure 4.7. Normal displacement of both high and low stiffness fractures gradually decreases from the injection point to the tips at the time B, and become close to uniform at the time C. However, it is important to note that the normal displacement of the low stiffness fracture is about 20 times higher in magnitude than the normal

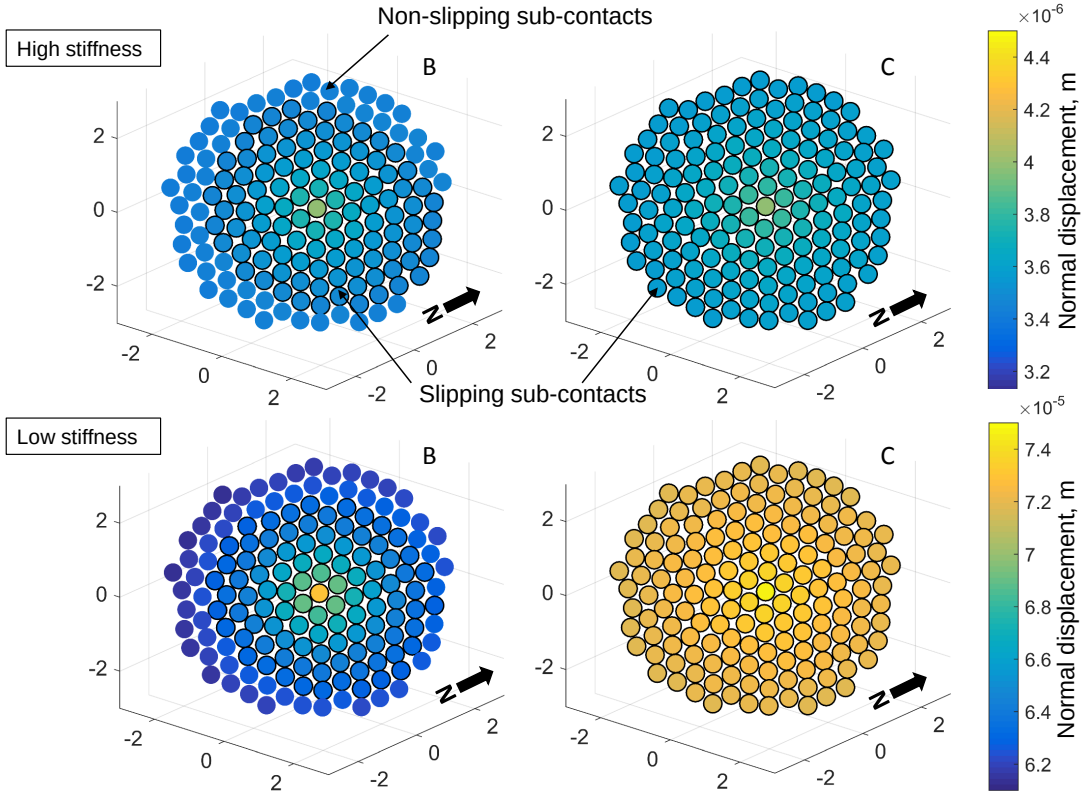

Figure 4.7: Fracture normal displacement for the high and low stiffness models computed at the time of B and at the time C. The black circles indicate the slipping sub-contacts. Axis scale is in meters.

displacement of the high stiffness fracture. The normal stiffness is 25 times higher, but we compare the activated patched in terms of the size of the activated patch, not the time, therefore, the obtained ratio differs from the stiffness ratio. These results clearly indicate the fracture planes change their form and become more planar with the fluid injection.

The Eshelby analytical solution [Eshelby, 1957] demonstrated the effect of these changes in the fracture shape on the slip deviation. Figure 4.8 compared the numerical and analytical solution for both models at the time B. Based on results of Figure 4.7, we represented the fracture shape as a spherical ellipsoid with a ratio of its vertical semi-axis to the horizontal semi-axis of $(1.17 \times 10^{-5})/3$ for the low stiffness fracture, $(5.9 \times 10^{-7})/3$ – for the high stiffness fracture. The vertical semi-axis of the oblate spheroids correspond to the absolute value of the normal displacements at the diffusion stage B (Figure 4.7). Analytical solution for such a "penny-shaped" fracture gives the misfit angle $\ll 1^\circ$ and the distribution of the misfit angles looks different in comparison to the numerical solution. However, if we compare the analytical solution for the low and high stiffness models, it is clearly observed that the curved fracture surfaces corresponding to the low stiffness fracture show higher misfit than the planar surfaces corresponding to the high stiffness fracture. In addition

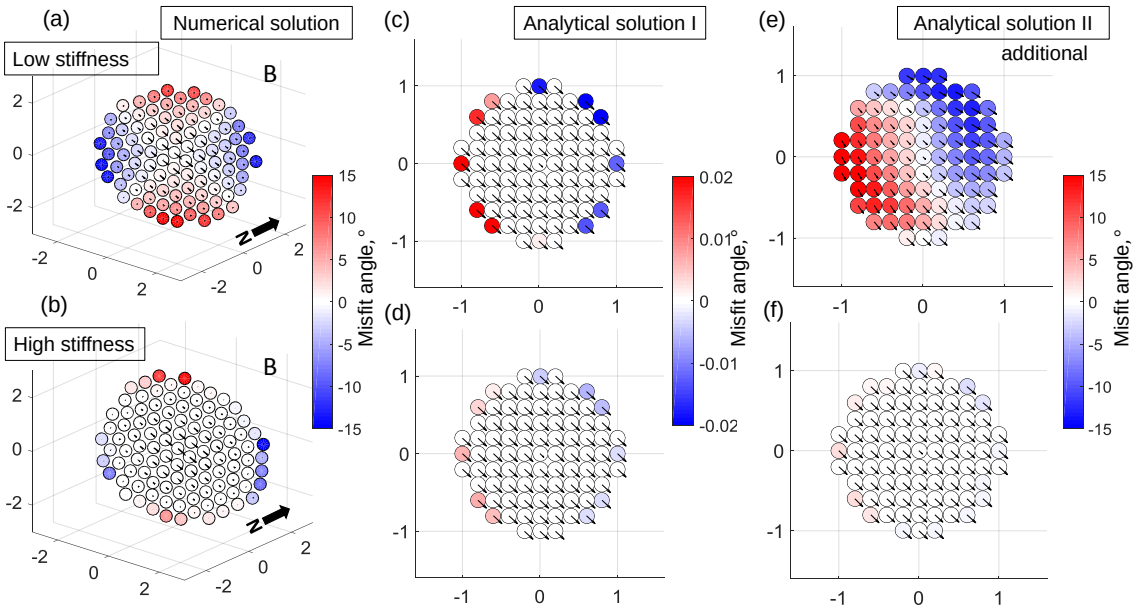

Figure 4.8: The directions (black arrows) of the resolved shear on the low (a) and high (b) stiffness numerical and analytical models. On the analytical model I the real apertures of the low (c) and high (d) stiffness fracture are represented, on the analytical model II - the increased apertures of the low (e) and high (f) stiffness fractures for visualization. The sub-contacts on the fractures (a) and (b) correspond to the slipping sub-contacts at the diffusion stage B on the high and low stiffness fractures in Figure 4.7. Axis scale is in meters.

we adapted the shape of the analytical fracture in order to have the maximum misfit angle of $\pm 15°$ for the high stiffness model. To adapt, we increased the ratio values in both models by 10^5, so that the ratio is 0.39 for the low stiffness model and 0.02 for the high stiffness model. When the fracture becomes more ellipsoidal in comparison to the previous "penny-shaped" it again can be seen that the more oblate fracture shape causes high slip deviation. This is the important result given by the Eshelby solution, that the shape of the pressure-activated patch can significantly impact the orientation of the slip vector.

4.5.2 Sensitivity analysis

Since the deviation is observed only at the initial pressure step of 2.0 MPa, the sensitivity study for both high and low stiffness models covering (i) dilation, (ii) friction angle and (iii) aperture was performed at this pressure step. The test parameters are given in Table 4.2. The results of the study are shown in Figure 9. For the friction angle and fracture aperture the investigation was made till all the sub-contacts will only grow in magnitude. As it has been shown before, after the fracture is filled with water the slip orientation becomes closer to the theoretical value.

Table 4.2: Fracture properties used in the sensitivity study.

Fracture properties	Test values		
Stiffness, [GPa/m]	Kn=500, Ks=250	Kn=20, Ks=2	
Friction angle, [°]	22	19	16
Dilation angle, [°]	0	15	30
Aperture, [m]	110-6	110-5	110-7

4.5.2.1 Dilation angle

The effect of joint dilation is illustrated in Figure 4.9a, b. For the low stiffness model, high dilation increases deviation by approximately 1° in the beginning of the pressurization and accelerates the time for the severe deviation. The same effect of acceleration is observed for the high stiffness model: the orientation of the slipping vectors of the high stiffness model with $\psi = 30$ become closer to the WB predicted value much earlier than for $\psi = 0$. The same slip magnitude is achieved much earlier for fractures with a lower dilation angle. The range of the misfit angle and the slip magnitude of the deviated vectors for both models does not differ significantly between the dilation values for both models. Therefore, for the tested conditions it can be said that dilation do not affect significantly the misfit angle between the slip directions and the WB theoretical angle for both models.

4.5.2.2 Fracture Hydraulic Aperture

The size of the fracture aperture affects its permeability and consequently the time of fluid diffusion into the fracture. It is clearly observed in Figure 4.9c,d that for the smaller aperture of 10 μm for both high and low stiffness models it takes more time to fulfill fracture with a fluid and achieve non-deviated vectors on the whole fracture. The range of the misfit angles for the low stiffness model is smaller and the time slip activation occurs is later for the lowest aperture case (0.1 μm). The discontinuities in the lowest aperture case arise due to the increased time step applied by the 3DEC to capture the slip orientation. However, the tendency of deviation is preserved – the deviated vectors tend to achieve the constant value consistent with the predicted WB orientation. After a certain amount of time (depending on the aperture size) the slip becomes consistent with the theoretical value. However, the longer it takes for fluid injection to propagate inside the fracture, the longer we observe the misfit.

4.5.2.3 Friction angle

Friction angles of 16° and 19° were tested and compared to the base case of 22°. Friction angle has the strongest effect on the misfit angle among all tested parameters in the sensitivity analysis (Figure 4.9e,f). For the low stiffness model

the friction angle of 16° causes the slip deviation up to ± 40°, the friction angle of 19° - the slip deviation of ± 25°, for the friction angle of 22° - deviation of 20°. For the high stiffness model the misfit range does not change significantly for the tested values of the friction angle.

Lower friction angle also accelerates the severe deviation of slip and increases the slip magnitude of the deviated vectors. Generally, the change in friction angle induces a significant change in the slip directions. For the low stiffness model it increases the misfit angle and the magnitude of the deviated vectors. For the high stiffness model it does not significantly increase the misfit or the magnitude of the deviated vectors. These results demonstrate that, friction angle plays a significant role in slip deviation for the present conditions.

The sensitivity study demonstrates that (i) for all of the tested cases the slip reaches a constant direction that is consistent with the WB hypothesis when the activated patch gets larger and is filled with water, (ii) the longer it takes for fluid injection to propagate inside the fracture, the longer we observe the misfit, (iii) dilation and aperture do not significantly affect the slip orientation, while the friction angle and the stiffness are key parameters influencing the misfit angle.

4.6 Discussion

The WB hypothesis is generally used to estimate stress state using stress inversion methods. However, it is known that many of the assumptions of the hypothesis are not respected in field cases. In this study we show, that a non-uniform pressure field induced by a local fluid injection in a planar fault can significantly deviate the slip vector orientation from the WB prediction, which is consistent with previous studies [Martínez-Garzón et al., 2016, Terakawa et al., 2012]. The injection of fluid pressure affects the three-dimensional fracture shape causing a complex stress perturbation at the tip between the activated fracture patch and the remaining not active zone of the fracture.

Generally, when fluid diffuses into the fracture and triggers the slip of sub-contacts, their primary orientation deviates from the WB predicted direction. With continued fluid propagation the orientation rotates towards the WB predicted value. After a given injection time the slip becomes constant on all the fracture sub-contacts and consistent with the WB hypotheses.

The primary deviation and then agreement of the slipping vectors with the WB predicted value is connected with the fracture shape during the pressurizing. The highest deviation is related to the sharp aperture gradient that dynamically propagates at the tip of the activated patch. After this patch was activated the fluid

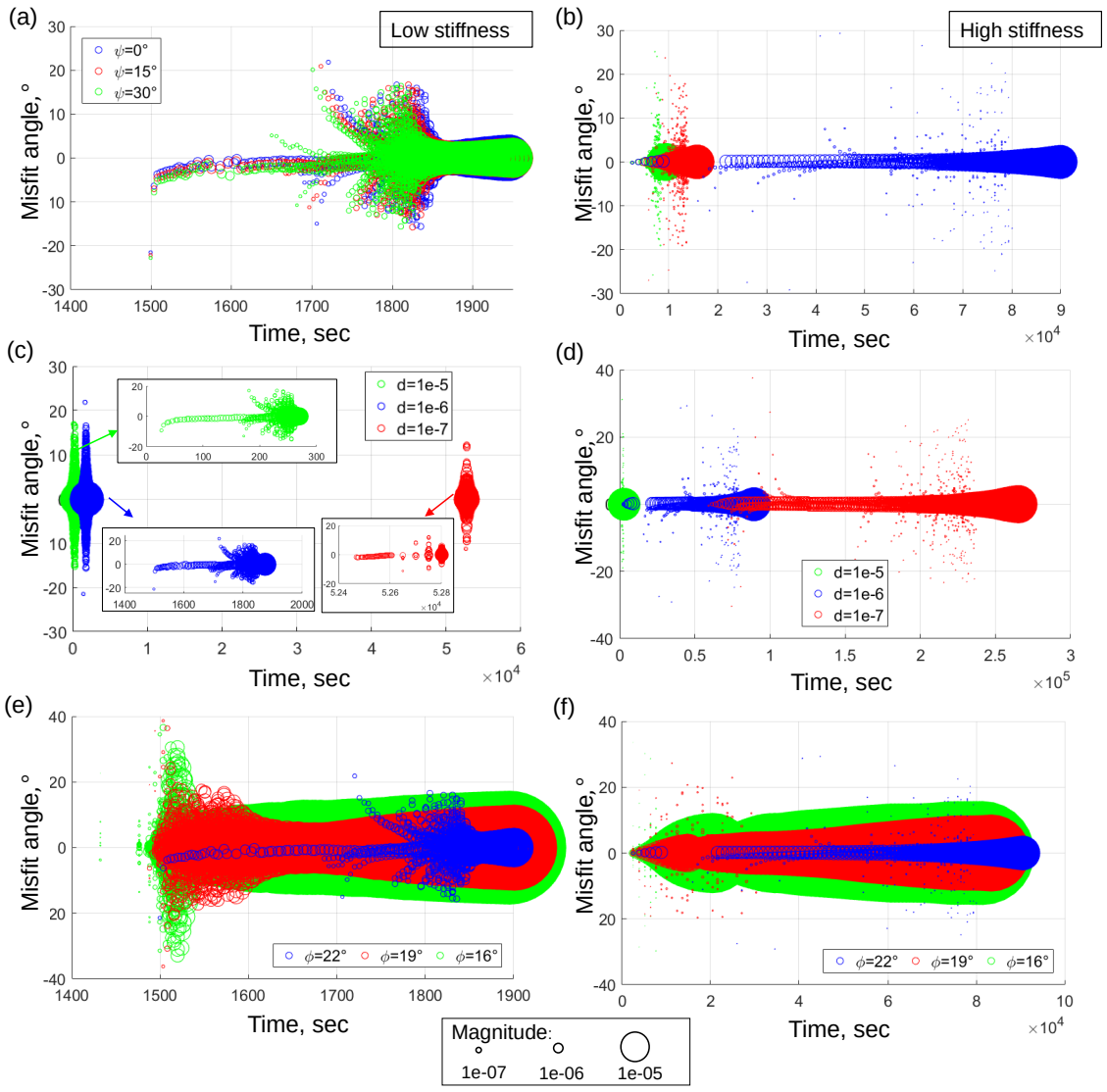

Figure 4.9: Sensitivity study. Similarly to Figure 4.6, we show here the misfit angle between the modeled slip and the expected slip according to the WB hypothesis (Misfit angle). a), b) - effect of dilation angle, c), d) - effect of initial aperture, and e), f) - effect of friction angle.

then filled the fracture, reducing the aperture gradient and uniformly aligning the slip orientation.

The fracture shape and propagation depends on the fracture stiffness. A high stiffness fracture tends to minimize deformation normal to the fracture. Therefore, the fracture opening is small, it does not deform the surrounded rock mass, and the deviation is only observed at the tip of the activated patch because of the inherent aperture difference and stress perturbation on the fracture tips. The slip vectors on the major part of the activated patch are mostly consistent with the WB predicted orientations. These results confirm the observations obtained by Dupin et al. [1993], who used the high fracture stiffness to validate the Wallace-Bott

hypothesis using 3DEC. A low stiffness fracture deforms progressively towards the tips, as a result gradual slip deviation towards the fracture tips is observed due to the higher distortion induced on the medium close to the fracture tip. Hence, more sub-contacts deviate during the fluid injection on the low stiffness fracture. However, for both stiffness models the direction of the slipping vector close to the injection point located in the central part of the activated fracture patch is consistent with the WB prediction.

The numerical 3DEC and the analytical WB models gave very different results in terms of the misfit angle value and its distribution on the fracture plane. While the fully coupled 3DEC numerical solution considered the pressure gradient inside the fracture, stress perturbation caused by the fracture deformation and transient stress changes associated with fracture tip propagation, the analytical solution only estimates the stress perturbation based on the shape of the inclusion. The Eshelby analytical solution does not consider internal stress perturbations, the interface between the inclusion and the matrix is considered bonded and friction properties of the fracture. The analytical solution is made for a perfect ellipsoid, when an activated patch in 3DEC has a shape more like a "bell". The numerical solution is calculated on the tetrahedral mesh, while the analytical was applied on a simple square grid. It can be concluded that the numerical model takes more aspects into account and its results are more reliable. However, the Eshelby solution helped in understanding the effect of the shape of the activated patch on the slip deviation and these results are very important. The comparison of the numerical and analytical solutions for the low and high stiffness model indicates that the more the fracture is deformed the more it causes the deviation.

The sensitivity analyses demonstrate that the friction angle has a strong influence on slip deviation in the low stiffness model, which is consistent with the results obtained by Pascal [2002]. The misfit of the high stiffness model does not change systematically with friction angle, which could be due to the high rigidity of non-deformable fracture planes. Lejri et al. [2015] also concluded that increasing friction will decrease the slip magnitude as well as the misfit angle until the slip vectors become consistent with the WB hypothesis. In this study, the slip magnitude indeed decreases with increasing friction, which is consistent with Lejri et al. [2015].

All our observations indicate that the observed slip deviation is likely generated by the stress perturbations associated with the non-uniform deformation induced by the non-uniform pressure distribution. However, the comparison between the analytical solution where only the shape is modeled and numerical where both shape and pressure are considered suggest that the shape of the fracture cannot explain fully value of the misfit angle and thus non-uniform fluid pressure contributes to the misfit angle. It is probable that the misfit angle depends on additional parameters

that are not considered in this study. The FS data shows that the orientation of the slip vectors rotates. These field observations are consistent with our numerical observations from the low stiffness model, (the Opalinus clay in Mont Terri shale rocks has relatively low stiffness). The sub-contacts deviate from the WB assumptions as soon as they are activated and then constantly rotate their direction parallel to the WB predicted value. The interruptions in the constant trajectory of slip rotations and, in general its deviation may be explained by the fact that the deviation occurs with injection time, and sharp changes in the fault opening with time can be potentially related to friction or stiffness variations, which are found to be the main parameters affecting the slip deviation in the present study. Fracture deformation might allow for a fracture initially unfavorably oriented towards stress to slip locally. This can propagate a weakening patch in the fracture and finally lead to larger slip, which is not yet predictable by the WB hypothesis. In addition, the slip directions varying with time may also have other explanations such as different asperities on the fracture, fracture curvature, activation of several fractures at the same time and other reasons that have not been studied in this paper.

The constant slip on all the fracture sub-contacts of the numerical model and its consistence with the WB hypothesis may be related to the numerical model boundary conditions and geometry. A larger model incorporating more realistic fractures or faults might produce larger deviation from the WB prediction compared to our study. In addition, the accuracy of the 3DEC model can also be improved by testing different meshing size and fracture scale, but this would require significantly more computational power.

4.7 Conclusions

The data obtained from the FS experiment in Mont Terri showed the rotation of the slip vectors during the fluid injection. To understand the origin of this rotation and possibility of using these vectors in the stress inversion methods we checked the fundamental assumption that slip in parallel to the resolved shear stress in the presence of a local fluid source such as a borehole injection across a fracture. In this study we thus focused on the validation of the WB hypothesis in the presence of a fluid point source that may induce slip reorientations using analytical and numerical methods.

We built two numerical models consisting of a homogeneous, isotropic, elastic and deformable block with an embedded low stiffness/high stiffness fracture using the 3DEC numerical method. We inject a fluid pressure step-by-step to trigger the slip along the fracture. The main result of this analysis is that for a given homogeneous far-field stress in all tested cases, we calculate that a non-uniform pressure

field induced by fluid injection does affect the slip direction. The effect is different for a low stiffness/high stiffness fracture and based on the fracture deformation and propagation during the fluid diffusion. The high stiffness fractures are more consistent with the Wallace-Bott theoretical solution, while the low stiffness fractures demonstrate the significant deviation. The sensitivity analysis show that among all the tested parameters, the stiffness and friction angle are the key factors influencing the misfit angle between the numeral observations and the theoretical WB values.

Therefore, the estimation of stresses based on the slip directions of activated fractures during borehole injection is not explicit. The fracture stiffness should be always considered and the slip direction calculated for a longer pressure injection. Based on the results obtained from the investigated numerical model, for the Mont Terri experimental site we propose to make a stress inversion only when the slip has a constant orientation during a significant time of pressurization.

4.8 Acknowledgements

The authors would like to thank the Itasca Consulting Group for providing with the software licensing in the frame of the Itasca Education Partnership (IEP) Program. Many thanks to the mentor of the program – Dr. Damjanac for his assistance and cooperation. This work is funded by the University of Neuchatel and by Swisstopo via the Mont Terri Consortium.

Chapter 5

In-situ direct displacement information on fault reactivation during fluid injection

5.1 Abstract

THE three dimensional (3D) displacement induced by fluid injection was measured during two fault reactivation experiments conducted in carbonate rocks at the Rustrel Low Noise Underground Laboratory (LSBB URL), France, and in shale rocks at the Mont Terri rock laboratory, Switzerland. The faults were activated by injecting high pressure fluid and using the Step-Rate Injection method for Fracture in-Situ properties (SIMFIP), which allows a coupled pressure-flowrate-3D displacement monitoring in boreholes. Both experiments mainly show complex aseismic deformation of preexisting fractures that depend on (i) the fluid pressure variations related to chamber pressurization and leakage into the formation and (ii) irreversible shear slip and opening of the reactivated fractures. Here we detail the processing of the three-dimensional displacement data from both experiments in order to isolate slip vectors from the complex displacement signal. Firstly, we explain the test protocol and describe the in-situ hydromechanical behavior of the borehole/fault system. Secondly, we define the methodology of the displacement data processing to isolate slip vectors with high displacement rates, which carry information about key orientation of fault reactivation. Finally, we discuss which slip vectors can potentially be used to solve the stress inversion problem.

5.2 Introduction

Fluid injection into the rock mass may lead to either new fracture development or activation of preexisting fractures by reducing the effective normal stress and driving the plane to shear failure associated with slip [Hubbert and Rubey, 1959]. The slip direction induced on fractures is a function of relative magnitudes and orientations of the principal stresses [Wallace, 1951, Bott, 1959]. Therefore, the orientation of the triggered slipped vector together with the orientation of the pre-existing fracture carry an important information about the stress and can potentially be used for stress inversion.

Slip induced by fluid injection is often associated with seismicity in the surrounding rock mass [Zoback and Harjes, 1997, Shapiro et al., 1999, Guglielmi et al., 2008, Shapiro and Dinske, 2009, Evans et al., 2012, Ellsworth, 2013, McGarr, 2014]. The seismic slip is known to be used for stress inversion by applying focal mechanism technique [Reasenberg, 1985], which provides constraints on two potential compression-extension zones bounded by potential fault planes and defined by considering the polarities of the P-wave first arrivals. Inversion of slip vectors deduced from focal mechanism can provide with the orientations of the principal stresses and the stress ratio using the methods described by Gephart and Forsyth [1984], Lund and Slunga [1999], Vavryčuk [2014].

Recent studies showed direct field evidence that fluid injection can cause significant aseismic deformation, typically defined as deformation with a slip velocity that is too slow to generate detectable seismic waves [Cornet, 2012, 2016, Zoback et al., 2012, Avouac, 2015, Guglielmi et al., 2015a, Duboeuf et al., 2017, Duboeuf, 2018, Cappa et al., 2018]. Aseismic motions constitute an important part of surrounding mass response during fluid injections. They were observed at large-scale experiments at geothermal sites in Soultz-sous-Forêts, France [e.g., Cornet et al., 1997, Evans et al., 2005], at meter-scale experiments at shallow depths (300 m) in shales [Barros et al., 2016, Guglielmi, 2016], carbonates [Guglielmi et al., 2015a, Duboeuf et al., 2017] and at laboratory scale [Zoback et al., 2012, Goodfellow et al., 2015].

Both seismic and aseismic motions are controlled by coupled frictional and fluid flow behavior [Scholz, 1998, Cornet, 2012, 2016, Guglielmi et al., 2015a] changes in mechanical and hydrologic properties [Bird, 1984, Saffer and Marone, 2003] and evolving effective stress perturbations during fluid injection [Duboeuf, 2018]. In terms of rate-and-state friction, aseismic motion is considered to be stable [Segall, 1991] and occurs when a fault strengthens during slip, demonstrating velocity strengthening behavior and rate-decreasing friction law. Seismic motion corresponds to an unstable slip, which represents a weakening behavior during slip.

The aseismic motion may occur prior to and work as a trigger for seismicity

[Zoback et al., 2012, Guglielmi et al., 2015a, Barros et al., 2016, Duboeuf et al., 2017, Duboeuf, 2018]. The transition from aseismic to seismic behavior was explained using a slip rate dependency of fault friction [Ruina, 1983, Avouac, 2015, Guglielmi et al., 2015a]. Guglielmi et al. [2015a] observed a slow slip rate (4 m/sec) with a high dilatancy associated with a 20-fold increase of permeability, which was followed by faster slip (∼10 m/sec) with reduced dilatancy and micro-earthquakes.

Since the seismic and aseismic motions are controlled by the same coupled processes, can we use the data of aseismic motion to invert stresses? It has always been a challenge to measure an aseismic slip during fluid injection [Cornet, 2016], however, nowadays it is possible by using the SIMFIP probe [Guglielmi et al., 2013], which allows a coupled 3D-displacement-pressure-flowrate continuous monitoring during the fluid injection. Guglielmi et al. [2015a] used the SIMFIP probe to capture the precise measurement of the displacement rate, mentioned above. In this paper, we use the SIMFIP data obtained during two fault reactivation experiments conducted in carbonate rocks at the Rustrel Low Noise Underground Laboratory (LSBB URL), France [Guglielmi et al., 2015a, Duboeuf, 2018, Duboeuf et al., 2017], and in shale rocks at the Mont Terri rock laboratory, Switzerland [Guglielmi, 2016, Guglielmi et al., 2017]. Both experiments consisted of fluid injections into a fault damage zone in order to reactivate the fault planes and to measure the slip during the injection. The 3D displacement data obtained during the fluid injections contain both reversible and irreversible responses of the surrounded rock mass. The irreversible response may be associated to either seismic and aseismic motions. Seismic motions were observed during the injection in carbonates and have been already used to invert stresses using focal mechanisms [Duboeuf, 2018]. However, the data for both carbonates and shales mostly show aseismic motion, which relate to a complex formation response to fluid injection [Guglielmi et al., 2015a, Duboeuf et al., 2017, Duboeuf, 2018, Guglielmi, 2016, Chapter 3, Section 3.1].

Here we show how to isolate slip on preexisting fractures from the irreversible response of the rock mass, using the continuous displacements of borehole wall monitored during the injection tests. We show that most of the reversible response is related to poroelastic effects associated to the injected fluid diffusion into the formation.

Irreversible response and eventually slip on preexisting fractures is evidenced by a non-zero net displacement at the end of the test and by periods of increased displacement rate during the injection. Thus, we discuss the possibility to isolate the irreversible response of the rock mass by first applying a threshold on the displacement rate. Second, we correlate the orientation of the high displacement-rate vectors (that can be related to aseismic or seismic events) with the orientation of

the tested fractures. Finally, we discuss the potential use of these vectors for a stress tensor inversion.

5.3 SIMFIP probe

The experimental protocol for both experimental sites followed the step-rate injection method for fracture in-situ properties (SIMFIP) developed by Guglielmi et al. [2013]. A 2.4 m test interval is isolated in a borehole between two inflatable packers (Figure 5.1). In comparison to traditional hydraulic methods, the SIMFIP probe enables simultaneous monitoring of the three-dimensional dislocation between two points anchored to the borehole wall and fluid pressure within the pressurizing the interval. Sampling rate is up to 1 kHz. In the experiments described in this paper, the pressure sensors range was 10 MPa allowing for high pressure Step Rate Testing (SRT). A downhole valve operated with N_2 gives control on the interval pressure and shut-in. Fluid pressure is monitored with pressure sensors below and above the packers, and in the test interval with the 0.001 MPa accuracy. Packers sealing the interval are inflated with water. The three-dimensional displacement of the injection chamber wall is monitored by a three-component extensometer centered along the axis straddling the two packers in the injection chamber (Figure 5.1b). This extensometer is fixed to the borehole wall by hydraulically operated anchors. Six small-diameter and deformable steel tubes connect two rings with varying orientations — making a cylindrical cage linking the upper and lower rings. Extension between the rings is resolved from the inversion of the deformations of the six tubes. The cage used in both experiments was the same, measuring 0.49 m long and 0.1 m diameter (Figure 5.1b). Tube deformations are captured with 6 fiber optic Bragg gratings (FBG) that are attached to each tube and distributed along one single continuous fiber that brings the sensor signals to the surface-mounted data acquisition system. An inversion algorithm is used to calculate the relative three-dimensional displacements of the center of the upper ring towards the center of the lower ring from the tube deformations that are continuously monitored during the test. For shales, x,y and z are oriented North, West, and Vertical (positive up), respectively. For carbonates, x,y and z are oriented North, Vertical (positive up), East, respectively. Figure 1b shows an example of measuring a relative displacement ($\overrightarrow{U_r}$), which represents normal movement along a fault. The relative displacement ($\overrightarrow{U_r}$) is the resulting sum of the displacement of the upper anchor ($\overrightarrow{U_{up}}$) and lower anchor ($\overrightarrow{U_{down}}$), which is arbitrarily considered to be fixed. In addition, there is a reference FBG subject to ambient pressure and temperature which remains unstressed. It is used to correct the strain measurements from temperature and pressure variations in the chamber. The 6+1 FBG are distributed along one single continuous fiber that

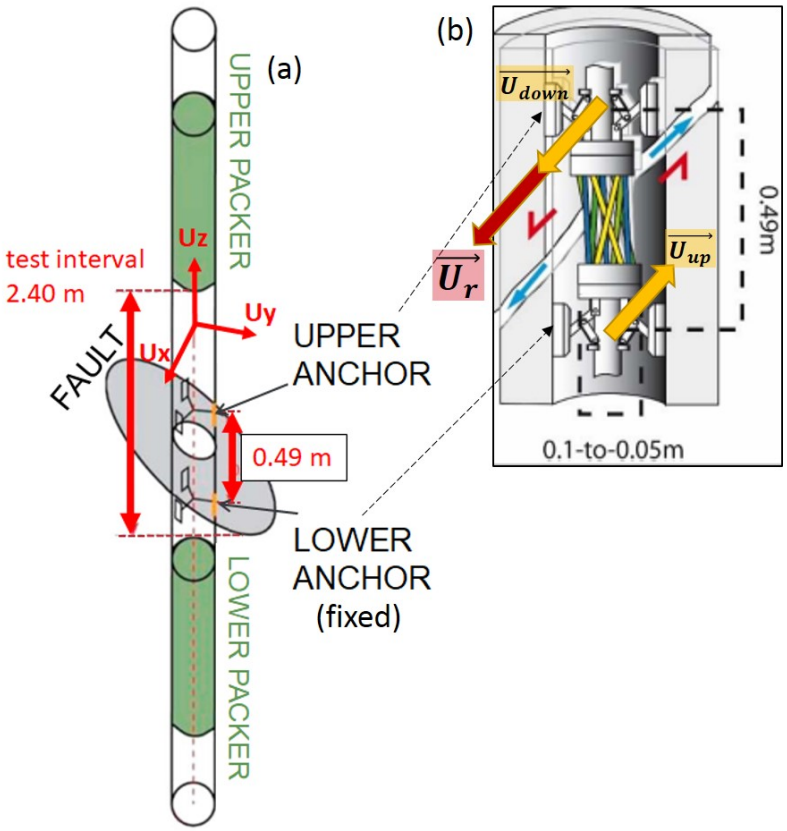

Figure 5.1: (a) SIMFIP Probe, (b) the deformation unit.

brings the sensor signals to the surface-mounted data acquisition system which is a MicronOptics optical interrogator (*http://www.micronoptics.com*). Attached to the straddle packer system is a magnetic orientation tool used to provide a measure the initial azimuthal positioning of the tool with a 0.1° accuracy.

5.4 Geological and experimental settings

In shales, the experiment is located at 37.2 m depth below laboratory gallery floor, which corresponds to a depth below ground surface of about 300 m, in the Opalinus clay formation at the Mont Terri research laboratory, Switzerland (Figure 5.2a). The laboratory is focused on studying the hydrogeological, geochemical and geomechanical coupled processes in the Opalinus Clay formation. The exposure of Opalinus clay formation in the laboratory galleries gives an excellent opportunity to investigate an unweathered clay fault system [Nussbaum et al., 2011, Jaeggi et al., 2017]. The study of this formation is important because it is a potential host rock for a deep nuclear waste disposal and a caprock analogue for a geological carbon dioxide (CO_2) storage in deep geological reservoirs [Goodman et al., 2017].

The most deformed zone and the main tectonic structure of the Opalinus clays,

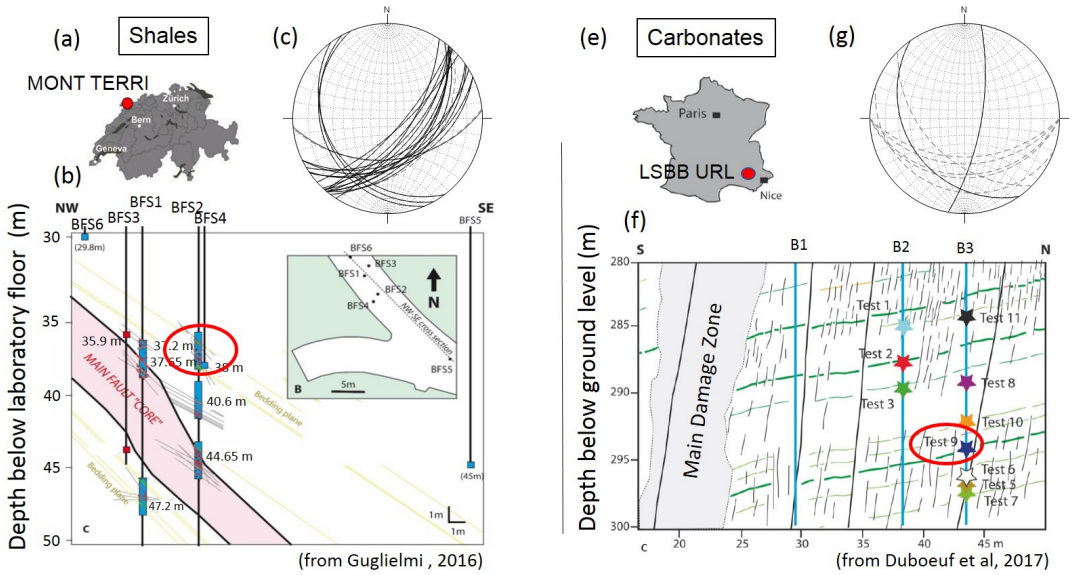

Figure 5.2: The experimental sites: a) Mont Terri rock laboratory, b) Rustrel LSBB URL. For each of the sites, there is an experimental location and vertical cross sections showing the different testing intervals in a simplified geology. Stars represent the 10 injections in LSBB and blue rectangles represent the injection intervals in Mont Terri. The highlighted tests are the studied tests in this paper.

the Main fault, crosses the galleries of the laboratory. The Main Fault consists of a complex thrust zone, about 0.8-3 m width, bounded by two major fault planes with dip orientations varying from 140°-to-165° and dip angles from 40°-to-65°SE. The internal structure of the Main Fault is characterized by three main tectonic families of faults: (1) sub-parallel to the bedding planes faults with dip direction and dip N055°-to-N065° and 50-to-55°SE, (2) SW-dipping faults with dip angles ranging from 10° to 40° and sub-horizontal faults (3) N-striking faults dipping between 20° and 60° to the east and steep NNE-striking faults dipping to the west. The variability of fault density and intersections observed at the gallery walls and on the boreholes cores make the fault zone very complex and heterogeneous [Nussbaum et al., 2011]. The fracture network intersects the bedding, which mainly dips towards SSE with a dip angle evolving from 30° to 50°. The stress state which is currently considered in Mont Terri was synthesized by [Martin and Lanyon, 2003] from different stress testing methods: σ_1 = 6-7 MPa sub-vertical to N210-70°plunge, σ_2 = 4-5 MPa N320° sub-horizontal to 7° plunge, and σ_3 = 0.6-2 MPa N052° sub-horizontal to 18° plunge.

The Fault Slip experiment, conducted in the Mont Terri laboratory in 2015, was focused on understanding the conditions for slip activation and leakage of a typical host rock or cap rock fault [Guglielmi et al., 2017, Jeanne et al., 2017]. The experiment consisted of injecting fluids into sealed intervals in upper, middle and lower parts of the Main Fault to eventually trigger a local fault reactivation. Here

we focus on one injection test conducted between 35.85 m – 38.33 m depth below the gallery floor in the vertical borehole BFS2 (Figure 5.2, a). The depth of 37.2 m corresponds to the center of the displacement cage in the interval. In this interval, the injection was performed above the Main Fault in its damage zone

The injection interval intersects a set of fractures sub-parallel to the bedding planes with the dip direction and dip angle varying from 123° to 154° and 36° to 74°, respectively, several South-West dipping fractures with an average orientation of 240°/23°, and one fault dipping South and oriented 174°/43°. The zone located between the two anchors of the displacement cage is highly fractured. There are two South-West dipping fractures (233°/25° and 247°/20°) with a 2 cm thick layer of scaly clays [Nussbaum et al., 2011, Laurich, 2015] located in the upper part of the displacement cage, and 5 south-east dipping fractures (130°/55°, 130°/46°, 131°/65°, 130°/37°, 130°/45°) - in the lower part of the cage.

In carbonates, the experiment is located at 280 m depth in the galleries of the Rustrel Low Noise Underground Laboratory (LSBB URL, *http://lsbb-new.prod.lamp.cnrs.fr*) in the South East of France sedimentary basin (Figure 5.2b). The laboratory is focused on the investigation of coupled THMC processes in porous fractured platform carbonates. The laboratory galleries give an excellent access to a particular environment of unaltered fractured cretaceous limestone (Urgonian facies), which are regarded as: (i) an exceptional access to the unsaturated zone of a large karstic aquifer, (ii) an analogue to the Middle East carbonate oil and gas reservoirs, (iii) the area of major seismogenic faults in Provence, South-Eastern France.

Carbonate layers have a <1 to 5 m thickness. The layers are affected by a normal fault at least 1 km long and oriented N030°/70°, and three secondary faults belonging to the same fault system. A ∼5 m thick and highly fractured damage zone is located close to the main fault and affects all the layers. There are also smaller damage zones of up to 1 m in thickness around the secondary faults.

A 20 m thick fracture zone is connected to the main fault and includes subvertical, subparallel fractures of 1 to 10 m length [Jeanne et al., 2012]. The fracture density progressively increases to the vicinity of the fault core. The experiment was conducted in a 40 m × 20 m × 20 m volume in the this fractured zone, which mainly includes N110°-to-135°-20-to-35°SW bedding planes, N10° to N30° and 70° dipping east or west fractures and secondary faults and N090°–20° to 50°S fractures. The experimental area has a strong heterogeneity in the rock quality and hydraulic properties [Jeanne et al., 2012].

The state of stress was estimated from hydraulic tests on preexisting fractures (HTPF) during a previous experiment using a straddle-packer probe and taking into account topographic stresses by Guglielmi et al. [2015a] and, from microseismic

events focal mechanisms inversion by Duboeuf [2018]. The regional stress state was estimated to be: $\sigma_1 = 6 \pm 0.4$ MPa is sub-vertical, $\sigma_2 = 5 \pm 0.5$ MPa is sub-horizontal and oriented N20° ± 20°, and $\sigma_3 = 3 \pm 1$ MPa is sub-horizontal and oriented N110° ± 20° [Guglielmi et al., 2015a]. Inversion of focal mechanisms showed a strong variability of the stress tensor related to the heterogeneity in the tests intervals geology.

The experiment consisted of injecting fluids at different depths and different geological intervals 18 m away from the main fault. Here we focus on one test (Injection test 9) which was conducted between 12.65 and 15.13 m below the gallery floor in the vertical borehole B3 (Figure 5.2). The upper and lower anchors of the SIMFIP are located at 13.76 and 14.24 m, respectively. The center of the deformation unit is at the depth of 14 m across a bedding plane oriented 235°/26°, which separates two different rock facies in the interval. The facies located above the bedding plane is a low fractured grainstone with a porosity of 12 to 16%. The facies below the bedding place is a highly fractured packstone with a low porosity (<3%). The structural mapping of the interval, given by Cochard [2018] shows many fractures in both facies that are not well defined. However, the interval is intersected by a continuous sub-vertical fracture, which dips East with an average dip angle 70-80°. This fracture belongs to the family of N10° to N30° and 70° dipping East or West fractures.

The stress state using focal mechanisms from test 9 showed differences from the regional stress state with σ_1 oriented N135° ± 20° and dipping 40° ± 10°SW, σ_2 sub-horizontal N240° ± 40° and σ_3 oriented N300° ± 10° and dipping 80° ± 5°NW [Duboeuf, 2018]. The stress computed using the focal mechanisms is different from the one computed by Guglielmi et al. [2015a]. Duboeuf [2018] propose that the reason for the discreapancy is stress change induced by aseismic slip prior to seismic events.

5.5 Injection protocols of the conducted tests and its first interpretation

This paper focuses on pressure step-up injection tests that were part of the hydraulic stimulation experiments conducted with an engine pump in shales [**?**, Chapter 3 Section 3.1]nd carbonates [Duboeuf et al., 2017, Duboeuf, 2018].

For both engine pump experiments pressure is increased step-wise in the intervals until a significant increase in the injected flowrate is measured. The pressure at which this is occurring is called the fault opening pressure. It is considered as a proxy to fault reactivation. Injection are maintained for several minutes above the

fault opening pressure in order to produce eventual significant slip on the reactivated faults or fractures. The sampling rate of all the monitored data is 10 Hz. Figures 5.3 and 5.4 show the coupled pressure-flowrate-3D displacement variations during both tests.

5.5.1 Injection protocol for shales and carbonates

The STR injection in shales lasted 800 seconds (Figure 5.3a). The initial pressure in the chamber was 0.6 MPa. The injection includes three initial steps that increased the pressure to 3.9 MPa. Then, five successive pressure steps of 0.5 MPa each were applied. Each pressure step was about one minute long. At the highest injection step of 6.3 MPa, the flow rate dramatically increased from small oscillations to $>$ 20 L/min. Total amount of injected fluid during this step is 100 L. The STR injection ended with a shut in pressure to constrain a fault closure pressure, which is the pressure at which the flowrate falls back to zero [Guglielmi, 2016]. Figure 5.3a (point 4) displays a kink in pressure during the shut-in period.

The high-pressure STR injection in carbonates lasted significantly longer than in shales, to approximately 1800 seconds (Figure 5.4a). The initial pressure in the chamber was 1 MPa. The test consisted of 12 pressure steps with a pressure increment of 0.5 MPa. Each pressure step lasted 1 min, except the pressure step from 4.4 to 4.7 MPa that lasted about 10 min. The maximum injected pressure during the final step is 5.9 MPa, which had a maximum flowrate of 13.3 L/min. A total volume of 700 L was injected during this test. The STR injection in carbonates ended by bleeding the chamber, which did not allow an observation of the shut-in pressure. However, a rapid kink in pressure was observed during the pressure decrease (Figure 5.4a, point 5). The meaning of this kink will be discussed later.

The injection in carbonates induced seismic events, which were analyzed in details by Duboeuf [2018], Duboeuf et al. [2017]. The first seismic event occurred at the pressure greater than 3.2 MPa and from 1 to 3 m away from the injection chamber. The orientation of the focal mechanism could not be defined due to a small magnitude of the event. Later, a sequence of seismic events occurred at the pressure range of 3.8 to 4.6 MPa, which indicated a primarily strike slip motion on the bedding plane with sometimes a normal and reverse component. All the events were located between 1 and 3 m away from the injection chamber. Distance between the seismic events and the injected chamber was increasing with time [Duboeuf, 2018, Duboeuf et al., 2017].

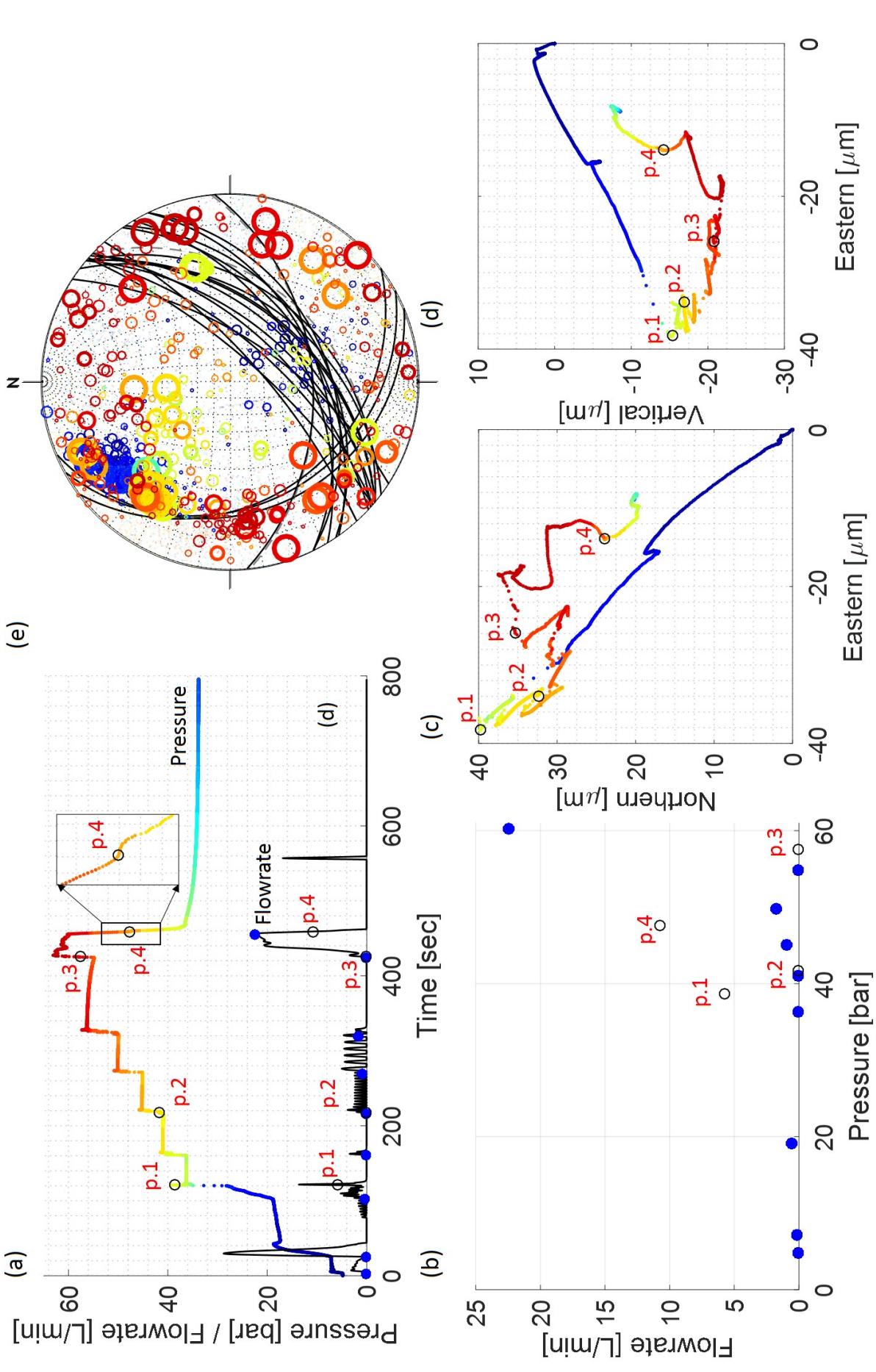

Figure 5.3: (a) The coupled pressure-flowrate variation during the STR injection in shales, (b) Flowrate steady-state vs. pressure, (c) and (d) 2D view on Eastern vs. Northern and Eastern vs. Vertical displacements, respectively. (e) A stereo projection of the displacement vector captured every 0.1 second. The scaling of the markers corresponds to the norm of the displacement vector magnitude. The color is related to the pressure at which the displacement is measured.

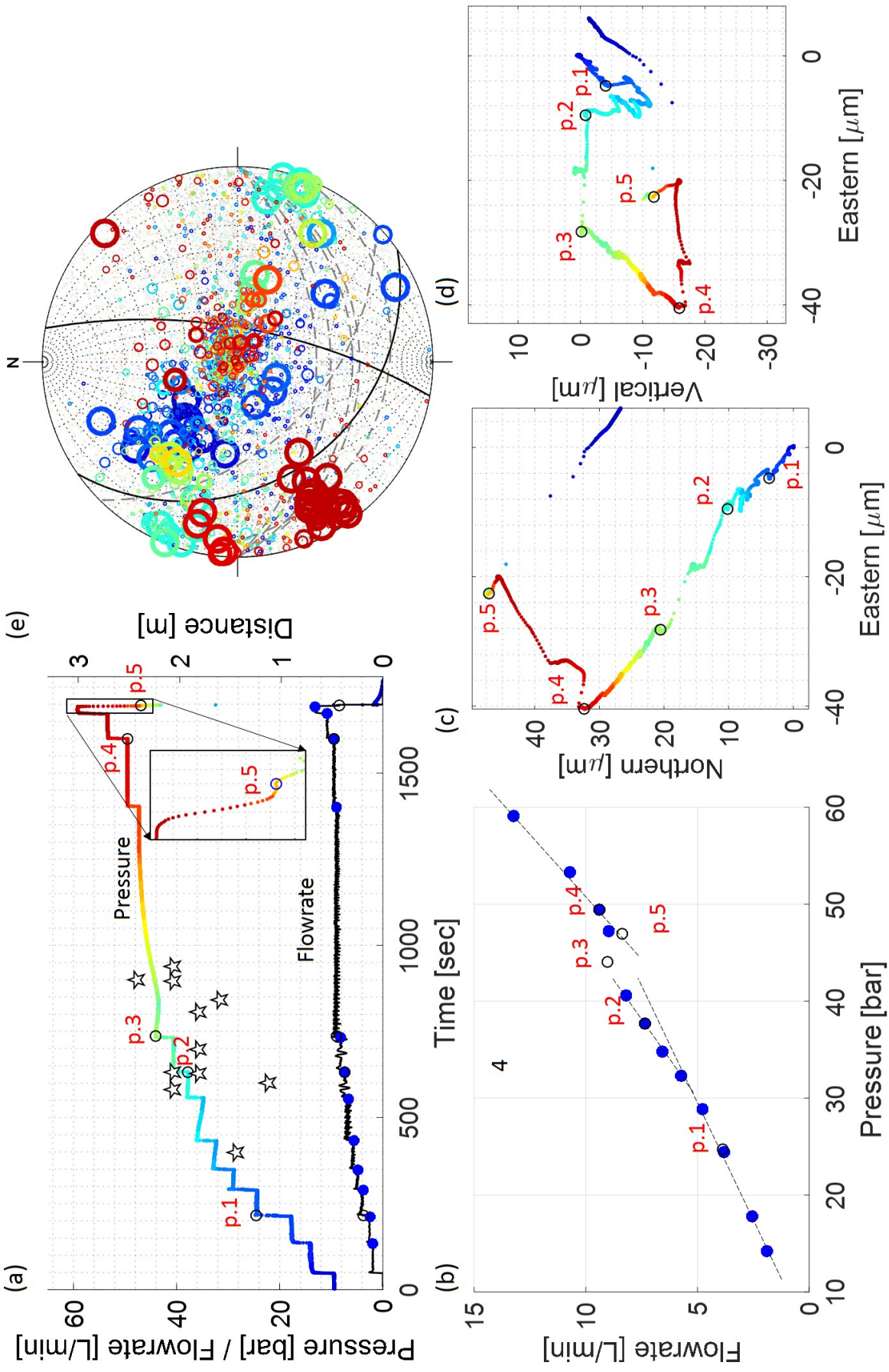

Figure 5.4: (a) The coupled pressure-flowrate variation during the STR injection in carbonates, (b) Flowrate steady-state vs. pressure, (c) and (d) 2D view on Eastern vs. Northern and Eastern vs. Vertical displacements, respectively. (e) A stereo projection of the displacement vector captured every 0.1 second. The scaling of the markers corresponds to the norm of the displacement vector magnitude. The color is related to the pressure at which the displacement is measured.

5.5.2 General analysis of the coupled pressure-flowrate-displacement data

5.5.2.1 Shales

A flowrate-vs-pressure plot is given in Figure 5.3b. 2D plots of Eastern-vs-Northern and Eastern-vs-Vertical displacements are given in Figures 5.3c and 5.3d. An orientation of the displacement vector captured every 0.1 second is projected on a lower-hemisphere equal-angle stereograph, which visualizes the displacement main orientation trends relatively to pressure (Figure 5.3e). The existing fractures in the interval are given in Figure 5.3e.

The flowrate measurements (dark blue markers in Figure 5.3a and 5.3b) are taken in the end of each pressure step. Figures 5.3b highlights three increases of flowrate at 2 MPa, 4.1 MPa and during the pressure increase at 5.8 MPa (black circle in Figure 5.3b). The pressure of 5.8 MPa represents a significant increase of flowrate up to 23 L/min. Figure 5.3c and 5.3d show that the norm of the displacement vector captured every 0.1 second and corresponding to the distance between sampling points is not constant. Displacements below 3.9 MPa (blue in Figure 5.3) show a NE-SW quasi-linear trend, and a much complex response above 3.9 MPa. The stereo projection highlights a NE-SW trend with a high density of displacements dipping from 5° to 45° to NE below 3.9 MPa, and a more chaotic behavior above 3.9 MPa (Figure 5.3e). Figure 5.3e also shows that the NE-SW trend below 3.9 MPa is mostly normal to the SE-dipping fractures.

To help in the interpretation of the complex response of the rock mass, we defined 4 important points during the STR injection:

- First (point 1), at 3.9 MPa identifies a change from a dominant NE-SW trend of the displacements. Considering that this NE-SW trend is observed since the beginning of the injection and the orientation of the bedding planes dipping SE, we assume that this indicates the end of the reversible response of the interval.

- Second, above 4.2 MPa there is a significant flowrate oscillation up to 2.5 and 5 L/min during the pressure steps of 4.5 and 5.0 MPa, respectively (Figure 5.3, point 2). Knowing that the shut-in pressure during the manual pump performed prior to studied STR varies between 4.3 and 4.5 MPa (Chapter 3 Section 3.1), we assume that the flowrate oscillations can be related to the reopening of activated fractures. This assumption is supported by normal orientations of the displacements relatively to the SE-dipping fractures (orange, light red markers in Figure 5.3e).

- Third, at 5.8 MPa there is the rapid increase of the flowrate to > 20 L/min and the rotation of the displacement towards ENE (Figure 5.3, point 3). This orientation is aligned with the strike of the SE-dipping fractures.

- Fourth, during the shut in period there is a kink at 4.7 MP (point 4), which is consistent with the shut-in pressure, defined by the manual pump (Chapter 3, Section 3.1).

5.5.2.2 Carbonates

The flowrate-vs-pressure plot is given in Figure 5.4b. 2D views and the stereoplot projection of the displacements are given in Figure 5.4c-e. As in the test in shales, significant variations of displacement vectors magnitudes are observed (Figure 5.4c, d). The flowrate measurements (dark blue markers in Figure 5.4a and 5.4b) taken in the end of each pressure step and representing quasi-steady-state conditions demonstrate different behaviors for high-permeable carbonates in comparison to low permeable clays. Figure 5.4b shows that the flowrate linearly increases until 3.2 MPa. Above 3.2 MPa, there are two changes in the flowrate increasing trend – from 3.2 until 4.1 MPa and from 4.95 until 5.9 MPa, respectively. The flowrate variations might be related to the fractures activation in the interval. The Eastern-vs-Vertical displacement shows that most complexity comes from the variation of the vertical component of the displacements , which might be related to the presence of the vertical fracture in the injection interval (Figure 5.4d). We defined 5 points to help in the interpretation of the complex behavior of the rock mass:

- Point 1 at 2.4 MPa the end of the linear displacement-vs-pressure response (Figure 5.4 c,d). We assume, that this point is related to the end of the reversible response of the interval, which mostly has a NW-SE trend (Figure 5.4e, blue markers), which is aligned with the strike of the bedding plane.

- Between points 2 at 3.7 MPa and 3 at 4.4 MPa there is a horizontal displacements WNW-ESE trend (Figure 5.4e, green markers) that corresponds to the first flowrate increase (Figure 5.4b). The WNW-ESE trend is normal to the sub-vertical fracture, which considering the flowrate increase, might correspond to its opening. It is important to mention, that the point 3 is taken not at the stabilization of the flowrate, therefore it is not considered when the flowrate behavior is discussed (Figure 5.4b).

- The displacements from 4.4 MPa (point 3) until 4.95 MPa (point 4) are mostly oriented towards NW or sub-vertically (Figure 5.4e, light green, yellow, orange

markers). The point 4 indicates a displacement rotation toward SW-NE (Figure 5.4e, dark red markers) and the second increase of the flowrate (Figure 5.4b). These displacements aligned with the strike-slip on a bedding plane.

- Point 5 at 4.7 MPa indicates a kink during the chamber opening, during which a NW-SE trend of displacements is observed.

5.6 Protocol for pre-processing the displacement data to identify slip vectors

The displacement response for both shales and carbonates intervals is complex (Figures 5.3 c-e and 5.4 c-e). This complexity of the data comes from the sum of the responses of the complex system including 1) the probe - borehole interaction, 2) the deformation associated with stress concentration at the borehole wall and background stress, 3) fluid diffusion from the injection interval into the formation. All these processes are influenced by the rock properties including the fractures. In Chapter 3 Section 3.1 we gave an overview of the coupled flowrate-displacement-pressure behavior during the fluid injections. However, it is clear that the data recorded during the experiment contained much more information, which needed to be simplified without losing important details. To simplify the displacement signal complexity and to define the key orientations that could be used for further stress inversion analyses, the following protocol has been applied. The challenge here was to identify slip direction on fractures that can then be analyzed using stress inversion techniques. The goal of the protocol was thus not to fully explain the complex rock mass response to injection, but to extract deformation events that could clearly be associated to fracture slip.

The protocol consists of several steps, which are explained in details below. Firstly, we isolate the time windows of constant pressure steps to avoid the influence of pump oscillation signal. Secondly, we defined limits of a linear displacement-vs-pressure response to later estimate the threshold between displacement rates during reversible and irreversible deformation. Thirdly, we apply the threshold to the displacement rates measured during the constant pressure steps to identify the steps, which include higher displacement rates and may indicate a fracture slip.

5.6.1 Isolating time windows when the injection pressure in the chamber is constant

The tests were performed as pressure-controlled injection with increasing pressure steps. A mobilization of the pumping system is required to climb from one

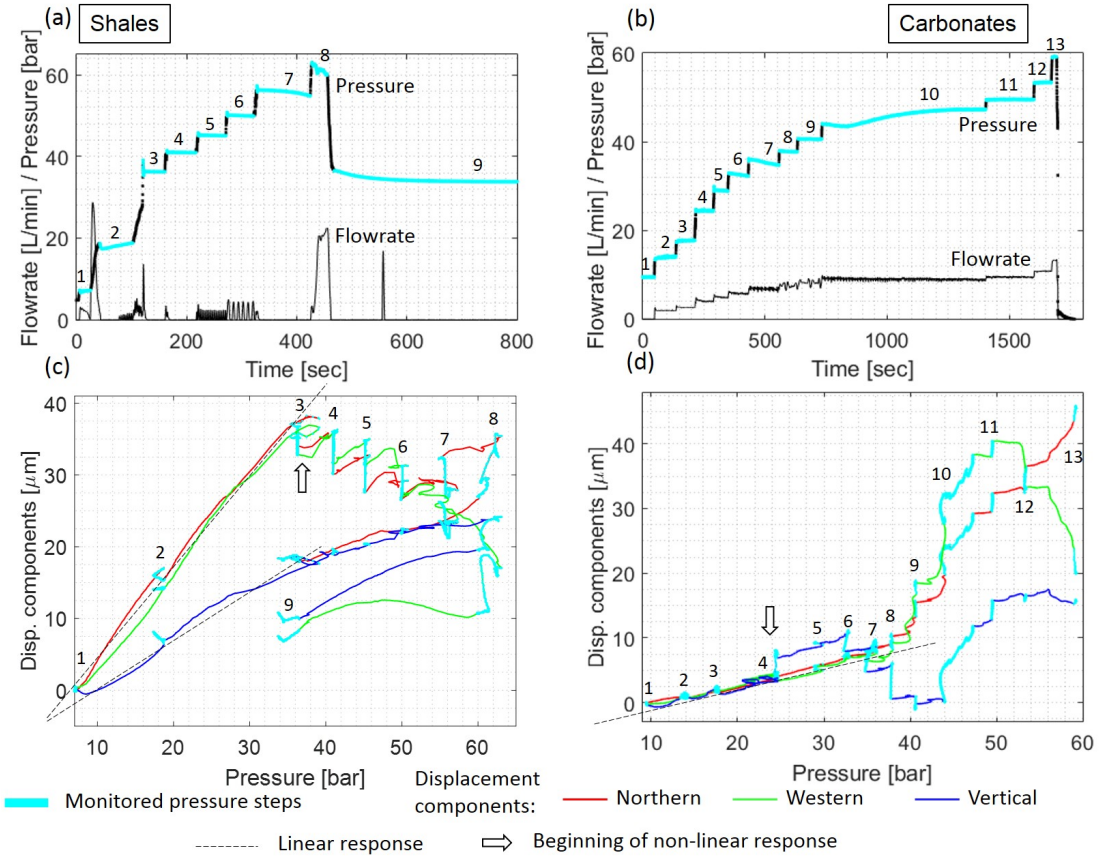

Figure 5.5: The coupled pressure-flowrate variations with the highlighted monitored pressure steps for (a) shales and (b) carbonates. Variation of three components of 3D displacement versus time for (c) shales and (d) carbonates.

pressure step to the next. During this rapid pressure increase strong deformation occurs which likely reflect the superposition of multiple processes. This deformation is influenced by the hydraulic response of the probe - borehole system. Extracting with confidence the signal that is capturing fracture slip during these phases is hazardous. This is why we focused our analyses on the time window when the pressure is maintained constant (Figure 5.5a,b, cyan markers). These time windows were determined manually on the recorded signal. They start from the time a quasi-constant pressure is reached after the pressure has been step increased and they end at the onset of the next step pressure increase.

5.6.2 Identification of a pseudo-linear displacement-vs-pressure response

The linear response of the displacement-vs-pressure is defined by plotting the three components of the displacement versus the injected pressure measured into the chamber. In Figures 5.5 c and d, we show that in the shale test the linear response of displacement is observed until 3.9 MPa (beginning of Step 3). In the carbonate test,

the linearity is preserved until 2.4 MPa (beginning of Step 4). We intentionally left the entire displacement series on the plot for the sake of comprehension, the time intervals previously defined are superimposed in light blue. This linear response mainly represents a reversible response of the rock mass in the borehole nearfield to the fluid pressure increase in the borehole. We do not expect any dislocation related to fracture slip to occur during this period. The end of this response is consistent with the point 1 found in Section 5.5.2.1. This reversible response can be modeled using a fully coupled hydromechanical elastic model [Jeanne et al., 2018a]. The curve kink when loosing linearity highlights the onset of a significant irreversible response of the formation (white arrows in Figures 5.5 c and d). Thus, the steps following this kink which respectively are steps 3-to-9 in the shale case and steps 4-to-13 in the carbonate case might contain slip events.

5.6.3 Identification of the highest displacement rate

During the time windows when the pressure is constant in the chamber, we assume that primarily two type of processes occur: 1) pressure diffusion into the formation that induced progressive and slow deformation and 2) fracture rupture and slip that induced sudden and rapid displacement. Being interested by the second process, we decided to analyze displacement rate during these time windows. The displacement rate is obtained by measuring the magnitude of the displacement every 0.1 second at each time window (Figure 5.6). Maximum displacements rates of 2 μm/sec (Steps 1-2 in shales, Figure 5.6a) and 2.4 μm/sec (Steps 1-3 in carbonates, Figure 5.6b) are observed at the low pressure steps and characterize reversible poroelastic strain rates. Significantly higher rates up to about 8 – to – 9 μm/sec are observed in steps 3, 7 and 8 for shales, and in steps 4, 10, 12, and 13 for carbonates (Figures 5.6 and 5.5). Carbonate step 10 is associated with seismicity.

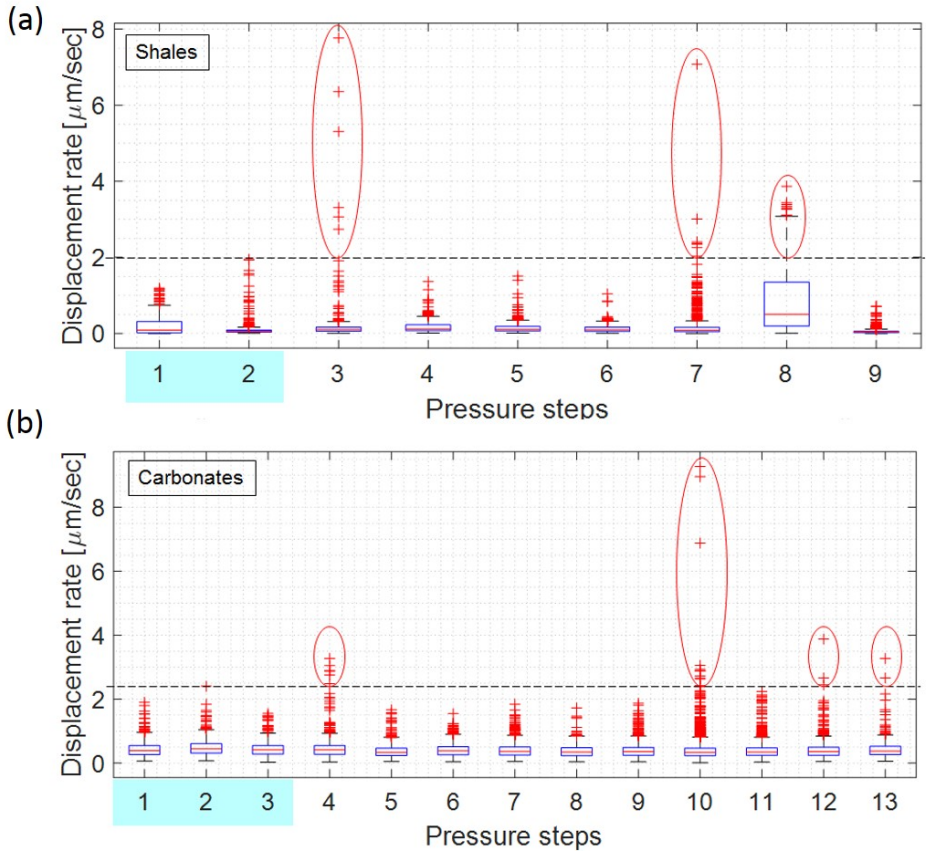

Figure 5.6: Variation of the displacement rates at each pressure step (boxplots). Light blue rectangles represent the pressure steps with the linear response, dashed black line – a threshold. Displacements rates highlighted in red ellipsoid exceed the threshold.

5.7 Analysis of the slip vectors orientation

The high displacement rate values correspond to a vector calculated between two positions of the SIMFIP sensor at a 0.1 seconds interval, and to a chamber pressure value. Such a high rate displacement vector will be called a "displacement event". We summarize the orientations and dip of each displacement event, corresponding pressure and displacement rate in Tables 5.1 and 5.2, respectively for the shale and carbonate tests.

5.7.1 Shales

The analysis of the three steps (3, 7 and 8) where displacement rates above the 2 μm/sec threshold were identified is shown in Figures 5.7 - 5.9 and in Table 5.1.

During step 3, 6 displacement events occurred as the pressure dropped from 3.9 to 3.5 MPa (Figure 5.7a, Table 5.1). The displacement events demonstrated both: rate-increasing (1-2, 3-4) and rate-decreasing (2-3, 4-6) behavior (Figure 5.7b). The sequence of rate-increasing followed by the rate-decreasing one is observed twice during the step 3. First, it is observed at the pressures >3.8 MPa and corresponds

Table 5.1: Characteristics of displacement events for steps 3, 7 and 8 in shales.

Pressure step	Displacement vectors	Time of occurrence [sec]	Pressure [Mpa]	Displacement rate [μm]	Orientation	
					Dip direction, °	Dip agnle, °
3	1	120.8	3.91	3.1	79	26
	2	120.9	3.90	6.4	72	25
	3	121.0	3.83	5.3	74	26
	4	121.1	3.75	7.8	200	15
	5	121.2	3.69	3.3	219	13
	6	121.6	3.57	2.7	119	-16
7	1	327.8	5.72	2.0	48	-11
	2	392.3	5.57	7.1	45	-32
	3-7	393.9-397.7	5.56-5.58	2.3-3.0	315-340	3-11
8	1-6	429.3-430.0	6.22-6.23	2.1-3.3	148-194	(-19)-17
	7-9	432.8-430.0	6.26	2.2-2.8	281-313	9-19
	10-26	434.8-437.0	6.04-6.22	2.0-3.4	140-229	(-37) - 2
	27-43	437.6-439.2	6.04-6.08	2.2-3.9	65-98	(-28)-(-12)

to the displacement events 1-3, occurring in the same ENE direction (Figure 5.7c). The average orientation of these vectors (075°/25°) is aligned with the SE dipping fractures in the interval. These events indicate the end of the compliant response of

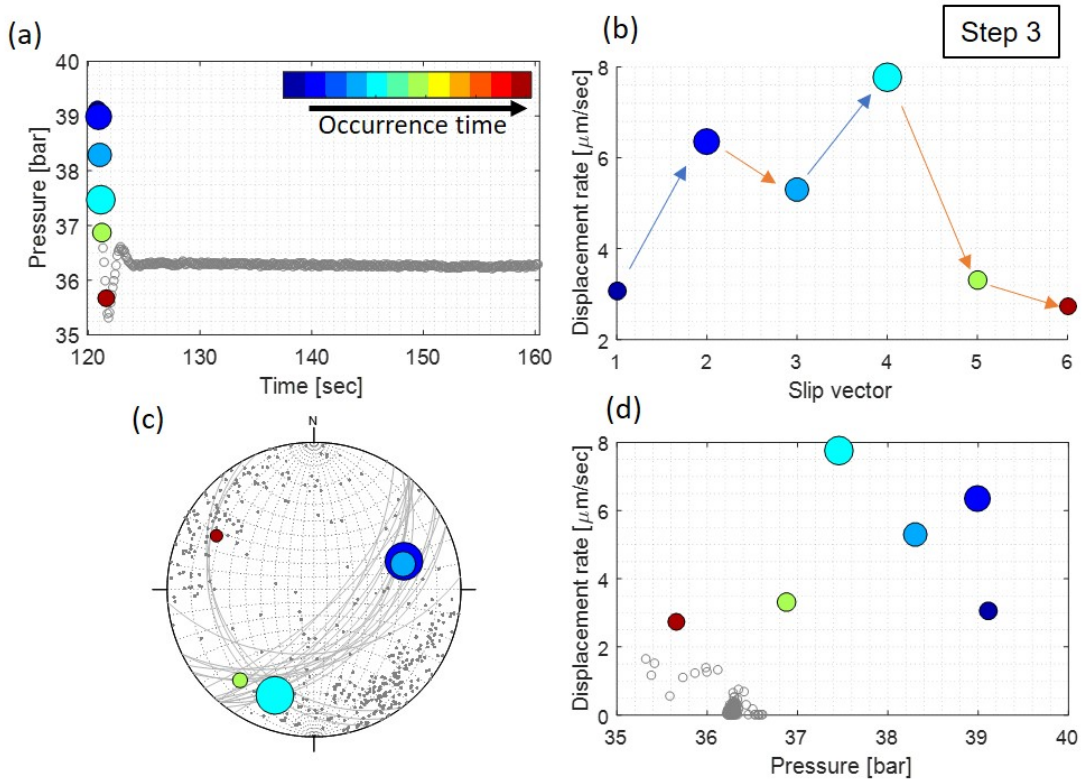

Figure 5.7: Analysis of the displacement orientation in shales for Step 3. (a) - Pressure variation at the step versus time, colored markers correspond to the displacement events. The marker size is a relative amplitude of the rates of the events, the market color – the time of occurence. (b) - The absolute magnitude of the displacement events. Blue arrows – slip weakening behavior, orange arrows – slip strengthening behavior. (c) – Lower hemisphere stereoplot with orientations of the displacements events. Black marker edge – positive plunge (normal faulting), red edge – negative plunge (reverse faulting). Grey markers display all the displacements belonging to this pressure step and below the rate threshold.

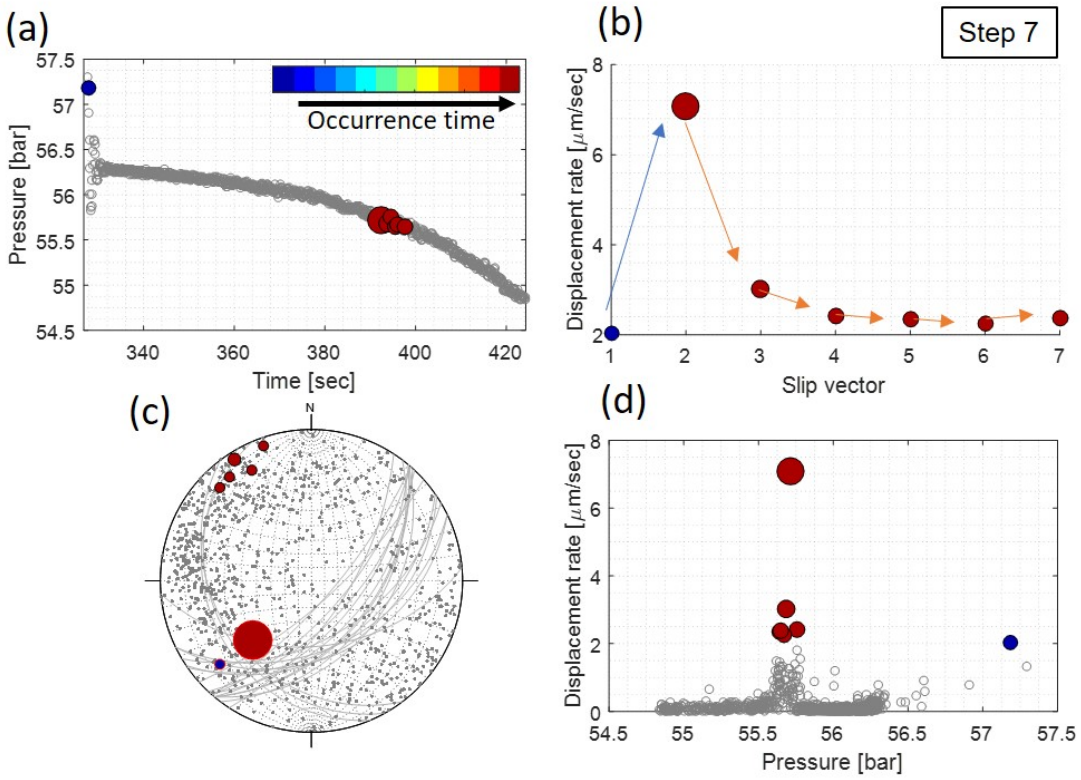

Figure 5.8: Analysis of the displacement orientation in shales for Step 7. (a) - Pressure variation at the step versus time. (b) - The absolute magnitude of the displacement events. (c) – Lower hemisphere stereoplot with orientations of the displacements events. Legend of the markers is given in Figure 5.7.

the interval and the beginning of some irreversible deformation (Figure 5.3, point 1, Figure 5.5c, white arrow). The second sequence corresponds to the displacement events 3-5. It is characterized by the rotation of the displacement vectors towards SW. The rotated vectors (4 and 5) are parallel to the intersection line between the SE-dipping fractures and the SW-dipping fractures. The last event of the step (6) has a rate-decreasing behavior. It rotates towards normal to the SE-dipping fractures. This orientation is consistent with an overall NW-SE trend, observed during this pressure step among the displacements with the low displacement rate (< 2 μm/sec) and with an orientation of the elastic response of the media. All of the displacement events figure normal slip (positive dip angle of $\overrightarrow{U_r}$, figure 5.1). Figure 5.7d shows that there is a slight tendency of decreasing rate with decreasing pressure.

Step 7 is characterized by pressure variation from 5.73 to 5.48 MPa and includes 7 displacement events (Figure 5.8a and Table 5.1). The first displacement events (1-2) demonstrate rate-increasing behavior (Figure 5.8b). Even though the events occurred within the 1 min, both are parallel to the intersection line between the SE-dipping and SW-dipping fractures and represent normal and reverse movement

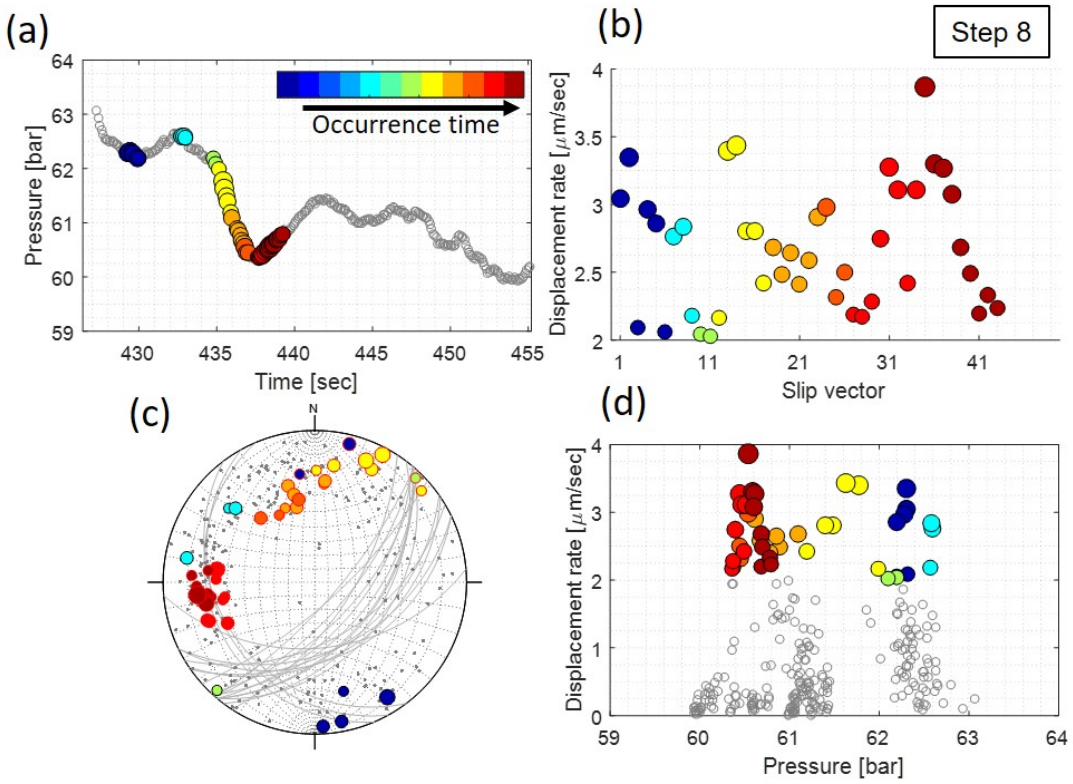

Figure 5.9: . Analysis of the displacement orientation in shales for Step 8. (a) - Pressure variation at the step versus time. (b) - The absolute magnitude of the displacement events. (c) – Lower hemisphere stereoplot with orientations of the displacements events. Legend of the markers is given in Figure 5.7.

(Figure 5.8c). The other displacement events (3-7) rotate towards NW with a rate-decreasing behavior. Disregarding the presence of the first event with a relatively low displacement rate, the same trend as in Step 6 of decreasing rate with decreasing pressure is observed in Figure 5.8d.

Step 8 corresponds to a pressure step with a variation from 5.99 to 6.31 MPa with 43 displacement events (Figure 5.9 and Table 5.1). Figure 5.9a shows that the events occur as sequences at different time during the pressure step. It is possible to define four sets of events based on their time occurrence and orientation. The first set of events (1-6 in Table 5.1 and dark blue in Figure 5.9c) displays six vectors dipping towards South, the second set of displacement events (7-9 in Table 5.1 and light blue in Figure 5.9c) consists of three displacement vectors dipping NW. Both sets occur within an interval of 3 sec and consist of mostly normal movements. Third set of displacement events (10-26 in Table 5.1 and green to bright orange in Figure 5.9c) occurred in 2 seconds after the second set and was associated with a decrease of pressure from 6.22 MPa to 6.04 MPa. The orientation of vectors during this event rotates from being horizontal and trending SW-NE to getting steeper and trending NE. The fourth set of displacement events (27-43 in Table 5.1 and

Table 5.2: Characteristics of displacement events for steps 4, 10, 12 and 13 in carbonates

Pressure step	Displacement vectors	Time of occurrence [sec]	Pressure [Mpa]	Displacement rate [μm]	Orientation	
					Dip direction [°]	Dip agnle [°]
4	1-6	228.4-228.9	2.42-2.45	2.5-3.3		sub-vertical
10	1-3	737.3-802.4	4.36-4.39	2.7-3.1	106-131	(-27)-(-17)
	4-5	847.0-851.3	4.36-4.37	2.4-2.6		sub-vertical
	6	890.5	4.41	9.3	119	-25
	7	897.5	4.42	2.4		sub-vertical
	8-11	924.0-1110.5	4.46-4.65	2.9-9.0	121-131	(-29)-(-25)
	12	1328.0	4.73	2.7		sub-vertical
12	1-2	1601.3-1601.4	5.33	2.7-3.9	91-95	-1
	3	1669.5	5.34	2.4		sub-vertical
13	1-2	1674.6-1674.7	5.90	2.7-3.3	65-70	(-2)-5

dark red in Figure 5.9c) was associated with an increase of pressure from 6.04 to 6.08 MPa and trends towards ENE. The third and the fourth sets consist of mostly reverse movements. The orientation of the displacement events overall demonstrates an "unstable" rotation tow ards being normal to being parallel to the SE-dipping or SW-dipping fractures. Figure 5.9b demonstrates that the rate behavior within each set is heterogeneous, however, it is possible to notice, that each set ends by the rate-decreasing . Figure 5.9d shows that the relationships between pressure and displacement rate are unclear.

5.7.2 Carbonates

The analysis of four pressure steps (4, 10, 12, and 13) with displacement rates above the 2.4 μm/sec threshold is given in Figure 5.10-5.13 and in Table 5.2.

Step 4 consists of six continuous displacements events, occurring in a pressure range of 2.42 to 2.47 MPa (Figure 5.10a). Figure 5.10b shows that the displacement events demonstrate the rate-decreasing behavior twice, which are given by the displacement events 1-3 and 4-6, respectively. Though the orientation of all the events is sub-vertical, it is possible to observe that the events 1-3 are mostly dipping NE, when the events 4-6 show the rotation from NW to ESE (Figure 5.10c). The transition between NE to NW is associated to a rate-increasing behavior. In addition, Figure 5.10d shows that before the transition, the events occur during the pressure increase, when the transition resulted in a slight decrease of pressure. All the displacement events demonstrate a normal movement and can be potentially aligned with the sub-vertical fracture oriented 110°/70°. There is no seismicity occurring during this pressure step.

Step 10 includes 12 displacement events (Figure 5.11a and Table 5.2), occurring between 4.34 and 4.74 MPa and accompanied by seismic events. Figure 5.11b shows that the seismic events are associated with the rate-increasing behavior of

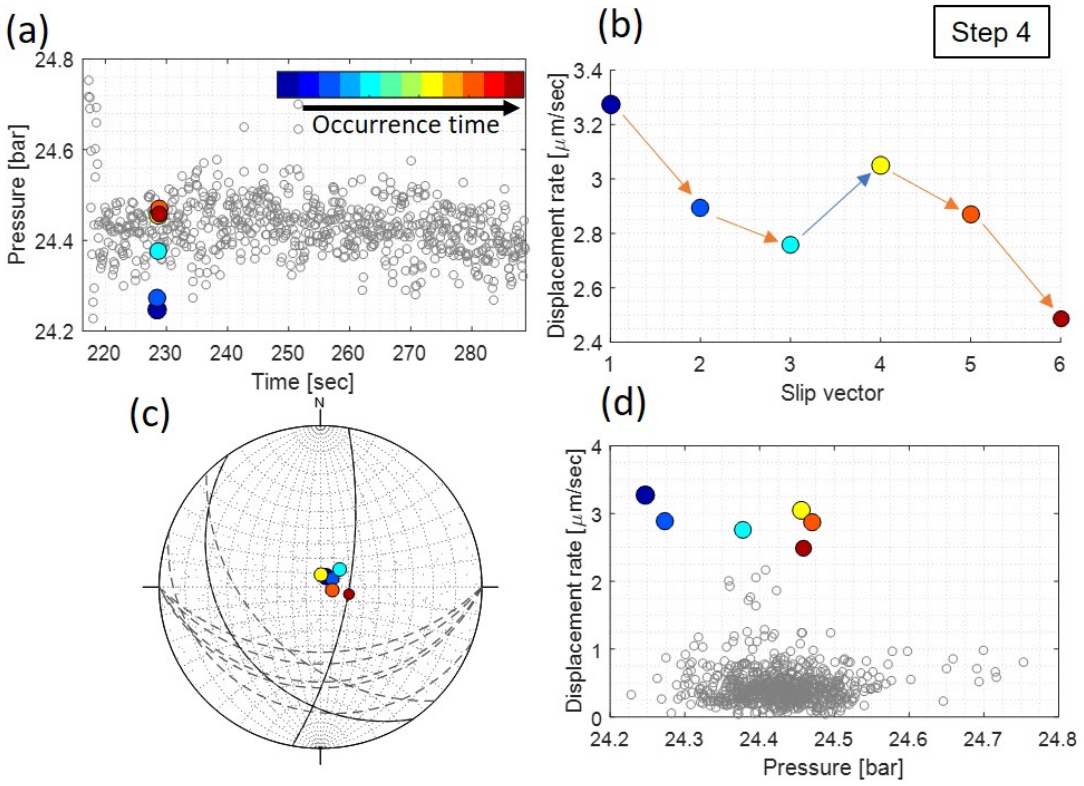

Figure 5.10: Analysis of the displacement orientation in carbonates for Step 4. (a) - Pressure variation at the step versus time. (b) - The absolute magnitude of the displacement events. (c) – Lower hemisphere stereoplot with orientations of the displacements events. Legend of the markers is given in Figure 5.7.

the displacement events suggesting that, the seismic events are a consequence of the rate-increasing of the displacement events 2-3, which in addition is associated by the pressure decrease. The seismic events 3, 4 and 5 can be a consequence of a rate-increasing behavior between the displacement events 5-6 and 7-9. Last displacement events (yellow and dark red markers) demonstrate a rate-increasing behavior and are not associated with any seismic event. The orientation of the displacement events is bimodal (Figure 5.11c). The displacement events of relatively low displacement rate either are sub-vertical and aligned with a sub-vertical fracture in the interval or dipping NW and aligned with a bedding plane. All the displacement events demonstrate a reverse motion. Figure 5.11d shows that during this pressure step the seismic events occurred at lower pressures than some of the aseismic events. It is also interesting to notice that the aseismic slip follows the orientation of the seismic slip.

Step 12 has a pressure range from 5.32 to 5.35 MPa and includes three displacement events occurring in the beginning (1-2) and in the end (3) of the pressure step (Figure 5.12a). The displacements events demonstrate a rate-decreasing behavior and are not associated with seismic events (Figure 5.12b). The first two displace-

ment events are subhorizontal trending E-W (Figure 5.12c) . The last displacement event is subvertical with a reverse movement. Step 13 consists of two displacement occurring at 5.9 MPa (Figure 5.13a). The displacement events demonstrate the rate-increasing behavior and have a subhorizontal NE orientation (Figure 5.13b,c) . The orientation of the displacement events at steps 12 and 13 is not aligned with any of the interval's fractures. For both steps 12 and 13, there is no evident dependency between pressure and displacement rate (Figure 5.12d, Figure 5.13d).

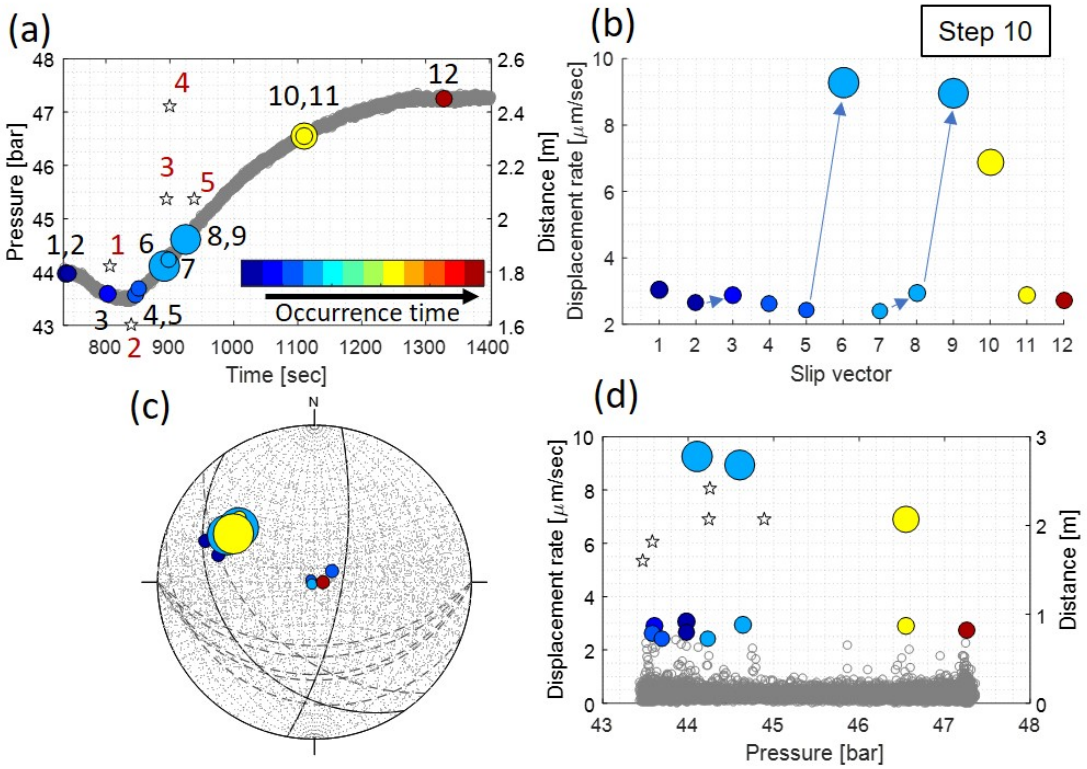

Figure 5.11: Analysis of the displacement orientation in carbonates for Step 10. (a) - Pressure variation at the step versus time. Stars represent seismic events and are given relatively to the distance from the injection point (right y axis, numbered in red). (b) - The absolute magnitude of the displacement events. (c) – Lower hemisphere stereoplot with orientations of the displacements events. Legend of the markers is given in Figure 5.7.

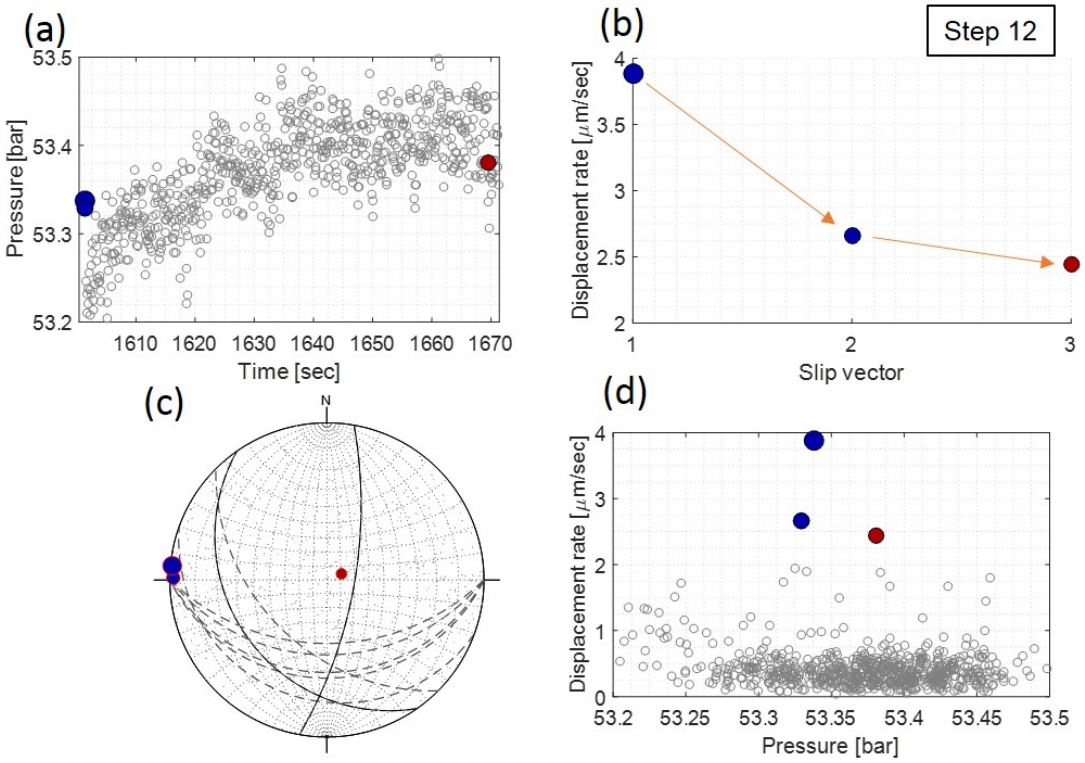

Figure 5.12: Analysis of the displacement orientation in carbonates for Step 12. (a) - Pressure variation at the step versus time. Stars represent seismic events and are given relatively to the distance from the injection point (right y axis). (b) - The absolute magnitude of the displacement events. (c) – Lower hemisphere stereoplot with orientations of the displacements events. Legend of the markers is given in Figure 5.7.

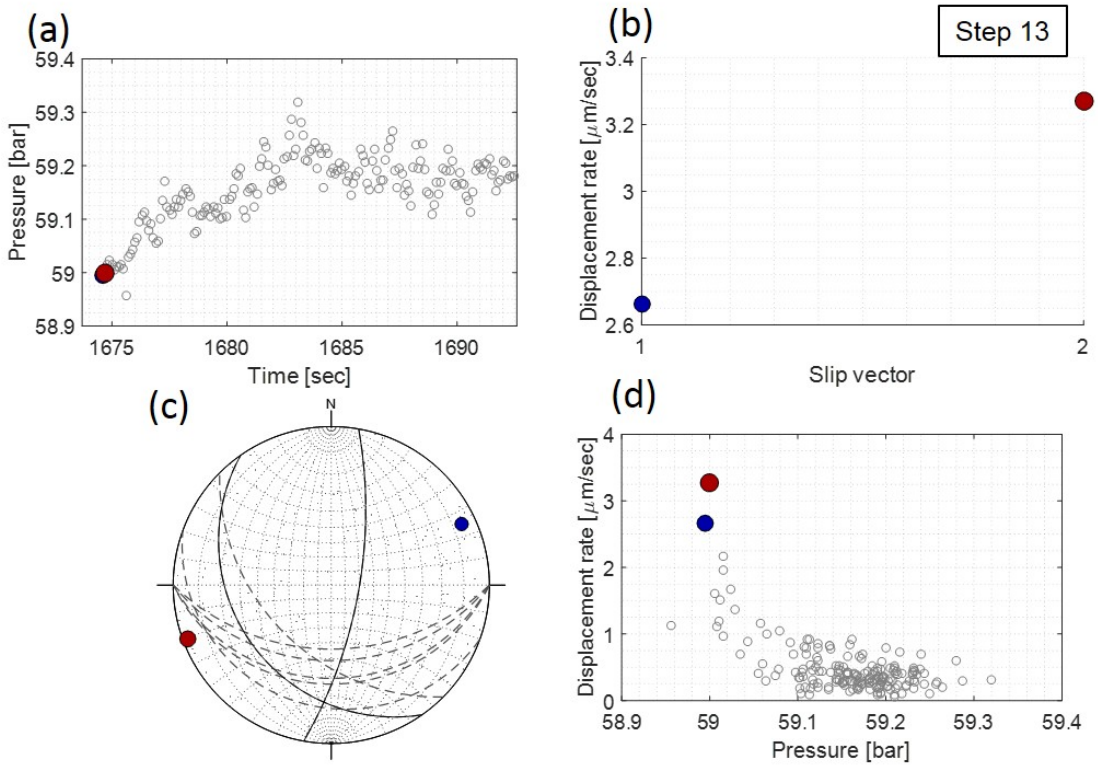

Figure 5.13: Analysis of the displacement orientation in carbonates for Step 13. (a) - Pressure variation at the step versus time. Stars represent seismic events and are given relatively to the distance from the injection point (right y axis). (b) - The absolute magnitude of the displacement events. (c) – Lower hemisphere stereoplot with orientations of the displacements events. Legend of the markers is given in Figure 5.7.

5.8 Discussion

The evolution of flowrate, pressure and 3D displacement of the borehole wall during fluid injection from two fault reactivation experiments conducted in carbonates and shales shows a complex response due to the superposition of multiple effects. We were interested in isolating fracture slip directions that we can interpret for stress estimation using the Wallace-Bott hypothesis. We developed a new protocol to isolate these slip vectors despite the complexity of the signal. The protocol is based on the extraction of displacement events that display high displacement rate during constant pressure periods. This approach is justified by the conceptualization of the main processes happening in the chamber during fluid injection. We compared the response to the fluid injection of fractured shales and carbonates and discussed which slip vectors can be driven by the current stress state according to the Wallace-Bott hypothesis.

5.8.1 Borehole near field response to a fluid

The analyses of our data in both shales and carbonates allowed identifying two main processes during injection in the open hole interval sealed sections (Figure 5.14). First, we observed a linear displacement-vs-pressure relationship that we interpret as an elastic response of the wellbore wall to pressurization (Figure 5.14a). Such a linear response is well-isolated for both shales and carbonates as a slow and progressive deformation in reaction to the borehole wall. The pressurization and the injected fluid diffusion into the formation during this linear response does not trigger slip events. We used the measured displacement rates during this period as a threshold to identify faster displacements that occurred in the chamber. The threshold was defined as the maximum displacement rate measured during the elastic response of the chamber. Later and at higher injection pressure,the relationship between pressure and displacement becomes non-linear and overall very complex. Several high displacement rate events occur. To avoid any misinterpretation of high rate increases, we chose to only pick these displacement events during the periods of time when the pressure in the interval is maintained constant. Thus, these events cannot be explained by rapid pressurization, pump oscillation or other complex response of the injection pump – downhole probe – borehole system. The displacement events represent non-reversible deformation resulted by a fracture activation. The high displacement rate of these events indicates their rapid and sudden occurrence, which we interpret as fault rupture, and consequently, slip. Some of them correlate with the observed induced seismicity. This is the second important process that we conceptualized in Figure 5.14. Later during the injection, continuing pressure

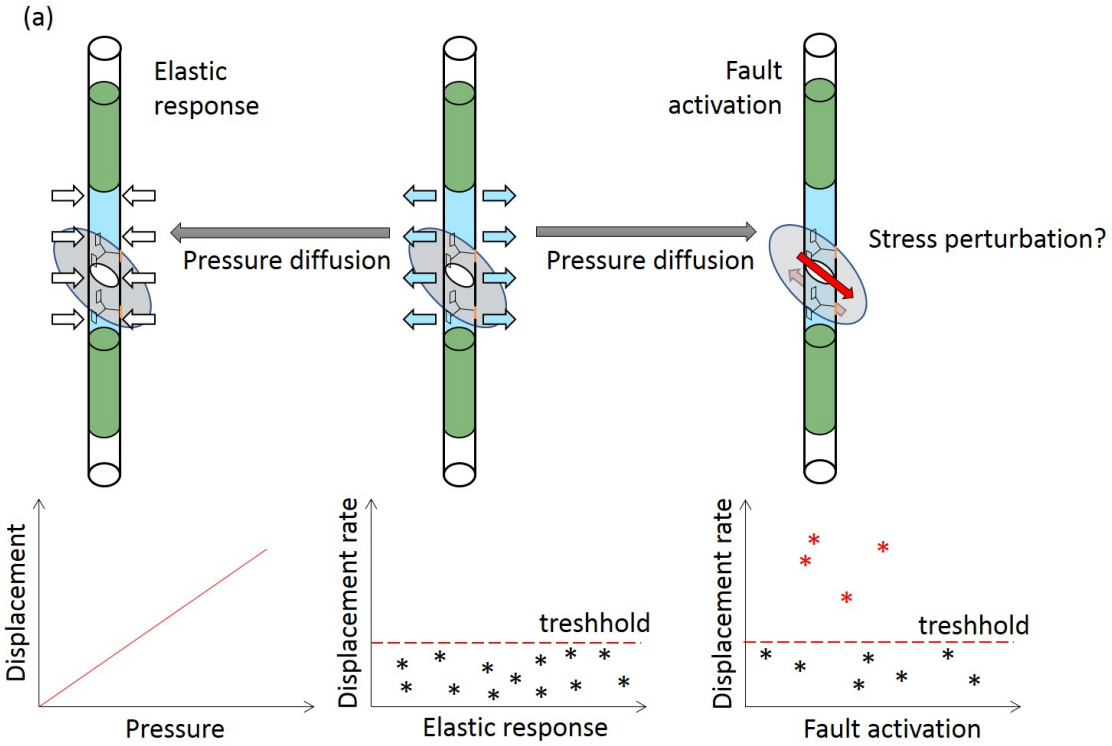

Figure 5.14: Conceptual model of the main processes happening during fluid injection

diffusion and fault activation lead to mechanical interactions in the system, which perturb the surrounded stresses and results in a complex response of the chamber.

5.8.2 Isolating displacement events on natural reactivated fractures

Three and four pressure windows including displacement events were identified for shales and carbonates, respectively, by applying our data processing protocol. The first displacement events are aseismic and the displacement rate of the displacement events mostly decreases during the pressure steps. Because these displacement events are aseismic and correspond to the beginning of the non-reversible deformation, we assumed that they can be trigged by an unperturbed stress state – background stress.

The background stress causes slip on a fracture which is consistent with the orientation of the resolved shear stress according to the Wallace-Bott hypothesis (Chapter 4). The normal and shear stresses on a fracture which define the failure of the fracture are controlled by the background stress. We showed in Chapter 4 that injection reduces the effective stress on a fracture until it reaches the Mohr Coulomb failure criteria and thus the fracture slips. We also showed that the direction of this slip is consistent with the slip direction resolved from the background stress. Therefore, we assume that the first slip results from the background stress. Moreover,

next slip events will increase the deformation in the chamber, which leads to increase of stress perturbation along the fracture and stress concentration on fracture tips. Therefore, we assume that the first slip event is the most consistent with the background stress. For shales and carbonates the first measured slip is aseismic. Because of different displacement rates, we assume that the seismic deformation with higher displacement rates and therefore, larger deformation, may affect the stress perturbation more. The fact that the first slips are aseismic makes the assumption to use these vectors to estimate the background stresses more reliable. To estimate if these events can be used for a stress inversion, we also analyzed their geometrical relationship with the existing interval fractures.

In shales, the first three displacement events with an average orientation 075°/25° are aligned with SE-dipping fractures. However, the interval also includes another SW-dipping family. Fractures from both families occur between the anchors, where the displacement magnitude is assumed to be the strongest. The existence of fractures with different orientation complicates the response. Consequently, the first displacement events do not keep the same orientation, but are quickly replaced by a vector, which is parallel to the intersection line between the SE-dipping SW-dipping fractures. The rotation of the orientation of the events occurred because of the mechanical interactions between closely spaced faults, which can strongly influence the local stress and slip direction [Pollard et al., 1993, Maerten, 2000, Nieto-Samaniego and Alaniz-Alvarez, 1997, Lisle, 2013]. Pascal [2002] demonstrated that the slip is strongly perturbed close to the line intersection of two faults. Maerten [2000] showed that this perturbed slip tended to be parallel to this intersection line. Displacements parallel to the intersection line are also observed among the displacement events, occurring at the pressures >5.5 MPa, which with an increase of flowrate, rotate towards being normal to the SE-dipping fractures.

Even though the first displacement event is aligned with the SE fractures, one may ask if this event could correspond to the opening of the SW-dipping fractures. Considering the regional stress state in Mont Terri [Martin and Lanyon, 2003] and low dip angle of the SW-dipping fractures, we assume that the normal stress on the SW-dipping fractures is higher than on the SE-dipping fractures, which prevents the SW-dipping fractures from slipping first. Moreover, the slip orientation on the SE-dipping fractures is consistent with the first slip event, occurring during the pressurization of the interval located 3 m below the analyzed test. Guglielmi et al. [2019] showed that this slip, occurring on a SE-dipping fracture (136°/32°), is favorable for activation under the stress state obtained by Martin and Lanyon [2003]. Thirdly, the SW-dipping fractures are typically sealed with calcite and celestite [Nussbaum et al., 2011], which may create an additional cohesion and prevent the reactivation of these fractures. Therefore, we conclude that the first displacement

events, or slip, occurred on the SE-dipping fractures. The variability in orientation and depth of the SE-dipping fractures requires further evaluation to define the exact orientation of the activated fracture (Chapter 6).

In carbonates, the first displacement vectors are sub-vertical and aligned with the sub-vertical fracture oriented 100°/70°. According to the regional stress by Guglielmi et al. [2015a], where the maximum stress is vertical, we conclude that this slip corresponds to the activation of the sub-vertical fracture. The bedding plane and other "diffuse" fractures cannot be activated because of low dip angle, and therefore, high normal stress. The activation of the bedding plane occurs at higher pressures (>4.3 MPa) and is associated with the seismic events. It is clear from the Figure 11, that all the displacements that are aligned with the bedding plane are related to high displacement rate and rate-increasing behavior. According to Duboeuf et al. [2017], seismicity was trigged by aseismic deformation. The seismicity perturbs the surrounded stress state, therefore supports the subsequent activation of the bedding plane.

The orientations of the first sub-vertical displacements rotate with time. According to the results from the chapter 4, the true slip orientation during the fluid injection corresponds to the last orientation, which would indicate a stable slip. Here, the last slip with high displacement rate is oriented 105°/69°, which shows the normal slip on the sub-vertical fracture.

5.8.3 Estimation of fracture normal stress

The kink during the shut-in pressure shows the value of 4.7 MPa, which exceeds the range of shut-in values 4.3-4.5 MPa defined during the manual pump (Chapter 3 Section 3.1). The shut-in pressure in the end of the test is 3.4 MPa. We have developed several scenarios how to explain two values of the shut-in pressure.

- The overestimated shut-in kink pressure during the engine pump can be related to the activation of the SW-dipping fractures (Section Data Processing). The activation of the SW-dipping fractures is also consistent with the sharp change in orientation occurred with the rapid flowrate increase during the pressurization until the maximum pressure step (point 3, Figure 5.3). The low pressure during the shut-in could be potentially related to the activation of a steep SE-dipping fracture located at 38 m below the gallery floor and 0.5 m below the anchors.

- The overestimated shut-in kink pressure might be related to the flowrate increase and uncertainties associated with a SE-dipping fracture growth, i.e. larger activation patch, non-planarity of the fracture surface, or activation of shallower SE-dipping fractures.

- The low value of the shut-in may indicate the initialization of a hydraulic fracture, which could be created at high injection pressures. In this case, the hydraulic fracture could explain a sharp change in orientation at point 3, Figure 5.3. And then the displacements events during the last and maximum pressure step would correspond to the activation of both: a SE-dipping fracture and a hydraulic fracture.

- The sharp change in orientation could be explained by the orientation of the first slip events. The new rotated displacements with sub-horizontal orientation along the strike of the SE-dipping fractures have similar orientation to this first displacement events. It may indicate that the injected pressure overcomes the mechanical interactions between SE- and SW-dipping fractures.

- In this complex chamber response all the processes mentioned above can be involved.

In view of this complexity and uncertainties, the stress estimate of 4.4 MPa derived from the manual pump test is considered the most reliable.

It is also important to mention, that this rotation occurs during the fluid injection which includes an additional interaction between probe and borehole, described before.

In carbonates, the increase of the flowrate after the sub-vertical fracture activation and the associated sub-horizontal displacements-oriented WNW-ESE, indicates the fracture opening between 3.2-4.4 MPa (Figure 5.4, points 2-3). The fracture opening pressure is usually higher than the normal stress on the fracture. However in this test the exact value is impossible to define, because of the lack of true shut-in. The kink during the chamber opening at 4.7 MPa does indicate the NW-SE trend of displacement, which could be related to the closure of the sub-vertical fracture, however, we cannot be certain, because the chamber opening occurs too fast. Therefore, we roughly assume that the normal stress on the activated sub-vertical fracture is around 3.2 MPa.

The sharp change in the direction of the displacements at point 4, Figure 5.4 corresponds to the activation of the bedding plane in reverse sense. It is also accompanied with the second increase of the flowrate (Figure 5.4b). These results are consistent with the observation from Duboeuf [2018]).

5.8.4 The Comparison between shales and carbonates behavior

The highest differences in behavior during the injection between shales and carbonates lies in displacement response, injected flowrate and associated seismicity.

For both shales and carbonates the displacement response is complex. The analysis of the applied protocol shows that the first displacement events, or slips, are aseismic. The rate-based concept works in identifying early slip within complex deformation signal. We assume that these early slip are driven by the background stress and can be used for stress estimation.

For both rock types, this slip in associated with the end of the linear response. However, these slip vectors do not demonstrate the maximum displacement rate . In shales this is caused by the existence of another family of fractures, which close mechanical interactions with SE-dipping fractures are strong and, therefore, affect and remove the unperturbed slip evolution. In carbonates, aseismic deformation predate seismicity which occurs 3 min after the first aseismic slip is observed. The maximum displacement that are associate with seismicity, since occurring later in test can reflect already perturbed stress by the aseismic deformation [Duboeuf, 2018, Duboeuf et al., 2017].

Another difference between shales and carbonates is the location of the slip events. The slip on shales occurs during the pressure drop in the beginning of the pressure step. In carbonates, the slip occurs in the middle of the pressure step and is not associated with a drastic pressure change. This difference may be related to the different rock permeability and, consequently, response to the fluid pressure.

Seismicity is also one of the key parameters that differentiates the response from shales and carbonates. No seismicity is observed in shales during the STR injection. In carbonates, however, there were 15 seismic events with estimated magnitude lower than zero observed during the injection [Duboeuf, 2018, Duboeuf et al., 2017]. The seismicity might be related to the difference in mineralogy, fracture stiffness, rock permeability, the amount of injected flowrate, which define the rock mass respond to the injection, rock brittleness, and stress state perturbation. In terms of flowrate, even though we observe some oscillations in the flowrate below 5 L/min, a rapid flowrate increase up to 23 L/min is observed after 5.8 MPa. Such a response to the fluid injection is typical for the shales with low permeability, which is 10^{-17} - 10^{-21} m^2 [Henry et al., 2018], Jeanne et al. [2018b]. In carbonates, the flowrate increases gradually, which is related to the high permeability of the rock mass up to 10^{-15} m^2 [Cochard, 2018, Jeanne et al., 2013]. Moreover, carbonates are associated with brittle deformation, which is more likely associated with seismicity, than shales. The dramatic activation of the non-favorably orientated bedding fracture in carbonates also indicates a perturbed stress state, which results in seismicity.

5.9 Conclusions

In this work we developed a protocol that helps capture slip vectors and better understanding the effects of fracture activation on the mass response during injection. The primary fluid injection induced deformation in both shales and carbonates is aseismic. Using the slip vectors derived from the SIMFIP probe, the stress state can be identified using the Wallace-Bott inversion technique for both shales and carbonates. Differences in behavior can be attributed to the difference in rock properties and permeability.

5.10 Acknowledgements

This research is supported by the University of Neuchatel and the FS partners (swisstopo, ENSI, JAEA and LBNL).The experiment in carbonated was conduced within HYDROSEIS project (*http ://hydroseis.oca.eu*) under contract ANR-13-JS06-0004-01 and by Total SA (PI. through the HPMS-Ca project (Albion, PI. G. Massonat).

Chapter 6

Estimation of the full stress tensor from fluid injection induced fault dislocation data

6.1 Abstract

THIS work focuses on developing a protocol to estimate in–situ stress by using the slip vectors obtained during fault activation by fluid injection. The slip vectors are measured using the Step-Rate Injection method for Fracture in-Situ properties (SIMFIP) and are discussed in Chapter 5. The protocol consists of an initial step during which multiple possible solutions, i.e. combination of stress orientation and stress ratio reproducing the measured slip orientation, are computed. The subsequent steps leads to reducing iteratively the number of allowable solutions by considering the normal stress acting across the reactivated fracture estimated from pressure record during the injection, the estimate of the vertical stress and the comparison of the slip tendency on the fractures present in the injection interval. This process allows proposing a best estimate of the full stress tensor and to evaluate confidence intervals on the tensor components. The protocol is applied at two experimental sites in different rock types: shales in Mont Terri rock laboratory and carbonates in LSBB. In both experiments, the estimated stress state is consistent with independent estimation of the in-situ stresses at the sites.

6.2 Introduction

In-situ stress orientations and magnitudes are essential for designing and operating oil and gas, geothermal, mining, and other subsurface engineering projects [Bell and Gough, 1979, Zoback, 2010, Jaeger et al., 2009, Willson et al., 1999, Zoback

et al., 2003, Zoback, 2010, Hubbert and Willis, 1957, Lin et al., 2008]. The most current stress measurements techniques to reconstruct stress tensor at a given point rely on detecting key pressure parameters while performing hydraulic tests in a borehole sealed section [Hubbert and Willis, 1957, Haimson, 1993, Haimson and Cornet, 2003, Zoback et al., 2003, Schmitt et al., 2012]. In this paper, we analyse how the direct measurement of borehole fracture displacements coupled to the usual pressure measurement allows a more complete estimation of the full stress tensor.

Traditional hydraulic fracturing methods [Haimson and Cornet, 2003] include hydraulic fracturing test (HF) and hydraulic tests on pre-existing fractures (HTPF). In both hydraulic fracturing methods a short segment of the borehole is sealed off using a straddle packer system, and fluid is injected to initiate a new fracture (HF) or to open or shear a pre-existing natural fracture (HTPF). Flow rate and pressure are recorded during these tests and used to identify pressure values that are interpreted as being related to fracturing and that can be used to estimate some components of the in-situ stress tensor. The injection protocol includes repeated injections cycles in order to gain confidence in the estimation of the diagnostic pressure levels.

Hydraulic fracturing is a convenient method for estimating some components of the in-situ stresses in boreholes. It does not require the knowledge of the elastic rock properties, no sophisticated instrumentation is needed inside the borehole, and tests can be successfully conducted at depths more than 1 km [Hung et al., 2009]. When the testing conditions are favorable, i.e. when the minimum principal stress is perpendicular to the test hole, a HF test gives the minimum principal stress magnitude with an estimated accuracy of $\pm$ 5% [Ljunggren et al., 2003] by picking the instantaneous shut-in pressure from the pressure-time record [Hubbert and Willis, 1957]. In these ideal conditions, the initiated hydraulic fracture is normal to the orientation of the minimum horizontal stress and parallel to the orientation of the maximum horizontal stress. However, the assumption that the minimum principal stress is equal to shut-in pressure is not always valid [Nelson et al., 2007, Guo et al., 1993, Ito et al., 1999]. In the presence of pre-existing weaknesses around the borehole and of complex stress concentration effects at the borehole wall, the fluid will initiate its propagation into the direction of these pre-existing weaknesses instead of initiating parallel to the minimum principal stress direction [e.g., Evans et al., 1988, Warpinski and Teufel, 1991]. When the borehole is unfavorably oriented compared to the far field stress, the propagating fracture may also rotate away from the borehole to be parallel to the non-disturbed far-field stress which brings complications in the interpretation of the pressure records [Daneshy, 1971]. Hydraulic fracturing stress tests are also hard to analyze in thrust faulting context because even if a vertical fracture eventually initiates at the borehole wall it will rotate to become horizontal away from the hole (i.e. perpendicular to the minimum principal stress which is

vertical). The interpretation of the pressure and of the posttest borehole fractures will then give ambiguous estimations of both the magnitudes and the orientations of the minimum horizontal stress [Evans et al., 1988, Gaines et al., 2012].

Another shortcoming of HF test is the difficulty to estimate the magnitude of the maximum horizontal stress. The challenging components required for the calculation of the horizontal maximum stress are the rock tensile strength and the breakdown pressure. Rock tensile strength can be directly measured in the laboratory, however, the scale effect between field and laboratory as well as effective stress law coefficient for tensile failure induce a lot of uncertainty when analyzing the field measurements. When a core is not available, or laboratory tests are not feasible, the determination of the magnitude of the maximum horizontal stress relies on the fracture reopening pressure [Bredehoeft et al., 1976]. However, it also has some uncertainties due to the plastic behavior of the surrounding rocks [Rutqvist et al., 2000], remaining apertures inducing leak off at the start of the repeated pressure cycle [Cornet, 1993], and difficulties in objectively identifying the reopening pressure on the pressure-time record [Lee and Haimson, 1989, Ito et al., 1999, Evans et al., 1988]. The accuracy of maximum horizontal principal stress calculation is ± 20% [Ljunggren et al., 2003]. It is also important to mention that a HF test requires subsequent borehole imaging to identify the orientation of initiated fracture which is not always easy to identify.

A complementary method to conventional hydraulic fracturing - Hydraulic tests on pre-existing fractures (HTPF) - was proposed by Cornet and Valette [1984]. This method is focused on the opening and closure of pre-existing fractures in the straddle packer interval. The normal stress on the pre-existing natural fracture plane is estimated from picking the shut-in pressure on the pressure-time record. Theoretically, 6 measurements of normal stress of differently oriented fractures are required to characterize the complete stress tensor. However, it is always preferable to conduct more tests than there are unknowns to calibrate the estimated values. Haimson and Cornet [2003] suggest that at least 8 tests are necessary for a complete stress determination. The distance between each individual test may increase uncertainties arising from stress gradient or stress heterogeneities which are present in a fractured rock mass. To take into account the stress gradient, a minimum of 14-15 tests are required [Haimson and Cornet, 2003]. In addition, non-planar fractures can lead to overestimation of the shut-in pressure, which results in uncertainty in evaluation of principal stress magnitudes. The amount of tests makes this method time consuming. It requires a refined structural mapping of the intervals using s suite of borehole imaging techniques.

As described above, the standard in-situ stress measurement methods using fluid injection in deep boreholes are based on the analyses of flow rate, pressure-time record and pre- and post-injection fracture mapping. These methods do not provide

a complete stress tensor at a point along the borehole, but some components of it, namely the minimum stress and its orientation or the stress magnitude normal to a pre-existing fracture. A full stress tensor can be derived only by combining a series of tests from multiple locations and by making restrictive assumptions on the in-situ stress state and its variability. Here we analyse a new technique to improve the estimation of the in-situ stress. This technique is coupling the direct measurement of the three-dimensional (3D) borehole wall displacement to the pressure measurement in the straddle packer interval. Measurements of both pressure and displacements are continuous during the injection. We propose a protocol to estimate the stress state by using the displacement-flowrate-pressure data. We take the example of two tests conducted in contrasted geological environments, a fault damage zone in shale rocks at the Mont Terri rock laboratory, Switzerland and fracture reactivations in carbonates conducted at the Rustrel Low Noise Underground Laboratory (LSBB URL), France.

The main objective of the protocol presented in this paper is the estimation of a complete stress tensor at one experimental location along a borehole by combining slip vectors trigged during the fluid injection with pressure and flow record. The general approach of our analyses is first to identify reduced stress tensors, i.e. principal stress orientation and relative magnitude, that are compatible with the observed slip direction measured on fractures within the tested interval. In a second step, we reduce the number of compatible stress tensors and estimate the absolute principal stress magnitudes by analyzing the injection flow and pressure record to identify the magnitude of the stress component normal to the activated plan. We also use an independent estimate of the magnitude of the vertical stress component based on overburden weight computation to set further constraints on our stress tensor and compute slip tendency on the fractures to assess consistency of the proposed stress solutions. We complete our analyses by a systematic uncertainty analyses of the derived stress tensor.

For this paper we use as a starting point for our analyses the data of direction of the slip vectors and the behavior of the fractures during the injection that were analyzed in Chapter 5. The inversion also requires the data of the normal stress on an activated fracture, the vertical stress, and friction parameters if available. We estimated the stresses in two different contexts: laminated shales with multiple bedding parallel fractures (Mont-Terri laboratory) and a single fracture activation in carbonate rock (LSBB laboratory, Rustrel). We first present the processing of slip data from the test performed in Mont-Terri (test 37.2). Then we show how slip and hydraulic pressures can be combined to improve the stress inversion methodology. Finally we apply the approach to both shales and carbonates and compare with existing stress data.

6.3 Stress state at study sites

The stress state in Mont Terri was established by Martin and Lanyon [2003]: σ_1=6-7 MPa sub-vertical to N210-70° plunge, σ_2 = 4-5 MPa N320° sub-horizontal to 7° plunge, and σ_3 = 0.6-2 MPa N052° sub-horizontal to 18° plunge. The stress was estimated by carrying out three stress measurements programs in the Mont Terri ED-B gallery, including a slotter probe [Bock, 1993], undercore method using the CSIRO triaxial strain cells [Wiles and Kaiser, 1994] and hydraulic fracturing [Haimson et al., 1967]. The greatest uncertainty in the measurements programs was related to the magnitudes of the minimum principal stress.

In the LSBB lab, the regional state of stress was estimated from hydraulic tests on preexisting fractures (HTPF) using the SIMFIP probe and taking into account topographic stresses [Guglielmi et al., 2015a]. Using a forward fully coupled numerical analysis of the injection tests, the stress state was refined to be: $\sigma_1 = 6 \pm 0.4$ MPa is sub-vertical, $\sigma_2 = 5 \pm 0.5$ MPa is sub-horizontal and oriented N20° $\pm$ 20°, and $\sigma_3 = 3 \pm 1$ MPa is sub-horizontal and oriented N110° $\pm$ 20°. The heterogeneity in fractures density and initial permeability strongly influenced the stress state estimate. The shut-in pressure was difficult to identify because the pre-existing fractures did not close completely. However, the SIMFIP probe helped identifiing the reopening pressure and the slip vector on reactivated planes to make a stress inversion. In the same boreholes but a few years later, Duboeuf [2018] estimated the state of stress at the experimental site using an inversion of focal mechanisms of earthquakes induced by new injection tests. They showed that the local stress state is not homogeneous and different from the regional stress state. The stress state defined by Duboeuf [2018] at the location of the injected interval is: σ_1 is oriented N135° $\pm$ 20° and dips 40° $\pm$ 10°SW, σ_2 is sub-horizontal N240° $\pm$ 40° and σ_3 is N300° $\pm$ 10° and dips 80° $\pm$ 5°NW.

6.4 Displacement and Pressure datasets

Both experiments in Mont Terri and LSBB laboratories consisted of fluid injections into the fault damage zone to reactivate fault planes and to measure the slip during the injection. The experiments procedure for both experimental sites followed the step-rate injection method for fracture in-situ properties (SIMFIP) developed by Guglielmi et al. [2013]. In comparison to traditional hydraulic methods, the SIMFIP probe enables simultaneous monitoring of the three-dimensional displacement of the injection chamber wall, the fluid pressure variation and the flowrate at up to 1 kHz sampling rate. The injection interval of 2.5 meters is sealed by inflatable packers

Table 6.1: Summary of the input structural data, including the geology of the interval, normal and vertical stresses measured on a reactivated fracture using the SIMFIP probe.

Depth [m]	Potentially activated fractures		Slip direction		Projected slip		Normal stress [MPa]	Vertical stress[MPa]
	Dip Dir []	Dip Angle [°]	Dip Dir [°]	Dip Angle [°]	Dip Dir [°]	Dip Angle [°]		
36.71	149	48				-17		
37.06	233	25				-23		
37.15	247	20				-20		
37.20	130	55				39		
37.28	130	46	75	25	75	31	4.4	7.9
37.30	131	65				50		
37.41	130	37				23		
37.52	130	45				30		
37.71	123	63				-53		

(sliding sleeves). The displacement cage of the SIMFIP probe is 0.58 cm long and it is set in the center of the interval.

Here, we focus only on the parameters from the experiment in the Mont Terri laboratory. The input parameters and results for the experiment in LSBB are derived using the same approach and are presented in the results section.

Nussbaum et al. [2011] and Guglielmi [2016] give a detailed overview of the geology near the experimental site, which is summarized in the following section. The SIMFIP probe is installed in the BFS2 borehole at the Mont Terri lab, at a depth of 35.85 to 38.33 m depth below the gallery floor, with the probe centered at 37.2 m depth. The injected interval intersects mainly two sets of fractures dipping South-East and South-West. The South-East dipping fractures are sub-parallel to the bedding planes with the dip direction and dip angle varying from 123° to 154° and 36° to 74°, respectively. The South-West dipping fractures have an average orientation of 240°/23°. One fault dips South and has an orientation of 174°/43°. The displacement cage with upper and lower anchors located at 36.91 and 37.49 m integrates the potential displacements of two south-west dipping fractures (233°/25° and 247°/20°) which are separated by a 2 cm layer of scaly clays Nussbaum et al. [2011], and 5 south-east dipping fractures (130°/55°, 130°/46°, 131°/65°, 130°/37°, 130°/45°), given in 6.1.

The high-density of fractures within the interval makes it difficult understanding which fracture(s) activated during the injection. We made several assumptions to exclude some fractures and simplify the analysis. First, we assumed that the measured slip corresponded to only one activated fracture. This assumption is reasonable because the captured slip vector corresponds to the earlier signal at the onset of activation, before fracture propagation that may involve complex multiple fractures interactions (5). Second, we showed that the largest slip could only be captured close to the displacement cage and the the displacement field induced by

a fracture dislocation decreases with the distance to the dislocated plane (3.5.1). Therefore, we considered fractures which are located within the interval of measurement of the displacement cage and ± 0.25 m above and below. It resulted that we considered 9 fractures within a 1 m long interval (36.7 to 37.7 m, see Table 6.1). In addition the fractures oriented 130°/46° and 130°/45° were analyzed as one fracture oriented 130°/46°, because of the very similar dip angle, and thus this let us with only 8 fracture as an initial input for the analyses.

The value of the vertical stress component (σ_v) was then estimated by considering the lithostatic load $\sigma_v = \sum_{i=1}^{n} p_i g \Delta z$, where p_i is the mean mass density of the overburden rock layer i ; g is the gravity; Δz is the thickness of the layer i ; and n is the number of layers overlying the site. The head of the borehole and the displacement cage are located at 294 m and 331.2 m below the surface, respectively. However, the topography of the ground surface is mountainous. The average density of overlying layers is 2.4-2.5 g/cm^3. Considering the complexity of the topography and the average density of the overlying layers, we estimated the vertical stress at the borehole head to be of 6.9 to 7.2 MPa, and 7.8 to 8.1 MPa at the depth of the test (Table 6.1).

Normal stress on a fracture was determined as an average 4.4 MPa from the shut-in pressure of 4.3 to 4.5 MPa (Table 6.1, column 9, Chapter 3 Section 3.1).

The fluid injection in the interval triggered slip that generated a displacement field that was captured by the SIMFIP. The overall displacement is complex as it encompass the superposition of multiple effects, including elastic and poroelastic deformation, plastic response, fracture slip. The processing of the complete displacement data based on displacement rate analyses presented in Chapter 5 enabled picking fracture slip. This is the starting point for our stress inversion computation. The slip signal that we used in our inversion occurred early in the test, thus before fracture propagation. It is considered to be induced in a non-perturbed in-situ stress state (Chapter 5). It occurred at 3.9 MPa and had an orientation of 075°/25° (Table 6.1, column 4-5). Because the activated fracture was unknown, we projected the measured slip on all the fractures previously selected. (Figure 6.1a,b). The slip induced dilation did not affect the orientation of the resolved slip direction, and consequently, did not affect the orientations and magnitudes of the in-situ stress state during the inversion (Chapter 4). The projections of the measured slip on the analyzed fractures are given in Table 6.1(columns 6-7). Positive and negative dip angles respectively figure normal and reverse faulting. Differences in the signs of the projected slip (Table 6.1, column 7-8) are related to the fracture location relative to the displacement cage (Figure 6.1c). The downwards direction of the slip (dip angle > 0, i.e. 075°/25°, lower hemisphere) and the location of the fractures above and

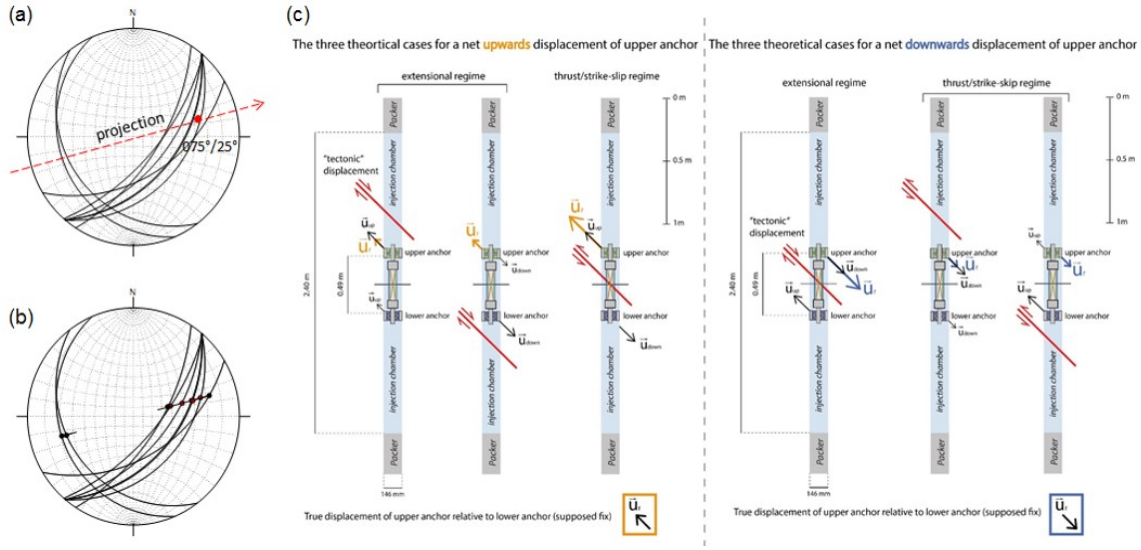

Figure 6.1: (a) Orientation of the original slip and its projection to all the fractures in the interval, (b) Projected slip on the fractures: red – normal slip, black – reverse slip; (c) Theoretical cases for a net upwards (left) and downwards (right) displacement of upper anchor (by Nussbaum et al. [2011])

below the displacement chamber represents reverse faulting, and for the fractures within the interval - normal faulting (Figure 6.1c, Figure 5.1).

To use the Wallace-Bott hypothesis in stress inversion which is based on the collinearity of the resolved shear stress with the slip direction [Wallace, 1951, Bott, 1959], we assumed that the angle between the measured and projected slip vector on a fracture plane should not exceed 45°. This criteria allowed the exclusion of fractures where opening was much larger than slip, thus very unlikely to explain the observed slip signal. The South-West dipping fractures have $> 45°$ of difference between the measured and projected slip on the fracture. Therefore, they are excluded from the next steps of the analysis. It results that only slip vectors on the fractures dipping South-East with a normal or a reverse faulting will be considered in the stress inversion.

6.5 Methodology for stress tensor estimation

This section provides a detailed description of the protocol to estimate the orientation and the magnitude of the complete stress tensor. In order to illustrate the protocol we show detailed examples considering two fractures: 130°/55° and 149°/48°. They represent normal and reverse faulting, respectively. The protocol consists of several steps, which are given in Figure 6.2 and explained in details below. With each step forward of the protocol the number of possible solutions decreases, giving more certainty to the final results:

- A grid search though all possible reduced stress tensors is performed to find optimal tensors, which have the lowest misfit angle between the measured and the calculated slip.
- The magnitudes of normal and vertical stresses, the orientation of a reactivated fracture and the orientations and stress ratio of the principal stresses are used to calculate the magnitudes of the principal stresses.
- The results are filtered by slip tendency analysis and by bounds of the stress magnitudes, which were discussed taking into account the tectonic stress history of the area.

6.5.1 Reduced stress tensor

The optimal reduced stress tensor was estimated by determining the minimum misfit angle between the measured slip vector and calculated slip in the four-dimensional space. The four-dimensional parameter space is described by three Euler angles representing stress orientations and one stress ratio $R = (\sigma_2 - \sigma_3)/(\sigma_1 - \sigma_3)$, where σ_1, σ_2 and σ_3 are the principal stresses magnitudes, so that $\sigma_1 \geq \sigma_2 \geq \sigma_3$ and $0 \leq R \leq 1$. The computational grid of the four-dimensional parameter space was calculated following the methodology described in Yamaji [2003] and using the Rakhmanov et al. [1994] algorithm. 300 directions of σ_3 with nearly equal intervals, 18 directions of σ_1 for each σ_3 with an interval of 10°, and 11 variations of stress ratio R with an incrent of 0.1 for each combination of σ_1 and σ_3 generate a mesh of $300 \times 18 \times 11 = 59400$ grid points. The angular distance between the directions of σ_3 is 8.3±1° [Yamaji, 2003].

The objective function F consists in maximizing the fit of the assumed stresses from the grid to the observed data $F = f(d^{(1)}) + \cdots + f(d^{(N)})$, where $d^{(i)}$ is an angular misfit between the predicted and observed slip directions on i fracture, $f(d^{(1)})$ is a decreasing function of $d^{(1)}$, and N the number of analyzed fractures [Yamaji, 2003]. The predicted slip direction is calculated using every reduced stress tensor at a grid point in the computational grid and the Wallace-Bott hypothesis Wallace [1951], Bott [1959], i.e. the slip direction on a fault plane is consistent with the direction of the resolved shear stress on the plane. The observed slip is the slip measured during the injection and projected on the previously selected fractures (Table 6.1). The angular misfit d varies from 0° to 180°. The function $f(d^{(1)})$ can be different [Yamaji, 2003]. We use the one recommended by Angelier [1979] which depends on both the direction and sense of each fault motion and suppresses the influence of outliers:

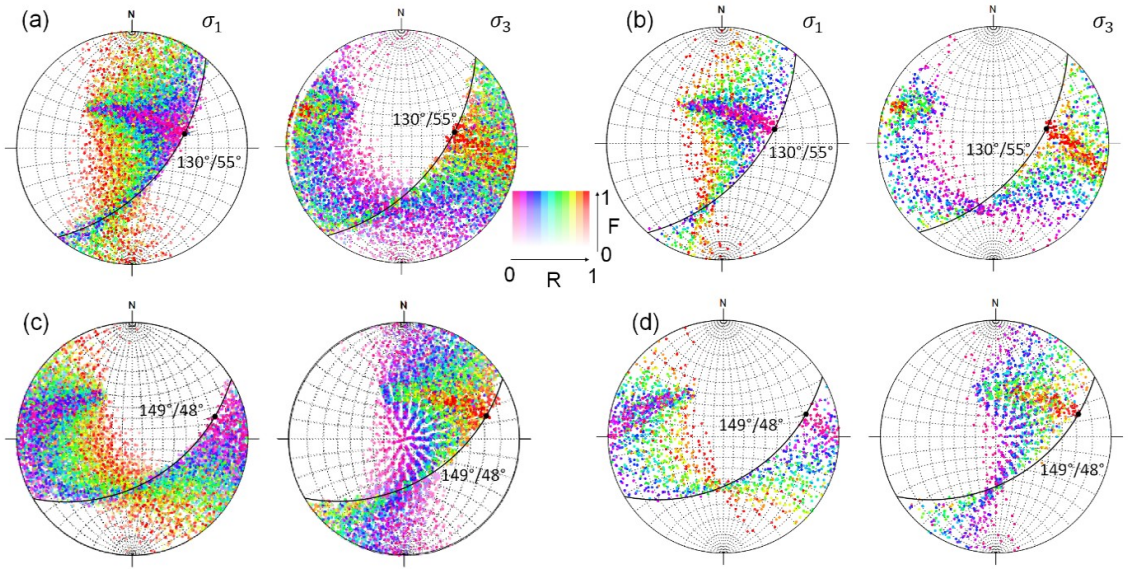

Figure 6.2: (a, b) Graphical representation of the object function F for the fractures 130°/55° and 149°/48°. Stress ratio (R) is represented by color, and the fitness of the function (F) by saturation. The direction of the stress axes is indicated by the position of the symbols. The directions of σ_1 and $\sigma_3$are indicated by grid points on lower-hemisphere equal-area projection. All reduced stress combinations and their objective function calculated for the fracture 130°/55° and 149°/48°, (c,d) Reduced stress tensor combinations with the misfit angle between measured and predicted slip of 5° or less.

$$f(x) = \begin{cases} 1 - \tan d & (0 \leq d \leq 45°) \\ 0 & (45° < \mathrm{d}) \end{cases}$$

The evaluation of the sum of the objective function F is relative. The values of F are compared to the minimum F found in the evaluation. The visualization of the results is given using the hue and saturation of color for R and F, respectively. Because the computation grid includes many identical stress orientations with varying stress ratio and for visualization purposes solely, a random noise with a range of 6° is added to the stress orientation to minimize the overlapping amongst the data points . Figure 6.2a,b illustrate the example of the grid with all possible stress combinations and their fit to the fracture slip projected to the fracture 130°/55° and 149°/48°. The graphic representation is given as a pair of stereograms showing the related directions of maximum (σ_1) and minimum (σ_3) principal stresses.

In this work, we calculated the objective function for every fracture separately to visualize the results. However, to compare all possible reduced stress tensors from different fractures we used the direct value of the misfit angle. To reduce the number of possible solutions, we kept only the reduced stress tensors with a maximum misfit angle between the predicted and observed slip vectors of 5° or less. Figure 6.2c,d show these reduced stress solutions applied on a fracture 130°/55° with normal faulting and 149°/48° with reverse faulting, respectively. The amount

Table 6.2: The decreasing of the optimal solutions with adding the step of analysis.

Potentially activated fractures		All reduced stress tensor	Reduced stress tensor, misfit <5°	+ Magnitudes	+ Slip tendency analysis
Dip Direction, °	Dip Angle, °				
149	48	59400	1621	6	-
130	55		1574	179	44
130	46		1603	81	3
131	65		1540	241	8
130	37		1579	-	-
123	63		1616	319	92

of stress tensors decreased from 59400 to 1574 for the fracture 130°/55°, and to 1621 for the fracture 149°/48° (Table 6.2, column 4).

6.5.2 Stress magnitudes and reduction of the possible stress solutions

The absolute principal stress magnitudes σ_1, σ_2,σ_3 are calculated by considering the optimal reduced stress tensors (Figure 6.2 c,d) , the estimations of the vertical stress σ_v and of the fracture normal stress σ_n. This is done by solving the system of equations:

$$\begin{cases} R = (\sigma_2 - \sigma_3)/(\sigma_1 - \sigma_3) \\ \sigma_n = l_1^2\sigma_1 + m_1^2\sigma_2 + n_1^2\sigma_3 \\ \sigma_v = l_2^2\sigma_1 + m_2^2\sigma_2 + n_2^2\sigma_3 \end{cases}$$

where l_1, m_1, n_1 and l_2, m_2, n_2 are the direction cosines of the normal and vertical component of the fracture with respect to the principal stress axes. The number of solutions is reduced by keeping the magnitudes within acceptable range on the principal stress magnitudes, i.e. for our example from Mont-Terri, $\sigma_3 \geq 2.0$ MPa and $\sigma_1 \leq 9.0$ MPa. The lower bound is imposed to avoid tensile effective stress conditions because the measured pore pressure in the Opalinus Clay of the Mont-Terri laboratory is varying about 2 MPa [Martin and Lanyon, 2003]. The upper bound is considered as not much larger than the maximum possible overburden weight (7.8 - 8.0 MPa).

Figure 6.3 a and b illustrate the solutions for the orientations and the magnitudes of the principal stresses for the fractures 130°/55° and 149°/48°. The number of possible solutions decreased from 1574 to 179 for the fracture 130°/55° and from 1621 to only 6 for the fracture 149°/48° (Table 6.2). Each stress tensor from the Figure 6.3 a and b was applied to each of the 8 potential reactivated fractures considered previously to calculate its normal (σ_n) and shear stress (τ). We then performed a slip tendency analysis T_s, where $T_s = \tau/\sigma_n$ [Morris et al., 1996]. The slip tendency analysis together with the frictional characteristics of the fractures

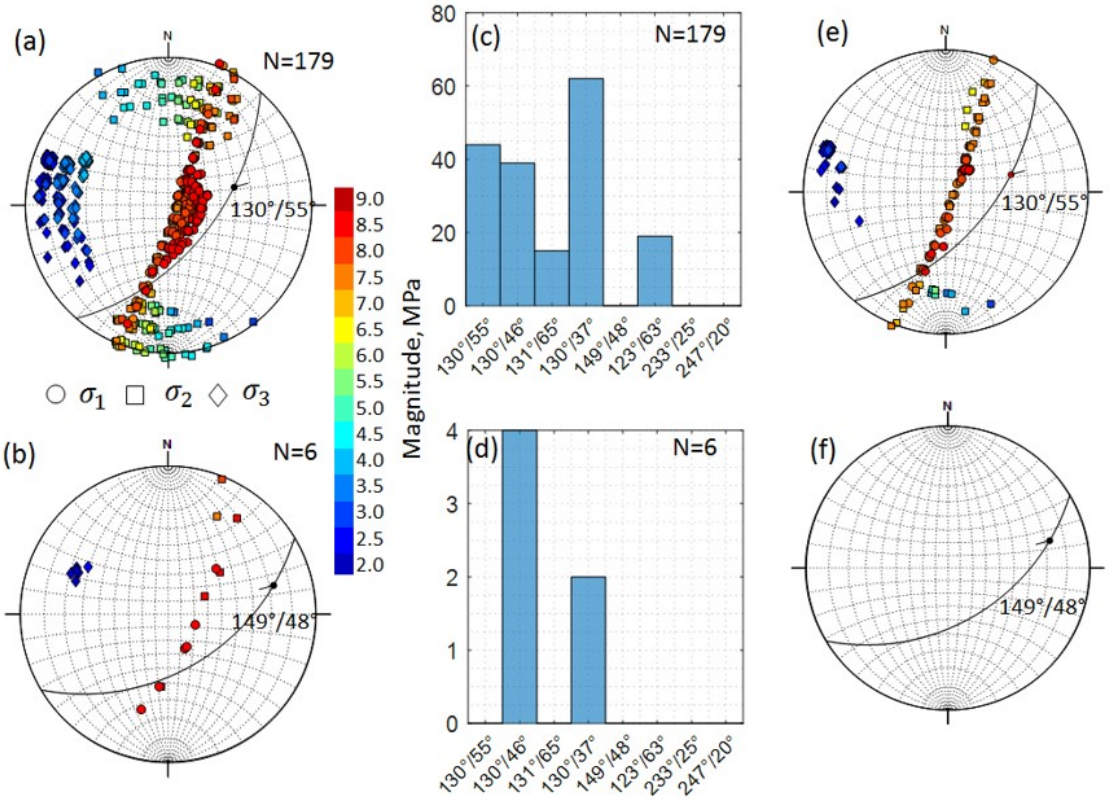

Figure 6.3: (a),(b) – orientation and magnitudes of the principal stresses and (c),(d) – histograms of distribution of magnitudes

determines a relative tendency of a fracture to slip under a given stress field. In this work, we assumed that the frictional characteristics of all the fractures were the same. However, we observed that the surfaces of the fractures may differ from each other in the field. The slip tendency analysis provided a rapid evaluation of the fractures that had the highest potential to slip within and near the displacement cage under the given stress state. This reduced the number of the solutions. The stress tensors defined for an individual fracture was validated only if this fracture had the highest slip tendency among the other fractures. Figure 6.4c shows that only 44 applied stress tensors out of 176 allow the fracture 130°/55° to slip first. None of the 6 applied stress tensors would enable the fracture orientated 149°/48° to slip first (Figure 6.4d). The slip tendency analysis also significantly reduced the number of possible stress solutions (Table 6.2).

In addition, figure 6.3b shows that the minimum stress is sub-horizonal and contradicts the inverse regime of faulting, indicated by the slip projection. This phenomenon is discussed later in Results.

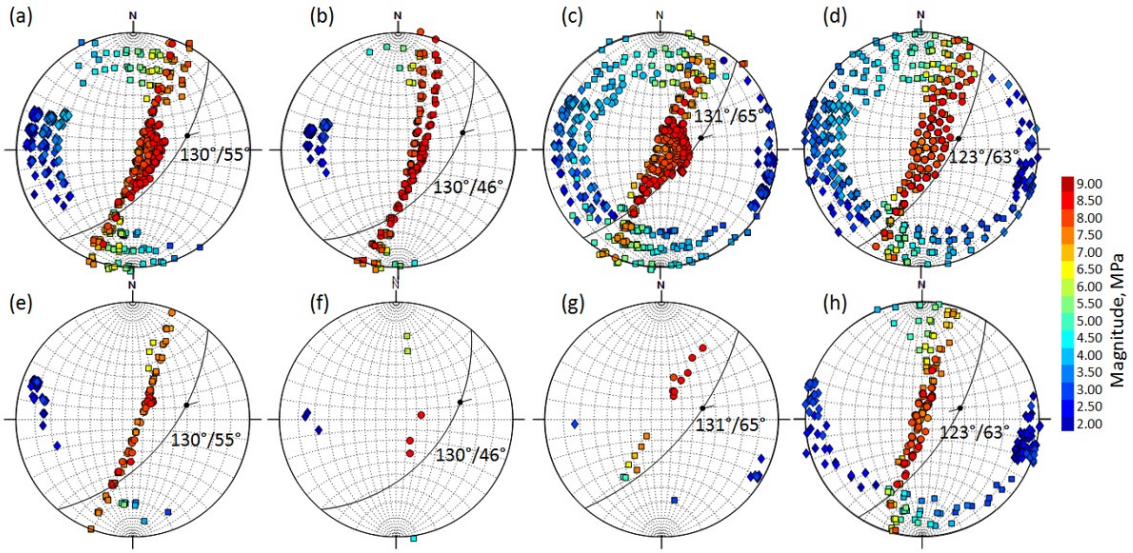

Figure 6.4: Orientation and magnitudes of the stress tensors after processing

6.5.3 Constructing confidence intervals for a mean of in-situ stresses

Finally, the results are given by simultaneously constructing the mean stress tensor and its confident intervals (CI) on each individual fracture. The mean stress tensor is estimated as an Euclidian mean of the tensor [Gao and Harrison, 2019, 2017, 2018a,b]. The eigenvalues of the tensor and the eigenvalues of the Euclidian mean are the magnitudes and directions of the principal stresses of the mean stress tensor. Such an estimation avoids an incorrect preprocessing of magnitudes and orientations separately. In this paper, we simplified the methodology to estimate the CI proposed by Feng et al. [2018] using a multivariate distribution model and Monte Carlo sampling.

The multivariate confidence regions for the Euclidian mean of the in-situ stress must be constructed in a tensorial manner in order to simultaneously analyze the principal stress magnitude and orientation [Feng et al., 2018, Gao and Harrison, 2019, 2017, 2018a,b]. Firstly, we calculate a covariance matrix (S) of the n number of the measured stress tensors. The eigenvalues (λ_i) and eigenvectors ($_i$) and of the matrix are used to determine the axes of the 6-dimensional confidence ellipsoid. Secondly, we defined lengths of the ellipsoid axis r:

$$r = \pm\sqrt{\lambda_i}\sqrt{\frac{p(n-1)}{n(n-p)}F_{p(n-p)}(a)e_i}$$

where $F_{p(n-p)}(a)$ is the value of the F-distribution with n and n-p degrees of freedom at a significance level, p is the dimension of stress tensor. In this paper, p =6 and a =0.05, which allows the 95% confidence interval of the mean of the stress tensor.

Thirdly, we sample a random value inside the rectangle (i.e. in 2 dimensions) of the confidence intervals, defined by r. Then, if this sample is within the ellipse, we transfer it to the principal stress coordinate system by multiplying it to the eigenvectors. The eigenvalues and eigenvectors of a new matrix which consists in samples from the ellipsoid, are the magnitudes and orientations of the principal stresses, which define the confidence intervals for the Euclidian mean of the stress tensor.

6.6 Results

In this section we show the summary of the results obtained by applying the protocol to all of the fractures and we compare the resulting stress tensor among each other.

6.6.1 Mont Terri test site

The fit of the objective function F at the computational grid points was calculated for single fractures. The shape of the objective function F through its graphical representation for fractures with normal faulting (130°/55°, 130°/46°, 131°/55°, 130°/37°) and with reverse faulting (149°/48°, 123°/63°) are similar to the Figure 6.2a,c and Figure 6.2b,d, respectively. The figures showed that the function has multiple peaks in the four-dimensional parameter space. The comparison between graphical representations of all possible reduced stress tensor and the one inducing a misfit less than 5° (Figure 6.2) show that if the number of solution reduce drastically, the orientation spread remains similar. The heterogeneity is expected because it is known that the inversion using just one fracture is poorly defined [Angelier, 1990]. While all these solutions are unclear, it is still possible to note, that the σ_1 for normal faults tends to be sub-vertical and range along South-South-West to North-North-East, and σ_3 tends to be mostly horizontal and mostly concentrated on imprecise West-South-West to West-North-West orientations. The principal stress orientations for reverse faulting tends to be the opposite . The low value of the stress ratio indicates axial compression ($\sigma_3 = \sigma_2 < \sigma_1$), while a high value of stress ratio indicates axial tension ($\sigma_3 < \sigma_2 = \sigma_1$). For the normal faulting (Figure 6.2a,b) the violet spots corresponding to low values of the stress ratio R are the most concentrated. The maximum principal stress scatters with increasing stress ratio, i.e. with the transformation from axial compression to axial tension. The situation is opposite for the minimum principal stress: low stress ratios are unclear, and high stress rations are more concentrated.

The solutions for normal and reverse faults with the maximum misfit angle of 5°

do significantly decrease the amount of solutions by 97%, however, the remaining orientations are scattered. For the normal faults, the highest concentration of the maximum principal stress trends from South-South-West to North-North-East with a predominant sub-vertical orientation. The minimum horizontal stress trends East-West and on average displays dip angles below 45°. The inverse faults have similar orientations but different motions, which results in principal stress orientations and stress ratios opposite to the normal fault ones.

The system of equations to find the magnitudes by considering the normal and vertical components reduced the amount of solutions by up to 80% (Table 6.2, Figure 6.4). Figure 6.4 illustrates the stress solutions for the fractures which are given in Table 6.2, column 6), i.e. have solutions at the end of protocol.

Figures 6.3b and 6.4d show that to fit the vertical and normal stress measured during the fluid injection to the stress ellipsoid defined by the reduced stress tensor, the maximum stress needs to be sub-vertical and the minimum stress needs to be sub-horizontal. However, these magnitudes and orientations of the principal stresses result in normal faulting. This contradiction arises from the system of equations used to estimate the magnitudes, where only the reduced stress tensor and vertical and normal stresses are considered. Therefore, it is possible to obtain the measured vertical and normal stress on the fracture for normal faulting regime. This observation excludes the reverse faults from the final results.

This leads us to the consideration that only the three fractures 130°/55°, 130°/46° and 131°/65° could have been potentially activated. Figure 6.5 shows the mean stress tensor and 95% of the CIs of the population principal mean stress magnitudes (b) and orientations (c). There more data is available, the better the mean estimation would be. Thus, the estimation of the mean stresses for the fracture 130°/55° with n=44 shows better confidence than for the fracture 131°/65° with n=8 (Table 6.2). For the fracture 130°/46° the confidence intervals cannot be defined because of the lack of the data (n=3) in the 6 dimensional space (p=6 for the stress tensor). Therefore, the fracture 130°/55° demonstrates the best CI in mean, and well defined maximum and minimum principal stresses respectively of 8.1±0.1 and 2.9±0.1 MPa. The CI for the intermediate principal stress is 7.2±0.7 MPa. Even though the mean of the stress tensor is well-defined, the range of the obtained magnitudes and orientation show a wide distribution given in boxplots (Figure 6.5a) and stereoplots (Figure 6.4e, f, g), respectively.

The CI for the fracture 131°/65° show that the mean value is not well-defined in the interval. As it was mentioned before, this is related to the small amount of slip data.

The mean of the principal stresses for different potentially activated fractures

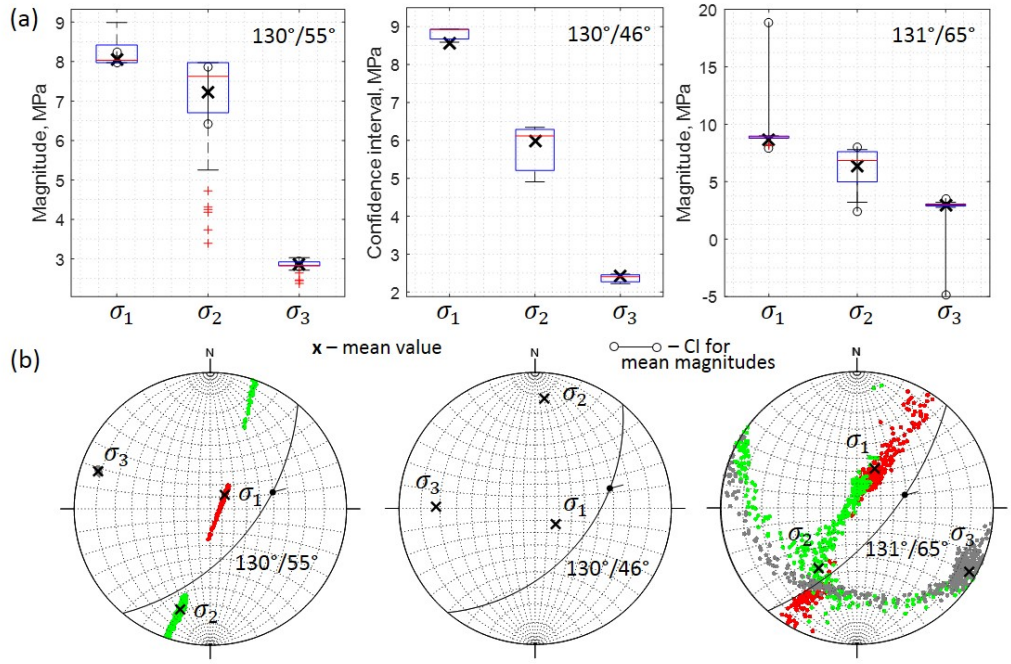

Figure 6.5: Results of the stress inversion for the activated fracture in shales: (a) CI for the mean stress magnitudes, boxplots represent distribution of the all magnitudes from Figure 6.4, and (b) CI for the mean stress orientations

are consistent with each other. The maximum principal stress is sub-vertical, the intermediate principal stress trends SW-NE, the minimum principal stress – NW-SE.

6.7 Application to stress measurements in carbonates at the LSBB test site

We applied our approach to another case study in a different rock type (carbonates). In chapter 5 we discussed the context of this cases study and the hydro-mechanical data that we briefly resume here. The injected interval (test 9 in Duboeuf et al. [2017] and Duboeuf [2018]) is located between 12.65 to 15.13 m, and the SIMFIP anchors are located at 13.76 and 14.24 m. The interval consists of two different facies [Duboeuf et al., 2017, Duboeuf, 2018], which are separated by a bedding plane (235°/36°) and intersected by a sub-vertical fracture (100°/70°). The protocol for the estimation of the magnitudes and orientation described above for shales, was applied to the same input data measured in carbonates. The slip used for the estimation occurred at 2.4 MPa and is oriented 105°/69°. The selected slip vector is preceded by slip measurements with similar orientation (Chapter 4, Chapter 5). To avoid slip perturbation due to fluid injection, the orientation of the last slip in the sequence is considered to be the most representative (Chapter 4, Chapter 5).

The slip 105°/69° occurred before the seismic events, meaning that the stress is likely not perturbed (Chapter 5). In Chapter 4, Chapter 5 we showed that the slip vector 105°/69° is related to the activation of the vertical fracture. Therefore, this fracture will be used for the stress inversion. Other fractures in the interval are not well-defined, therefore, could not be used for the slip tendency analysis. Moreover, these other fractures and the bedding plane have low dip angles which make them unlikely to be activated prior to the sub-vertical fracture, considering that the maximum principal stress is vertical as estimated by Guglielmi et al. [2015a].

The normal stress to the sub-vertical fracture is estimated to be 3.2 MPa (Chapter 5). We could not use the instantaneous shut-in pressure to define this normal stress because no shut-in was performed at the end of the test. Alternatively, the value was estimated by considering the onset of the flowrate increase related to the opening of the sub-vertical fracture.

The vertical stress estimate, required for the protocol, is also difficult to quantify because of high heterogeneity of the limestone series in LSBB which is karstified and displays strong porosity variations [Cochard, 2018, Duboeuf, 2018]. Moreover, the topography of the LSBB location is mountainous, which might bring an additional overestimation of the vertical stress. The average density measured from wellbore density logging in the injection borehole is 2.5 g/cm^3 [Cochard, 2018] which is within expectations for intact carbonate rock. Taking this value and an overburden of 294 m would lead to a vertical stress estimate of 7.2 MPa. Wellbore section density log present density values down to 2.2 g/cm^3. At the rock mass scale and considering topography effects, one can assume that the effective density value would be even lower. We considered an average rock mass scale density of 2 g/cm^3, which would results for an overburden of 294 m in an estimated vertical stress of 5.8 MPa. This estimate is also consistent with the maximum vertical stress magnitude estimated by Guglielmi et al. [2015a].

The orientations of the maximum (σ_1) and minimum (σ_3) principal stresses with a misfit angle between the observed and the calculated slip less than 5° is given in Figure 6.6a. As in shales, the stress orientations are very heterogeneous. The estimated magnitudes of the stresses considering vertical and normal stress constraints on the re-activated fracture are given in Figure 6.6b. To estimate an upper and lower bounds for the maximum (σ_1) and minimum (σ_3) principal stresses, we determined a limiting ratio of principal stress magnitudes by [Jaeger et al., 2009]:

$$\frac{\sigma_1 - P_p}{\sigma_3 - P_p} \leq [\sqrt{(\mu^2 + 1)} + \mu]^2,$$

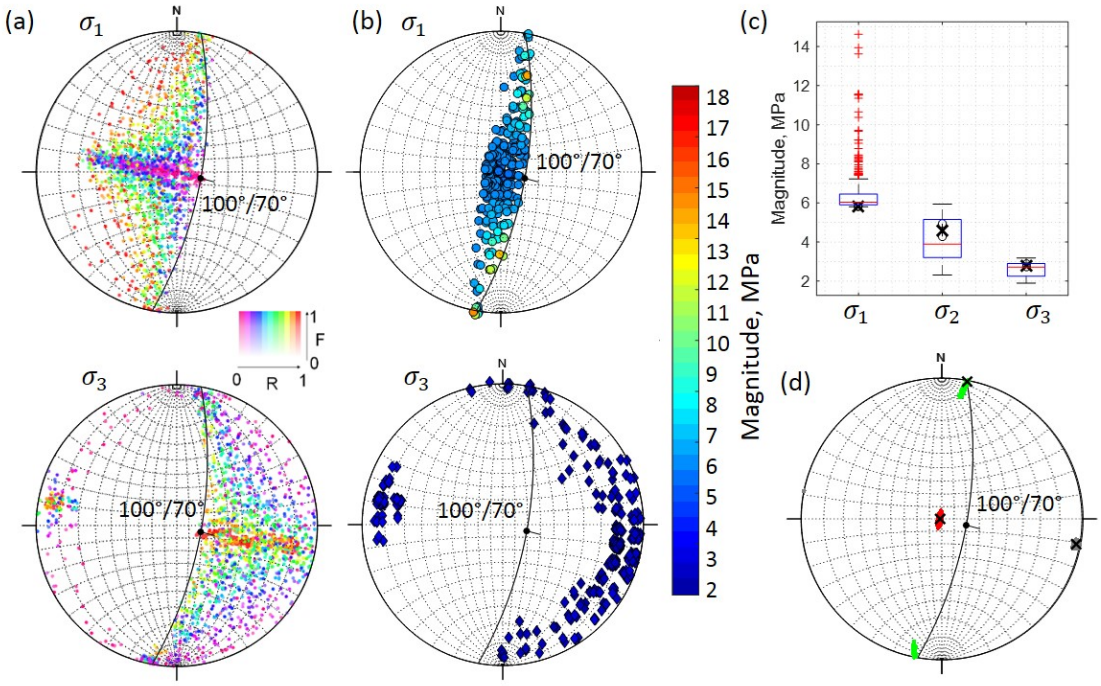

Figure 6.6: Results of the stress inversion for the activated fracture in carbonates: (a) Reduced stress tensor combinations with the misfit angle between measured and predicted slip of 5° or less for the fracture 100°/70°, (b) Orientation and magnitudes of the stress tensors after processing, (c) CI for the mean stress magnitudes, boxplots represent distribution of the all magnitudes from (b), and (d) CI for the mean stress orientations

Table 6.3: Results of the stress inversion for the activated fracture in carbonates

Potentially activated fractures		Mean values:	σ_1		σ_2			σ_3		
Dip Direction [°]	Dip Angle [°]	σ_1 [MPa]	Trend [°]	Plunge [°]	σ_1 [MPa]	Trend [°]	Plunge [°]	σ_1 [MPa]	Trend [°]	Plunge [°]
100	70	5.80	260	89	4.60	11	1	2.80	101	1
Regional stress by Guglielmi et al. [2015a]		6 ± 0.4	210	70	5 ± 0.5	320	7	3 ± 1	52	18

that for μ =0.6 and $P_p = 0$ in unsaturated zone of the test location,

$$\frac{\sigma_1}{\sigma_3} = 3.1$$

. Considering the value of 5.8 MPa as one of the principal vertical stress, we can define that the upper and lower bounds of the stresses are 18 MPa and 1.9 MPa, respectively. The mean stress tensor is given in Table 6.3. The CI are given in Figure 6.6c and show that the mean magnitudes and the orientations are well-defined, because the final number of optimal solutions is 347.

6.8 Discussion

Our stress inversion protocol allowed us to determine the full stress tensor from a single test. It is based on the assumption that reactivation occurs on a single fracture. Thus if we were just using the measured slip direction, the uncertainty on possible stress orientation would cover an entire quadrant [Angelier and Mechler, 1977, Yamaji, 2003].

While traditional stress inversion methods combine activation from multiple fracture with different orientations to reduce the possible stress orientation [Angelier, 1990], the nature of our test implies that we can use only the first fracture reactivation because subsequent slip could be driven by already perturbed stresses and thus not representative of the original in-situ stress conditions. To limit the uncertainty on stress orientation, we add some information on the fracture normal stress that we get from the flow/pressure response during our injections. This allows a reasonable stress orientation and magnitudes constraint. It is reflected in the confidence interval on our mean estimate that we derived in our analyses. These confidence intervals were estimated using a new method which is similar to the estimation of the CI by Feng et al. [2018], but makes the calculation faster.

Our method can thus derive reasonably precise stress estimates, i.e. with a solid constraint variability in the estimate. To evaluate if the method is accurate, i.e. truly reflects the in-situ stresses, our results are compared with other stress state estimates in the studied sites. The estimated means of the stress inversion results are compared with previous stress tensors obtained in Mont Terri laboratory by Martin and Lanyon [2003] and in the LSBB by Guglielmi et al. [2015a] and Duboeuf [2018] and given in Figure 6.7.

For the Mont Terri test site, Figure 6.7 (left) and 6.4 compare the stress orientations from our analysis to regional stresses, Borehole Slotter method, and by ROSAS1 [Martin and Lanyon, 2003].

The orientation of the maximum principal stress defined from the protocol is consistent with the regional stress orientation defined by Martin and Lanyon [2003]. Table 6.4 shows that the mean magnitude of the maximum principal stress is 2 MPa higher than the magnitude defined by Martin and Lanyon [2003]. The high value of the maximum principal stress results from the high value of the vertical stress and in the sub-vertical orientation.

The orientations of the principal horizontal stresses determined from our analysis are opposite to the orientations of the regional stress defined by Martin and Lanyon [2003]. The switch is related to the unfavorable orientation of the activated fractures relative to the principal stress axes. The error might have occurred in the very beginning when defining the stress orientations with the minimum misfit

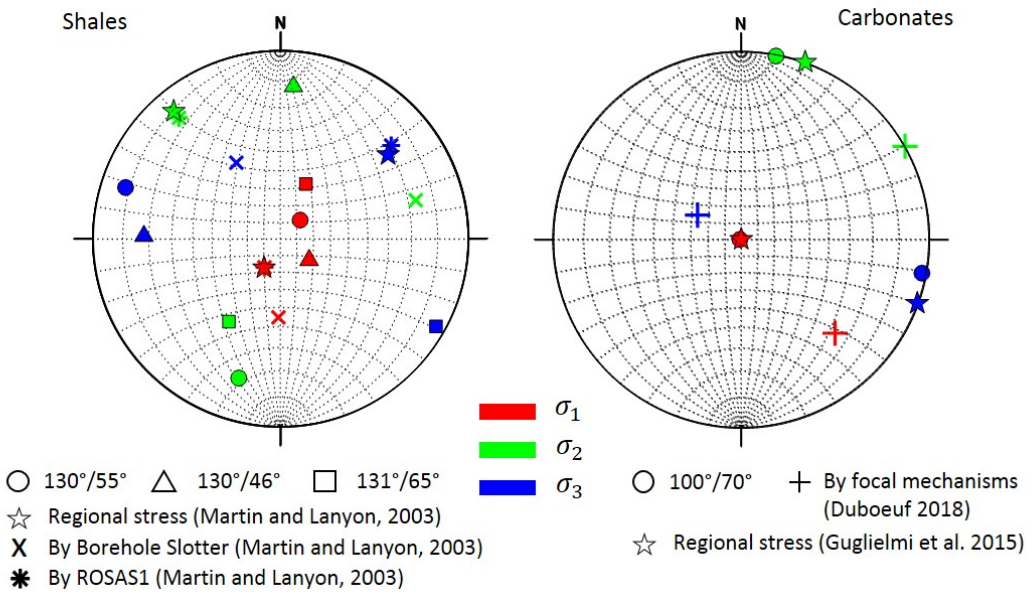

Figure 6.7: Comparison between the stress inversions in Mont Terri (left) and LSBB (right) for the activated fractures in shales and carbonates, respectively

Table 6.4: Results of means of the stress tensor from potentially activated fractures

Potentially activated fractures		Mean values:	σ_1		σ_2			σ_3		
Dip Direction [°]	Dip Angle [°]	σ_1 [MPa]	Trend [°]	Plunge [°]	σ_1 [MPa]	Trend [°]	Plunge [°]	σ_1 [MPa]	Trend [°]	Plunge [°]
130	55	8.06	47	73	7.21	197	15	2.87	289	8
130	46	8.57	127	69	5.98	5	12	2.42	271	18
131	65	8.68	25	55	6.35	212	35	2.99	120	3
Regional stress by Martin and Lanyon [2003]		6-7	210	70	4-5	320	7	0.6-2	052	18
ROSAS1		6.5	210	70	4	320	10	0.6	050	15
Borehole Slotter		3.1	181	45	1.6	0.74	16	0.15	330	40

with the measured angle. Due to the orientation of the regional minimum principal stress being parallel to the strike of the activated fracture, and considering the normal sense of the measured slip, the compressional quadrant from the moment tensor would be parallel to the slip. This leads to assigning this quadrant to be the orientation of the minimum principal stress, and not as the intermediate as it was found by Martin and Lanyon [2003]. Such horizontal swapped orientation was observed by Martin and Lanyon [2003] by using the Borehole Slotter from three orthogonal boreholes drilled in one of the galleries of the Mont Terri lab. The orientations and magnitudes measured by the Borehole Slotter are given in Figure 6.6. Table 6.4 shows that magnitudes are lower than the ones measured by the Undercore technique (ROSAS1) because of the lower Young's Modulus [Martin and Lanyon, 2003]. The ROSAS1 in-situ stress tensor together with the numerical modelling better fits with the orientations of the breakouts and tangential stress magnitudes to cause break-

outs compared with the Slotter stress tensor. Moreover, Kastrup [2002] found that the maximum and minimum horizontal stresses are oriented Northwest-Southeast and Northwest-Southeast in this region of Switzerland, which is consistent with the orientations from the ROSAS1. Therefore, the NorthWest-SouthEast direction of the maximum principal stress is considered the most likely in Mont Terri. However, considering the unfavorable orientation of the minimum stress to the activated fracture, we would suggest that the estimation of the orientations made by the protocol are reasonable.

The estimation of the magnitudes of the regional minimum principal stress by Martin and Lanyon [2003] has a high uncertainty because the magnitude is very low. Using the slip vector occurred 3 m below the tested interval, Guglielmi et al. [2019] adapted the stress tensor by Martin and Lanyon [2003] to match the orientation of the measured slip: σ_1 = 6 MPa oriented N210 - 65°, σ_2 = 4.8 MPa oriented N300 - 0° and σ_3 = 3.0 MPa oriented N30 - 25°. Here, the magnitude of the minimum principal stress is closer to the values obtained by the protocol. The magnitude of the intermediate stress are higher than the ones obtained by Martin and Lanyon [2003] and Guglielmi et al. [2019], which might be related to the higher values of the magnitude of the maximum principal stress.

For a rock mass whose strength is governed by a Coulomb friction criteria, the friction coefficient can be estimated by using the pressure at which we measured the slip occurrence. The Mohr-Coulomb failure criteria postulates $\tau = (\sigma_n - P_c)\tan\phi + C$, where C is cohesion, ϕ is an angle of internal friction, $\tau-$ shear stress, σ_n- normal stress, P_c- injection pressure at failure. For the slipping faults, we assume cohesion to be 0. Knowing the stress orientations and magnitudes we can estimate a shear and normal stress on a potentially activated fracture. The pressure at which the slip was observed is 3.9 MPa. Applying the Mohr-Coulomb failure criteria, we estimated the friction angles for the mean stresses. For all of the fractures, the friction angle is 78°, which is unrealistic and much higher that the measured value of the friction angle ϕ =24° [Bossart, 2011]. High friction angle may indicate different phenomena and more complex failure mechanisms than Mohr-Coulomb failure. Thirdly, we do not consider the injected pressure gradient occurring in the fracture during injection (Chapter 4), which can lead to the overestimation of normal and shear stresses on the fracture.

6.8.1 LSBB test site

For the LSSB test site, Figure 6.7 (right) compares the stress orientations from our analysis to focal mechanisms [Duboeuf, 2018] and regional stresses [Guglielmi et al., 2015a]. The magnitudes and orientation of the principal stress defined from

the protocol are consistent with the orientations defined by Guglielmi et al. [2015a] (Figure 6.7 right and 6.6c). The consistency of the stress from the inversion and the stress obtained by the HTPF method confirms that the slip vectors result from a non-perturbed stress state and validates the accuracy of our approach.

Figure 6.6 shows that the stress tensor from the focal mechanism [Duboeuf, 2018] derived from the same test (test 9) is rotated relatively to the static regional stress computed by Guglielmi et al. [2015a]. According to Duboeuf [2018], the stress found by the focal mechanisms likely represents perturbed stress state due to precursory aseismic slip and seismic events. This is similar to rotation of the stress directions driven by fault structures in the damage zone, affected by fluid injections [Faulkner et al., 2006]. Duboeuf [2018] showed that the perturbation cannot result from the excavation induced stresses because the test was performed more than 3 diameters away from the excavation and because the results from a test located closer to the excavation already showed unperturbed conditions.

The rotation of stresses caused by the fluid injection is often observed [Valley and Evans, 2007, Martínez-Garzón et al., 2013, Jeanne et al., 2015]. Martínez-Garzón et al. [2013] showed that the principal stresses strongly correlate with the flowrate. The same result was observed by Jeanne et al. [2015] using a 3D thermohydromechanical numerical model. Altmann et al. [2014] found that the pore pressure changes affect the tectonic stress regime. These changes may lead to local rotation of the principal stresses and to the reactivation of non-favourably oriented fractures as suggested by the regional stress. We computed the resolved shear and normal stress on the activated fracture for the mean stress tensor estimate from which we can determine the required friction to enable slip at the injection pressure of 2.4 MPa when slip is actually observed. The computed friction angle is 52°, which is close to the laboratory measurements of 53° [Cappa et al., 2019].

6.9 Conclusions

In this study, we described a protocol to estimate the stress using a direct in-situ measurement of the 3D displacement on faults reactivated by fluid injections. The results of the stress inversion in shales and carbonates reasonably match the known regional stress tensors, however an inconsistency with horizontal stress orientations is observed in shales. The reverse orientations of the horizontal compounds in shales are related to non-favorable orientations of the existing fractures in the interval and/or to a strong mechanical anisotropy.

Application of the protocol requires an estimation of the normal stress on the reactivated fracture. The estimation accuracy of these values may affect the re-

Table 6.5: Comparison of different stress measurement methods

Method	HF	HTPF	SIMFIP
Settings	A segment of borehole is sealed using a straddle packer system		
Requirements	Minimum principal stress is perpendicular to the test hole	Minimum 6 measurements of normal stress	Defining a slip vector and normal stress on a reactivated fracture
Mechanism	New fracture opening	Open or shear a preexisting fracture	
Records	Flowrate & Pressure records		
	-	3D displacement	
	Structural mapping of the tested intervals		
	Pre- and Post-injection mapping	Pre-injection mapping	
Results	Minimum principal stress magnitude and orientation	Complete stress tensor	
Confidence	High for minimum principla stress, low for maximum principal stress	Depends on the number of tests	Depends on the test protocol and picking the input data
Main advantages	Easy maintance, fast	Estimation of complete stress tensor	Estimation of complete stress tensor with 1 test
	Deep depth		
Main disadvantages	Estimation of only minimum principal stress	Uncertainty due to different tested locations	Requires an additional knowledge of vertical stress, friction, etc.
	Works under a specific stress condition (see Requirements)	Economically unfavorable, time consuming	Requires activation in shear
	Repeated multiple times to gain confidence		

sults of the protocol. Moreover, it is important to give reasonable assumptions in considering or excluding the potentially activated fractures.

Finally, we compared the proposed protocol with traditional hydraulic stress measurement methods and summarized them in Table 6.5. The protocol for the stress estimation using the SIMFIP probe shows promising perspectives compared to current hydraulic tests.

6.10 Acknowledgements

This research is supported by the University of Neuchatel and the FS partners (swisstopo, ENSI, JAEA and LBNL).The experiment in carbonated was conduced within HYDROSEIS project (*http ://hydroseis.oca.eu*) under contract ANR-13-JS06-0004-01 and by Total SA (PI. through the HPMS-Ca project (Albion, PI. G. Massonat).

Chapter 7

Synthesis, Conclusions, Outlook

7.1 Synthesis

ESTIMATING magnitudes and orientations of in-situ stresses is important in designing of stable and safe underground engineered projects, such as nuclear waste, geothermal energy exploitation or CO_2 storage. Measuring stress in-situ remains challenging: integrated approaches combining multiple techniques is currently the best way forward. Proposing new techniques that can be integrated in a stress characterization approach for a site is thus important. In this project, we proposed to use a technique based on fault or fracture reactivation to estimate the in-situ stress. The technique is made possible by the availability of a new measuring tool (called SIMFIP) allowing precise measurement of displacement while injecting fluid in a fault or a fracture. The main contribution of the thesis is to develop and validate an approach allowing using this information to estimate in-situ stress from a single injection experiment.

Fluid injection tests with simultaneous 3D displacement monitoring was performed in two underground laboratories consisting of different rocks – shales in Mont Terri rock laboratory and carbonates in Low Noise underground rock laboratory (LSBB). In addition to displacement, flowrate and pressure records were constantly monitored in the injection chamber. This thesis focused on analysis of the coupled displacement-flowrate-pressure response during the injection at Mont Terri, with supplementary studies on the carbonates of the LSBB. The Opalinus clay at Mont Terri is a potential rock for nuclear waste storage in Switzerland. Mont Terri laboratory provides exceptional conditions to study geomechanical properties, not only of the intact rock, but also of the fault zones, which increase the risk of leakage.

The challenge of the approach is that the data collected by the SIMFIP are intrinsically complex. The complexity reflects partly the complexity of the rock mass structure surrounding the borehole but also the superposition of multiple processes.

In order to assess the rock mass complexity, we analyzed borehole images and cores. The compilation of fracture information is central to the understanding complex response observed during the tests. Borehole image logs show that the injection intervals, which are located above, between and below the main tectonic zone ("Main Fault") within the Mont Terri Opalinus clay, are highly fractured. There are different types of fractures intersecting the intervals, however, the most abundant one is parallel to the bedding of Opalinus clays – SE-dipping fractures. The structural mapping of the boreholes that intersected in the Main Fault displays that the intervals have common fault rock types. This analyses also allowed us to identify striation on the fracture capturing past fracture activation in shear. The typical fracture striation orientation indicated a paleostress thrust tectonic regime, which is consistent with the tectonic regime of Mont Terri anticline folding, but not consistent with the current regional stress state obtained by Martin and Lanyon (2003).

The multiple and superposing processes activated during injection are related to the stress redistribution around the borehole, to the fluid diffusion within the rock mass, to the elastic response of the rock and fractures and to the slip occurring possibly on one or more fractures. We studied this complex signal (Chapter 3 Sections 3.1-3.4) and focus on isolating signal elements that can be used for stress inversion. In the complex signal of our tests, we can isolate the main phases in the rock mass response to injection: in a first phase, there is a clear linear relationship between pressure and displacement and in a second phase, the linearity is lost and displacement occurs at constant pressure. We interpret the first phase as being an elastic response of the rock and fractures. We modeled this response (Chapter 3 Section 3.5.1) and observed that it is strongly influenced by the presence and geometry of fractures. The second phase results from the superposition of further rock mass deformation related to pressure diffusion and the onset of fracture slip.

For a given stress state, in order to trigger the onset of slip on fracture planes, the effective normal stress must be decreased by fluid injection to reach the Mohr-Coulomb failure criteria. The slip orientation contains valuable information on the in-situ stress. It is used in stress inversion techniques relying on the Wallace-Bott hypothesis, which postulates that slip on fractures is parallel to the resolved shear stress. The directions of the fracture striae traditionally used in kinematic analyses for paleostress inversion, can be considered to be analogues of the slip vectors measured by the SIMFIP probe under the in-situ stress conditions. However, the fluid injection perturbs the surrounding effective stresses in a heterogeneous way controlled by fluid diffusion. Is the slip measured in such conditions still valid for the background stress estimation? We checked the validity of the Wallace-Bott hypothesis during fluid injection and concluded that the slip orientation can rotate due to the pressure gradient on the fracture (Chapter 4). The slip direction becomes

consistent with the theoretical Wallace-Bott value when the injected pressure in the vicinity of the borehole becomes homogeneous, i.e. after a longer pressure injection.

During long-term injections, structural complexities (i.e., multiple fracture intersecting the borehole) impact on the coupled displacement-flowrate-pressure response during the injection, which can lead to the activation of several fractures. The impact of the structural complexity is mostly observed at the end of the reversible response of the rock mass, when displacement components stop being linear relatively to the pressure change. The beginning of irreversible response of the rock mass is characterized by a fracture activation, which affects the displacement response and is often accompanied by pressure drops and flowrate change. To simplify the interpretation of the coupled displacement-flowrate-pressure response after a fracture activation and to capture its slip vector, we developed a protocol that helps to distinguish slip vectors based on displacement rate (Chapter 5). At the beginning of the test the displacement rate is low. The protocol identifies a threshold where displacement rates are higher and are no longer reversible, and which can represent slip events. Using the SIMFIP probe the orientation of the slip events were compared with the known fractures in the interval, enabling us to determine potential activated fractures.

After identifying the slip events within the interval, our protocol determines which of them can be representative of the background stress. We assume that the first slip vectors that occur during the injection would represent the background stress (i.e., unperturbed stress state). We assume that the first slip vectors are guided by reduction of the effective normal stress on the fractures, which are dependent on the background stress. Moreover, we assume that the first slip represents the activation of one fracture. Later slips can result in activation of several fractures, where the Wallace-Bott hypothesis will not be valid anymore. The first slip we identify in both laboratories were quicker than the background deformation but not quick enough to result in seismic signal. Seismic signal recorded at the LSBB occur later during the test when aseismic deformation already accumulated and perturbed the in-situ stress. This observation raises concerns that stress inversions based on seismic data analyses are not representative of in-situ stress but to already perturbed stress. There is a clear advantage in measuring deformation in-situ and capturing early aseismic deformation so that the slip used for stress inversion is not yet perturbed by significant amount of rock mass deformation. Traditional stress inversion requires combining at least 4 measurements of the slip data on distinctly oriented fracture planes (Angelier, 1990). Since we want to base our inversion approach on a single test, we have only one measurement on one reactivated fracture, which is not enough to perform the inversion. We developed a protocol for stress estimation which can be applied for single intervals (Chapter 6). The protocol requires an estimation of the vertical and normal stress on reactivated fracture to

reduce the number of solutions and to compensate for the absence of other slip measurements. The estimation of the vertical and normal stress components on the reactivated fracture allows us to use these data for the stress inversion. The normal stress component is estimated by considering the shut-in pressure in the end of the injection test, and the vertical stress – by measuring the overburden weight. The results of the stress inversion are consistent with the regional stress states estimated in both laboratories.

We have shown that it is possible to obtain the complete tensor by executing only one injection test. The reliability of the results depends on the accuracy of the measurements of critical parameters for the stress estimation: fracture orientations (borehole image logs), and slip orientations together with normal and vertical stress components of the reactivated fracture (SIMFIP probe). We tested the approach in two different type of rock masses. The approach was effective even in the complex conditions of the Opalinus Clay at the Mont-Terri laboratory.

7.2 Conclusions

The work performed in this thesis lead to the following main outcomes and conclusions:

1. It is possible to extract slip orientation information out of the complex SIMFIP signal by applying a selective approach based on displacement rate threshold.

2. The slip orientation can be used to estimate the complete stress tensor from a single test by combining it with the normal stress obtained from pressure / flowrate analyses and the vertical stress component estimated by overburden weight.

3. The slip extraction and stress inversion technique has been tested and validated in two different underground laboratories with different lithological conditions and stress regime.

4. Such inversion relies on a detailed mapping of the structural conditions encountered in the test intervals.

7.3 Outlook

In the future, the protocols proposed in this thesis have to be applied to more sites in order to further validate the approach. The protocol has the advantage to allow deriving the complete stress tensor from a single injection experiment. This

enables the possibility to derive complete stress tensor profiles and to better assess the stress heterogeneities within the earth crust. This will also allow assessing the repeatability and reliability of the method.

The protocol will also need to be improved in order to find the best injection strategy to estimate stresses. The tests performed in Mont-Terri and LSBB had for primary objective to study fault reactivation but not to estimate stress. A flowrate-controlled test with clean shut-in would likely be best for the stress estimation, allowing a better estimation of the slip direction and the normal stress to the activated fracture.

Test interval selection would be also important and using interval with less fractures should prevent ambiguities in identifying the activated fracture. This will also prevent multiple fractures interaction complexing the SIMFIP signal. In case this cannot be achieved, one potential path forward that we did not pursue in this thesis is to develop in the case of very fractured test intervals numerical simulation including discrete fracture network capturing the actual conditions in the test interval and use inverse modeling techniques to estimate the in-situ stresses.

Appendices

Appendix A

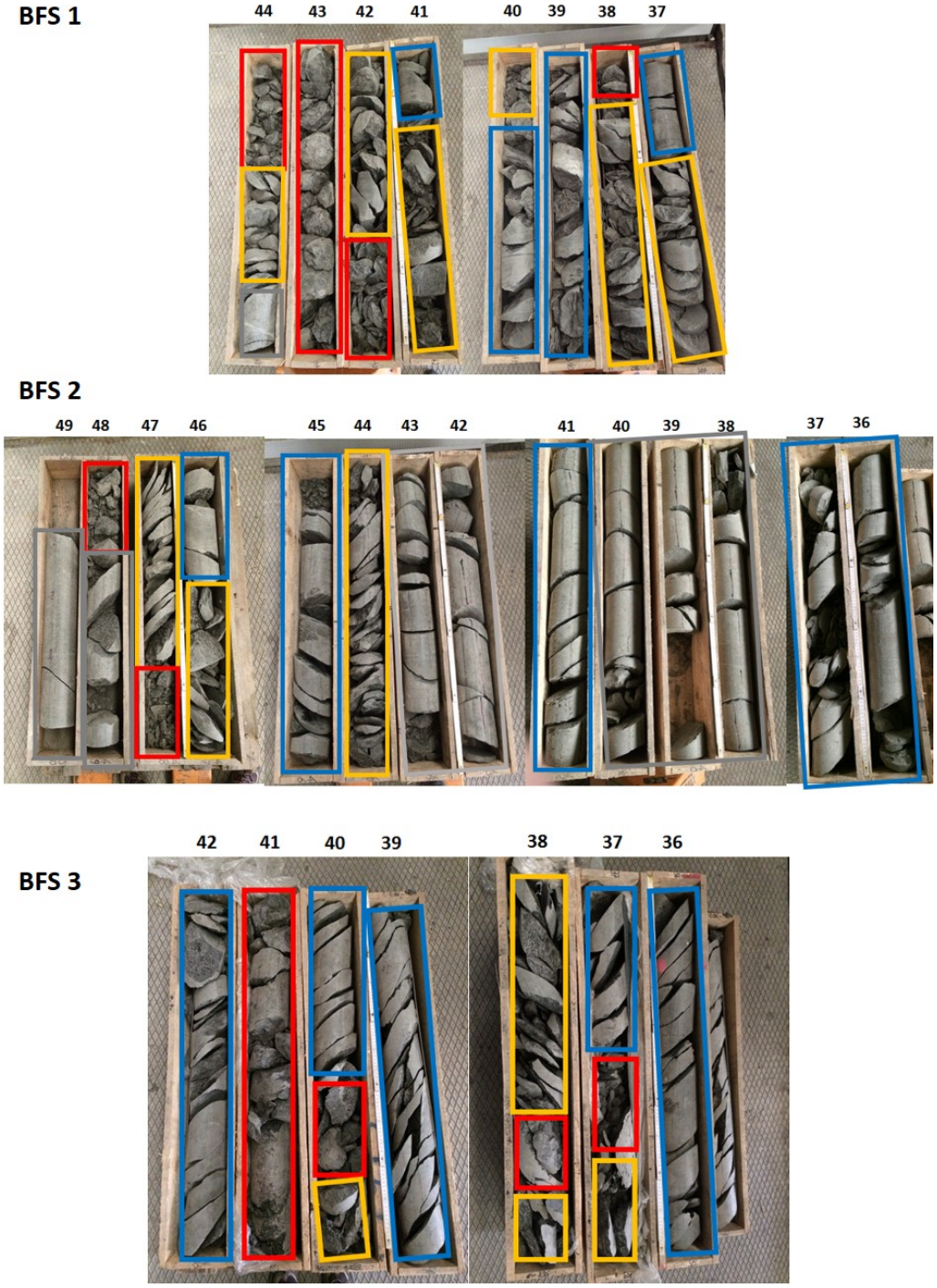

Figure A.1: Visual classification of the boreholes. Red – rock type I, orange – rock type II, blue – rock type III and grey – rock type IV.

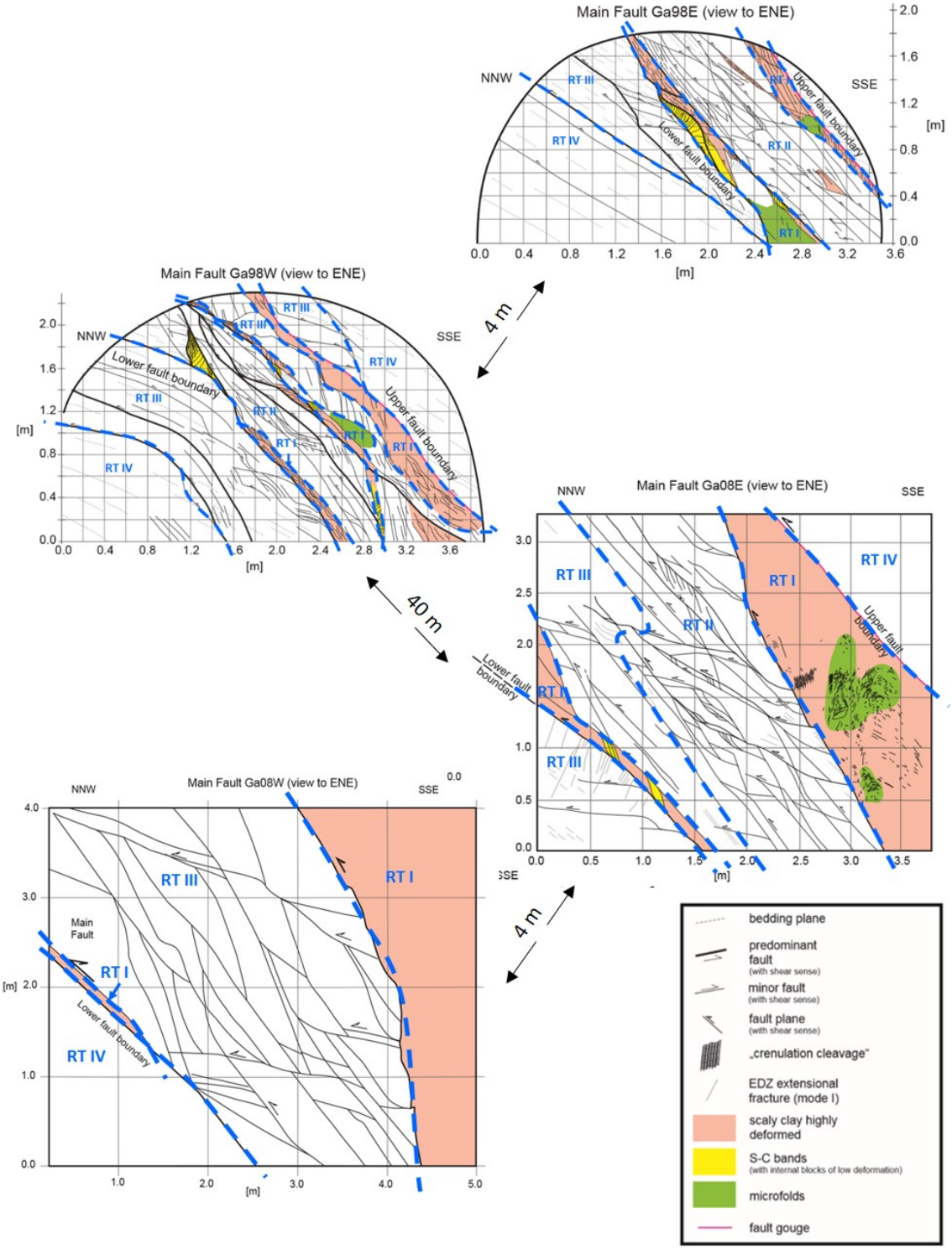

Figure A.2: Outcrops with rock types (after Jaeggi et al. [2017])

Appendix B

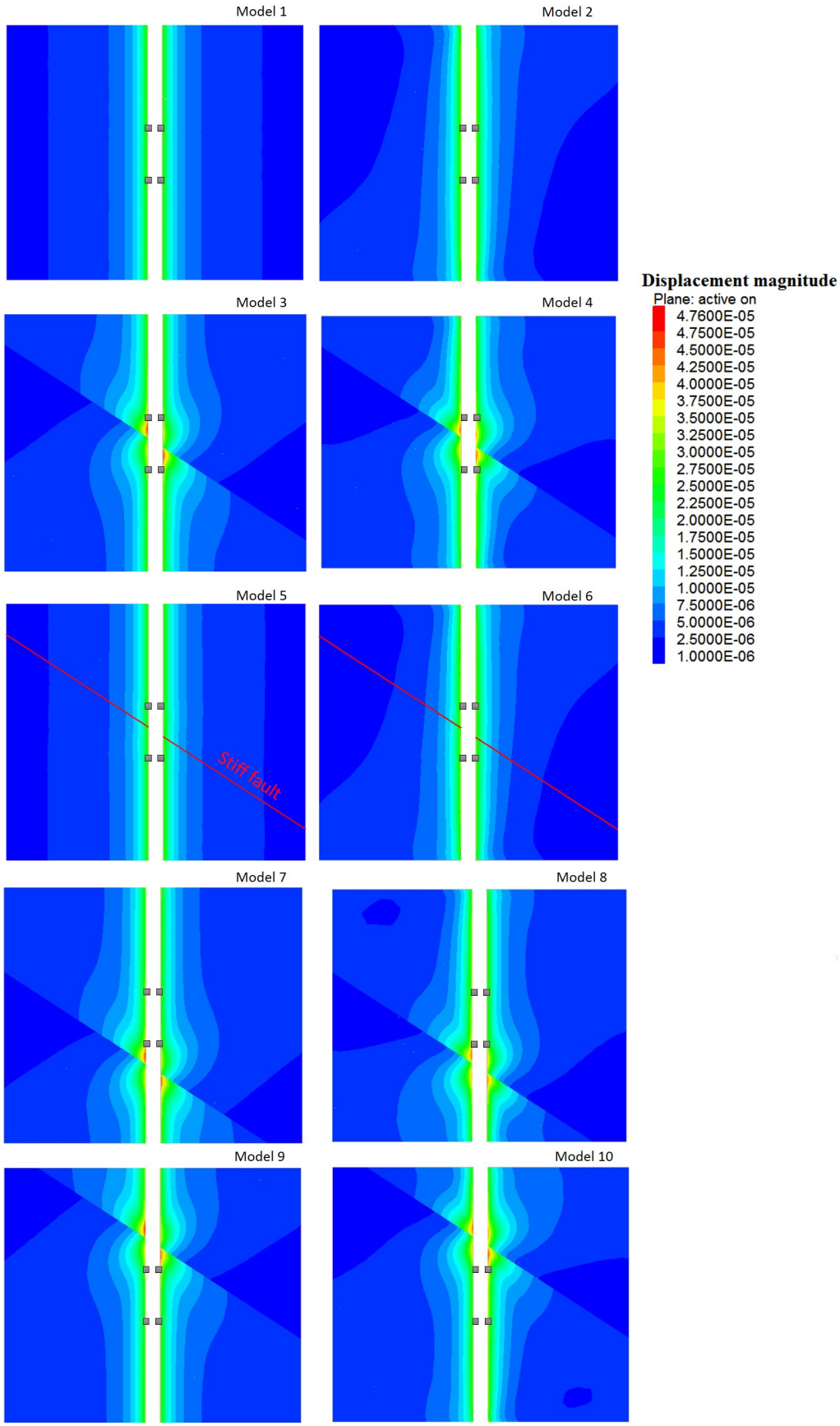

Figure B.1: Results of the numerical modelling. Grey cubes are the anchors.

Bibliography

R. W. Allmendinger, N. Cardozo, and D. M. Fisher. *Structural geology algorithms: Vectors and tensors*. Cambridge University Press, 2011. ISBN 1139505009.

J. Altmann, B. Müller, T. Müller, O. Heidbach, M. Tingay, and A. Weißhardt. Pore pressure stress coupling in 3d and consequences for reservoir stress states and fault reactivation. *Geothermics*, 52:195–205, 2014.

E. Anderson. *The Dynamics of Faulting and Dyke Formation with Applications to Britain.* Oliver and Boyd, Edinburgh, 2nd edition, 1951.

J. Angelier. Sur l'analyse des deplacements dus au jeu d'une population de failles. Exemple en Crete (Grece). *Comptes Rendus de l'Academie des Sciences Paris D*, 280:1657–1660, 1975.

J. Angelier. Determination of the mean principal directions of stresses for a given fault population. *Tectonophysics*, 56(3-4):T17–T26, 1979.

J. Angelier. Inversion of field data in fault tectonics to obtain the regional stressâIII. A new rapid direct inversion method by analytical means. *Geophysical Journal International*, 103(2):363–376, 1990. ISSN 1365-246X.

J. Angelier. Inversion of earthquake focal mechanisms to obtain the seismotectonic stress iv—a new method free of choice among nodal planes. *Geophysical Journal International*, 150(3):588–609, 2002.

J. Angelier and P. Mechler. Sur une méthode graphique de recherche des contraintes principales également utilisable en tectonique et en séismologie: la méthode des dièdres droits. *Bulletin de la Société géologique de France*, 7(19):1309–1318, 1977.

J. Angelier, B. Colletta, and R. E. Anderson. Neogene paleostress changes in the Basin and Range: A case study at Hoover Dam, Nevada-Arizona. *Geological Society of America Bulletin*, 96(3):347–361, 1985. ISSN 1943-2674.

F. Arthaud. Méthode de détermination graphique des directions de raccourcissement, d'allongement et intermédiaire d'une population de failles. *Bulletin de la Société géologique de France*, 7(5):729–737, 1969. ISSN 1777-5817.

J.-P. Avouac. From geodetic imaging of seismic and aseismic fault slip to dynamic modeling of the seismic cycle. *Annual Review of Earth and Planetary Sciences*, 43:233–271, 2015.

E. Barrier and J. Angelier. Active collision in eastern taiwan: the coastal range. *Tectonophysics*, 125(1-3):39–72, 1986.

L. D. Barros, G. Daniel, Y. Guglielmi, D. Rivet, H. Caron, X. Payre, G. Bergery, P. Henry, R. Castilla, P. Dick, and E. Barbieri. Journal of Geophysical Research : Solid Earth of fl uid-induced fault reactivation. pages 1–17, 2016. doi: 10.1002/2015JB012633.Received.

C. A. Barton and M. D. Zoback. Stress perturbations associated with active faults penetrated by boreholes: Possible evidence for near-complete stress drop and a new technique for stress magnitude measurement. *Journal of Geophysical Research: Solid Earth*, 99(B5):9373–9390, 1994.

J. S. Bell and D. I. Gough. Northeast-southwest compressive stress in Alberta evidence from oil wells. *Earth and planetary science letters*, 45(2):475–482, 1979. ISSN 0012-821X.

F. Bergerat. Stress fields in the european platform at the time of africa-eurasia collision. *Tectonics*, 6(2):99–132, 1987.

P. Bird. Hydration-phase diagrams and friction of montmorillonite under laboratory and geologic conditions, with implications for shale compaction, slope stability, and strength of fault gouge. *Tectonophysics*, 107(3-4):235–260, 1984. ISSN 0040-1951.

H. R. Blaesi, T. J. Peters, and M. Mazurek. Der Opalinuston des Mont Terri (Kanton Jura). Lithologie, Mineralogie und physiko-chemische Gesteinsparameter. *Unpublished NAGRA internal report*, 1991.

T. Blenkinsop, R. Lisle, and D. Ferrill. Introduction to the special issue on new dynamics in palaeostress analysis. *Journal of Structural Geology*, 28(6):941–942, 2006.

H. F. Bock. Measuring in situ rock stress by borehole slotting. In *Rock Testing and Site Characterization*, pages 433–443. Elsevier, 1993.

P. Bossart. Overview of key experiments on repository characterization in the Mont Terri Rock Laboratory. *Geological Society, London, Special Publications*, 284(1): 35–40, 2007.

P. Bossart. Characteristics of the Opalinus Clay at Mont Terri. *Mont Terri Project, Wabern Switzerland*, 2011.

P. Bossart, F. Burrus, D. Jaeggi, and C. Nussbaum. The Mont Terri rock laboratory. In *Rock Mechanics and Engineering Volume 2*, pages 469–510. CRC Press, 2017.

P. Bossart, F. Bernier, J. Birkholzer, C. Bruggeman, P. Connolly, S. Dewonck, M. Fukaya, M. Herfort, M. Jensen, J.-M. Matray, and Others. Mont Terri rock laboratory, 20 years of research: introduction, site characteristics and overview of experiments. In *Mont Terri Rock Laboratory, 20 Years*, pages 3–22. Springer, 2018.

M. H. P. Bott. The mechanics of oblique slip faulting. *Geological Magazine*, 96(2): 109–117, 1959.

J. D. Bredehoeft, R. G. Wolff, W. S. Keys, and E. Shuter. Hydraulic fracturing to determine the regional in situ stress field, Piceance Basin, Colorado. *Geological Society of America Bulletin*, 87(2):250–258, 1976. ISSN 1943-2674.

J. S. Caine, J. P. Evans, and C. B. Forster. Fault zone architecture and permeability structure. *Geology*, 24(11):1025–1028, 1996.

F. Cappa, Y. Guglielmi, J. Rutqvist, C.-F. Tsang, and A. Thoraval. Hydromechanical modelling of pulse tests that measure fluid pressure and fracture normal displacement at the coaraze laboratory site, france. *International Journal of Rock Mechanics and Mining Sciences*, 43(7):1062–1082, 2006.

F. Cappa, Y. Guglielmi, C. Nussbaum, and J. Birkholzer. On the Relationship Between Fault Permeability Increases, Induced Stress Perturbation, and the Growth of Aseismic Slip During Fluid Injection. *Geophysical Research Letters*, (October), 2018. ISSN 00948276. doi: 10.1029/2018GL080233. URL `http://doi.wiley.com/10.1029/2018GL080233`.

F. Cappa, M. M. Scuderi, C. Collettini, Y. Guglielmi, and J.-P. Avouac. Stabilization of fault slip by fluid injection in the laboratory and in situ. *Science advances*, 5 (3):eaau4065, 2019.

E. Carey. *Analyse numérique d'un modèle mécanique élémentaire appliqué à l'étude d'une population de failles: calcul d'un tenseur moyen des contraintes à partir des stries de glissement. Thèse de troisième cycle, Tectonique Générale.* PhD thesis, Université de Paris Sud, Orsay, 1976.

E. Carey and B. Brunier. Analyse théorique et numérique d'un modèle mécanique élémentaire appliqué à l'étude d'une population de failles. *C. R. Acad. Sci.*, 279 (D):891–894, 1974.

M. E. Carey. Analyse théorique et numérique d'un modèle mécanique élémentaire appliqué à l'étude d'une population de failes. *Compte Rendus Hebdomadaires des Seances de l'Academie des Science*, 279:891–894, 1974.

B. Célérier, A. Etchecopar, F. Bergerat, P. Vergely, F. Arthaud, and P. Laurent. Inferring stress from faulting: from early concepts to inverse methods. *Tectonophysics*, 581:206–219, 2012. ISSN 0040-1951.

C. Chang and Y. Jo. Heterogeneous in situ stress magnitudes due to the presence of weak natural discontinuities in granitic rocks. *Tectonophysics*, 664:83–97, 2015.

J. Cochard. *Analysis of thereservoir properties of a fractured microporous carbonate series:Integrated sedimentological, diagenetical and mechanicalmultiscalar approaches*. PhD thesis, 2018.

F. H. Cornet. Stresses in rock and rock masses. In *Rock Testing and Site Characterization*, pages 297–327. Elsevier, 1993.

F. H. Cornet. Relation entre des mouvements sismiques et non sismiques induits par des injections de fluides sous pression. *Hydrogeology Journal*, 20(8):1463–1466, 2012. ISSN 14312174. doi: 10.1007/s10040-012-0901-z.

F. H. Cornet. Seismic and aseismic motions generated by fluid injections. *Geomechanics for Energy and the Environment*, 5:42–54, 2016. ISSN 23523808. doi: 10.1016/j.gete.2015.12.003. URL `http://dx.doi.org/10.1016/j.gete.2015.12.003`.

F. H. Cornet and P. Julien. Stress determination from hydraulic test data and focal mechanisms of induced seismicity. In *International Journal of Rock Mechanics and Mining Sciences & Geomechanics Abstracts*, volume 26, pages 235–248. Elsevier, 1989. ISBN 0148-9062.

F. H. Cornet and B. Valette. In situ stress determination from hydraulic injection test data. *Journal of Geophysical Research: Solid Earth*, 89(B13):11527–11537, 1984. ISSN 0148-0227.

F. H. Cornet, J. Helm, H. Poitrenaud, and A. Etchecopar. Seismic and aseismic slips induced by large-scale fluid injections. *Pure and Applied Geophysics*, 150 (3-4):563–583, 1997. ISSN 00334553. doi: 10.1007/s000240050093.

C. Coulomb. Test on the applications of the rules of maxima and minima to some problems of statics related to architecture. *Mem Math Phys*, 7:343–382, 1773.

P. A. Cundall. Formulation of a three-dimensional distinct element model—part i. a scheme to detect and represent contacts in a system composed of many polyhedral blocks. In *International Journal of Rock Mechanics and Mining Sciences & Geomechanics Abstracts*, volume 25, pages 107–116. Elsevier, 1988.

A. A. Daneshy. True and apparent direction of hydraulic fractures. In *Drilling and Rock Mechanics Conference*. Society of Petroleum Engineers, 1971. ISBN 1555638015.

L. De Barros, G. Daniel, Y. Guglielmi, D. Rivet, H. Caron, X. Payre, G. Bergery, P. Henry, R. Castilla, P. Dick, et al. Fault structure, stress, or pressure control of the seismicity in shale? insights from a controlled experiment of fluid-induced fault reactivation. *Journal of Geophysical Research: Solid Earth*, 121(6):4506–4522, 2016.

L. De Barros, Y. Guglielmi, D. Rivet, F. Cappa, and L. Duboeuf. Seismicity and fault aseismic deformation caused by fluid injection in decametric in-situ experiments. *Comptes Rendus Geoscience*, 350(8):464–475, 2018.

L. De Barros, F. Cappa, Y. Guglielmi, L. Duboeuf, and J.-R. Grasso. Energy of injection-induced seismicity predicted from in-situ experiments. *Scientific reports*, 9(1):1–11, 2019.

D. Delvaux and B. Sperner. New aspects of tectonic stress inversion with reference to the TENSOR program. *Geological Society, London, Special Publications*, 212(1): 75–100, 2003. ISSN 0305-8719. doi: 10.1144/GSL.SP.2003.212.01.06. URL `https://pubs.geoscienceworld.org/books/book/1591/chapter/107360955/`.

B. Derode, Y. Guglielmi, L. De Barros, and F. Cappa. Seismic responses to fluid pressure perturbations in a slipping fault. *Geophysical Research Letters*, 42(9): 3197–3203, 2015. ISSN 19448007. doi: 10.1002/2015GL063671.

E. Detournay. HYDRAULIC CONDUCTIVITY OF CLOSED ROCK FRACTURE: AN EXPERIMENTAL AND ANALYTICAL STUDY. In *Can Rock Mech Symp Proc 13th, Underground Rock Eng, The HR Rice Mem Symp*. CIM, 1980.

T. Doe and J. Remer. Analysis of constant-head well tests in nonporous fractured rock. Technical report, 1981.

L. Duboeuf. *Injections de fluide dans une zone de faille (LSBB , Rustrel) : sismicité induite et déformation asismique .* PhD thesis, 2018.

L. Duboeuf, L. De Barros, F. Cappa, Y. Guglielmi, A. Deschamps, and S. Seguy. Aseismic Motions Drive a Sparse Seismicity During Fluid Injections Into a Fractured Zone in a Carbonate Reservoir. *Journal of Geophysical Research: Solid Earth*, 122(10):8285–8304, 2017. ISSN 21699356. doi: 10.1002/2017JB014535.

J. M. Dupin, W. Sassi, and J. Angelier. Homogeneous stress hypothesis and actual fault slip: a distinct element analysis. *Journal of Structural Geology*, 15(8):1033–1043, 1993. ISSN 01918141. doi: 10.1016/0191-8141(93)90175-A.

B. Edwards, T. Kraft, C. Cauzzi, P. Kästli, and S. Wiemer. Seismic monitoring and analysis of deep geothermal projects in st gallen and basel, switzerland. *Geophysical Journal International*, 201(2):1022–1039, 2015.

W. L. Ellsworth. Injection-induced earthquakes. *Science*, 341(6142):1225942, 2013.

J. Eshelby. The determination of the elastic field of an ellipsoidal inclution and related problems. *Proceedings of the Physical Society of London, Series A*, 241: 376–396, 1957. ISSN 1364-5021. doi: 10.1098/rspa.1983.0054.

J. D. Eshelby. The elastic field outside an ellipsoidal inclusion. *Proc. R. Soc. Lond. A*, 252(1271):561–569, 1959. ISSN 0080-4630.

J. D. Eshelby. Elastic inclusions and inhomogeneities. *Progress in solid mechanics*, 2(1):89–140, 1961.

A. Etchecopar, G. Vasseur, and M. Daignieres. An inverse problem in microtectonics for the determination of stress tensors from fault striation analysis. *Journal of Structural Geology*, 3(1):51–65, 1981. ISSN 0191-8141.

K. F. Evans, C. H. Scholz, and T. Engelder. An analysis of horizontal fracture initiation during hydrofrac stress measurements in granite at North Conway, New Hampshire. *Geophysical Journal International*, 93(2):251–264, 1988. ISSN 1365-246X.

K. F. Evans, A. Genter, and J. Sausse. Permeability creation and damage due to massive fluid injections into granite at 3.5 km at soultz: 1. borehole observations. *Journal of Geophysical Research: Solid Earth*, 110(B4), 2005.

K. F. Evans, A. Zappone, T. Kraft, N. Deichmann, and F. Moia. A survey of the induced seismic responses to fluid injection in geothermal and CO2reservoirs in Europe. *Geothermics*, 41:30–54, 2012. ISSN 03756505. doi: 10.1016/j.geothermics.2011.08.002. URL `http://dx.doi.org/10.1016/j.geothermics.2011.08.002`.

D. Faulkner, T. Mitchell, D. Healy, and M. Heap. Slip on'weak'faults by the rotation of regional stress in the fracture damage zone. *Nature*, 444(7121):922, 2006.

Y. Feng, J. P. Harrison, et al. A novel method for constructing confidence intervals for in situ stress. In *ISRM International Symposium-10th Asian Rock Mechanics Symposium*. International Society for Rock Mechanics and Rock Engineering, 2018.

S. Gaines, M. S. Diederichs, and D. J. Hutchinson. Review of borehole in situ stress measurement techniques for various ground conditions and numerical stress estimation considerations. In *46th US Rock Mechanics/Geomechanics Symposium*. American Rock Mechanics Association, 2012.

K. Gao and J. P. Harrison. Generation of random stress tensors. *International Journal of Rock Mechanics and Mining Sciences*, 94:18–26, 2017.

K. Gao and J. P. Harrison. Multivariate distribution model for stress variability characterisation. *International Journal of Rock Mechanics and Mining Sciences*, 102:144–154, 2018a.

K. Gao and J. P. Harrison. Re-examination of the in situ stress measurements on the 240 level of the aecl's url using tensor-based approaches. *Rock Mechanics and Rock Engineering*, 51(10):3179–3188, 2018b.

K. Gao and J. P. Harrison. Examination of mean stress calculation approaches in rock mechanics. *Rock Mechanics and Rock Engineering*, 52(1):83–95, 2019.

J. W. Gephart and D. W. Forsyth. An improved method for determining the regional stress tensor using earthquake focal mechanism data: application to the San Fernando earthquake sequence. *Journal of Geophysical Research: Solid Earth*, 89(B11):9305–9320, 1984. ISSN 2156-2202.

S. D. Goodfellow, M. H. Nasseri, S. C. Maxwell, and R. P. Young. Hydraulic fracture energy budget: Insights from the laboratory. *Geophysical Research Letters*, 42(9): 3179–3187, 2015. ISSN 19448007. doi: 10.1002/2015GL063093.

H. E. Goodman, S. W. Imbus, T. Espie, C. Minnig, U. Rösli, T. Fierz, and Y. Lettry. Large Rock Mass Experimentation @ Mont Terri Underground Research Laboratory - CO 2 Containment Assurance Experiments. *Energy Procedia*, 114(November 2016):5139–5150, 2017. ISSN 18766102. doi: 10.1016/j.egypro.2017.03.1668. URL `http://dx.doi.org/10.1016/j.egypro.2017.03.1668`.

Y. Guglielmi. Mont Terri Project. Technical note 2015-60. Phase 21. In-situ clay faults slip hydro-mechanical characterizatiom (FS experiment), Mont Terri underground rock laboratory. Technical Report February, 2016.

Y. Guglielmi, F. Cappa, and D. Amitrano. High-definition analysis of fluid-induced seismicity related to the mesoscale hydromechanical properties of a fault zone. *Geophysical Research Letters*, 35(6):1–6, 2008. ISSN 00948276. doi: 10.1029/2007GL033087.

Y. Guglielmi, F. Cappa, H. Lançon, J. B. Janowczyk, J. Rutqvist, C. F. Tsang, and J. S. Y. Wang. ISRM Suggested Method for Step-Rate Injection Method for Fracture In-Situ Properties (SIMFIP): Using a 3-Components Borehole Deformation Sensor. In *The ISRM Suggested Methods for Rock Characterization, Testing and Monitoring: 2007-2014*, pages 179–186. Springer International Publishing, Cham, 2013. doi: 10.1007/978-3-319-07713-0{_}14. URL `http://link.springer.com/10.1007/978-3-319-07713-0_14`.

Y. Guglielmi, F. Cappa, J. P. Avouac, P. Henry, and D. Elsworth. Seismicity triggered by fluid injection-induced aseismic slip. *Science*, 348(6240):1224–1226, 2015a. ISSN 10959203. doi: 10.1126/science.aab0476.

Y. Guglielmi, D. Elsworth, F. Cappa, P. Henry, C. Gout, P. Dick, and J. Durand. In situ observations on the coupling between hydraulic diffusivity and displacements during fault reactivation in shales. *Journal of Geophysical Research: Solid Earth*, 120(11):7729–7748, 2015b.

Y. Guglielmi, P. Henry, C. Nussbaum, P. Dick, C. Gout, F. Amann, et al. Underground research laboratories for conducting fault activation experiments in shales. In *49th US Rock Mechanics/Geomechanics Symposium*. American Rock Mechanics Association, 2015c.

Y. Guglielmi, J. Birkholzer, J. Rutqvist, P. Jeanne, and C. Nussbaum. Can Fault Leakage Occur before or Without Reactivation? Results from an in Situ Fault Reactivation Experiment at Mont Terri. *Energy Procedia*, 114(July):3167–3174, 2017. ISSN 18766102. doi: 10.1016/j.egypro.2017.03.1445. URL `http://dx.doi.org/10.1016/j.egypro.2017.03.1445`.

Y. Guglielmi, C. Nussbaum, P. Jeanne, J. Rutqvist, F. Cappa, and J. Birkholzer. Influence of Stress on Fluid Leakage in a Fault Zone in Shales Estimated from Downhole Displacements and Pressure Measurements Recorded During In Situ Hydraulic Injection. *Submitted to ...*, 2019.

F. Guo, N. R. Morgenstern, and J. D. Scott. Interpretation of hydraulic fracturing pressure: a comparison of eight methods used to identify shut-in pressure. In *International journal of rock mechanics and mining sciences & geomechanics abstracts*, volume 30, pages 627–631. Elsevier, 1993. ISBN 0148-9062.

B. Haimson, C. Fairhurst, et al. Initiation and extension of hydraulic fractures in rocks. *Society of Petroleum Engineers Journal*, 7(03):310–318, 1967.

B. C. Haimson. The hydraulic fracturing method of stress measurement: theory and practice. In *Rock testing and site characterization*, pages 395–412. Elsevier, 1993.

B. C. Haimson and F. H. Cornet. ISRM suggested methods for rock stress estimationâpart 3: hydraulic fracturing (HF) and/or hydraulic testing of pre-existing fractures (HTPF). *International Journal of Rock Mechanics and Mining Sciences*, 40(7-8):1011–1020, 2003. ISSN 1365-1609.

P. L. Hancock. Brittle microtectonics: principles and practice. *Journal of structural geology*, 7(3-4):437–457, 1985. ISSN 0191-8141.

J. A. Hansen. Direct inversion of stress, strain or strain rate including vorticity: A linear method of homogenous fault-slip data inversion independent of adopted hypothesis. *Journal of Structural Geology*, 51:3–13, 2013. ISSN 01918141. doi: 10.1016/j.jsg.2013.03.014. URL `http://dx.doi.org/10.1016/j.jsg.2013.03.014`.

M. O. Häring, U. Schanz, F. Ladner, and B. C. Dyer. Characterisation of the basel 1 enhanced geothermal system. *Geothermics*, 37(5):469–495, 2008.

R. Hart, P. A. Cundall, and J. Lemos. Formulation of a three-dimensional distinct element modelâPart II. Mechanical calculations for motion and interaction of a system composed of many polyhedral blocks. In *International Journal of Rock Mechanics and Mining Sciences & Geomechanics Abstracts*, volume 25, pages 117–125. Elsevier, 1988. ISBN 0148-9062.

D. Healy. Elastic field in 3D due to a spheroidal inclusionâMATLABâ code for Eshelby's solution. *Computers & Geosciences*, 35(10):2170–2173, 2009. ISSN 0098-3004.

P. Henry, A. Morereau, and Y. Guglielmi. Estimation of permeability in mont terri fault zone from fs experiments. *Presentation at the Mont Terri conference in Nancy*, pages –, 2018.

B. Hostettler, A. G. Reisdorf, D. Jaeggi, G. Deplazes, H. Bläsi, A. Morard, S. Feist-Burkhardt, A. Waltschew, V. Dietze, and U. Menkveld-Gfeller. Litho-and biostratigraphy of the Opalinus Clay and bounding formations in the Mont Terri rock laboratory (Switzerland). In *Mont Terri Rock Laboratory, 20 Years*, pages 23–39. Springer, 2018.

M. K. Hubbert and W. W. Rubey. Mechanics of fluid-filled porous solids and its application to overthrust faulting. *Geological Society of America Bulletin*, 70(2): 115–166, 1959.

M. K. Hubbert and D. G. Willis. Mechanics of hydraulic fracturing: Transactions of the American Institute of Mining and Engineering, v. 210. 1957.

J.-H. Hung, K.-F. Ma, C.-Y. Wang, H. Ito, W. Lin, and E.-C. Yeh. Subsurface structure, physical properties, fault-zone characteristics and stress state in scientific drill holes of Taiwan Chelungpu Fault Drilling Project. *Tectonophysics*, 466 (3-4):307–321, 2009. ISSN 0040-1951.

Itasca Consulting Group. Inc. 3DEC (Three-Dimensional Distinct Element Code), Version 5.0. Minneapolis, MN., 2007.

T. Ito, K. Evans, K. Kawai, and K. Hayashi. Hydraulic fracture reopening pressure and the estimation of maximum horizontal stress. *International Journal of Rock Mechanics and Mining Sciences*, 36(6):811–826, 1999. ISSN 1365-1609.

J. C. Jaeger, N. G. Cook, and R. Zimmerman. *Fundamentals of rock mechanics*. John Wiley & Sons, 2009.

D. Jaeggi, B. Laurich, C. Nussbaum, K. Schuster, and P. Connolly. Tectonic structure of the âMain Faultâ in the Opalinus Clay, Mont Terri rock laboratory (Switzerland). *Swiss Journal of Geosciences*, 110(1):67–84, 2017. ISSN 1661-8726.

D. Jaeggi, B. Laurich, C. Nussbaum, K. Schuster, and P. Connolly. Tectonic structure of the a Main Fault in the Opalinus Clay, Mont Terri rock laboratory (Switzerland). In *Mont Terri Rock Laboratory, 20 Years*, pages 69–86. Springer, 2018.

P. Jeanne, Y. Guglielmi, J. Lamarche, F. Cappa, and L. Marié. Architectural characteristics and petrophysical properties evolution of a strike-slip fault zone in a fractured porous carbonate reservoir. *Journal of Structural Geology*, 44: 93–109, 2012. ISSN 01918141. doi: 10.1016/j.jsg.2012.08.016. URL `http://dx.doi.org/10.1016/j.jsg.2012.08.016`.

P. Jeanne, Y. Guglielmi, and F. Cappa. Dissimilar properties within a carbonate-reservoir's small fault zone, and their impact on the pressurization and leakage associated with co2 injection. *Journal of Structural Geology*, 47:25–35, 2013.

P. Jeanne, J. Rutqvist, C. Hartline, J. Garcia, P. F. Dobson, and M. Walters. Reservoir structure and properties from geomechanical modeling and microseismicity analyses associated with an enhanced geothermal system at the geysers, california. *Geothermics*, 51:460–469, 2014.

P. Jeanne, J. Rutqvist, P. F. Dobson, J. Garcia, M. Walters, C. Hartline, and A. Borgia. Geomechanical simulation of the stress tensor rotation caused by injection of cold water in a deep geothermal reservoir. *Journal of Geophysical Research: Solid Earth*, 120(12):8422–8438, 2015.

P. Jeanne, Y. Guglielmi, J. Rutqvist, C. Nussbaum, and J. Birkholzer. Field characterization of elastic properties across a fault zone reactivated by fluid injection. *Journal of Geophysical Research: Solid Earth*, 122(8):6583–6598, 2017. ISSN 21699356. doi: 10.1002/2017JB014384.

P. Jeanne, Y. Guglielmi, J. Rutqvist, C. Nussbaum, and J. Birkholzer. Permeability Variations Associated With Fault Reactivation in a Claystone Formation Investigated by Field Experiments and Numerical Simulations. *Journal of Geophysical Research: Solid Earth*, (1):1–17, 2018a. ISSN 21699356. doi: 10.1002/2017JB015149.

P. Jeanne, Y. Guglielmi, J. Rutqvist, C. Nussbaum, and J. Birkholzer. Permeability variations associated with fault reactivation in a claystone formation investigated by field experiments and numerical simulations. *Journal of Geophysical Research: Solid Earth*, 123(2):1694–1710, 2018b.

J. Ju and L. Sun. A novel formulation for the exterior-point Eshelby's tensor of an ellipsoidal inclusion. *Journal of applied mechanics*, 66(June 1999):570–574, 1999. ISSN 00218936. doi: 10.1115/1.2791090. URL `http://appliedmechanics.asmedigitalcollection.asme.org/article.aspx?articleid=1413730`.

J. W. Ju and L. Z. Sun. Effective elastoplastic behavior of metal matrix composites containing randomly located aligned spheroidal inhomogeneities. Part I: micromechanics-based formulation. *International Journal of Solids and Structures*, 38(2):183–201, 2001. ISSN 0020-7683.

U. Kastrup. *Seismotectonics and stress field variations in Switzerland*. PhD thesis, 2002.

J. Kaven, F. Maerten, and D. Pollard. Mechanical analysis of fault slip data: Implications for paleostress analysis. *Journal of structural geology*, 33(2):78–91, 2011.

O. Lacombe, J. Angelier, P. Laurent, F. Bergerat, and C. Tourneret. Joint analyses of calcite twins and fault slips as a key for deciphering polyphase tectonics: Burgundy as a case study. *Tectonophysics*, 182(3-4):279–300, 1990.

B. Laurich. Evolution of microstructure and porosity in faulted Opalinus Clay, 2015.

B. Laurich, J. L. Urai, G. Desbois, C. Vollmer, and C. Nussbaum. Microstructural evolution of an incipient fault zone in Opalinus Clay: Insights from an optical and electron microscopic study of ion-beam polished samples from the Main Fault in the Mt-Terri Underground Research Laboratory. *Journal of Structural Geology*, 67:107–128, 2014.

X. Le Pichon, F. Bergerat, and M.-J. Roulet. Plate kinematics and tectonics leading to the Alpine belt formation; a new analysis. *Geological Society of America Special Papers*, 218:111–132, 1988. ISSN 0072-1077.

M. Y. Lee and B. C. Haimson. Statistical evaluation of hydraulic fracturing stress measurement parameters. In *International Journal of Rock Mechanics and Mining Sciences & Geomechanics Abstracts*, volume 26, pages 447–456. Elsevier, 1989. ISBN 0148-9062.

Q. Lei and K. Gao. A numerical study of stress variability in heterogeneous fractured rocks. *International Journal of Rock Mechanics and Mining Sciences*, 113:121–133, 2019.

M. Lejri, F. Maerten, L. Maerten, and R. Soliva. Paleostress inversion: A multi-parametric geomechanical evaluation of the wallace–bott assumptions. *Tectonophysics*, 657:129–143, 2015.

J. Letouzey. Cenozoic paleo-stress pattern in the alpine foreland and structural interpretation in a platform basin. *Tectonophysics*, 132(1-3):215–231, 1986.

C. L. Liesa and J. L. Simón. Evolution of intraplate stress fields under multiple remote compressions: The case of the Iberian Chain (NE Spain). *Tectonophysics*, 474(1-2):144–159, 2009. ISSN 0040-1951.

W. Lin, K. Yamamoto, H. Ito, H. Masago, and Y. Kawamura. Estimation of minimum principal stress from an extended leak-off test onboard the Chikyu drilling vessel and suggestions for future test procedures. *Scientific drilling*, 6:43–47, 2008. ISSN 1816-8957.

R. J. Lisle. New method of estimating regional stress orientations: application to focal mechanism data of recent British earthquakes. *Geophysical Journal International*, 110(2):276–282, 1992. ISSN 1365-246X.

R. J. Lisle. Simple graphical constructions for the direction of shear. *Journal of Structural Geology*, 20(7):969–973, 1998. ISSN 0191-8141.

R. J. Lisle. A critical look at the Wallace-Bott hypothesis in fault-slip analysis. *Bulletin de la Societe Geologique de France*, 184(4-5):299–306, 2013. ISSN 00379409. doi: 10.2113/gssgfbull.184.4-5.299.

C. Ljunggren, Y. Chang, T. Janson, and R. Christiansson. An overview of rock stress measurement methods. *International Journal of Rock Mechanics and Mining Sciences*, 40(7-8):975–989, 2003. ISSN 1365-1609.

B. Lund and R. Slunga. Stress tensor inversion using detailed microearthquake information and stability constraints: Application to Ölfus in southwest Iceland. *Journal of Geophysical Research: Solid Earth*, 104(B7):14947–14964, 1999. doi: 10.1029/1999jb900111.

L. Maerten. Variation in slip on intersecting normal faults: Implications for paleostress inversion. *Journal of Geophysical Research: Solid Earth*, 105(B11):25553–25565, 2000. doi: 10.1029/2000jb900264.

L. Maerten, F. Maerten, and M. Lejri. Along fault friction and fluid pressure effects on the spatial distribution of fault-related fractures. *Journal of Structural Geology*, 108:198–212, 2018. ISSN 0191-8141.

R. Marrett and R. W. Allmendinger. Kinematic analysis of fault-slip data. *Journal of structural geology*, 12(8):973–986, 1990. ISSN 0191-8141.

P. Marschall, J. Croisé, L. Schlickenrieder, J. Y. Boisson, P. Vogel, and S. Yamamoto. Synthesis of hydrogeological investigations at the Mont Terri site (phases 1 to 5). *Mont Terri Project–Hydrogeological Synthesis, Osmotic Flow, Report of the Federal Office for Water and Geology (Bern, Switzerland). Geology Series*, 6:7–92, 2004.

C. D. Martin and G. W. Lanyon. Measurement of in-situ stress in weak rocks at Mont Terri Rock Laboratory, Switzerland. *International Journal of Rock Mechanics and Mining Sciences*, 40(7-8):1077–1088, 2003. ISSN 1365-1609.

P. Martínez-Garzón, M. Bohnhoff, G. Kwiatek, and G. Dresen. Stress tensor changes related to fluid injection at the geysers geothermal field, california. *Geophysical Research Letters*, 40(11):2596–2601, 2013.

P. Martínez-Garzón, G. Kwiatek, M. Bohnhoff, and G. Dresen. Impact of fluid injection on fracture reactivation at The Geysers geothermal field. *Journal of Geophysical Research: Solid Earth*, 121(10):7432–7449, 2016. ISSN 21699356. doi: 10.1002/2016JB013137.

M. Mattauer and J. L. Mercier. Microtectonique et grande tectonique. *Mémoires hors série de la Societé géologique de France*, 10:141–161, 1980.

a. McGarr. Journal of Geophysical Research : Solid Earth. *Journal of Geophysical Research: Solid Earth*, pages 1–12, 2014. ISSN 21699313. doi: 10.1002/2013JB010597.Received.

C. Meng, W. Heltsley, and D. D. Pollard. Evaluation of the Eshelby solution for the ellipsoidal inclusion and heterogeneity. *Computers and Geosciences*, 40:40–48, 2012. ISSN 00983004. doi: 10.1016/j.cageo.2011.07.008. URL `http://dx.doi.org/10.1016/j.cageo.2011.07.008`.

J. L. Mercier, D. Sorel, P. Vergely, and K. Simeakis. Extensional tectonic regimes in the Aegean basins during the Cenozoic. *Basin research*, 2(1):49–71, 1989. ISSN 1365-2117.

A. J. Michael. Use of focal mechanisms to determine stress: a control study. *Journal of Geophysical Research: Solid Earth*, 92(B1):357–368, 1987.

T. M. Mitchell and D. R. Faulkner. The nature and origin of off-fault damage surrounding strike-slip fault zones with a wide range of displacements: A field study from the Atacama fault system, northern Chile. *Journal of Structural Geology*, 2009. ISSN 01918141. doi: 10.1016/j.jsg.2009.05.002.

M. J. A. Moein, B. Valley, and K. F. Evans. Scaling of fracture patterns in three deep boreholes and implications for constraining fractal discrete fracture network models. *Rock Mechanics and Rock Engineering*, 52(6):1723–1743, 2019.

A. Morris, D. A. Ferrill, and D. B. Henderson. Slip-tendency analysis and fault reactivation. *Geology*, 24(3):275–278, 1996.

T. Mura. Mechanics of elastic and inelastic solids, 1982.

E. J. Nelson, S. T. Chipperfield, R. R. Hillis, J. Gilbert, J. McGowen, and S. D. Mildren. The relationship between closure pressures from fluid injection tests and the minimum principal stress in strong rocks. *International Journal of Rock Mechanics and Mining Sciences*, 44(5):787–801, 2007. ISSN 1365-1609.

Á. Nieto-Samaniego and S. Alaniz-Alvarez. Origin and tectonic interpretation of multiple fault patterns. *Tectonophysics*, 270(3-4):197–206, 1997. ISSN 00401951. doi: 10.1016/S0040-1951(96)00216-8. URL `http://dx.doi.org/10.1016/S0040-1951(96)00216-8`.

C. Nussbaum, P. Bossart, F. Amann, and C. Aubourg. Analysis of tectonic structures and excavation induced fractures in the Opalinus Clay, Mont Terri underground rock laboratory (Switzerland). *Swiss Journal of Geosciences*, 104(2):187, 2011.

C. Pascal. Interaction of faults and perturbation of slip: Influence of anisotropic stress states in the presence of fault friction and comparison between Wallace-Bott and 3D distinct element models. *Tectonophysics*, 356(4):307–322, 2002. ISSN 00401951. doi: 10.1016/S0040-1951(02)00413-4.

J. P. Petit. Criteria for the sense of movement on fault surfaces in brittle rocks. *Journal of Structural Geology*, 9(5-6):597–608, 1987. ISSN 01918141. doi: 10.1016/0191-8141(87)90145-3.

D. Pollard, S. Saltzer, and A. M. Rubin. Stress inversion methods: are they based on faulty assumptions? *Journal of Structural Geology*, 15(8):1045–1054, 1993.

D. D. Pollard. The theoretical displacements and stresses near fractures in rock: with applications to faults, joints, veins, dikes, and solution surfaces. *Fracture mechanics of rock*, pages 277–349, 1987.

P. M. Quinn, B. L. Parker, and J. A. Cherry. Using constant head step tests to determine hydraulic apertures in fractured rock. *Journal of Contaminant Hydrology*, 2011. ISSN 01697722. doi: 10.1016/j.jconhyd.2011.07.002.

M. Rajabi, M. Tingay, R. King, and O. Heidbach. Present-day stress orientation in the clarence-moreton basin of new south wales, australia: a new high density dataset reveals local stress rotations. *Basin Research*, 29:622–640, 2017.

E. A. Rakhmanov, E. Saff, and Y. Zhou. Minimal discrete energy on the sphere. *Math. Res. Lett*, 1(6):647–662, 1994.

P. A. Reasenberg. Fpfit, fpplot, and fppage: Fortran computer programs for calculating and displaying earthquake fault-plane solutions. *US Geol. Surv. Open-File Rep.*, pages 85–739, 1985.

Z. Reches. Determination of the tectonic stress tensor from slip along faults that obey the Coulomb yield condition. *Tectonics*, 6(6):849–861, 1987. ISSN 1944-9194.

D. Rivet, L. De Barros, Y. Guglielmi, F. Cappa, R. Castilla, and P. Henry. Seismic velocity changes associated with aseismic deformations of a fault stimulated by fluid injection. *Geophysical Research Letters*, 43(18):9563–9572, 2016. ISSN 19448007. doi: 10.1002/2016GL070410.

V. Roche, M. van Der Baan, and G. Preisig. A study of 3D modeling of hydraulic fracturing and stress perturbations during fluid injection. *Journal of Petroleum Science and Engineering*, 170(November 2017):829–843, 2018. ISSN 09204105. doi: 10.1016/j.petrol.2018.06.037. URL `https://doi.org/10.1016/j.petrol.2018.06.037`.

A. Ruina. Slip Instability and State Variable Friction Laws. *Journal of Geophysical Research*, 88(B12):10359–10370, 1983.

J. Rutqvist, C.-F. Tsang, and O. Stephansson. Uncertainty in the maximum principal stress estimated from hydraulic fracturing measurements due to the presence of the induced fracture. *International Journal of Rock Mechanics and Mining Sciences*, 37(1-2):107–120, 2000. ISSN 1365-1609.

D. M. Saffer and C. Marone. Comparison of smectite-and illite-rich gouge frictional properties: application to the updip limit of the seismogenic zone along subduction megathrusts. *Earth and Planetary Science Letters*, 215(1-2):219–235, 2003.

D. P. Sahara, M. Schoenball, T. Kohl, and B. I. Müller. Impact of fracture networks on borehole breakout heterogeneities in crystalline rock. *International Journal of Rock Mechanics and Mining Sciences*, 71:301–309, 2014.

G. Schaeren and J. Norbert. Tunnels du Mont Terri et du Mont Russelin. La traversée des âroches à risques': marnes et marnes à anhydrite. *Juradurchquerungen aktuelle Tunnelprojekte im Jura Mitteilungen der Schweizerischen Gesellschaft für Boden-und Felsmechanik*, 119:19–24, 1989.

D. R. Schmitt, C. A. Currie, and L. Zhang. Crustal stress determination from boreholes and rock cores: Fundamental principles. *Tectonophysics*, 580:1–26, 2012. ISSN 0040-1951.

M. Schoenball and N. C. Davatzes. Quantifying the heterogeneity of the tectonic stress field using borehole data. *Journal of Geophysical Research: Solid Earth*, 122(8):6737–6756, 2017.

C. H. Scholz. Earthquakes and friction laws. *Nature*, 391(6662):37–42, 1998. ISSN 00280836. doi: 10.1038/34097.

P. Segall. Fault mechanics. *Reviews of Geophysics Supplement*, 29:864–876, 1991. ISSN 8755-1209.

G. Shamir and M. D. Zoback. Stress orientation profile to 3.5 km depth near the san andreas fault at cajon pass, california. *Journal of Geophysical Research: Solid Earth*, 97(B4):5059–5080, 1992.

S. A. Shapiro and C. Dinske. Fluid-induced seismicity: Pressure diffusion and hydraulic fracturing. *Geophysical Prospecting*, 57(2):301–310, 2009. ISSN 13652478. doi: 10.1111/j.1365-2478.2008.00770.x.

S. A. Shapiro, P. Audigane, and J. J. Royer. Large-scale in situ permeability tensor of rocks from induced microseismicity. *Geophysical Journal International*, 137(1): 207–213, 1999. ISSN 0956540X. doi: 10.1046/j.1365-246X.1999.00781.x.

S. a. Shapiro, R. Patzig, E. Rothert, and J. Rindschwentner. Triggering of Seismicity by Pore-pressure Perturbations: Permeability-related Signatures of the Phenomenon. *Pure and Applied Geophysics*, 160(5):1051–1066, 2003. ISSN 0033-4553. doi: 10.1007/PL00012560.

R. H. Sibson. Fault rocks and fault mechanisms. *Journal of the Geological Society*, 133(3):191–213, 1977. ISSN 00167649. doi: 10.1144/gsjgs.133.3.0191.

R. Soliva, F. Maerten, J.-P. Petit, and V. Auzias. Field evidences for the role of static friction on fracture orientation in extensional relays along strike-slip faults: comparison with photoelasticity and 3-D numerical modeling. *Journal of Structural Geology*, 32(11):1721–1731, 2010. ISSN 0191-8141.

T. Terakawa, S. A. Miller, and N. Deichmann. High fluid pressure and triggered earthquakes in the enhanced geothermal system in Basel, Switzerland. *Journal of Geophysical Research: Solid Earth*, 117(7):1–15, 2012. ISSN 21699356. doi: 10.1029/2011JB008980.

M. Thury and P. Bossart. Results of the hydrogeological, geochemical and geotechnical experiments performed in the Opalinus Clay (1996-1997). Chapter 6.4 Organic Matter Characterisation of Rocks and Pore Waters. Technical report, Geological report, 1999.

R. J. Twiss and M. J. Gefell. Curved slickenfibers: a new brittle shear sense indicator with application to a sheared serpentinite. *Journal of Structural Geology*, 12(4): 471–481, 1990.

B. Valley and K. F. Evans. Stress state at soultz-sous-forêts to 5 km depth from wellbore failure and hydraulic observations. In *Proceedings, 32nd workshop on geothermal reservoir engineering*, pages 17481–17469, 2007.

B. Valley, M. Jalali, M. Ziegler, and K. Evans. Constraining dfn characteristics for deep geothermal projects by considering the effects of fractures on stress variability. In *International discrete fracture network engineering conference DFNE*, 2014.

B. C. Valley. *The relation between natural fracturing and stress heterogeneities in deep-seated crystalline rocks at Soultz-sous-Forêts (France)*. PhD thesis, ETH Zurich, 2007.

S. Vandycke, F. Bergerat, and C. Dupuis. Meso-cenozoic faulting and inferred palaeostresses in the mons basin, belgium. *Tectonophysics*, 192(3-4):261–271, 1991.

V. Vavryčuk. Iterative joint inversion for stress and fault orientations from focal mechanisms. *Geophysical Journal International*, 199(1):69–77, 2014. ISSN 1365246X. doi: 10.1093/gji/ggu224.

R. E. Wallace. Geometry of shearing stress and relation to faulting. *The Journal of Geology*, 59(2):118–130, 1951. ISSN 0022-1376. doi: 10.1086/625831. URL `http://www.journals.uchicago.edu/doi/abs/10.1086/625831`.

R. E. Wallace and H. T. Morris. Characteristics of faults and shear zones in deep mines. *Pure and Applied Geophysics*, 124(1-2):107–125, 1986. ISSN 0033-4553.

J. B. Walsh. Effect of pore pressure and confining pressure on fracture permeability. In *International Journal of Rock Mechanics and Mining Sciences & Geomechanics Abstracts*, volume 18, pages 429–435. Elsevier, 1981. ISBN 0148-9062.

N. R. Warpinski and L. W. Teufel. In situ stress measurements at Rainier Mesa, Nevada test siteâinfluence of topography and lithology on the stress state in tuff. In *International Journal of Rock Mechanics and Mining Sciences & Geomechanics Abstracts*, volume 28, pages 143–161. Elsevier, 1991. ISBN 0148-9062.

C. A. J. Wibberley and Z. K. Shipton. Fault zones: A complex issue. *Journal of Structural Geology*, 32(11):1554–1556, 2010.

T. Wiles and P. Kaiser. In situ stress determination using the under-excavation technique—i. theory. In *International journal of rock mechanics and mining sciences & geomechanics abstracts*, volume 31, pages 439–446. Elsevier, 1994.

S. M. Willson, N. C. Last, M. D. Zoback, and D. Moos. Drilling in South America: a wellbore stability approach for complex geologic conditions. In *Latin American and Caribbean petroleum engineering conference*. Society of Petroleum Engineers, 1999. ISBN 155563365X.

P. A. Witherspoon, J. S. Y. Wang, K. Iwai, and J. E. Gale. Validity of cubic law for fluid flow in a deformable rock fracture. *Water resources research*, 16(6): 1016–1024, 1980. ISSN 1944-7973.

D. P. Yale. Fault and stress magnitude controls on variations in the orientation of in situ stress. *Geological Society, London, Special Publications*, 209(1):55–64, 2003.

A. Yamaji. The multiple inverse method: a new technique to separate stresses from heterogeneous fault-slip data. *Journal of Structural Geology*, 22(4):441–452, 2000.

A. Yamaji. Are the solutions of stress inversion correct? visualization of their reliability and the separation of stresses from heterogeneous fault-slip data. *Journal of Structural Geology*, 25(2):241–252, 2003.

A. Zang and O. Stephansson. *Stress field of the Earth's crust*. Springer Science & Business Media, 2009. ISBN 1402084447.

M. D. Zoback. *Reservoir geomechanics*. Cambridge University Press, 2010.

M. D. Zoback and S. M. Gorelick. Earthquake triggering and large-scale geologic storage of carbon dioxide. *Proceedings of the National Academy of Sciences*, 109 (26):10164–10168, 2012.

M. D. Zoback and H.-P. Harjes. Injection-induced earthquakes and crustal stress at 9 km depth at the KTB deep drilling site, Germany. *Journal of Geophysical Research: Solid Earth*, 102(B8):18477–18491, 1997. ISSN 01480227. doi: 10.1029/96JB02814. URL `http://doi.wiley.com/10.1029/96JB02814`.

M. D. Zoback, C. A. Barton, M. Brudy, D. A. Castillo, T. Finkbeiner, B. R. Grollimund, D. B. Moos, P. Peska, C. D. Ward, and D. J. Wiprut. Determination of stress orientation and magnitude in deep wells. *International Journal of Rock Mechanics and Mining Sciences*, 40(7-8):1049–1076, 2003. ISSN 1365-1609.

M. D. Zoback, A. Kohli, I. Das, and M. McClure. The importance of slow slip on faults during hydraulic fracturing stimulation of shale gas reservoirs. *Society of Petroleum Engineers - SPE Americas Unconventional Resources Conference 2012*, (2011):344–352, 2012.

M. L. Zoback, G. Thompson, and R. Anderson. Cainozoic evolution of the state of stress and style of tectonism of the basin and range province of the western united states. *Philosophical Transactions of the Royal Society of London. Series A, Mathematical and Physical Sciences*, 300(1454):407–434, 1981.